High Resolution Spectroscopy, Normal Mode Analysis, and Franck-Condon Factors Calculation of Transition Metal-Containing Molecules

by

Anh Thu Le

A Dissertation Presented in Partial Fulfillment
of the Requirements for the Degree
Doctor of Philosophy

Approved April 2013 by the
Graduate Supervisory Committee:

Timothy Steimle, Chair
Ranko Richert
Andrew Chizmeshya

ARIZONA STATE UNIVERSITY

May 2013

ABSTRACT

The objective of the present investigations is to experimentally determine the fundamental molecular properties of the transient metal containing pieces. The transient molecules have been generated using laser ablation production technique and detected by using laser induced fluorescence technique. Ultra-high resolution spectra of the diatomic molecules, ^{87}SrF, $^{135\&137}$BaF, YbF, HfF, and IrSi were recorded at a resolution of approximately 30 Mhz. The fine and hyperfine structure of these molecules were determined for the ground and the excited state. The optical Stark splittings of ^{180}HfF and IrSi were recorded and analyzed to determine the permanent electric dipole moments of the ground and the excited state. An effective Hamiltonian operator, including the rotational, centrifugal distortion, spin-orbit, spin-spin, spin-rotation, λ-doubling, magnetic hyperfine and quadrupole interactions, and Stark effect, was employed to model and analyze the recorded spectra.

The electronic spectra of the triatomic molecules, TiO_2 and ZrO_2, were recorded using pulsed dye laser, LIF, spectrometer at a resolution of 300MHz. These molecules have C_{2v} symmetry. The harmonic frequencies, lifetime measurements were determined. These spectra of ZrO_2 and TiO_2 were modeled using a normal coordinate analysis and Franck-Condon factor predictions. High resolution field-free and Stark effect spectra of ZrO_2 were recorded and for future investigation.

DEDICATION

This thesis is dedicated to my parent for their love, endless support and encouragement.

ACKNOWLEDGMENTS

First and foremost, I would like to thank my parents for their support and motivation throughout my life. I could not have done this without them. My parents are the people who have always been there for me, listened to all of my problems, stood by all of my decision (good or bad), given me their unconditional love. My parents are the best teacher that I ever had, I was born neither talent nor a scientist, however what my parents have taught me over the years are: in order to succeed, I always have to try hard, never quit, and put 100% effort in what I do. My parents are people who always believe in me and set a high standard for me to accomplish, make me a better person.

I would like to gratefully acknowledge many professors that have guided me along my academy. At University of Wisconsin – La Crosse, I would like to acknowledge my undergraduate research advisor Prof. Michael Jackson for first introducing to me the subject of molecular spectroscopy. I must thank my undergraduate academic advisor Prof. Adrienne Loh who patiently taught me the subject of Quantum Chemistry.

Though only my name appears on the cover of this dissertation, a great many people have contributed to its production here at Arizona State University. I would like to express the deepest appreciation to my research advisor Prof. Timothy C. Steimle, for his insights, guidance, support and giving me such an opportunity to work in his well equipped research laboratory. I could not have imagined having a better advisor and mentor for my Ph.D study. Prof. Steimle encouraged me not only to grow as an experimentalist and a chemist but also as an independent thinker. Additional to the research, his caring, forgiving and kindness to the students made the graduate study much easier.

I would like to thank my final dissertation committee members, Prof. Ranko Richert, Prof. Andrew Chizmeshya, for their support and their valuable advice in the process of this dissertation work. I am also grateful to my oral exam committee members, Prof. Ulrich Hausermann, Prof. Peter Williams, and Prof. Don-Kyun Seo, for their guidance during my Ph.D candidacy assessment.

Additionally, I also would like to thank Prof. Colan Linton, Prof. Michael Morse (U of Utah), Prof. John P. Maier (Univ. of Basel), Prof. Sheng H. Lin (National Chiao Tung University), Prof. Sheng H. Lin (National Chiao Tung University), Prof. John Stanton (The University of Texas at Austin), Dr. Hailing Wang, and Dr. Xiujuan Zhuang, Dr. Lan Cheng (The University of Texas at Austin) for their help throughout the years.

Finally, I would like to thank all of my friends, my host family, many wonderful people I met along the way, without their help, support, encouragement, I would not stand still.

TABLE OF CONTENTS

Page

CHAPTER Page

APPENDIX Page

LIST OF TABLES

Table Page

LIST OF FIGURES

Figure Page

Figure Page

Figure Page

Chapter 1

INTRODUCTION

1.1. Historical background of spectroscopy

Spectroscopy is the study of how radiated energy interacts with matter. Spectroscopy has a long tradition and was first recognized by Isaac Newton. In 1666 Newton demonstrated that the white light from the sun could be dispersed into continuous series of colors. William Hyde Wollaston in 1802 improved Newton's discover by using the narrow slit to observe dark lines in the solar spectrum[1]. In 1814, Frauenhofer invented the transmission diffraction grating and made a detailed study of the dark lines in the solar spectrum [2]. In 1852, August Beer published a paper (now known as the famous Beer's laws) showing that the amount of light absorbed was proportional to the amount of solute in aqueous solutions. In 1859, Kirchoff and Bunsen discovered that spectral lines are unique to each element. A year later, they discovered the elements of cesium and rubidium using their new technique of spectral analysis [3]. In 1885, J. J. Balmer observed the spectrum of hydrogen, the lightest element, which showed the simplest visible line spectrum with emission wavelengths at 6563, 4861, 4341, 4102 and 3970Å [4], etc. As a result of theoretical calculations by Balmer and J. Rydberg**,** a mathematical relationship was later developed that accounted for these lines in the visible emission spectrum of hydrogen.

These early spectroscopic experiments clearly showed that atoms did not emit a continuous distribution of frequencies. They emitted light at discrete frequencies that were only characterized for each atom. The two ideas back in those days were: atomic

spectra could provide a key to the structure of the atom and electrons were responsible for producing the emitted light. However, the precise connection between the two ideas had not been made.

Spectroscopic studies greatly improved with the development of quantum mechanics in the late nineteenth and early twentieth century. These developments began with Planck's study of the light emitted by heated solid in 1900. About a decade later, in 1913, Bohr initiated a new era in spectral interpretation by proposing that electrons exist in states of constant energy and only change energy by undergoing a transition from one state to another. During the transition, electrons either absorb or emit an amount of energy that is exactly equal to the energy difference between the two states, resulting in the characteristic spectral lines. In 1923 Louis de Broglie, in his Ph.D. thesis, proposed that the particle behavior of light should have its counterpart in the wave behavior of particles. In the three-year period from January 1925 to January 1928, there are many scientific events and scientific revolution. Wolfgang Pauli proposed the exclusion principle, providing a theoretical basis for the Periodic Table. At the same time, Werner Heisenberg, with Max Born and Pascual Jordan, discovered matrix mechanics, the first version of quantum mechanics. Erwin Schrödinger invented wave mechanics, a second form of quantum mechanics in which the state of a system is described by a wave function, the solution to Schrödinger's equation. Matrix mechanics and wave mechanics, apparently incompatible, were shown to be equivalent by Heisenberg. Electrons were shown to obey a new type of statistical law, Fermi-Dirac statistics. It was recognized that all particles obey either Fermi-Dirac statistics or Bose-Einstein statistics, and that the two classes have fundamentally different properties. Heisenberg announced the famous

Heisenberg Uncertainty Principle. Dirac developed a relativistic wave equation for the electron that explained electron spin and predicted antimatter. Dirac laid the foundations of quantum field theory by providing a quantum description of the electromagnetic field. Bohr announced the complementarily principle that helped to resolve apparent paradoxes of quantum theory, particularly wave-particle duality [5].

1.2. Application of Spectroscopy

Spectroscopy is a powerful tool for physical and analytical chemistry because atoms and molecules have unique spectra upon excitation. Spectroscopy is also a useful tool for studying the structures of atoms and molecules. The large number of wavelengths emitted by these systems makes it possible to investigate their structures in detail, including the electron configurations of ground and various excited states. Spectroscopy also provides a precise analytical method for finding the constituents in material having unknown chemical composition.

Production and analysis of a spectrum usually requires the following: (A) a source of light (or other electromagnetic radiation), (B) a disperser to separate the light into its component wavelengths, and (C) a detector to sense the presence of light after dispersion. The apparatus used to accept light, separated it into its component wavelengths, and detect the spectrum is called a spectrometer. The three major processes of spectroscopy in use today are absorption, spontaneous emission, and stimulated emission. Absorption spectroscopy measures the wavelengths of light that a substance absorbs to give information about its structure. Spontaneous emission spectroscopy, such as fluorescence, measures the amount of light of a certain wavelength that a substance emits. Lastly,

stimulated emission is similar to spontaneous emission spectroscopy but detects and analyzes radiation with the coherently emitted at the excitation wavelength.

The era of modern spectroscopy began with the invention of the laser in 1960 by Theodore Maiman using a lasing medium of ruby that was stimulated using the high energy flashes of intense light. The invention of the laser was a remarkable technical breakthrough. Since then, lasers, with its advantages (for examples: high intensity, narrow spectral linewidth, mono-chromaticity, well-characterized polarization, and phase coherence), opened up the field of ultra-high resolution spectroscopy. Laser spectroscopy nowadays includes: laser-induced fluorescence spectroscopy (LIF), resonantly enhanced multiphoton ionization spectroscopy (REMPI), zero kinetic energy spectroscopy (ZEKE), and infrared photon dissociation spectroscopy (IRPD), etc.

1.3. Present work

The field of simple diatomic and triatomic molecular spectroscopy is a very broad, rich, and mature discipline which are described in detail by Herzberg in his three books [6, 7, 8], Brown and Carrington, on "*Rotational Spectroscopy of Diatomic Molecules"*[9] and many other spectroscopy textbook. Diatomic and triatomic transition metal-containing molecules, the focus of this work, have been recognized as a building block of more complex metal clusters. A detailed understanding of the structures and bonding at molecular level of these molecules can shed light on the wide range of applications in catalytic and biological processes of these metal clusters. The ground atomic configuration for most transition metal atoms is $nd^m(n+1)s^2$. The open *d*-subshells gives rise to a large density of electronic states and often results in spectral congestion.

However, these complicated spectra provided the details information on the electronic structure of the molecules.

Diatomic and triatomic transition metal-containing molecules in the gas-phase are the focus of my thesis. Spectroscopic detection of these transient species that formed in the gas phase requires very sensitive techniques which can be provided using laser-based spectroscopy. In this thesis, all of the studies are using LIF detection techniques. LIF in theory is a background-free technique, therefore it has great sensitivity. Three types of LIF experiments were performed: (A) low resolution (± 0.05 cm^{-1}) using a pulsed dye laser, (B) high resolution (± 0.0005 cm^{-1}) spectroscopy using a continuous wave dye laser, and (C) high resolution spectroscopy in the presence of an applied external electric field. Type (A) experimental set-up is used for the initial investigation on the molecules of interest. This set-up also provides a valid way to study vibrational spectroscopy via excitation, and dispersed fluorescence, and also perform lifetime measurements. Type (B) experiment allows for fine and hyperfine structures determinedly of the molecules. Type (C) experiment provides the information on the Stark effects to extract out one of the most crucial properties of molecules: the electric dipole moment, μ_e. Chapter 2 describes all experimental techniques that were used throughout this research. Chapter 3 is description of quantum chemistry and molecular theory that were used to analyze and model the observed spectra.

My thesis is divided into two sub-directions: (a) spectroscopy of heavy metal halides molecules in support of parity non-conservation and (b) normal modes analysis of triatomic C_{2v} molecules. The first part (heavy metal halides) provides the needed information on fine and hyperfine structure of the molecules for the parity non-

conservation experiments. Bond lengths all distance were determined from fine structure via rotational and vibrational analysis. Magnetic and electric quadrupole hyperfine parameters were also determined. Magnetic hyperfine structure results from the interaction of the unpaired valence electrons with any non-zero nuclear spins. The electric quadrupole structure results from the interaction of electric field gradient produced by all the electrons with the electric quadrupole moment of the nuclei. Magnetic and electric quadrupole hyperfine terms provide the most detailed on the electron wavefunction. Furthermore these interactions have matrix elements that are in close connection with the parameters associated with parity non-conservation terms [10] (see below). If the hyperfine parameters can be accurately calculated by theorists in comparison with experimental determined values, then the non parity terms that appear in the Halmitonian (e.g. W_A, W_S, and W_d) should be accurately calculated. My work on ^{87}SrF, ^{135,137}BaF, YbF, HfF and YbF provides critical information needed for parity non-conservation experiments and are described in Chapter 4.

The second part of my thesis is on the normal mode analysis of the bent structure of dioxides (TiO_2, ZrO_2). The dioxides can have one of three isomeric forms: a) the inserted form, with a large apex angle, b) a "T-Shaped" form with a small apex angle and an O-O distance close to that of O_2, and c) a M-O-O superoxide form [11]. ZrO_2 and TiO_2 which are studied in this thesis have inserted form, C_{2v}, symmetry. The details of the normal mode analysis, Franck-Condon calculation for C_{2v} molecules (TiO_2 and ZrO_2) is describe in Chapter 5. The last chapter, Chapter 6, presents a work on other molecule: IrSi.

References

1. W. H. Wollaston, Phil. Trans. R. Soc. Lond., **92**, *365-380*,(1802)
2. J. Fraunhofer, *Denkschriften der Königlichen Akademie der Wissenschaften zu München*, **5** (Die Akademie, 1817).

3. G. Kirchhoff and R. Bunson, *Annalen der Physik und der Chemie*, **110**, 161-189 (1860)

4. V.Thomsen, Spectrostopy **21**(10), 32, (2006).

5. I.N. Levine, *Quantum Chemistry*, (6th edition, Pearson Prentice Hall).

6. G. Herzberg, *Molecular Spectra and Molecular Structure: I. Spectra of Diatomic Molecules* (D. Van Nostrand Company Inc, New Jersey, 1950)

7. G. Herzberg, *Molecular Spectra and Molecular Structure: II. Infrared and Raman Spectra Of Polyatomic Molecules* (D. Van Nostrand Company Inc, New Jersey, 1945)

8. G. Herzberg, *Molecular Spectra and Molecular Structure: III. Electronic Spectra of Polyatomic Molecules* (D. Van Nostrand Company Inc, New Jersey, 1967)

9. J. M. Brown, A Carrington, *Rotational Spectroscopy of Diatomic Molecules* (Cambridge University Press, 2003)

10. J.A.J. Fitzpatrick, F. R. Manby and C. M. Western, J. Chem . Phys. **122** 084312/1-12 (2005).

11. Y. Gong, M. Zhou, L. Andrews, Spectroscopic and Theoretical Studies of Transition Metal Oxides and Dioxygen Complexes. Chem. Rev. **109**, 6765 (2009).

Chapter 2

EXPERIMENTAL METHOD

2.1. Overview

The experimental set up for the generation and detection of transition metal containing molecules is complex. All of the projects in this thesis were done using laser ablation generation and laser induced fluorescence (LIF) detection. A rotating metal rod was laser ablated in the presence of a gas mixture of ~5% reagent (O_2, SF_6, SiH_4) and ~95% Ar to generate the plasma of metal-containing products. The plasma products then entered the vacuum chamber through supersonic free-jet expansion and were skimmed to create a well collimated molecular beam. The molecular beam was probed at 90˚ by a continuous wave (cw) dye laser or pulsed-dye laser to induce the fluorescence. The fluorescence signal was focused onto a photomultiplier tube (PMT) by a set of lens and a band-pass filter. The output from the PMT was then processed through either the gated boxcar integrator or gated photon counter. The results were then transferred, plotted and stored in digital form using a Visual basic 6.0 program.

The spectra were recorded while simultaneously recording the sub-Doppler I_2 absorption spectrum. Interpolation between I_2 absorption features was achieved by simultaneously recording the transmission of two confocal etalons. One etalon was actively stabilized and calibrated to have a free spectral range of 751.5 MHz. Another unstabilized etalon, with a free spectral range of 75 MHz, was used to interpolate between transmission peaks of the stabilized etalon. The Stark effects were recorded by applying the static electric field across a pair of conducting plates straddling the region of

molecular fluorescence. Figure 2.1 illustrates the experimental scheme for high resolution LIF. The following sub-chapter will describe the experimental procedure in detail.

2.2. Generation of target molecule

2.2.1. Ablation

The production of the target molecules requires three things: the metal sample rod, the pulsed ablation laser and the pulsed valve. Laser ablation is the process that results when intense laser light is allowed to impinge on a solid surface. The history of ablation studies began with the discovery of laser ablation back in 1960 by Maimon [1]. Throughout the 1960s, numerous studies were done using ablation laser. A review by Miller [2] gave a complete picture of many laser ablation studies in the 1960s. The number of studies using laser ablation increased exponentially around 1985 with numerous applications on film growth, laser medicine and laser ablation mass spectrometry. One of the most well known studies is that of laser ablating graphite resulting in producing a remarkably stable cluster consisting of 60 carbon atoms by Kroto et. al [3].

High energy (≈5mJ) and short (<10ns) laser pulses were focused on a rotating metal to produce the active plasma. The rotation of the rod was controlled under the variable speed commercial stepper motor via a homemade controller. Two ablation laser were used: New Wave Tempest Nd: YAG (neodymium-doped yttrium aluminum) with radiation of 532nm, 20Hz for the high resolution LIF set- up and Surelite I series with radiation of 355 nm, 10Hz for the low resolution LIF set-up. The reagent was delivered to a vacuum chamber through commercial solenoid Series 9 made by Parker Precision Fluid Corp. The pulse valve was controlled either by a homemade controller on high resolution

LIF set-up or by the commercial pulse valve driver (Iota One Valve Driver) for the low resolution set-up. The vaporized metal plasma then reacted with the mixture of reagent and carrier gases in a typical backing pressure of 600 psi. The presence of the Ar gas allows the reagent to accelerate to the velocity of carrier gas and "cool" the internal degrees of freedom of the seeded molecules. The time between the ablation laser pulse and gas pulse are optimized for each different molecules of interest so that the collecting signals have the best signal-to-noise ratio. The metal rods were used on this thesis were pure metal rods Strontium (^{87}SrF), Barium ($^{135,\ 137}$BaF), Ytterbium (YbF), Zirconium (ZrO_2), and Iridium (IrSi) (ESPI, USA).

2.2.2. Supersonic free jet expansion and molecular beam

The supersonic free jet expansion provides the ideal environment to study the physical properties of transient metal containing molecules. The properties of jet free expansion was first discovered by Kantrowitz et al [4]. In a supersonic free jet, the molecules can be cooled to the rotational temperature of approximately 10-20 K.

In the high resolution experiments, the free-jet expansion products were "skimmed" to produce a well collimated molecular beam. An adjustable iris with diameter of 2.5 cm was placed approximately 5 cm downstream between the two chambers: source chamber and detecting chamber. This allows the supersonic beam to be collimated to reduce the Doppler broadening. In the low resolution experiments (e.g. ZrO_2), there is no separate chamber between the source and detecting chamber. In the low resolution studies, an adjustable iris was put in front of the PMT, 5 cm away from the source, to reduce the chemiluminescence (hence better signal-to-noise). All experiments were run under pressure of $\sim 8.0\times10^{-5}$ Torr inside the chamber.

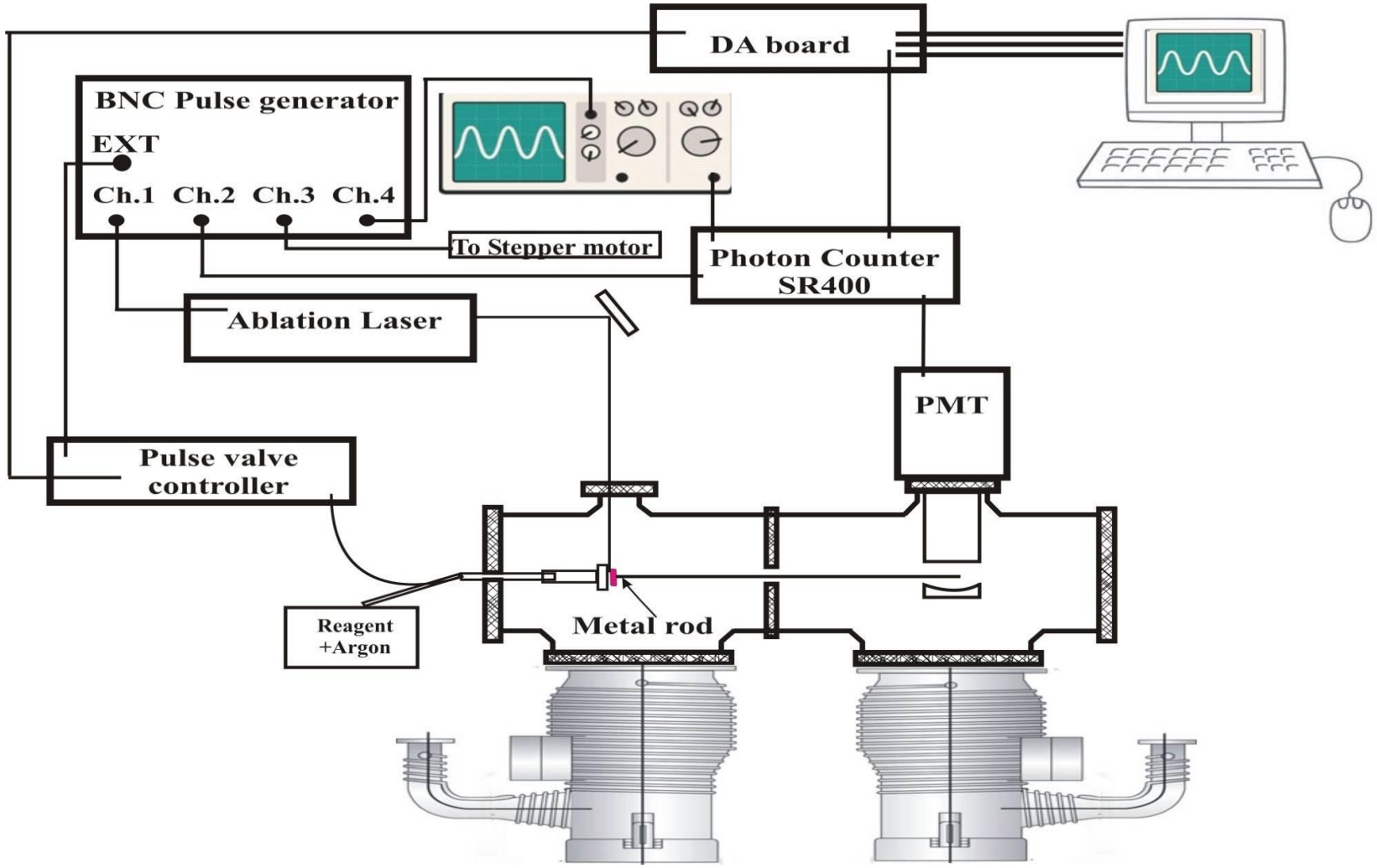

Figure 2.1. Diagram of laser ablation and molecular beam high resolution LIF spectrometer

2.3. Detection methods

2.3.1. Laser Induced Fluorescence

In the high resolution studies, the molecular beam was excited by a Coherent 699 continuous wave ring dye laser pumped by Coherent Inova Argon ion laser in the visible range. For the molecule in the near infrared (BaF), the molecular beam was excited by a Coherent 899 Titanium: Sapphire ring laser pump by a Coherent Verdi-V10 diode-pumped solid-state laser. In the low resolution studies, the molecular beam was excited by a Lambda Physic Excimer XeCl (308nm) laser pumping a Lumonics Hyperdye-300 pulse dye laser.

As the wavelength of the laser is scanned, the molecules of interest are excited to an electronic excited state. The molecules emitted light is often at a wavelength longer than the excitation wavelength. Since fluorescence takes place in all directions, it can be preferentially detected in the absence of the laser light hence the signal-to-noise ratio of the fluorescence signal is very high, providing a good sensitivity to the process. The fluorescent signal then passed through a band-pass filter to remove any remaining scattered laser light and light from the ablation source or from chemiluminescence of meta-stable products. The signals were focused onto a cooled photomultiplier tube (PMT) (Hamamatsu R093) through a collection of lens and aspherical lens. The LIF signal for the high resolution was collected using the gated photon counter (Stanford Research System SR400). However, the LIF signal for low resolution was collected through a gated boxcar integrator (Stanford Research System SR250). A digital oscilloscope was used to view and optimize the signal-to-noise.

2.3.2. Dispersed Fluorescence

Dispersed laser induced fluorescence (DLIF) detection technique provides the information about the ground state vibrational structure. The DLIF spectra were recorded by tuning the wavelength of the pulsed dye laser to excite the most intense feature of each band and the LIF signal was viewed through a McPherson 2/3 m scanning monochromator. The slit widths were adjusted to produce a spectral linewidth FWHM-of approximately 20 Å. The signal was detected using a cooled photomultiplier tube and processed using gated photon counting (see above). Due to the low signal-to-noise, the DLIF of ZrO_2 and YbF were recorded multiple times and co-added together to obtain good spectra.

2.3.3. Fluorescence lifetime

The radiative decay curves caused by spontaneous emission were also recorded. The excited state of any molecule will have an intrinsic lifetime due to this radiative decay. The lifetime depends on the Einstein spontaneous emission coefficients, A_{ij}, for all of the radiative transitions. Strong molecular transitions have Einstein spontaneous emission coefficient of 10^8 to 10^9 s^{-1}, so lifetimes of 1 to 10 ns. The radiative lifetimes were measured using the same LIF low resolution set-up but with the LIF decay signal recorded using a 500 Mhz digital storage oscilloscope. Lifetimes of ZrO_2 and TiO_2 are in the order of ~1μs, thus are associated with weaker transitions.

2.3.4. Stark measurements

The splitting and shift of the Stark spectra were measured to determine the permanent electric dipole moments, μ_{el}, of the molecules. In our apparatus, the static electric field strengths can range from 0 to 7000 V/cm and were generated by application

of a voltage across a pair of conducting plates straddling the region of molecular fluorescence. The Stark plates were two 5×5 cm^2 density filters that transmit approximately 90% of the light. A polarization rotator and polarizing filter were used to orient the static electric field vector of the linearly polarized laser radiation either parallel, //, or perpendicular, ⊥, to that of the applied field. The spacing of the Stark plates in the experiment of HfF and IrSi is 1.72±0.02 cm.

2.4. Calibration: Sub-Doppler Iodine and Etalons

In the high resolution experiment, the laser light from the Coherent 699 CW ring dye laser went through a wavemeter (model WA1500) with a built-in HeNe laser wavelength standard to determine the absolute wavelength to a precision of ± 0.002 cm^{-1}. To further improve the precision, the absolute wavenumber of the laser were determined to an accuracy of ±0.0001 cm^{-1} by simultaneously recording the sub-Doppler iodine, I_2 absorption spectrum [5, 6]. Interpolation between I_2 shown in Figure 2.2 absorption features was achieved by simultaneously recording the transmission of two confocal etalons (Fabry–Pérot interferometer). One etalon was actively stabilized and calibrated to have a free spectral range (FSR) of 751.5MHz. Another unstabilized etalon with a FSR of 75 MHz was used to interpolate between transmission peaks of the stabilized etalon.

The sub-Doppler Iodine absorption spectrum was set up as illustrated in Figure 2.2. The laser light was divided into two nearly equal intense beam using a cube beam splitter. These two beams passed through the gaseous I_2 cell in opposite directions. One beam was chopped by a mechanical chopper with a frequency of ~2KHz, and went through a polarizer splitter. The second beam went through the 90˚ polarizer rotator. The I_2 signal then was directed to a photodiode and the output of which went to a lock-in-

amplifier. The photodiode only sees a modulated signal for those molecules simultaneously seeing both counter polarizing beams, thus a Doppler-free spectrum.

One etalon, which was thermally stabilized, has a 10 cm confocal optics. This stabilized etalon was controlled by monitoring the transmission of a frequency stabilized Melles Griot Model 05 STP 903 He-Ne laser. One mirror was mounted to PZT crystal with a variable voltage application to adjust the spacing. The modulated transmission intensity was detected by a photodiode and used as an input into a lock-in-amplifier. The output of the lock-in amplifier was monitored by a computer and a correction voltage sent to the driving electronic of PZT crystal to keep the He-Ne transmission intensity constant. The set-up for actively stabilized confocal etalon set-up is shown in Figure 2.3.

In the low resolution experiment (ZrO_2), the laser frequency was calibrated by recording the optogalvanic spectrum of Ne. In optogalvanic spectroscopy, the current passing through a gas discharge is monitored as a laser light source is tuned through the frequencies of allowed transitions for excited atoms in the discharge. As the Ne atom is excited to a less bound state, there is an increasing probability that the Ne atom is ionized by discharge collisions and hence contributes to an increase in the discharge current. Optogalvanic spectroscopy does not require a photomultiplier tube or photodiode detector to obtain atomic transition spectra because the gas discharge itself serves as a resonant photo-detector.

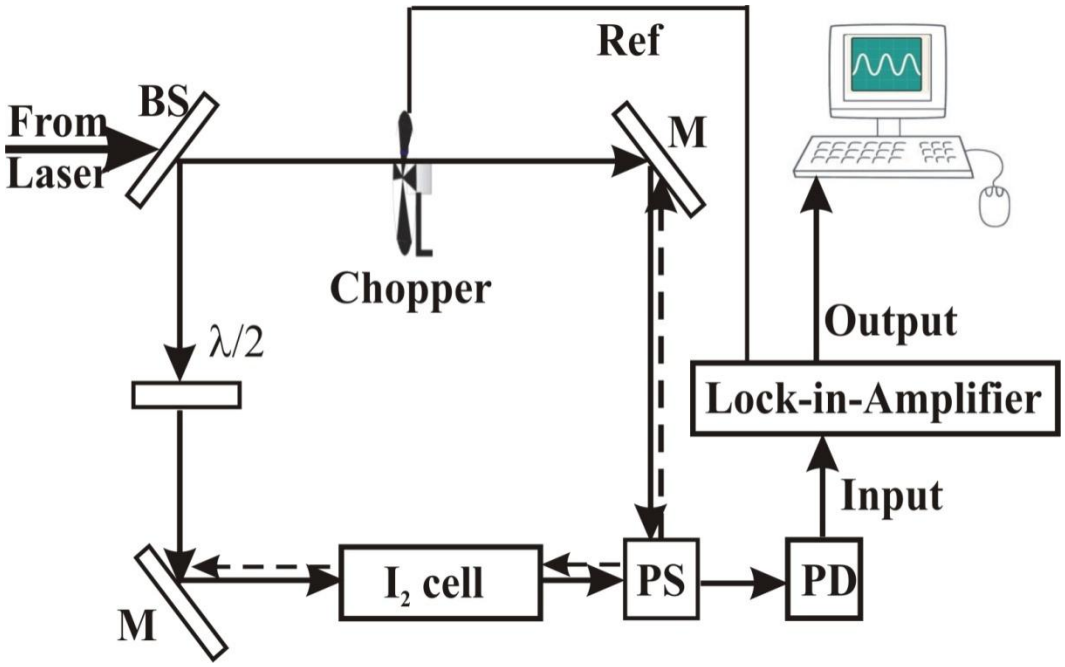

Figure 2.2. Sub-Doppler polarization spectroscopy of I_2 for absolute wavelength calibration; "BS" is beam splitter, "λ/2" is 90˚ polarizer rotator, "M" is notation for mirror, "PS" is polarizer splitter, "PD" is photodiode.

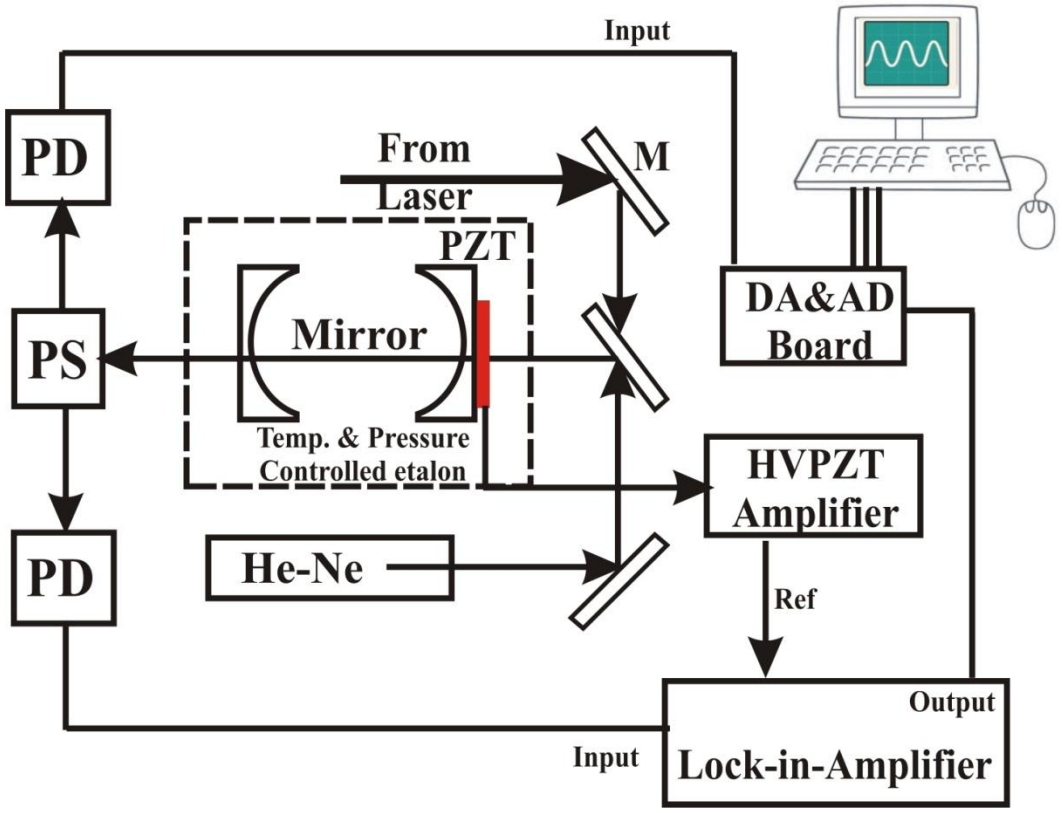

Figure 2.3. Block diagram of the actively stablized confocal etalon used for interpolation between I_2 calibration features; "PD" is photodiode, "PS" is polarizer splitter, "M" is for Mirror.

References

1. T.H. Maimon, Nature **187**, 493 (1960).

2. J. C. Miller, AIP Conf. Proc. **288**, pp. 619-622

3. H. W. Kroto, J. R. Heath, S. C. O'Brien, R. F. Curl & R. E. Smalley, Nature **318**, 162 - 163 (1985)

4. A.Kantrowitz and J. Grey, Rev. Sci. Instrum. **22**, 328 (1951)

5. IODINESPEC4, Toptica Photonics, Munich, Germany (www.toptica.com).

6. A. L. Schawlow, Rev. Mod. Phys. **54,** 697 (1982).

Chapter 3

MOLECULAR THEORY

A spectroscopist cannot analyze an observed spectrum without knowledge of quantum chemistry and molecular theory. The effective Hamiltonian describes the intra-molecular dynamics and interactions. The complexities in understanding molecular spectra are due to interaction of various nuclei with each other and with the electrons. In order to analyze molecular spectra it is necessary to consider all of the effects together. A complete picture of the molecular theory can be found in numerous molecular spectroscopy books [1, 2, 3, 4, 5, 6, 7]. This chapter only describes briefly the theory that will be used to analyze the observed spectra of diatomic molecules: ^{87}SrF: the $(0,0)^2\Pi$-$^2\Sigma^+$ band, $^{137\&135}$BaF the $(0,0)^2\Pi$- $^2\Sigma^+$ band, YbF: the $(0,0)A^2\Pi_{1/2} \leftarrow X\,^2\Sigma^+$ band, IrSi the (6,0)[16.0]1.5$\leftarrow X^2\Delta_{5/2}$, (7,0) [16.0]3.5$\leftarrow X^2\Delta_{5/2}$ band and the triatomic, C_{2v} molecules: TiO_2, ZrO_2: the $\tilde{A}^1B_2 \leftarrow \tilde{X}\,^1A_1$ bands.

3.1. Diatomic molecules

Diatomic molecules are important to the physical sciences because they are the basic building blocks of large molecules. The process of analyzing a complex diatomic molecule spectra with electron spin, nuclear hyperfine and external field interactions has several stages which involve the process of choosing a suitable basis set and a suitable 'effective Hamiltonian'. Our choice of effective Hamiltonian is also determined by the basis set chosen. The procedure is to set up a matrix representation of the effective Hamiltonian operating within the chosen basis set. The matrix is often truncated artificially and we then diagonalize it to obtain the energies of the levels and as linear combination of the basis set.

3.1.1 Terms symbols:

Electronic states of diatomic molecules are designated by molecular term symbols which give the details of total electronic spin, and electronic orbital angular momentum of the molecule and other symmetries associated with it. The general form of term symbol is:

$$^{2S+1}|\Lambda|^{(+/-)}_{(\Omega \text{ or } u/g)}. \quad (1)$$

In equation 1, $2S+1$ is called the spin multiplicity, where $\boldsymbol{S}$ is the total electronic spin angular momentum quantum number resulting from individual electron spin angular momenta, $\boldsymbol{s}_i$ =1/2. For example, if there is one unpaired electron, S=1/2, resulting in doublet state. In equation 1, Λ is the quantum number for the projection of total orbital angular momentum, L, of the electron along the internuclear axis such that:

$$\hat{\mathrm{L}}_z\psi^{\mathrm{el}} \cong \Lambda\psi^{\mathrm{el}}. \quad (2)$$

Λ=0,±1,±2,±3... which gives Σ, Π, Δ, Π. Ω is the total electronic angular momentum (Ω=Σ (molecular fix projection of S)+Λ) along the inter-nuclear axis, where Σ is molecular fix projection, such that:

$$\hat{\mathrm{J}}_z\psi^{\mathrm{el}} \cong \Omega\psi^{\mathrm{el}}. \quad (3)$$

The +/- superscript is only used in Σ states, which is related reflection symmetry. Consider $\hat{\sigma}$(x,z) is the reflection operator of electronic wavefunction through the xz-plane of molecular fixed coordinates where z-axis contains the nuclei. The +/- superscripts are as:

$$\hat{\sigma}\psi^{\mathrm{el}} \cong \pm\psi^{\mathrm{el}} \quad (4)$$

The g/u subscript is parity of the electronic states belonging to the term, and it is only relevant for the homonuclear molecule such that:

$$\hat{i}\,\psi^{el} \cong \pm\psi^{el} \qquad (5)$$

where g and u represent + and -, respectively.

3.1.2. Coupling of electronic and rotational motion: Hund's coupling cases

Hund's coupling cases are idealized situations which help spectroscopists understand the pattern of rotational levels and the resulting spectra. There are five Hund's coupling cases which are described in detail in Ref 6 and 7. This subchapter only describes in details the Hund's case that are used in analyzing of my spectra: Hund's case $a_{\beta J}$.

A basis set in theoretical and computational chemistry is a set of functions which are combined in linear combinations to create molecular eigenfunction. The angular momentum basis for Hund's case (a)-(e) derives are: Hund's case (a)$\left|nJS\Omega\Lambda\Sigma\right\rangle$, Hund's case (b)$\left|nJSN\Lambda(S_R)\right\rangle$, Hund's case (c) $\left|nJ[J_a]\Omega\right\rangle$, Hund's case (d) $\left|nJSN(S_R)J^+N^+S^+\Lambda^+l(l_R,s_R)\right\rangle$, Hund's case (e) $\left|nJJ^+[J_a^+ or S^+ and \Lambda^+]\Omega^+lj(j_R)\right\rangle$.

The details of the denotation can be found in Ref [7]. In the Hund's case (a), illustrated in Figure 3.1(A), the orbital angular momentum **L** is strongly coupled to the inter-nuclear axis by electrostatic forces, the electronic spin angular momentum, **S**, is coupled with internal magnetic field along inter-nuclear axis, then **S** is coupled to **L** through spin-orbit coupling. The axial components of **L** and **S** are well defined and denoted as Λ and Σ, and their sum is $\Omega=\Lambda+\Sigma$. The angular momentum of the rotating

nuclei, **R,** is coupled with a vector **Ω** pointing along the axis to form the resulting total angular momentum, **J**. Therefore, the vector coupling can be written as:

$$\mathbf{\Omega} + \mathbf{R} = \mathbf{J} \qquad (6)$$

which corresponds to the basis set $|\eta\Lambda\rangle|(S\Sigma)|\Omega JM_J\rangle$. Hund's case (a) is a good representative whenever $A\Lambda$, is much larger than BJ, where A is a spin-orbit coupling constant, and B is a rotational constant. In the case where the nuclear spin exists, there are two main possibilities that arise for Hund's case (a) coupling: case (a_α) (very rare) and case ($a_{\beta J}$) (most common situation).

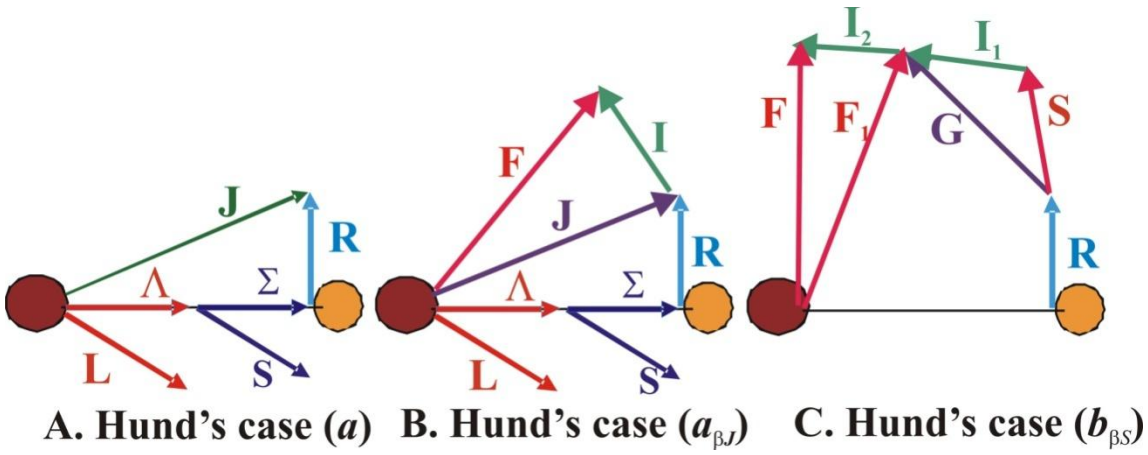

Figure 3.1. A. Hund's cases (a), B. Hund's cases ($a_{\beta J}$), C. Hund's cases ($a_{\beta S}$)

Hund's case ($a_{\beta J}$) is the extension of case (a) in which nuclear spin angular momentum, **I,** is coupled to **J** to form a grand total angular momentum, **F.** Hund's case ($a_{\beta J}$) limit, given in Figure 3.1 (B) with the approximately good intermediate quantum number, J ,resulting from coupling the rotational angular momentum, **R**, with the electron spin angular momentum, **S.** When nuclear spin, **I,** is strongly coupled with **J,** it produces total angular momentum, **F**. The resulting Hund's case ($a_{\beta J}$) vector coupling can be written as:

$$\mathbf{\Omega + R = J};\ \mathbf{I + J = F}, \qquad (7)$$

which corresponds to the basis set $|\eta\Lambda\rangle|(S\Sigma)\rangle(JI)\Omega, mF\rangle$.

3.1.3. New labeling scheme for ^{87}SrF,$^{135\&137}$ BaF

Given that the ground states of SrF and BaF have no orbital angular momentum (i.e. "Σ" state). Hund's case (b) is appropriate. New labeling schemes for ^{87}SrF, $^{135\&137}$ BaF is using Hund's case ($b_{\beta S}$) limit coupling scheme for the $^2\Sigma^+$ state. The Hund's case ($b_{\beta S}$) limit given in Figure 3.1(C), is the extension from Hund's case (b), with the approximately good intermediate quantum number being G resulting from coupling the metal (^{87}Sr and $^{135\&137}$Ba) nuclear spin angular momentum, $\mathbf{I_1}$, with the total electron spin angular momentum, **S**. The second nuclear spin, $\mathbf{I_2}$, is weakly coupled to **G** to produce the total angular momentum, **F**. The Hund's case ($b_{\beta S}$) vector coupling for low rotational levels can be written as:

$\mathbf{S + I_1}$ (^{87}Sr, $^{135\&137}$Ba) = **G** (^{87}Sr, $^{135\&137}$Ba);

$\mathbf{N + G}$(^{87}Sr and $^{135\&137}$Ba) = $\mathbf{F}_1$; $\mathbf{F}_1 + \mathbf{I}_2$ (^{19}F) = **F**, (8)

which corresponds to the basis function $|\eta\Lambda\rangle|(SI_1)G(GN)F_1(F_1I_2)F\rangle$. The twelve branches of the $^2\Pi$ (*case* $a_{\beta J}$) - $^2\Sigma^+$ (*case* $b_{\beta J}$) labeling scheme ($^PP_{11}$, $^QQ_{11}$, $^RR_{11}$, $^PQ_{12}$, $^OP_{12}$, $^QR_{12}$, $^PP_{22}$, $^QQ_{22}$, $^RR_{22}$, $^RQ_{21}$, $^QP_{21}$, and $^SR_{21}$) [1] regroup into sixteen branch features of the $^2\Pi$ (*case* $a_{\beta J}$) - $^2\Sigma^+$ (*case* $b_{\beta S}$) scheme. The branches are designated as ^OP_1G, ^PP_1G + ^PQ_1G, ^QQ_1G + ^QR_1G, and ^RR_1G for the $^2\Pi_{1/2}$ (*case* $a_{\beta J}$) - $^2\Sigma^+$ (*case* $b_{\beta J}$) sub-band and ^PP_2G, ^QP_2G + ^QQ_2G, ^RQ_2G + ^RR_2G, and ^SR_2G for the $^2\Pi_{3/2}$ (*case* $a_{\beta J}$) - $^2\Sigma^+$ (*case* $b_{\beta S}$) sub-band with $G = |\mathbf{S + I_1}|$ and $|\mathbf{S - I_1}|$. The abbreviation ^PP_1G, ^QQ_1G, ^QP_2G and ^RQ_2G will be

used for the ${}^{P}P_1G + {}^{P}Q_1G$, ${}^{Q}Q_1G + {}^{Q}R_1G$, ${}^{Q}P_2G + {}^{Q}Q_2G$ and ${}^{R}Q_2G + {}^{R}R_2G$ branches, respectively [8].

3.1.3. Effective Hamiltonian for diatomic molecule in given electronic state

Hamiltonian operator corresponding to the total energy of any system is very complicated [6]. The "effective" Hamiltonian is derived from total Hamiltonian, which produces the eigenvalues and eigenvectors with much simpler representation than those of the total Hamiltonian. The derivation of the "effective" Hamiltonian from the total Hamiltonian is described in detail in Brown and Carrington [6]. The schematic diagram of the transformation from the total Hamiltonian matrix representation to the effective Hamiltonian is shown in Figure 3.2. The effective Hamiltonian is a sum of terms representing the various interactions within the molecule; each term contains angular momentum operators and molecular parameters. The effective Hamiltonian operates only within the levels (rotational, spin and hyperfine) of a single vibrational state of the particular electronic state of interest. Most, but not all, of the important terms in an effective Hamiltonian have been worked out. The effective Hamiltonian of any given vibrational state of diatomic molecules in the absence of an external field can be described by the following sum of terms [6, 7]:

$$\hat{H}^{eff} = \hat{H}^{rot} + \hat{H}^{CD} + \hat{H}^{spin\text{-}orbit} + \hat{H}^{spin\text{-}spin} + \hat{H}^{spin\text{-}rot} + \hat{H}^{LD} + \hat{H}^{hfs} + \hat{H}^{eq} \qquad (9)$$

includes: the Hamiltonian operator for rotation, $\hat{H}^{rot}$, the Hamiltonian operator centrifugal distortion, $\hat{H}^{CD}$, the Hamiltonian operator for spin-orbit coupling $\hat{H}^{spin\text{-}orbit}$, the Hamiltonian operator for spin-spin interaction, $\hat{H}^{spin\text{-}spin}$, the Hamiltonian operator for spin-rotation interaction, $\hat{H}^{spin\text{-}rot}$, the Hamiltonian operator for Λ–doubling, $\hat{H}^{LD}$, the

Hamiltonian operator for magnetic hyperfine interactions, $\hat{H}^{hfs}$, and the Hamiltonian operator for nuclear electric quadrupole interaction, $\hat{H}^{eq}$.

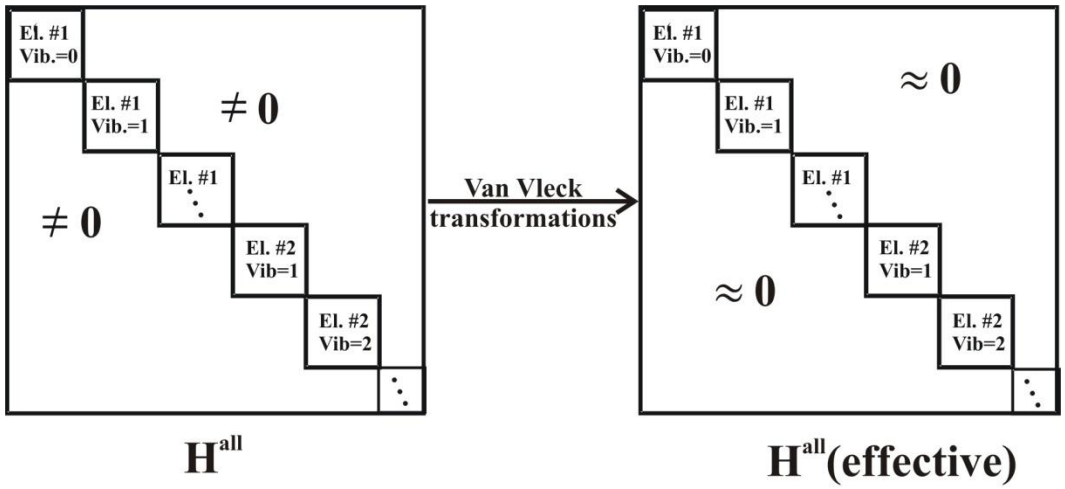

Figure 3.2. A schematic diagram of the transformation of the total Hamiltonian matrix representation (left) to the effective Hamiltonian (right).

The Hamiltonian operator for rotation, $\hat{H}^{rot}$:

$$\hat{H}^{rot}(\hat{R}) = B\hat{R}^2, \tag{10}$$

where $B = \frac{h}{8\pi^2 \mu r^2}$ is rotational constant, μ is reduced mass of the molecule, *h* is Planck's constant, r is the bond distance. $\hat{R}$ is the rotation of the molecule operator.

The Hamiltonian operator centrifugal distortion, $\hat{H}^{CD}$:

$$\hat{H}^{CD} = -D\hat{R}^2\hat{R}^2, \tag{11}$$

where *D* is the centrifugal distortion constant.

The Hamiltonian operator for spin-orbit coupling, $\hat{H}^{spin\text{-}orbit}$:

$$\hat{H}^{spin\text{-}orbit} = A\hat{L}_z\hat{S}_z, \tag{12}$$

where, *A* is the spin-orbital coupling constant, $\hat{L}_z$ and $\hat{S}_z$ are the orbital and spin angular momentum operators, respectively.

The Hamiltonian operator for spin-spin interaction, $\hat{H}^{spin\text{-}spin}$:

$$\hat{H}^{spin\text{-}spin} = \frac{2}{3}\lambda(3\hat{S}_z^2 - \hat{S}^2) \qquad (13)$$

where λ is the spin-spin parameter.

The Hamiltonian operator for spin-rotation interaction, $\hat{H}^{spin\text{-}rot}$:

$$\hat{H}^{spin\text{-}rot} = \gamma\hat{N}.\hat{S}, \qquad (14)$$

where γ is the spin-rotation parameter, $\hat{N} = \hat{J} - \hat{S}$, $\hat{J}$ is the total angular momentum operator, $\hat{S}$ is the spin angular momentum operator.

The Hamiltonian operator for Λ-doubling, $\hat{H}^{LD}$:

$$\hat{H}^{LD} = \frac{1}{2}o(\hat{S}_+^2 + \hat{S}_-^2) - \frac{1}{2}p(\hat{N}_+\hat{S}_+ + \hat{N}_-\hat{S}_-) + \frac{1}{2}q(\hat{N}_+^2 + \hat{N}_-^2) \qquad (15)$$

where *o, p, q* are Λ-doubling parameters .

The Hamiltonian operator for magnetic hyperfine interactions, $\hat{H}^{hfs}$:

$$\hat{H}^{hfs} = a\hat{I}_z\hat{L}_z + b_F\hat{I}.\hat{S} + \frac{c}{3}(\hat{I}_z.\hat{S}_z - \hat{I}.\hat{S}) - \frac{d}{2}(\hat{S}_+\hat{I}_+ + \hat{S}_-\hat{I}_-) \qquad (16)$$

where *a* is orbital hyperfine constant, b_F is Fermi contact constant, *c* is dipolar constant, *d* is nuclear spin–electron spin dipolar interaction constant. $\hat{I}$ and $\hat{I}_z$ are nuclear spin angular momenta, $\hat{I}_\pm$ and $\hat{S}_\pm$ are ladder operators.

Scalar portion of the Hamiltonian operator for nuclear electric quadrupole interaction, $\hat{H}^{eq}$:

$$\hat{H}^{eq} = \frac{eq_0 Q}{4I(2I-1)}(3\hat{I}\cdot\hat{I}^2) \tag{17}$$

where Q is the quadrupole moment of nucleus, e is the charge of electrons, q_0 is quadrupole charge distribution. There are also other, non-scalar operator terms but they are not required for my studies

3.1.1 Matrix elements Hamiltonian for diatomic molecule in a given electronic state

The matrix elements of an effective Hamiltonian operator using a Hund's case ($a_{\beta J}$) basis sets $\left|\eta\lambda; S\Sigma; J\Omega(JI_1)F_1(F_1I_2)F\right\rangle$ are taken from Ref. [6, 9], listed in this subchapter.

Matrix elements for rotation, $\hat{\mathrm{H}}^{\mathrm{rot}}$:

$$\begin{aligned}&\left\langle \eta\Lambda; S\Sigma'; J\Omega'(JI_1)F_1'(F_1I_2)F' \middle| \hat{H}^{rot} \middle| \eta\Lambda; S\Sigma; J\Omega(JI_1)F_1(F_1I_2)F \right\rangle \\ &= B\left\{\begin{array}{l}\delta_{\Sigma\Sigma'}\delta_{\Omega\Omega'}\times[J(J+1)-\Omega^2+S(S+1)-\Sigma^2] \\ -2\sum\limits_{q=\pm1}(-1)^{J-\Omega'+S-\Sigma'}\begin{pmatrix} J & 1 & J \\ -\Omega' & q & \Omega\end{pmatrix}\begin{pmatrix} S & 1 & S \\ -\Sigma' & q & \Sigma\end{pmatrix} \\ \times\sqrt{J(J+1)(2J+1)S(S+1)(2S+1)}\end{array}\right\}\end{aligned} \tag{18}$$

Matrix elements for centrifugal distortion, $\hat{\mathrm{H}}^{\mathrm{CD}}$:

$$\begin{aligned}&\left\langle \eta\Lambda; S\Sigma'; J\Omega'(JI_1)F_1(F_1I_2)F \middle| \hat{H}^{CD} \middle| \eta\Lambda; S\Sigma; J\Omega(JI_1)F_1(F_1I_2)F \right\rangle \\ &= -D\left\{\begin{array}{l}\delta_{\Sigma'\Sigma}\delta_{\Omega'\Omega}\times\left\{\begin{array}{l}[J(J+1)-\Omega^2+S(S+1)-\Sigma^2]^2 \\ +4\sum\limits_{q=\pm1}\sum\limits_{\Omega''}\begin{pmatrix} J & 1 & J \\ -\Omega & q & \Omega''\end{pmatrix}^2\begin{pmatrix} S & 1 & S \\ -\Sigma & q & \Sigma''\end{pmatrix}^2 \\ \times J(J+1)(2J+1)S(S+1)(2S+1)\end{array}\right\} \\ -2\sum\limits_{q=\pm1}(-1)^{J-\Omega'+S-\Sigma'}\begin{pmatrix} J & 1 & J \\ -\Omega' & q & \Omega\end{pmatrix}\begin{pmatrix} S & 1 & S \\ -\Sigma' & q & \Sigma\end{pmatrix} \\ \times\sqrt{J(J+1)(2J+1)S(S+1)(2S+1)} \\ \times[2J(J+1)-(\Omega')^2-\Omega^2+S(2S+1)-(\Sigma')^2-\Sigma^2]\end{array}\right\}\end{aligned} \tag{19}$$

Matrix elements for spin-orbit coupling interaction, $\hat{\mathrm{H}}^{\text{Spin-orbit}}$:

$$\begin{aligned}&\left\langle \eta\Lambda; S\Sigma; J\Omega(JI_1)F_1(F_1I_2)F \left| \hat{\mathrm{H}}^{\text{Spin-orbit}} \right| \eta\Lambda; S\Sigma; J\Omega(JI_1)F_1(F_1I_2)F \right\rangle \\ &= A\Lambda\Sigma\end{aligned} \tag{20}$$

Matrix elements for spin-spin interaction, $\hat{\mathrm{H}}^{\text{Spin-spin}}$:

$$\begin{aligned}&\left\langle \eta\Lambda; S\Sigma; J\Omega(JI_1)F_1(F_1I_2)F \left| \hat{\mathrm{H}}^{\text{Spin-spin}} \right| \eta\Lambda; S\Sigma; J\Omega(JI_1)F_1(F_1I_2)F \right\rangle \\ &= \frac{2}{3}\lambda[3\Sigma^2 - S(S+1)]\end{aligned} \tag{21}$$

Matrix elements for spin-rotation interaction, $\hat{\mathrm{H}}^{\text{Spin-rot}}$:

$$\begin{aligned}&\left\langle \eta\lambda; S\Sigma'; J\Omega'(JI_1)F_1(F_1I_2)F \left| \hat{\mathrm{H}}^{\text{Spin-rot}} \right| \eta\Lambda; S\Sigma; J\Omega(JI_1)F_1(F_1I_2)F \right\rangle \\ &= \gamma \left\{ \begin{array}{l} \delta_{\Sigma'\Sigma}\delta_{\Omega'\Omega} \times [\Sigma^2 - S(S+1) -] + \sum\limits_{q=\pm 1} (-1)^{J-\Omega'+S-\Sigma'} \begin{pmatrix} J & 1 & J \\ -\Omega' & q & \Omega \end{pmatrix}^2 \begin{pmatrix} S & 1 & S \\ -\Sigma' & q & \Sigma \end{pmatrix}^2 \\ \times \sqrt{J(J+1)(2J+1)S(S+1)(2S+1)} \end{array} \right\}\end{aligned} \tag{22}$$

Matrix elements for Λ-doubling, $\hat{\mathrm{H}}^{\text{LD}}$:

$$\begin{aligned}&\left\langle \eta\Lambda; S\Sigma'; J\Omega'(JI_1)F_1(F_1I_2)F \left| \hat{\mathrm{H}}^{\text{LD}} \right| \eta\Lambda; S\Sigma; J\Omega(JI_1)F_1(F_1I_2)F \right\rangle \\ &= \sum_{q=\pm 1} \delta_{\Lambda', \Lambda \mp 2} \left\{ \begin{array}{l} \delta_{\Omega'\Omega}(o+p+q) \sum\limits_{\Sigma''} (-1)^{S-\Sigma'} \begin{pmatrix} S & 1 & S \\ -\Sigma' & q & \Sigma'' \end{pmatrix} \\ (-1)^{S-\Sigma''} \begin{pmatrix} S & 1 & S \\ -\Sigma'' & q & \Sigma \end{pmatrix} \times [(S(S+1)(2S+1)] \\ +(p+2q)(-1)^{J-\Omega'} \begin{pmatrix} J & 1 & J \\ -\Omega' & -q & \Omega \end{pmatrix} \\ (-1)^{S-\Sigma'} \begin{pmatrix} S & 1 & S \\ -\Sigma' & q & \Sigma \end{pmatrix} \times \sqrt{[(J(J+1)(2J+1)S(S+1)(2S+1)]} \\ \delta_{\Sigma'\Sigma} q \sum\limits_{\Omega''} (-1)^{J-\Omega'} \begin{pmatrix} J & 1 & J \\ -\Omega' & -q & \Omega'' \end{pmatrix} (-1)^{J-\Omega''} \\ \times \begin{pmatrix} J & 1 & J \\ -\Omega'' & -q & \Omega \end{pmatrix} [J(J+1)(2J+1)] \end{array} \right\}\end{aligned} \tag{23}$$

Matrix elements for magnetic hyperfine interaction, $\hat{\mathrm{H}}^{\text{hfs}}$:

$$\left\langle \eta\Lambda; S\Sigma'; J\Omega'(JI_1)F_1(F_1I_2)F \left| \hat{\mathrm{H}}^{\mathrm{hfs}} \right| \eta\Lambda; S\Sigma; J\Omega(JI_1)F_1(F_1I_2)F \right\rangle = \delta_{\Lambda'\Lambda}$$

$$\left\{ \begin{array}{l} (-1)^{J'+I_1+I_2+2F_1+F+1}\sqrt{I_2(I_2+1)(2I_2+1)(2F_2'+1)(2F_1+1)} \\ \times\sqrt{(2J'+1)(2J+1)} \begin{Bmatrix} F & I_2 & F_1 \\ 1 & F_1 & I_2 \end{Bmatrix} \begin{Bmatrix} I_1 & J' & F_1' \\ 1 & F_1 & J \end{Bmatrix} \sum_q (-1)^{J'-\Omega'} \begin{pmatrix} J' & 1 & J \\ -\Omega' & q & \Omega \end{pmatrix} \\ \times[a\Lambda\delta_{\Sigma\Sigma'}\delta_{\Omega\Omega'} + b_F(-1)^{S-\Sigma'} \begin{pmatrix} S & 1 & S \\ -\Sigma' & q & \Sigma \end{pmatrix} \times \sqrt{S(S+1)(2S+1)} \\ + \dfrac{\sqrt{30}}{3} c(-1)^q (-1)^{S-\Sigma'} \begin{pmatrix} S & 1 & S \\ -\Sigma' & q & \Sigma \end{pmatrix} \begin{pmatrix} 1 & 2 & 1 \\ -q & 0 & q \end{pmatrix} \sqrt{(S(S+1)(2S+1)]} \end{array} \right\}$$

$$-d\sum_{q=\pm1} \delta_{\Lambda',\Lambda\mp2}(-1)^{J+I_1+I_2+2F_1+F+1}\sqrt{I_2(I_2+1)(2I_2+1)(2F_1'+1)(F_1+1)} \qquad (24)$$

$$\times\sqrt{(2J'+1)(2J+1)} \begin{Bmatrix} F & I_2 & F_1 \\ 1 & F_1 & I_2 \end{Bmatrix} \begin{Bmatrix} I_1 & J' & F_1' \\ 1 & F_1 & J \end{Bmatrix} (-1)^{J'-\Omega'}$$

$$\times \begin{pmatrix} J' & 1 & J \\ -\Omega' & -q & \Omega \end{pmatrix} (-1)^{q+S-\Sigma'} \begin{pmatrix} S & 1 & S \\ -\Sigma' & q & \Sigma \end{pmatrix} \sqrt{(S(S+1)(2S+1)}$$

Matrix elements for quadrupole interaction, $\hat{\mathrm{H}}^{\mathrm{eq}}$:

$$\left\langle \left\langle \eta\lambda; S\Sigma'; J\Omega'(JI_1)F_1'(F_1'I_2)F \right\| \hat{\mathrm{H}}^{\mathrm{eq}} \left| \eta\lambda; S\Sigma; J\Omega(JI_1)F_1(F_1I_2)F \right\rangle \right.$$

$$= \delta_{\Lambda\Lambda'}\delta_{\Omega'\Omega}(-1)^{J+I_1+I_2+2F_1'+F+1} \begin{Bmatrix} F & I_2 & F_1 \\ 2 & F_1 & I_2 \end{Bmatrix} \begin{Bmatrix} I_1 & J' & F_1' \\ 2 & F_1' & J \end{Bmatrix} \qquad (25)$$

$$\times\sqrt{(2J'+1)(2J+1)}\,\frac{eQq_0}{4}(-1)^{J'-\Omega} \begin{pmatrix} J' & 2 & J \\ -\Omega & 0 & \Omega \end{pmatrix} \begin{pmatrix} I_2 & 2 & I_2 \\ -I_2 & 0 & I_2 \end{pmatrix}^{-1}$$

Matrix elements for Stark shift, $\hat{\mathrm{H}}^{\mathrm{Stark}}$:

$$\left\langle \eta\Lambda; S\Sigma'; J\Omega'(JI_1)F_1(F_1I_2)FM_F \left| \hat{\mathrm{H}}^{\mathrm{Stark}} \right| \eta\Lambda; S\Sigma; J\Omega(JI_1)F_1(F_1I_2)FM_F \right\rangle$$

$$= \mu E_z\delta_{SS'}\delta_{\Sigma\Sigma'}\sum_{pq}(-1)^{F'-M_{F'}} \begin{pmatrix} F' & 1 & F \\ -M_F' & 0 & M_F \end{pmatrix} (-1)^p (-1)^{F+F_1'+1+I_2}$$

$$\times\sqrt{(2F+1)(2F'+1)} \begin{Bmatrix} I_2 & F_1' & F \\ 1 & F & F_1 \end{Bmatrix} (-1)^{F_1+J'+1+I_1}\sqrt{(2F_1+1)(2F_1'+1)} \qquad (26)$$

$$\times \begin{Bmatrix} I_1 & J' & F_{11}' \\ 1 & F & J' \end{Bmatrix} (-1)^{J'-\Omega'}\sqrt{(2J+1)(2J'+1)} \begin{pmatrix} J' & 1 & J \\ -\Omega' & q & \Omega \end{pmatrix}$$

where q=0 for parallel polarization, and q=±1 for perpendicular polarization.

Matrix elements for Zeeman shift, $\hat{\mathrm{H}}^{\mathrm{Zeeman}}$:

$$\left\langle \eta\lambda; S\Sigma'; J\Omega'(JI_1)F_1^{'}(F_1I_2)F^{'}M_{F'}\left|\hat{\mathrm{H}}^{\mathrm{Zeeman}}\right|\eta\lambda; S\Sigma; J\Omega(JI_1)F_1(F_1I_2)FM_F\right\rangle$$
$$=\delta_{\eta\eta'}\mu_B B_z(-1)^{F'-M_{F'}}\times\begin{pmatrix} F' & 1 & F \\ -M_F^{'} & 0 & M_F\end{pmatrix}(-1)^{F+F_1^{'}+1+I_2}\sqrt{(2F+1)(2F'+1)}$$
$$\begin{Bmatrix} F_1 & F & I_2 \\ -F^{'} & F_1^{'} & 1\end{Bmatrix}(-1)^{F_1+J'+1+I_1}\sqrt{(2F_1+1)(2F_1^{'}+1)}\begin{Bmatrix} J & F_1 & I_1 \\ F_1^{'} & J^{'} & 1\end{Bmatrix}\sum_q(-1)^{J'-\Omega'}\begin{pmatrix} J' & 1 & J \\ \Omega' & q & \Omega\end{pmatrix} \quad (27)$$
$$\times\sqrt{(2J'+1)(2J+1)}\begin{bmatrix}\delta_{\Lambda,\Lambda'}g_s(-1)^{S-\Sigma'}\begin{pmatrix} S & 1 & S \\ -\Sigma' & q & \Sigma\end{pmatrix}\sqrt{S(S+1)(2S+1)}- \\ \delta_{\Lambda,\Lambda'}g_l\Sigma+\delta_{\Sigma,\Sigma'}g_l(-1)^{L-\Lambda'}\begin{pmatrix} L & 1 & L \\ -\Lambda' & q & \Lambda\end{pmatrix}\sqrt{L(L+1)(2L+1)}\end{bmatrix}$$

Matrix element for Relative intensities in a case ($a_{\beta J}$) basis set:

$$\left\langle \eta'\Lambda'S\Sigma'J'\Omega'IF'M_F'\left|T_p^1(\mu)\right|\eta\Lambda S\Sigma J\Omega IFM_F\right\rangle$$
$$=(-1)^{F'-M_F'}\begin{pmatrix} F' & 1 & F \\ M_F' & p & M_F\end{pmatrix}\left\langle \eta'\Lambda'S\Sigma'J'\Omega'IF'\left\|T^1(\mu)\right\|\eta\Lambda S\Sigma J\Omega IF\right\rangle$$
$$=(-1)^{F'-M_F'}\begin{pmatrix} F' & 1 & F \\ M_F' & p & M_F\end{pmatrix} \quad (28)$$
$$\times\delta_{\Sigma'\Sigma}(-1)^{J'+I+F+1}\begin{Bmatrix} I & J' & F' \\ 1 & F & J\end{Bmatrix}[(2F'+1)(2F+1)]^{1/2}$$
$$\times\sum_q(-1)^{J'-\Omega'}\begin{pmatrix} J' & 1 & J \\ -\Omega & q & \Omega\end{pmatrix}[(2J'+1)(2J+1)]^{1/2}\left\langle \eta'\Lambda'\left|T_p^1(\mu)\right|\eta\Lambda\right\rangle$$

3.2. Triatomic, C_{2v} molecules

For polyatomic molecules, symmetry labels play most of the term symbols roles. Character tables describe how each object transforms under all operations of a symmetry. Each object may have one particular set of characters. A set of characters for an object is called a representation. A representation is irreducible if it cannot be reduced into the sum of other representations. Irreducible representations of the symmetry groups are commonly used to label electronic states, which to some extent serve as term

symbols. For example, a C_{2v} molecule is the molecule with the cyclic group with 2-fold proper axis of rotations with a vertical mirror plane.

A characters table of C_{2v} molecules taken from [3] is shown in Table 3.1. In Table 3.1, "A" means the irreducible representation is symmetric with respect to rotation about the principle axis. "B" means the irreducible representation is antisymmetric with respective to rotation about the principle axis. The subscripts 1 and 2 are denoted the transformation property with respect to the reflection in the xz-plane.

Table 3.1. Characters table of C_{2v} molecules:

C_{2v}	E	C_2	$\sigma_v(xz)$	$\sigma'_v(yz)$		
A_1	1	1	1	1	z	x^2, y^2, z^2
A_2	1	1	-1	-1	R_z	Xy
B_1	1	-1	1	-1	x, R_y	Xz
B_2	1	-1	-1	1	y, R_x	Yz

Table 3.2. Representation table of C_{2v} molecule in a atom centered Cartesian coordinate system, x_i, y_i, z_i

C_{2v}	E	C_2	$\sigma_v(xz)$	$\sigma'_v(yz)$
atoms	3	1	1	3
χ(per atom)	3	-1	1	1
Γ	9	-1	1	3

In order to determine the symmetry of the molecular, the irreducible representation spanned when every atom of a molecule is free to move in any directions must be considered. This is achieved by building a large matrix that has an *x, y, z* component for each atom. The reducible representation determines how each vector $\vec{x}$, $\vec{y}$, $\vec{z}$ on each atom transforms under every symmetry operation. The size of these matrices

grows as 3N. The traces of these matrices are more to the interest. The traces of these matrices, Γ, can be recorded in a representation in Table 3.2.

The reducible representation can then be broken up into contributions from each irreducible representation. Every reducible representation, Γ^{R}, can be written as a sum of the irreducible representations, Γ^{IR}, of a point group, where n_{IR} is the number of times a particular irreducible representation occurs:

$$\Gamma_{R} = \sum_{IR} n_{IR} \Gamma^{IR} \tag{29}$$

where:

$$n_{IR} = \frac{1}{h} \sum_{Q} k \bullet \chi^{IR}(Q) \bullet \chi^{R}(Q) \tag{30}$$

in equation (30), h is the number of operations in the group, Q is a particular class of symmetry operation, k is the number of operations in that class, $\chi^{IR}(Q)$ is the character of the irreducible representation under Q, $\chi^{R}(Q)$ is the character of the reducible representation under Q. Therefore:

$$n_{A_1} = \frac{1}{4}[(1\times 9\times 1) + (1\times -1\times 1) + (1\times 1\times 1) + (1\times 3\times 1)] = 3 \tag{31}$$

$$n_{A_2} = \frac{1}{4}[(1\times 9\times 1) + (1\times -1\times 1) + (1\times 1\times -1) + (1\times 3\times -1)] = 1 \tag{32}$$

$$n_{B_1} = \frac{1}{4}[(1\times 9\times 1) + (1\times -1\times -1) + (1\times 1\times 1) + (1\times 3\times -1)] = 2 \tag{33}$$

$$n_{B_2} = \frac{1}{4}[(1\times 9\times 1) + (1\times -1\times -1) + (1\times 1\times -1) + (1\times 3\times 1)] = 3 \tag{34}$$

There are $\Gamma^{coor}=3A_1\oplus A_2\oplus 2B_1\oplus 3B_2$, representation from the atom centered characters table, the symmetry associated with rotation motion are A_2, B_1, B_2 for R_z, R_y,

and R_x, respectively, the symmetry associated with translation motions are A_1, B_1, B_2 for z, x, and y respectively. Therefore, the associated symmetry with vibration motion is: $3A_1 \oplus A_2 \oplus 2B_1 \oplus 3B_2 - A_2 \oplus B_1 \oplus B_2$(rotation)- $A_1 \oplus B_1 \oplus B_2 = 2A_1 \oplus B_2$. Therefore, A_1 and B_2 are symmetry of the vibrational modes in TiO_2 and ZrO_2, where A_1 vibrational mode contains symmetric stretch and bending while B_2 vibrational mode is the asymmetric stretch mode. These symmetry considerations play a major role in the Geometry-Force approach [4] was used and described in detail in Chapter 5.

References

1. G. Herzberg, *Molecular Spectra and Molecular Structure* (Van Nostrand Reinhold Company, New York, 1950).

2. G. Herzberg; *Molecular Spectra and Molecular Structure; Vol III-Electronic Spectra and Electronic Structure of Polyatomic Molecules* (Kreiger, Malabar, 1991).

3. P. R. Bunker and Per Jensen, *Molecular Symmetry and Spectroscopy,* (Canadian Science Publishing (NRC Research Press); 2nd Revised edition (December 23, 2009).

4. E. B. Wilson, Jr. J. C. Decius, and P. C. Cross, *Molecular Vibrations* (McGraw-Hill, New York, 1955).

5. C.H Townes and A. L. Schawlow, *Microwave spectroscopy (*Courier Dover Publications)

6. J. M. Brown, A Carrington, *Rotational Spectroscopy of Diatomic Molecules* (Cambridge University Press, 2003)

7. H. Lefebvre-Brion, R. W. Field, *The Spectra and Dynamics of Diatomic Molecules* (Academic Press; 1 edition (April 15, 2004)

8. W.J. Childs, O. Poulsen, T.C. Steimle, J. Chem. Phys., **88** (2), 598, 1988

9. J M Brown, I Kopp, C Malmberg and B Rydh, *Phys. Scr.* **17** 55(1978).

Chapter 4

SPECTROSCOPY OF HEAVY POLAR MOLECULES IN SUPPORT OF PARITY NON-CONSERVATION

Parity is the operator involving a transformation that changes the algebraic sign of the coordinate system. In quantum mechanics, parity, **P**, can be viewed as the operator which transforms a given quantum state into its mirror image ($\mathbf{P}^2$=1). The law of conservation of parity is valid for both the strong and the electromagnetic interactions but is not valid for the weak interaction. The Parity Non-conservation (PNC) in the weak interaction inside the nucleus was first predicted by T. D. Lee and C. N. Yang [1]. It was later observed experimentally by Wu et al [2] the beta decay of ^{60}Co. PNC effects are strongly enhanced in heavy atoms and molecules due to the high value of the electron density at the nucleus [3]. Sometimes ago, it was pointed out by Sandars [4] that PNC phenomena are more readily observed in heavy polar molecules. The matrix elements of the weak interaction depend strongly on nuclear charge, Z, and the PNC experiment requires that molecules are polarized in an external electric field. The diatomic molecules meeting these criteria are MX where M is heavy metal and X is Halogen, Oxygen, and Sulfur. Strontium monofluoride (SrF), barium monofluoride (BaF), ytterbium monofluoride (YbF) and hafnium monofluoride (HfF) are good candidates for PNC experiments because they are all late metal halides molecules.

Experiments involving the study of PNC effects are very difficult because the weak interaction has effects in a very short distance from the nucleus. At the range of 10^{-17} m from the nucleus, the weak interaction is 10000 times weaker than the electromagnetic interaction. At distances typical for quarks in a proton or neutron (10^{-15}

m), the weak interaction force is even smaller. There are two types of PNC experiments: experiments to measure the electric dipole moments of the electron (eEDM), d_e [5], and the experiment measures the anapole moments of the nucleus, k_A [6].

The electron electric dipole moment (eEDM), d_e is the intrinsic property of the electron. The eEDM only exists when both parity (P) and time reversal (T) invariance are violated [7]. The simple approach used in early eEDM experiment was to measure the spin-flip frequency of a free electron in an electric field, analogous to Zeeman flip of spin[5]**.** However, measuring the eEDM is this way to proved futile. The proposed experiments to measure d_e involved molecules: PbO, YbF, PbF, ThO, WC, HfF^+, HfH^+, PtH^+, PtF^+, ThH^+, ThF^+. My work on HfF and YbF provides critical information needed for the eEDM experiments.

The anapole moment is defined as the asymmetric contribution to the magnetic quadrupole induced in the nucleus [8]. The anapole moment is a vector, which produces spiral spin structure and toroidal currents. Only nuclei with non-zero spin are appropriate (i.e this is a NSD-PNC term). The anapole moment is a parity (P)-odd and time (T)-reversal-even electromagnetic moment. Many heavy atoms and polar molecules are candidates for PNC, anapole, experiments. A recent review by DeMille et al. [6] suggests a number of promising candidates including ^{87}SrF, ^{137}BaF, ^{171}YbF, ^{91}ZrN, ^{27}AlS, ^{69}GaO, ^{139}LaO... The proposed experiment to measure the anapole moments involves molecules with a single valence electron in a $^2\Sigma$ electronic state. My work on ^{87}SrF, ^{135,137}BaF, and YbF are in support of NSD-PNC measurement.

The effective Hamiltonian with the PNC terms, for example in the $^2\Sigma$ state, is given by [9, 10]:

$$\mathbf{H}^{eff}(^2\Sigma) = B\mathbf{N}^2 + \gamma\mathbf{N}\cdot\mathbf{S} + b_F\mathbf{I}\cdot\mathbf{S} + c(I_z S_z - \tfrac{1}{3}\mathbf{I}\cdot\mathbf{S}) + eq_0 Q\frac{3I_z - \mathbf{I}^2}{4I(2I\text{-}1)}$$
$$+ W_A k_A \mathbf{n}\times\mathbf{I}\cdot\mathbf{S} + (W_S k_S + W_d d_e)\mathbf{S}\cdot\mathbf{n} \quad , \qquad (1)$$

where the first five terms in the effective Hamiltonian are described in detail in Chapter 3. These are the rotation, spin-rotation interaction, magnetic hyperfine interactions, and nuclear electric quadrupole interaction terms. The last two terms in Equation 1 are the PNC terms: anapole moment of the nucleus and the eEDM with the internal electric field where k_A and k_S are anapole constant, and d_e is the eEDM, respectively. The term $W_S k_S$ is a scalar term. The PNC related parameters W_A, W_S, and W_d, cannot be measured experimentally and have to be obtained from the molecular electronic structure calculations. The parameters W_A, W_S, and W_d have the matrix elements that are similar to matrix elements of magnetic hyperfine interaction which can be measured experimentally (see below)[11]. Therefore, if the magnetic hyperfine interaction can be accurately predicted by theorist in comparison with the experimental determined values, the W_A, W_S, and W_d can be accurately predicted. The knowledge of W_A, W_S, and W_d is crucial to the experiments that measure anapole moment and eEDM.

4.1. Odd isotope of Strontium monofluoride, ^{87}SrF

Before the new interest on PNC effects, the early works on strontium monofluoride, SrF, have focused on obtaining the spectroscopic parameter primarily for the published even isotopes. A combined study of $B^2\Sigma^+$–$X^2\Sigma^+$ electronic transitions and $X^2\Sigma$ ground state microwave transitions was done by Ernst et al. [12] many years ago. This study produced the spectroscopic constants for the $B^2\Sigma^+$. Sub-Doppler optical-optical double-resonance spectra of ^{88}SrF were recorded using two single-mode cw-dye

lasers by Nitsch et. al [13]. The $F^2\Sigma^+$ and $G^2\Pi$ states were observed through the intermediate $B^2\Sigma^+$ state and analyzed in the 32000 cm^{-1} to 35000 cm^{-1} region above the ground state. The electric dipole moments and hyperfine structures have been determined for $A^2\Pi$–$X^2\Sigma^+$ and $B^2\Sigma^+$ and $X^2\Sigma^+$ state by Kändler et al [14]. The dipole moments are $\mu(A^2\Pi)$ = 2.064(50) D, $\mu(B^2\Sigma^+)$ = 0.91(4) D, and $\mu(X^2\Sigma^+_{v=0})$ = 3.4963(40) D and $\mu(X^2\Sigma^+_{v=1})$ = 3.5538(37) D. A higher resolution, recent study of ^{88}SrF was done by Steimle et al [15] to fully determine the spectroscopy constants of $A^2\Pi$ and $X^2\Sigma^+$ states. The new interests on NSD-PNC by Demille et al [6] show the need in understanding the spectroscopy $A^2\Pi$–$X^2\Sigma^+$transition of the odd isotope, ^{87}SrF, which I present here.

4.1.1. Observation

Strontium has four stable, naturally occurring, isotopes: ^{84}Sr (0.56%), ^{86}Sr (9.86%), ^{87}Sr (7.0%) and ^{88}Sr (82.58%). Only the ^{86}SrF, ^{87}SrF, and ^{88}SrF were observed here through laser induced fluorescence (LIF) spectroscopy; the ^{84}SrF spectral features were not observed due to the small percent of abundance. The spectral features of ^{87}SrF are markedly different from those of ^{88}SrF and ^{86}SrF because of the nonzero nuclear spin. ^{87}Sr has nuclear spin of 9/2, and the magnetic moment μ=-1.09283μ_N. Portions of the LIF spectrum for the $A^2\Pi_{1/2}$–$X^2\Sigma^+$(0,0) and $A^2\Pi_{3/2}$–$X^2\Sigma^+$(0,0) sub-bands, and the associated energies levels, are shown in Figure 4.1 and Figure 4.2, respectively. Figure 4.1(A) shows the example of the observed spectrum from $A^2\Pi_{1/2}$–$X^2\Sigma^+$(0,0) sub-band. The intense spectral feature is an overlap of the $^QQ_{11}(0)$ line of the ^{88}SrF and the ^{86}SrF isotopologues. The two small features on both sides of the intense line are due to the magnetic hyperfine splitting in the ground $X^2\Sigma^+$ state of ^{87}SrF [16]. Figure 4.1(B) shows

the predicted spectrum of ^{88}SrF using the parameters from Ref. 15. The predicted spectrum for ^{87}SrF is shown in Figure 4.1(C) and its associated energy levels were calculated using the final set of parameters that came from the fit (*vide infra*) given in Table 4.2.

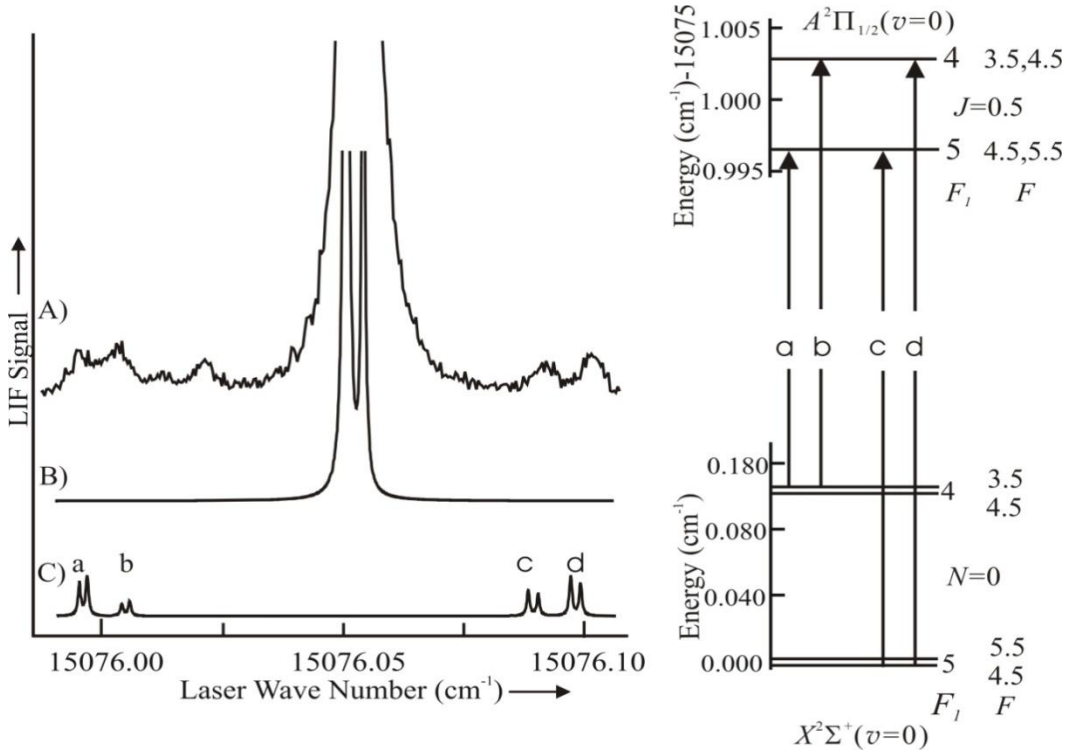

Figure 4.1. Observed (A) and predicted (B, C) spectra of $A^2\Pi_{1/2}$–$X^2\Sigma^+$ (0,0) sub-band of SrF in the region of $^{Q}Q_{11}(0)$ (ν=15076.05 cm^{-1}) of the ^{88}SrF. The two features of ^{87}SrF are $^{Q}Q_{14}(0)$ (ν= 15076.00 cm^{-1}) and the $^{Q}Q_{15}(0)$ (ν= 15076.99 cm^{-1}) with splitting due to the hyperfine interaction in the $A^2\Pi_{1/2}$. The associated energy patterns of ^{87}SrF are present on the right side. The predicted (B) spectrum of ^{88}SrF is using the spectroscopic parameters from Ref. 16. The predicted (C) spectrum of ^{87}SrF using the optimized parameter in Table 4.2 and the isotopic scale parameter from ^{88}SrF in Ref 16.

Figure 4.2(A) shows an example of the observed spectrum from $A^2\Pi_{3/2}$–$X^2\Sigma^+$(0,0) sub-band. The intense spectral feature is an overlap of the $^RR_{22}(1)$ and $^RQ_{21}(1)$ line of ^{88}SrF and ^{86}SrF. Figure 4.2(B) shows the predicted spectrum of ^{88}SrF using the parameter from Ref. 15. The two small features on both sides of the intense line are due to the magnetic hyperfine splitting in the ground state of ^{87}SrF [16]. Figure 4.2(C) shows the predicted spectrum of ^{87}SrF and the right side of Figure 4.2 shows the associated energy levels. The predicted spectrum and the associated energy levels were obtained using the optimized set of parameters (*vide infra*) given in Table 4.2.

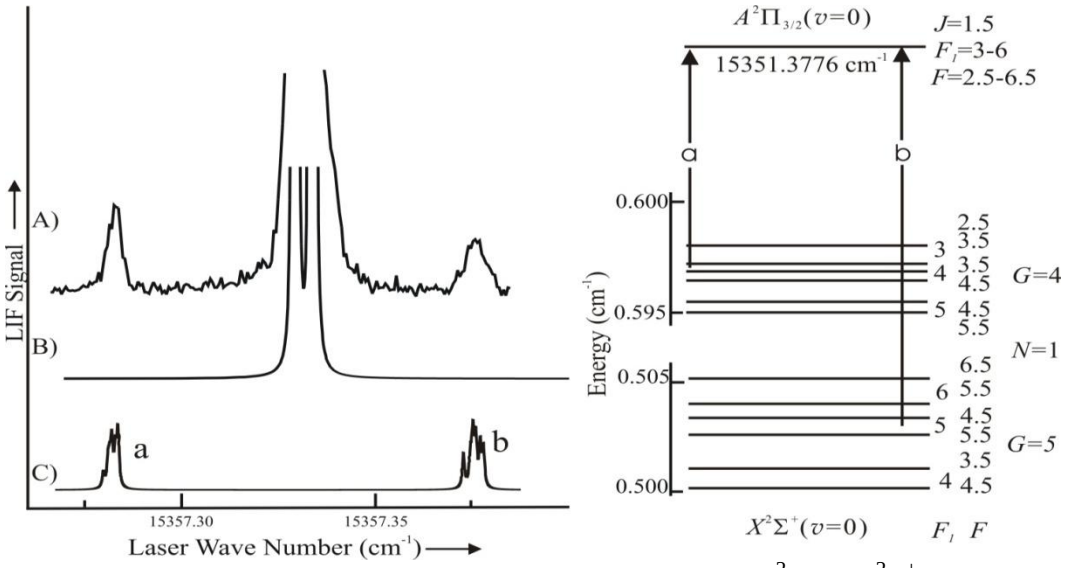

Figure 4.2. Observed (A) and predicted (B, C) spectra of $A^2\Pi_{3/2}$–$X^2\Sigma^+$ (0,0) sub-band of SrF in the region of $^RR_{22}(1)$ and $^RQ_{21}(1)$ (ν=15357.34 cm^{-1}) of the overlap feature of ^{88}SrF & ^{86}SrF. The two features of ^{87}SrF are $^RQ_{24}(1)$ (ν= 15357.28 cm^{-1}) and the $^RQ_{24}(1)$ (ν= 15357.38 cm^{-1}) with no evidence of hyperfine interaction in the $A^2\Pi_{3/2}$ state. The associated energy patterns of ^{87}SrF are present on the right side. The predicted (B) spectrum of ^{88}SrF is using the spectroscopic parameters from Ref. 16. The predicted (C)

spectrum of ^{87}SrF using the optimized parameter in Table 4.2 and the isotopic scale parameter from ^{88}SrF in Ref 16.

Both spectral features of $A^2\Pi_{1/2}$–$X^2\Sigma^+(0,0)$ and $A^2\Pi_{3/2}$–$X^2\Sigma^+(0,0)$ sub-bands exhibit a small splitting due to the excited state hyperfine interactions. Assigning the spectra is rather complicated because there are numerous unresolved transitions due to small magnetic hyperfine splitting in the $A^2\Pi(v=0)$ and ^{87}Sr has nuclear spin of 9/2. Figure 4.1 and Figure 4.2 show evidence that the magnetic hyperfine splitting only has an effect of the *e*-parity component in the $A^2\Pi_{1/2}(v=0)$ sub-state.

4.1.2. Analysis

The previous *rf*-measurements [16] determined the optimized set of parameters for the $X^2\Sigma^+(v=0)$ state of ^{87}SrF. The calculated energy patterns for the $X^2\Sigma^+(v=0)$ state of the ^{87}SrF isotopologue, using the previously determined parameters from Ref. 16 are present in Figure 4.3. Figure 4.3 illustrates the contributions of the spin-rotation and hyperfine terms to the energy level by subtracting rotational energy [$\approx B\times N(N+1)$] of the ^{87}SrF isotopologues. Figure 4.3 shows that at very high rotational excitation of the $X^2\Sigma^+(v=0)$ state of ^{87}SrF, the energy levels patterns are those of a molecule near sequentially coupled Hund's case($b_{\beta J}$). The arrows indicated the previous *rf*-measurement [16]. At very low rotational excitation, the large ^{87}Sr magnetic hyperfine interaction causes the energy level patterns to be that of a molecule near Hund's case ($b_{\beta S}$) limit, which is also described in detail in Chapter 3. In the Hund's case ($b_{\beta S}$) limit, the good intermediate quantum number is **G**(=4 and 5) which results from the coupling of the

nuclear spin angular momentum, $\mathbf{I_1}$(=9/2), of ^{87}Sr with the total electron spin angular momentum, **S(**=1/2).

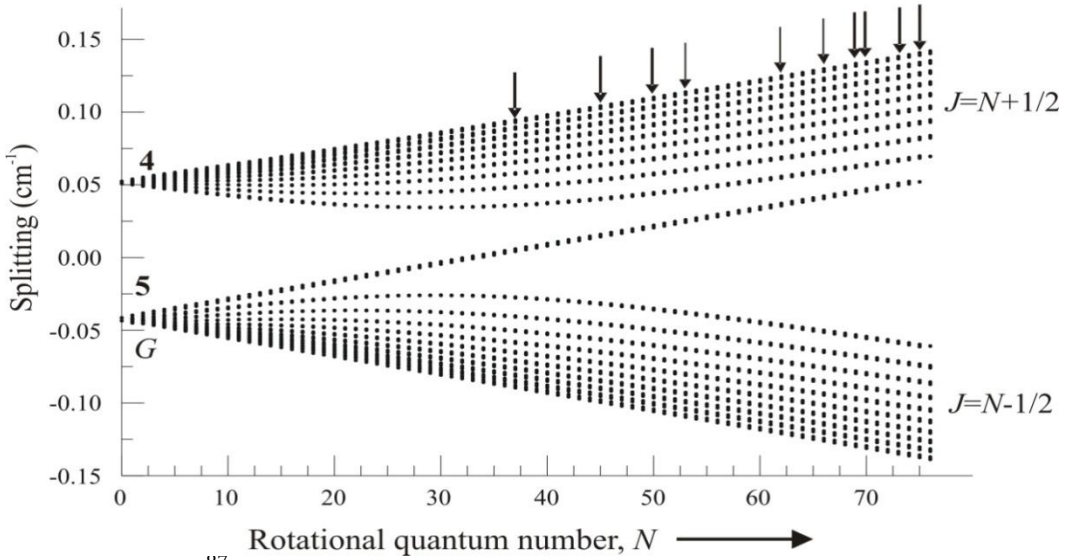

Figure 4.3. The ^{87}SrF spin-rotation and hyperfine energy pattern as the function of rotational quantum number, N. The arrows are the previous measured of laser-*rf* transitions [16].

The last step of analyzing the spectra of ^{87}SrF is to perform a direct fit to the measured transition wavenumbers. The effective Hamiltonian for the $X^2\Sigma^+$ state is given by [17], which is also described in Chapter 3:

$$\mathbf{H}^{eff}(^2\Sigma) = B\mathbf{N}^2 - D(\mathbf{N}^2)^2 + \gamma\mathbf{N}\cdot\mathbf{S} + b_F\mathbf{I}\cdot\mathbf{S} + c(I_zS_z - \tfrac{1}{3}\mathbf{I}\cdot\mathbf{S}) + eq_0Q\frac{3I_z - \mathbf{I}^2}{4I(2I\text{-}1)}, \qquad (2)$$

includes the rotation (*B)*, the associated centrifugal distortion correction *(D)*, spin-rotation coupling constant*(*γ*),* Fermi contact (b_F), dipolar magnetic hyperfine (c), electric quadrupole hyperfine (eq_0Q) parameters. In equation 2, **N** is total angular momentum excluding electron and nuclear spin, **S** is electron spin angular momentum, **I** is nuclear spin angular momentum operators. The expressions for the matrix elements were taken

out from Ref. [17]. The eigenvalues and eigenvectors for the $X^2\Sigma^+$ state of ^{87}SrF were obtained by constructing and numerically diagonalizing a matrix representation with a dimension of 40(=(2S+1)×[2I_1(^{87}Sr)+1]×[2I_2(^{19}F)+1]). The matrix representation was numerically diagonalized to give eigenvalues and eigenvectors.

The effective Hamiltonian for the $A^2\Pi$ state is given by [17]:

$$\mathbf{H^{eff}}\,(^2\Pi) = T_{0,0} + AL_zS_z + B\mathbf{R}^2 - D(\mathbf{R}^2)^2$$
$$+ \tfrac{1}{2}(p+2q)(e^{-2i\phi}J_+S_+ + e^{+2i\phi}\,J_-S_-) + \tfrac{1}{2}d(e^{-2i\phi}I_+S_+ + e^{+2i\phi}\,I_-S_-). \qquad (3)$$

Equation 3 includes the origin, $T_{0,0}$, the spin-orbit interaction, A, the rotation, B, and the associated centrifugal distortion correction, D, Λ-doubling, (p+2q), and the parity dependent magnetic hyperfine, d, parameters. In Equation 3, $J_\pm$, $S_\pm$, $I_\pm$ are raising (+) and lowering (-) operators of the total angular momentum in the absence of nuclear spin, **J**, total electron spin, **S**, and nuclear spin angular momentum, $\mathbf{I_1}$ (^{87}Sr) operators. The eigenvalues and eigenvectors for the $A^2\Pi$ state of ^{87}SrF were obtained by constructing numerically diagonalizing a matrix representation of dimension 80(=2×(2S+1)×[2I_1(^{87}Sr)+1]×[2I_2(^{19}F)+1]). The matrix representation was constructed using a sequentially coupled Hund's case ($a_{\beta J}$) basis set, which is described in detail in Chapter 3.

A total of 75 transitions (40 transitions from the $A^2\Pi_{3/2}$–$X^2\Sigma^+$(0,0) sub-band and 35 transitions from the $A^2\Pi_{1/2}$–$X^2\Sigma^+$ sub-band) were entered into the fit. Various fits were performed. The ground state parameters: D, γ, b_F (^{87}Sr and ^{19}F), c(^{87}Sr and ^{19}F), eq_0Q are constrained to the determined values from Ref. 16. The rotation, B, was constrained to the predicted value using the isotopic scaling: B(^{87}SrF)=B(^{88}SrF)[μ(^{88}SrF)/ μ(^{87}SrF)]. The

best fit was obtained by optimizing $T_{0,0}$, A, B, $p+2q$, and $d(^{87}\mathrm{Sr})$ for the $A^2\Pi$. The observed transition wavenumber, the difference between observed and calculated values, and the associated assignments are present in Table 4.1. The optimized parameters and theirs associated errors are given in Table 4.2. The standard deviation of the fit is 0.0012 cm^{-1} which corresponds to the measured uncertainty.

4.1.2. Discussion

The newly determined parameters allow for a precise determination of the field free transition wavenumbers, which is critical to implementation of the proposed NSD-PNC measurement involving ^{87}SrF. The isotopic scaled parameters are also listed in Table 4.2 with the exception of newly determined hyperfine parameter, d. Overall, the isotopic scaled parameters are slightly different from the fitted values. The determined hyperfine parameter, $d(^{87}\mathrm{Sr})$, was needed to explain the small splitting exhibited in the $^{Q}Q_{14}(0)$ (ν= 15076.00 cm^{-1}) and $^{Q}Q_{15}(0)$ (ν= 15076.99 cm^{-1}) transitions in Figure 4.1. The determined hyperfine parameter, $d(^{87}\mathrm{Sr})$ is more sensitive to the lowest energy level in the excited state.

In the proposed Parity Non-Conservation (PNC) experiment to measure the anapole moment, DeMille et al [6] proposed using the magnetic field to Zeeman shift the N=0 (+ parity) and N=1(- parity) of the $X^2\Sigma^+$ sublevels into near degeneracy. The magnetic field will be strong enough to decouple electronic spin, **S**, from nuclear spin, **I**, and rotation, **N.** If parity is conserved, then there will be no interaction between the opposite parities of the N=0 (+ parity) and N=1(- parity) in the $X^2\Sigma^+$ state. However, the existence of PNC terms will mix these pairs of nearly-degenerate levels described by the anapole term.

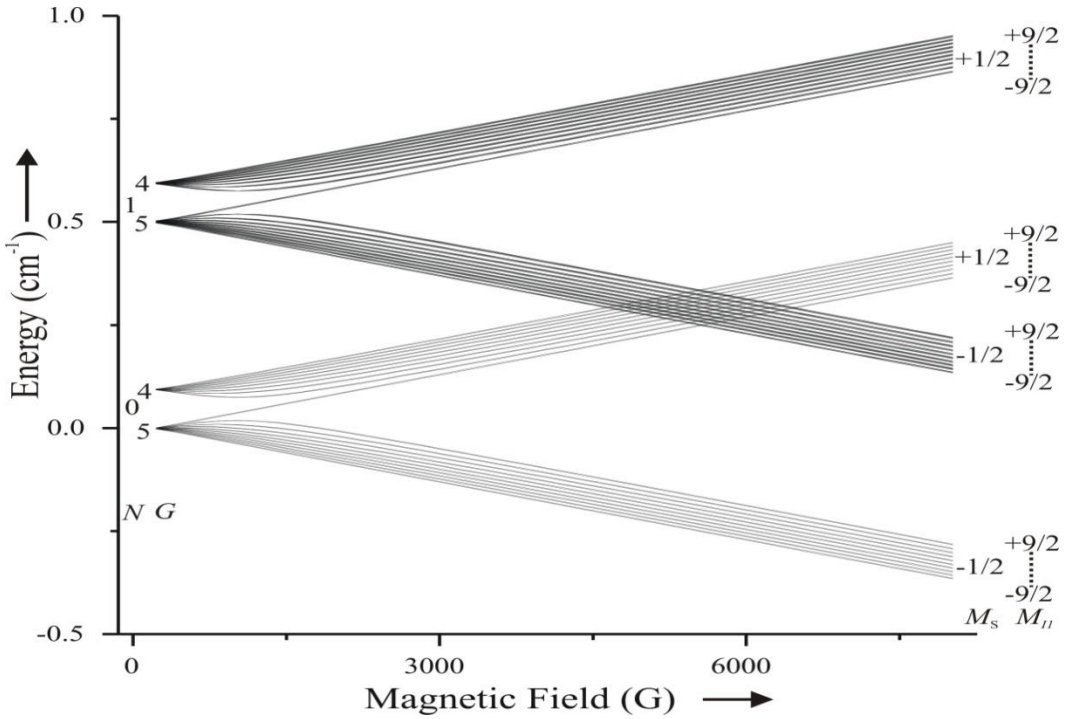

Figure 4.4. The predicted magnetic tuning N=0 (+ parity) and N=1 (- parity) of $X^2\Sigma^+$ state. The pattern was calculated using the field-free hyperfine and spin-rotation parameters from Ref. 16, rotational constant, B=0.250268 cm^{-1}, g_S=2.002 and $g_{l=}$-0.005.

Figure 4.4 shows the predicted magnetic tuning of the N=0 (+ parity) and N=1 (- parity) levels in $X^2\Sigma^+$ state. Figure 4.4 was obtained using the effective Zeeman Hamiltonian shifting[17]:

$$\mathbf{H}^{Zee}(eff) = g_S \mu_B \hat{\mathbf{S}} \cdot \hat{\mathbf{B}} + g_\ell \mu_B (\hat{S}_x \hat{B}_x + \hat{S}_y \hat{B}_y) \qquad (4)$$

The pattern was calculated using the field-free hyperfine and spin-rotation parameters from Ref 16, and a rotational constant B=0.250268 cm^{-1}. Figure 4.4 was predicted using g_S=2.002 and g_l=-0.005, which was calculated using the Curl relationship [17]. The eigenvalues and eigenvectors were obtained by constructing and numerically diagonalizing a 200×200 matrix representation of $\mathbf{H}^{Zee}(\text{eff}) + \mathbf{H}^{field-free}(\text{eff})$ using a

sequentially coupling Hund's case ($a_{\beta J}$) basis sets for F=2.5-6.5. $\mathbf{H}^{Zee}(eff)$ matrix elements were also taken from Ref. 17 and are described in detail in Chapter 3. Figure 4.4 shows that at high magnetic field, $Ms = \pm ½$ becomes the approximately good quantum numbers. Figure 4.4 also shows the range of magnetic field from 4300G to 6200G that the NSD-PV is needed to tune the rotation level of N=0 (+ parity) to near degeneracy with rotational level of N=1(- parity) in the $X^2\Sigma^+$ of the interest molecules (^{87}SrF) [6] for the proposed the anapole measurement.

Table 4.1. Observed and calculated transition position in wavenumber (cm^{-1}) and the associated assignment of the $A^2\Pi$–$X^2\Sigma^+$(0,0) band of ^{87}SrF

Branch	F''_1,F''-F'_1,F'	Observed-15000	Obs-calc
$^{S}R_{24}(0)$	4.0, 3.5 – 5.0, 4.5	357.7840	0.0002
$^{S}R_{25}(0)$	5.0, 4.5 – 6.0, 5.5	357.8790	0.0010
$^{Q}P_{24}(2)$	6.0, 6.5 – 5.0, 5.5	356.2790	-0.0008
$^{Q}P_{25}(2)$	6.0, 6.5 – 6.0, 6.5	356.3740	0.0028
$^{R}Q_{24}(1)$	5.0, 5.5 – 6.0, 6.5	357.2820	-0.0001
$^{R}Q_{25}(1)$	5.0, 5.5 – 6.0, 6.5	357.3740	-0.0025
$^{R}Q_{24}(10)$	9.0, 9.5 –9.0, 9.5	359.9100	-0.0016
	12.0, 12.5–12.0, 12.5	359.9200	0.0001
	13.0, 13.5–13.0, 13.5	359.9230	0.0000
	14.0, 14.5–14.0, 14.5	359.9270	0.0002
$^{R}Q_{25}(10)$	15.0, 15.5 –15.0, 15.5	359.9960	-0.0007
	14.0, 14.5 –14.0, 14.5	360.0020	-0.0014
	13.0, 12.5 –13.0, 12.5	360.0070	-0.0021
	9.0, 8.5 – 9.0, 8.5	360.0170	-0.0021
	14.0, 14.5–14.0, 14.5	360.0240	0.0012
$^{R}Q_{24}(11)$	9.0, 8.5–9.0, 8.5	360.2360	0.0005
	12.0, 12.5–12.0, 12.5	360.2430	0.0002
	13.0, 13.5–13.0,13.5	360.2460	0.0000
	14.0, 14.5–14.0,14.5	360.2500	0.0006
	15.0, 15.5–15.0,15.5	360.2530	-0.0003
$^{R}Q_{25}(11)$	15.0, 15.5–15.0, 15.5	360.3300	0.0005
	14.0, 14.5–14.0, 14.5	360.3340	-0.0004
	8.0, 8.5–8.0, 8.5	360.3500	0.0001
$^{R}Q_{24}(12)$	9.0, 9.5–9.0, 9.5	360.5660	0.0017
	12.0, 12.5–12.0, 12.5	360.5710	-0.0018

	14.0, 14.5–14.0, 14.5	360.5800	0.0003
	15.0, 15.5–15.0, 15.5	360.5840	0.0010
	16.0, 16.5–16.0, 16.5	360.5880	-0.0003
${}^{R}Q_{25}(12)$	15.0, 15.5–15.0, 15.5	360.6680	0.0005
	14.0, 14.5–14.0, 14.5	360.6720	0.0000
	13.0, 13.5–13.0, 13.5	360.6750	-0.0003
	12.0, 12.5–12.0, 12.5	360.6780	-0.0004
	8.0, 8.5–8.0, 8.5	360.6850	0.0007
${}^{R}Q_{24}(13)$	18.0, 18.5–18.0, 18.5	360.9930	0.0007
	17.0, 17.5–17.0, 17.5	361.0020	0.0011
	16.0, 16.5–16.0, 16.5	361.0070	0.0005
	15.0, 15.5–15.0, 15.5	361.0120	-0.0002
	14.0, 14.5–14.0, 14.5	361.0150	-0.0007
	13.0, 13.5–13.0, 13.5	361.0180	-0.0011
${}^{R}Q_{25}(13)$	9.0, 9.5–9.0, 9.5	361.0260	0.0019
${}^{P}P_{14}(1)$	3.0,2.5 – 4.0, 4.5	75.6260	0.0003
	4.0,4.5 – 5.0,5.5	75.6340	-0.0005
${}^{P}P_{15}(1)$	5.0,5.5– 4.0, 4.5	75.7261	0.0026
${}^{Q}Q_{14}(0)$	4.0,4.5 –5.0,5.5	75.9997	0.0017
	4.0,4.5– 4.0, 4.5	76.0072	0.0029
${}^{Q}Q_{15}(0)$	5.0,5.5–5.0,5.5	76.0890	-0.0013
	5.0,5.5– 4.0, 4.5	76.0980	-0.0005
${}^{R}R_{14}(0)$	4.0,4.5 –5.0,5.5	76.9584	-0.0009
${}^{R}R_{15}(1)$	6.0, 6.5- 7.0, 7.5	77.8853	-0.0029
${}^{R}R_{14}(2)$	5.0, 4.5 –5.0, 4.5	78.6294	-0.0008
${}^{R}R_{15}(2)$	7.0, 7.5–8.0, 8.5	78.7257	0.0006
${}^{Q}Q_{14}(4)$	8.0, 8.5–9.0, 9.5	76.8021	-0.0008
${}^{Q}Q_{15}(4)$	9.0, 9.5–9.0, 9.5	76.8862	0.0003
	7.0, 7.5–7.0, 7.5	76.8964	-0.0002
	5.0, 4.5–5.0, 4.5	76.9039	0.0006
${}^{Q}Q_{14}(10)$	6.0, 5.5–6.0, 5.5	78.1697	0.0008
	13.0,12.5–14.0,13.5	78.1784	0.0005
${}^{Q}Q_{15}(10)$	15.0,15.5–15.0,15.5	78.2523	0.0014
	14.0,14.5–14.0,14.5	78.2585	-0.0003
	13.0,13.5–13.0,13.5	78.2649	-0.0002
	12.0,12.5–12.0,12.5	78.2696	-0.0007
${}^{Q}Q_{14}(11)$	7.0, 7.5–7.0, 7.5	78.4172	0.0017
	15.0,15.5–16.0,16.5	78.4302	-0.0001
${}^{Q}Q_{15}(11)$	16.0,16.5–16.0,16.5	78.5006	0.0019
	15.0,15.5–15.0,15.5	78.5069	-0.0001
	14.0,14.5–14.0,14.5	78.5126	-0.0010
	13.0,13.5–13.0,13.5	78.5169	-0.0022
${}^{Q}Q_{15}(12)$	16.0,16.5–16.0,16.5	78.7602	-0.0009
	15.0,15.5–15.0,15.5	78.7679	-0.0002

	14.0,14.5–14.0,14.5	78.7730	-0.0009
	13.0,13.5–13.0,13.5	78.7914	-0.0004
$^{Q}Q_{15}(13)$	16.0,16.5–16.0,16.5	79.0289	0.0002
	15.0,15.5–15.0,15.5	79.0344	-0.0003
	13.0,13.5–13.0,13.5	79.0384	-0.0009
	9.0,9.5–9.0,9.5	79.0549	0.0009
	Sdt. Dev.=0.0012 cm^{-1}		

Table 4.2. Determined parameters (in wavenumber) for the $A\,^2\Pi(v=0)$ state of ^{87}SrF.

Parameter[a]	Fitted Values[b]	Scaled Values[c]	Correlation Matrix[d]				
A	281.4615(8)	281.459(2)	1				
B	0.253762(5)	0.25387(3)	-0.702	1			
p+2q	-0.13333 (16)	-0.130(1)	0.821	-0.716	1		
d	-0.00187(20)	_	-0.028	0.085	-0.128	1	
T_{00}	15216.5954(5)	15216.6016(20)	0.318	-0.757	0.251	-0.094	1

[a] The γ, eq_0Q, $b_F(^{87}Sr)$, $c(^{87}Sr)$, $b_F(^{19}F)$ and $c(F)$ parameters of the $X\,^2\Sigma^+$ (v =0) state were constrained values in Ref.16 and *B* of the $X\,^2\Sigma^+$ (v =0) state to 0.2502680cm^{-1}.

[b] Numbers in parentheses represent a 2σ error estimate in the last quoted decimal point.

[c] The values obtained by scaling the values for ^{88}SrF.

[d] Elements of correlation matrix given in the order in which the parameters are presented.

4.2. Odd isotopes of Barium monofluoride, $^{135\&137}$BaF

The spectroscopy of ^{138}BaF has been well studied experimentally and theoretically [18, 19, 20, 21, 22]. The ground electronic state, $X^2\Sigma$, of the three even isotopes has been well studied by microwave spectroscopy [19]. The electric dipole moment of the $X^2\Sigma$ state was measured by Ernst et al., μ=3.170(3) D [23]. There is only one study of the hyperfine interaction for ^{137}BaF in the $X^2\Sigma$ [20]. The measured hyperfine coupling constants are: $b(^{137}Ba)$ =2301(9) MHz, $c(^{137}Ba)$ = 75(6) MHz, $eqQ(^{137}Ba)$ = -117(12) MHz, and $b(^{19}F)$ = 60(6) MHz. The radiative lifetime of the $A\,^2\Pi_{3/2}(\upsilon=0)$ state

and the $A\,^2\Pi_{1/2}(\upsilon=0)$ state of the BaF are 46.1(9)ns [24] and 56.0(9)ns [25], respectively. Prior to my work, the $A\,^2\Pi$ electronic state of both ^{137}BaF and ^{135}BaF were not well characterized. The new interests on NSD-PNC [6] show the need for understanding the spectroscopy of $A^2\Pi–X^2\Sigma^+$transition for ^{137}BaF, and ^{135}BaF, because optical spectroscopy will be used.

4.2.1. Observation

Barium has seven stable, naturally occurring, isotopes: ^{130}Ba (0.11%), ^{132}Ba (0.10%), ^{134}Ba (2.42%), ^{135}Ba (6.59%), ^{136}Ba (7.85%) and ^{137}Ba (11.23%), and ^{138}Ba (71.70%). The observed spectra are complicated because the transitions from all the isotopes overlap. Due to the percent of abundance, only spectral features from the $A^2\Pi–X^2\Sigma^+$ transitions associated with the ^{134}BaF, ^{135}BaF, ^{136}BaF and ^{137}BaF isotopologues were observed. Spectral features of ^{135}BaF and ^{137}BaF are markedly different from those spectral features of the even isotopologues because both ^{135}Ba and ^{137}Ba have nuclear spin I=3/2 with the *g* factors of +0.5586 and +0.6249, respectively. Similar to $A^2\Pi–X^2\Sigma^+$ transitions of ^{87}SrF, spectral features of ^{135}BaF and ^{137}BaF exhibit large splitting due to the hyperfine interaction in the $X^2\Sigma^+(\nu=0)$ state. The observed and calculated laser induced fluorescence (LIF) spectrum of the $A^2\Pi_{1/2}–X^2\Sigma^+$ (0,0) sub-band in the region of the $R_1(4)$ branch feature at 11634.25 cm^{-1} are shown in Figure 4.5. The intense features in the center of the spectrum are overlap ^{138}BaF and ^{136}BaF transitions. The weaker features straddling the intense features at 11634.20 cm^{-1} and 11634.34 cm^{-1} are overlapping ^{135}BaF and ^{137}BaF transitions. The predicted spectra for ^{135}BaF, ^{137}BaF and the associated energy level for ^{137}BaF were obtained using the optimized parameters (*vide infra*) taken from Table 4.5.

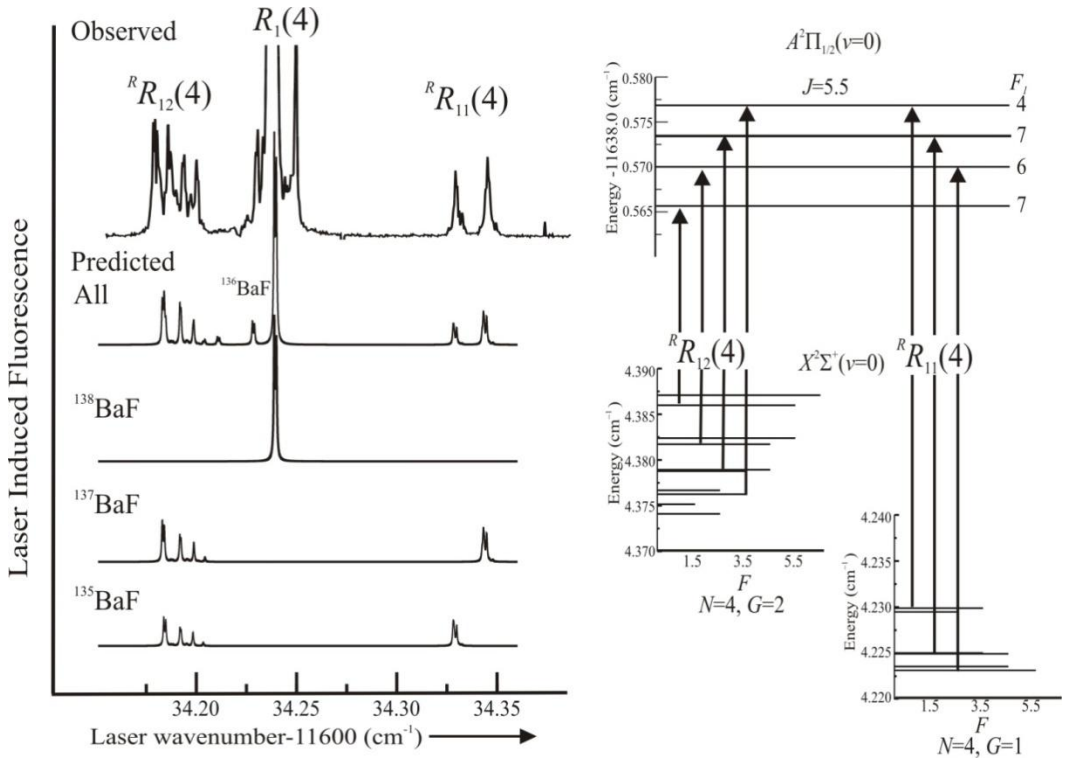

Figure 4.5. The observed and calculated laser induced fluorescence (LIF) spectrum of the $A^2\Pi_{1/2}$–$X^2\Sigma^+$ sub-band in the region of the $R_1(4)$ at 11634.25 cm^{-1} of the ^{138}BaF. Predicted energy pattern on the right side is associated with $^{R}R_{12}(4)$ line (ν=11634.19 cm^{-1}) and the $^{R}R_{11}(4)$ line (ν=11634.35 cm^{-1}) line of the ^{137}BaF. The predicted spectra of ^{135}BaF and ^{137}BaF as well as predicted energy pattern associated with ^{137}BaF were calculated using the optimized parameters taken from Table 4.5.

The observed and calculated laser induced fluorescence (LIF) spectrum of the $A^2\Pi_{3/2}$–$X^2\Sigma^+(0,0)$ sub-band in the region of the $Q_2(6)$ line (ν=12260.60 cm^{-1}) and $^{Q}P_{21}(6)$ line (ν=12260.58 cm^{-1}) of the ^{138}BaF isotope are shown in Figure 4.6. The spectral features for the ^{135}BaF and ^{137}BaF isotopologues are on both sides of the spectral features of ^{138}BaF. Other smaller features are identified as transitions belonging to ^{134}BaF and ^{136}BaF. The predicted energy pattern for the ^{137}BaF is given on Figure 4.6. The predicted

spectra of ^{135}BaF and ^{137}BaF as well as predicted energy pattern associated with ^{137}BaF transitions were calculated using the optimized parameters taken from Table 4.5.

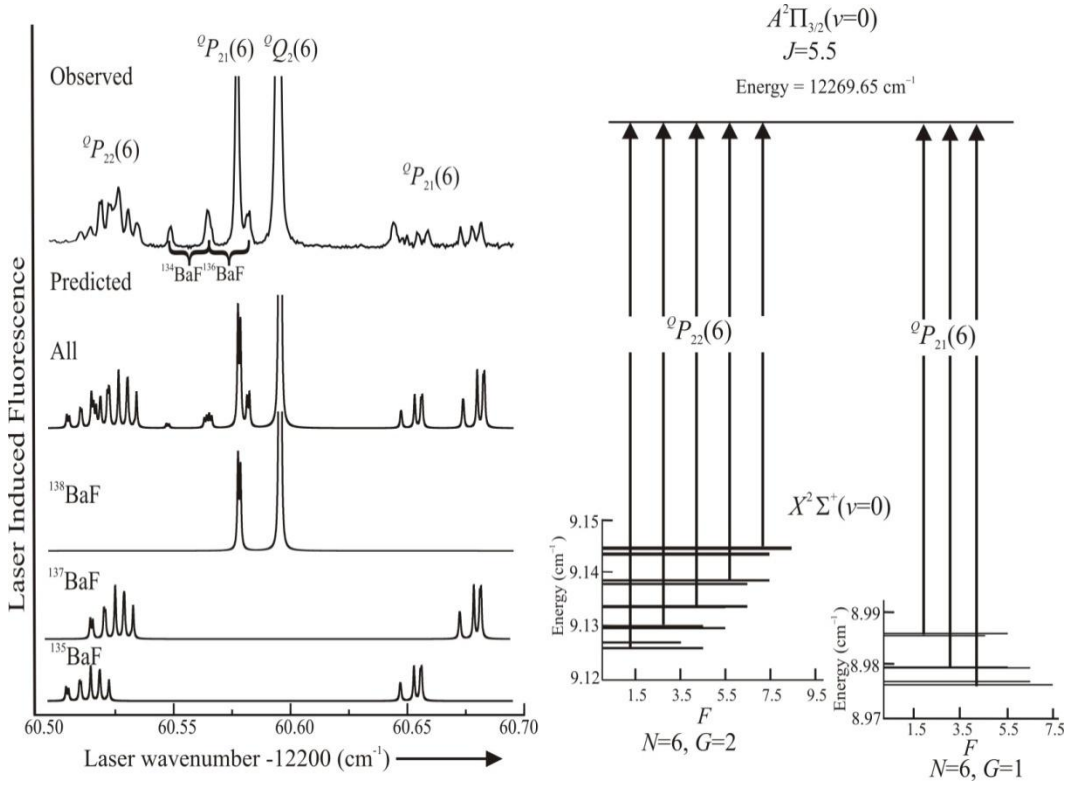

Figure 4.6. The observed and calculated laser induced fluorescence (LIF) spectrum of the $A^2\Pi_{3/2}$–$X^2\Sigma^+$ sub-band in the region of the $Q_2(6)$ line (ν=12260.60 cm^{-1}) and $^{Q}P_{21}(6)$ line (ν=12260.58 cm^{-1}) of the ^{138}BaF isotope. Predicted energy pattern on the right side is associated $^{Q}P_{22}$ (6) line (ν=12260.52 cm^{-1}) and the $^{Q}P_{21}(6)$ line (ν=12260.68 cm^{-1}) line of the ^{137}BaF. The predicted spectra of ^{135}BaF, ^{137}BaF and predicted energy patterns associated with ^{137}BaF transitions were calculated using the optimized parameters taken from Table 4.5.

4.2.2. Analysis

Figure 4.7 shows the calculated energy pattern for the $X^2\Sigma^+$(ν=0) state of the ^{137}BaF, using the previously determined parameters from Ref. 20. Figure 4.7 emphasizes

the contributions of the spin-rotation and hyperfine terms to the energy level by subtracting the rotational energy [$\approx B \times N(N+1)$]. Similar to ^{87}SrF, the high rotational levels of the $X^2\Sigma^+$ state of ^{137}BaF, exhibit an energy pattern of a molecule near sequentially coupled Hund's case ($b_{\beta J}$) limit(i.e. the nuclear spin decouples from rotation). At very low rotational excitation, the large ^{137}BaF magnetic hyperfine interaction in the $X^2\Sigma^+$ causes the energy levels to be at energy near the Hund's case ($b_{\beta S}$). In the Hund's case ($b_{\beta S}$) limit, the good intermediate quantum number is **G**(=1 and 2)(**S**+**I**). The energy patterns of ^{135}BaF and ^{137}BaF have similar effects since ^{135}Ba and ^{137}Ba have the same nuclear spin, I=3/2, and similar nuclear *g*-factors(^{135}BaF)=+0.5586 and *g*-factors(^{137}BaF)=+0.6249.

Similar to ^{87}SrF, the effective Hamiltonian for the $X^2\Sigma^+$ and $A^2\Pi$ of ^{135}BaF and ^{137}BaF are given in Eqs 2 and 3. The eigenvalues and eigenvectors for the $X^2\Sigma^+$ states of ^{135}BaF and ^{137}BaF were obtained by constructing and numerically diagonalizing a matrix representation using the sequentially coupled Hund's case ($a_{\beta J}$) basis set. The representation for the $X^2\Sigma^+$ states of ^{135}BaF and ^{137}BaF have dimension of 16(=(2*S*+1)×[2I_1($^{135\&137}$Ba)+1]×[2I_2(^{19}F)+1]). The eigenvalues and eigenvectors for the $A^2\Pi$ state of ^{135}BaF and ^{137}BaF were obtained by constructing and numerically diagonalizing a matrix representation using the sequentially coupled Hund's case ($a_{\beta J}$) basis set. The representation for ^{135}BaF and ^{137}BaF have dimension of 32(=2×(2*S*+1)×[2I_1($^{135\&137}$Ba ^{87}Sr)+1]×[2I_2(^{19}F)+1]). The expressions for the matrix elements were taken out from Ref. 17. These expressions are described in detail in Chapter 3.

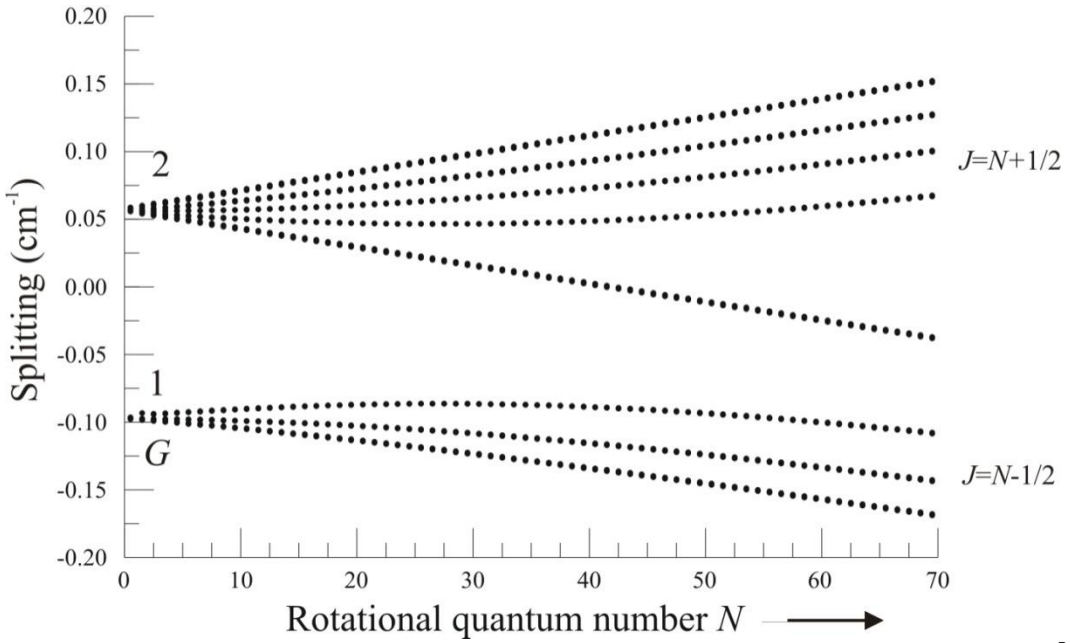

Figure 4.7. The predicted spin-rotation and hyperfine energy pattern for the $X^2\Sigma^+$ of ^{137}BaF as the function of rotational quantum number, *N*. The set of parameters came from Ref. 20 and the rotational energy has been subtracted.

The 73 and 99 precisely measured transitions for ^{135}BaF and ^{137}BaF, respectively, were designated using the new labeling scheme and are described in detail in Chapter 3 (Hund's case ($a_{\beta j}$)→ Hund's case ($b_{\beta S}$)) . The new labeling scheme uses the intermediate approximately good quantum number, *G"*(=1 and 2), associated with a Hund's case ($b_{\beta S}$) scheme, as shown in Figure 4.7.

First, various fits were performed using the 99 measured transitions of ^{137}BaF first. The $X^2\Sigma^+(v=0)$ state parameters were constrained to the determined values from Ref. 20, with the exception of the centrifugal distortion correction, *D* was constrained to the determined value of ^{138}BaF [26] and isotopic scaled using the relationship [$\mu(^{138}BaF)^2/\ \mu(^{137}BaF)^2$]. The best fit was obtained by optimizing $T_{0,0}$, *A, B, p+2q*, and $d(^{137}BaF)$ for the $A^2\Pi$ state. The A_D parameter was constrained to the previous

determined value [20] and D parameter in the $A^2\Pi$ was isotopic scaled from ^{138}BaF. The fluorine magnetic hyperfine parameters for ^{137}BaF, b_F (^{19}F), and c (^{19}F) were constrained to the previously determined value for ^{138}BaF [19]. The observed transition wavenumber, the difference between observed and calculated values, and the associated assignments are present in Table 4.3. The optimized parameters and the associated errors are given in Table 4.5. The standard deviation of the fit is 0.0014 cm^{-1}, which is consistent with the measured uncertainty.

There are no previously determined parameters for ^{135}BaF. Both sets of parameters for the $X^2\Sigma^+(v=0)$ and $A^2\Pi(v=0)$ states were needed to be varied to fit the observed 73 transitions. In the end, only B, and b_F (^{135}Ba) for the $X^2\Sigma^+(v=0)$ state and the origin $T_{0,0}$, rotation, B, spin-orbit parameter, A of the $A^2\Pi(v=0)$ state were varied. The D-values ($X^2\Sigma^+$ and $A^2\Pi$) were constrained to the mass scaled ^{138}BaF values. The dipolar parameter, c (^{135}Ba) of the $X^2\Sigma^+$ state and the magnetic hyperfine parameter, d(^{135}Ba) of the $A^2\Pi$ state were scaled to the ^{137}Ba values by nuclear g-factors. The quadrupole parameter, eq_0Q (^{135}Ba), was scaled to the ^{137}Ba value by quadrupole moment, Q. The fluorine magnetic hyperfine parameter for ^{135}BaF, b_F(^{19}F), and c(^{19}F) in the $X^2\Sigma^+$ state were constrained to the previously determined values [19]. The observed transition wavenumbers, the difference between observed and calculated values, and the associated assignments are present in Table 4.4. The optimized parameters and the associated errors are given in Table 4.5. The standard deviation of the fit is 0.0015 cm^{-1} which is consistent with the measured uncertainty.

4.2.2. Discussion

Spectroscopic parameters for the $A^2\Pi$ (υ=0) and $X\,^2\Sigma^+$(υ=0) for ^{137}BaF and ^{135}BaF were precisely determined. The spectroscopic parameters from Table 4.5 accurately predicted the energy levels and the observed spectra in Figure 4.5 and Figure 4.6, which is a prerequisite for PNC studies. It is interesting to compare the *d*-hyperfine parameter of ^{87}SrF(=-0.00187 cm^{-1}) and that for ^{137}BaF(=+0.0076cm^{-1}). The ratio of *g*-factor (^{87}Sr)/*g*-factor(^{137}Ba)=-0.5829 is not in a good agreement with *d*(^{87}Sr)/*d*(^{137}Ba)=0.246.

Similar to ^{87}SrF, the Zeeman shift the sublevels of the *N*=0 (+ parity) and *N*=1(- parity) of the $X^2\Sigma^+$ of ^{137}BaF were predicted using equation 4 and shown in Figure 4.8. If parity is conserved, then there is no interaction between the opposite parities of the *N*=0 (+ parity) and *N*=1(- parity) in the $X^2\Sigma^+$ state. However, when PNC terms are considered, these pairs of the nearly-degenerate levels can mix by the anapole term in the effective Hamiltonian in Equation 1. Figure 4.8 shows the prediction of the magnetic tuning between the *N*=0 (+ parity) and *N*=1 (- parity) in $X^2\Sigma^+$ state. The pattern was calculated using the field-free hyperfine and spin-rotation parameters from Table 4.5. Figure 4.8 was predicted by using g_S=2.002 and g_l=-0.005, where g_e was calculated using the Curl relationship [17]. The eigenvalues and eigenvectors were obtained by constructing and numerically diagonalizing a 64×64 matrix representation $\mathbf{H}^{Zee}(\text{eff}) + \mathbf{H}^{field-free}(\text{eff})$ using a sequentially coupling Hund's case ($a_{\beta J}$) basis sets for *F*=1.5-4.5. The $\mathbf{H}^{Zee}(eff)$ matrix elements come from Ref. 17. Figure 4.8 shows that at high magnetic field, *Ms*= ± ½ becomes an approximately good quantum number. Figure 4.8 provides the range of magnetic field from 3000G to 6200G that the NSD-PV is needed to tune the rotation

level of N=0 (+ parity) to near degeneracy with rotational level of N=1(- parity) in the $X^2\Sigma^+$ of the interest molecules ($^{135\&137}$BaF)[6].

A comparison of Figure 4.4 and Figure 4.8 reveals that the tuning of the levels of opposite parity into near degeneracy occurs at much lower field for ^{87}SrF than it does for ^{137}BaF. This has implementations for PNC experiment.

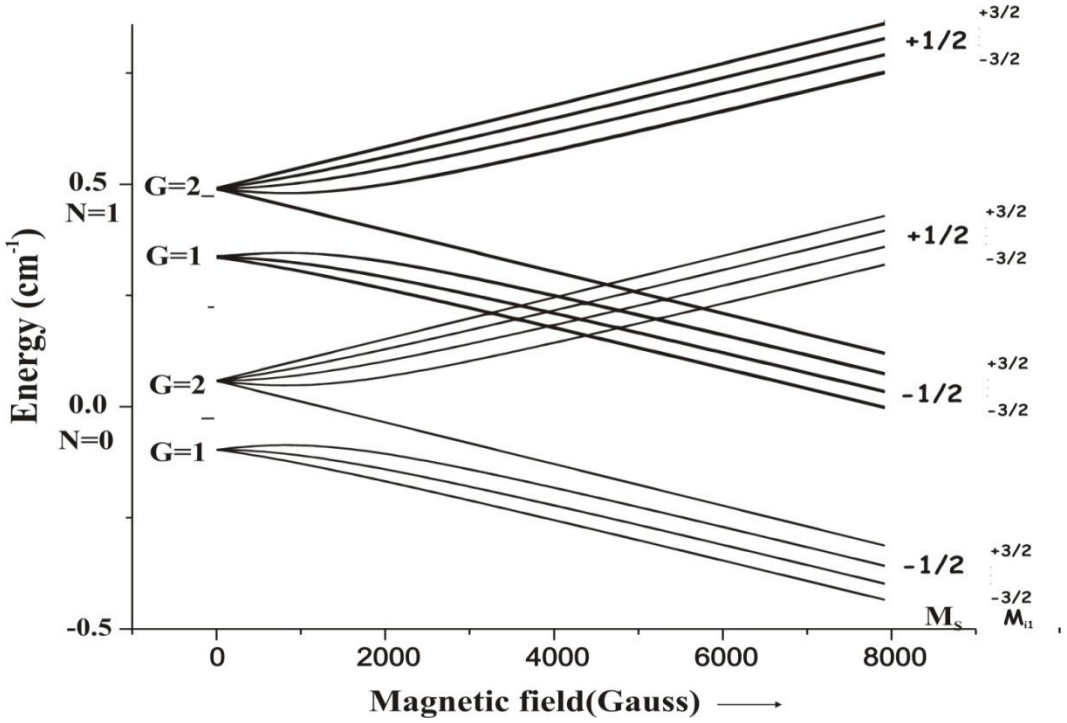

Figure 4.8. The predicted of ^{137}BaF splitting of the magnetic tuning N=0 (+ parity) and N=1(- parity) in $X^2\Sigma^+$ state. The pattern was calculated using the field-free hyperfine and spin-rotation parameters from Table 4.5, g_S=2.002 and $g_{l=}$-0.005.

Table 4.3. Observed and calculated line positions in wavenumber (cm^{-1}) of $A^2\Pi$-$X^2\Sigma^+$(0,0) band system of ^{137}BaF.

Branch	F''_1,F''-F'_1,F'	Observed - 10000	Obs-cal
$^RR_{12}(4)$	7.0, 6.5-8.0, 7.5	1634.1865	0.0030
	6.0, 5.5-7.0, 6.5	1634.1931	0.0004
	5.0, 4.5-6.0, 5.5	1634.2012	0.0012

	4.0, 3.5-5.0, 4.5	1634.2078	0.0019
$^{R}R_{11}(4)$	4.0, 3.5-5.0, 4.5	1634.3518	-0.0005
	5.0, 4.5-6.0, 5.5	1634.3525	-0.0015
$^{O}P_{12}(7)$	6.0, 5.5-5.0, 4.5	1624.8673	-0.0015
	6.0, 5.5-5.0, 4.5	1624.8691	-0.0014
$^{O}P_{11}(7)$	8.0, 7.5-7.0, 6.5	1625.0221	-0.0010
	9.0, 8.5-8.0, 7.5	1625.0286	-0.0027
$^{O}P_{12}(10)$	12.0, 11.5-11.0, 10.5	1622.3420	0.0018
	11.0, 10.5-10.0, 9.5	1622.3430	-0.0002
	10.0, 9.5-9.0, 8.5	1622.3453	-0.0009
	8.0, 7.5-7.0, 6.5	1622.3482	-0.0007
	9.0, 8.5-8.0, 7.5	1622.3496	-0.0004
	10.0, 9.5-9.0, 8.5	1622.4894	0.0029
$^{O}P_{11}(10)$	11.0, 10.5-10.0, 9.5	1622.5008	0.0015
	12.0, 11.5-11.0, 10.5	1622.5089	-0.0001
$^{R}R_{12}(1)$	4.0, 3.5-5.0,4.5	1631.9721	0.0005
	3.0, 2.5-4.0,3.5	1631.9736	0.0008
	3.0, 2.5-4.0, 3.5	1631.9784	-0.0013
	2.0, 1.5-3.0, 2.5	1631.9803	-0.0006
$^{R}R_{11}(1)$	3.0, 2.5-4.0, 3.5	1632.1338	-0.0010
	2.0, 1.5-3.0,2.5	1632.1371	-0.0018
	2.0, 1.5-2.0, 1.5	1632.1400	-0.0016
$^{Q}P_{22}+^{Q}Q_{22}$ (7)	6.0, 5.5-6.0, 5.5	2260.2697	0.0001
	7.0, 6.5-7.0, 6.5	2260.2646	-0.0005
	8.0, 7.5-8.0, 7.5	2260.2600	-0.0003
	9.0, 8.5-9.0, 8.5	2260.2548	-0.0001
	10.0, 9.5-9.0, 8.5	2260.2502	0.0017
$^{Q}P_{21}+^{Q}Q_{21}$ (7)	9.0, 8.5-9.0, 8.5	2260.4196	0.0007
	8.0, 7.5-8.0, 7.5	2260.4149	-0.0003
	7.0, 6.5-6.0, 5.5	2260.4088	0.0006
$^{Q}P_{22}+^{Q}Q_{22}$ (8)	5.0, 4.5-5.0, 4.5	2260.5373	-0.0006
	6.0, 5.5-6.0, 5.5	2260.5333	-0.0008
	7.0, 6.5-7.0, 6.5	2260.5293	-0.0007
	8.0, 7.5-8.0, 7.5	2260.5257	0.0004
	8.0, 7.5-7.0, 6.5	2260.5210	0.0005
$^{Q}P_{21}+^{Q}Q_{21}$ (8)	8.0, 7.5-8.0, 7.5	2260.6888	0.0011
	7.0, 6.5-7.0, 6.5	2260.6848	0.0002
	6.0, 5.5-5.0, 4.5	2260.6783	0.0000
$^{R}Q_{22}+^{R}R_{22}$ (1)	3.0, 2.5-4.0, 3.5	2262.3893	-0.0004
$^{R}Q_{21}+^{R}R_{21}$ (1)	3.0, 2.5-3.0, 2.5	2262.5425	-0.0024
$^{Q}P_{22}+^{Q}Q_{22}$ (3)	6.0, 5.5-5.0, 4.5	2261.2820	-0.0009
	5.0, 4.5-5.0, 4.5	2261.2851	-0.0019

	4.0, 3.5-4.0, 3.5	2261.2882	-0.0016
	3.0, 2.5-3.0, 2.5	2261.2906	-0.0011
$^{Q}P_{22}+{}^{Q}Q_{22}$ (4)	7.0, 6.5-6.0, 5.5	2261.0375	0.0009
	6.0, 5.5-6.0, 5.5	2261.0422	0.0009
	5.0, 4.5-5.0, 4.5	2261.0443	-0.0005
	4.0, 3.5-4.0, 3.5	2261.0455	-0.0020
	3.0, 2.5-3.0, 2.5	2261.0467	-0.0029
$^{O}P_{12}(4)$	2.0, 1.5-1.0, 0.5	1627.3119	-0.0008
	4.0, 3.5-3.0, 2.5	1627.3143	0.0000
	5.0, 4.5-4.0, 3.5	1627.3162	0.0007
	6.0, 5.5-5.0, 4.5	1627.3191	0.0018
$^{R}R_{12}(7)$	10.0- 9.5-11.0, 10.5	1636.3194	0.0013
	9.0, 8.5-10.0, 9.5	1636.3281	-0.0007
	8.0, 7.5-9.0, 8.5	1636.3372	-0.0009
	7.0, 6.5-8.0, 7.5	1636.3463	0.0000
$^{R}R_{11}(7)$	7.0, 6.5-8.0, 7.5	1636.4902	0.0008
	8.0, 7.5-9.0, 8.5	1636.4921	-0.0008
$^{S}R_{22}(4)$	7.0, 6.5-8.0, 7.5	2265.2782	0.0013
	6.0, 5.5-7.0, 6.5	2265.2815	-0.0001
	5.0, 4.5-6.0, 5.5	2265.2865	0.0014
	4.0, 3.5-5.0, 4.5	2265.2910	0.0032
$^{S}R_{21}(4)$	4.0, 3.5-5.0, 4.5	2265.4368	0.0027
	5.0, 4.5-6.0, 5.5	2265.4404	0.0013
	6.0, 5.5-7.0, 6.5	2265.4428	0.0018
$^{S}R_{22}(7)$	10.0, 9.5-11.0, 10.5	2267.0346	0.0022
	9.0, 8.5-10.0, 9.5	2267.0396	0.0007
	8.0, 7.5-9.0, 8.5	2267.0446	0.0003
	7.0, 6.5-8.0, 7.5	2267.0493	0.0002
$^{S}R_{21}(7)$	7.0, 6.5-8.0, 7.5	2267.1947	0.0025
	8.0, 7.5-9.0, 8.5	2267.1997	0.0005
	9.0, 8.5-10.0, 9.5	2267.2047	0.0019
$^{S}R_{22}(10)$	13.0, 12.5-14.0, 13.5	2268.7139	0.0006
	12.0, 11.5-13.0, 12.5	2268.7190	-0.0023
	11.0, 10.5-12.0, 11.5	2268.7202	-0.0018
	11.0, 10.5-12.0, 11.5	2268.7265	-0.0020
	10.0, 9.5-11.0, 10.5	2268.7277	-0.0011
	10.0, 9.5-11.0, 10.5	2268.7340	-0.0014
$^{R}R_{12}(0)$	3.0, 2.5-4.0, 3.5	1631.2192	0.0018
	3.0, 2.5-3.0,2.5	1631.2242	0.0006
	3.0, 2.5-2.0,1.5	1631.2272	-0.0005
$^{R}R_{11}(0)$	2.0, 1.5-3.0,2.5	1631.3816	0.0020
	2.0,1.5-2.0,1.5	1631.3863	0.0026

	2.0,1.5-1.0, 0.5	1631.3875	0.0018
$^{R}R_{12}(2)$	5.0, 4.5-6.0, 5.5	1632.7155	-0.0019
	4.0, 3.5-5.0, 4.5	1632.7258	0.0000
	3.0, 2.5-4.0, 3.5	1632.7296	-0.0021
$^{R}R_{11}(2)$	4.0, 3.5-5.0, 4.5	1632.8811	-0.0012
	2.0, 1.5-3.0, 2.5	1632.8851	-0.0002
	3.0, 2.5-3.0, 2.5	1632.8878	-0.0010
$^{R}Q_{22}+{}^{R}R_{22}$ (2)	4.0, 3.5-5.0, 4.5	2262.5856	0.0010
$^{R}Q_{21}+{}^{R}R_{21}$ (2)	2.0, 1.5-2.0, 1.5	2262.7347	-0.0018
	4.0, 3.5-4.0, 3.5	2262.7387	-0.0024
$^{Q}P_{22}+{}^{Q}Q_{22}$ (2)	4.0, 3.5-4.0, 3.5	2261.5249	0.0004
$^{Q}P_{21}+{}^{Q}Q_{21}$ (2)	4.0, 3.5-3.0, 2.5	2261.6815	0.0006
	Std. dev= 0.00144cm^{-1}		

Table 4.4. Observed and calculated line positions in wavenumber (cm^{-1}) of $A^2\Pi$-$X^2\Sigma^+(0,0)$ band system of ^{135}BaF

Branch	$F''_1,F''-F'_1,F'$	Observed - 10000	Obs-cal
$^{R}R_{12}(0)$	3.0, 2.5-4.0, 3.5	1631.2145	0.0011
	3.0, 2.5-3.0, 2.5	1631.2192	0.0005
	3.0, 2.5-2.0, 1.5	1631.2217	-0.0006
$^{R}R_{11}(0)$	2.0, 1.5-3.0, 2.5	1631.3618	0.0020
	2.0, 1.5-2.0, 1.5	1631.3646	0.0013
	2.0, 1.5-1.0, 0.5	1631.3666	0.0015
$^{R}R_{12}(1)$	3.0, 2.5-4.0, 3.5	1632.1150	-0.0015
	2.0, 1.5-3.0, 2.5	1632.1179	-0.0020
	2.0, 1.5-2.0, 1.5	1632.1200	-0.0022
$^{R}R_{11}(1)$	4.0, 3.5-5.0, 4.5	1632.8635	-0.0017
	2.0, 1.5-3.0, 2.5	1632.8660	-0.0016
	3.0, 2.5-3.0, 2.5	1632.8690	-0.0018
$^{R}R_{12}(4)$	7.0, 6.5-8.0, 7.5	1634.1865	0.0022
	6.0, 5.5-7.0, 6.5	1634.1931	0.0003
	5.0, 4.5-6.0, 5.5	1634.2012	0.0016
	4.0, 3.5-5.0, 4.5	1634.2078	0.0027
$^{R}R_{11}(4)$	4.0, 3.5-5.0, 4.5	1634.3368	0.0002
	5.0, 4.5-6.0, 5.5	1634.3375	-0.0010
$^{R}R_{12}(7)$	9.0, 8.5-10.0, 9.5	1636.3244	0.0018
	9.0, 8.5-10.0, 9.5	1636.3306	-0.0009
	8.0, 7.5-9.0, 8.5	1636.3381	-0.0021
	7.0, 6.5-8.0, 7.5	1636.3455	-0.0025
$^{R}R_{11}(7)$	7.0, 6.5-8.0, 7.5	1636.4785	0.0022

	8.0, 7.5-9.0, 8.5	1636.4808	0.0007
$^{O}P_{12}(7)$	9.0, 8.5-8.0, 7.5	1624.8484	-0.0001
	8.0, 7.5-7.0, 6.5	1624.8498	-0.0002
	7.0, 6.5-6.0, 5.5	1624.8516	0.0000
	6.0, 5.5-5.0, 4.5	1624.8535	0.0001
$^{R}Q_{22}(1)$	3.0, 2.5-4.0, 3.5	2262.3838	0.0002
$^{R}Q_{21}(1)$	2.0, 1.5-2.0,1.5	2262.5233	0.0003
	3.0, 2.5-3.0, 2.5	2262.5245	0.0007
$^{R}Q_{21}(2)$	2.0, 1.5-2.0, 1.5	2262.7144	-0.0014
	4.0, 3.5-4.0, 3.5	2262.7184	-0.0020
$^{S}R_{22}(4)$	7.0, 6.5-8.0, 7.5	2265.2782	0.0004
	6.0, 5.5-7.0, 6.5	2265.2815	-0.0009
	5.0, 4.5-6.0, 5.5	2265.2865	0.0007
	4.0, 3.5-5.0, 4.5	2265.2910	0.0024
$^{S}R_{21}(4)$	4.0, 3.5-5.0, 4.5	2265.4193	-0.0007
	5.0, 4.5-6.0, 5.5	2265.4233	-0.0015
	6.0, 5.5-7.0, 6.5	2265.4263	-0.0006
$^{S}R_{22}(7)$	10.0, 9.5-11.0, 10.5	2267.0383	0.0016
	9.0, 8.5-10.0, 9.5	2267.0423	-0.0007
	8.0, 7.5-9.0, 8.5	2267.0469	-0.0015
	7.0, 6.5-8.0, 7.5	2267.0521	-0.0012
$^{S}R_{21}(7)$	7.0, 6.5-8.0, 7.5	2267.1840	0.0024
	8.0, 7.5-9.0, 8.5	2267.1880	-0.0004
	9.0, 8.5-10.0, 9.5	2267.1920	-0.0002
$^{Q}P_{22}+^{Q}Q_{22}$ (2)	4.0, 3.5-4.0, 3.5	2261.5170	0.0011
$^{Q}P_{21}+^{Q}Q_{21}$ (2)	4.0, 3.5-4.0, 3.5	2261.6578	0.0003
$^{Q}P_{22}+^{Q}Q_{22}$ (3)	3.0, 2.5-2.0, 1.5	2261.4146	-0.0005
	4.0, 3.5-3.0, 2.5	2261.4197	0.0005
	5.0, 4.5-5.0, 4.5	2261.4228	0.0021
$^{Q}P_{22}+^{Q}Q_{22}$ (4)	7.0, 6.5-6.0, 5.5	2261.0280	0.0015
	6.0, 5.5-6.0, 5.5	2261.0292	-0.0019
$^{Q}P_{21}+^{Q}Q_{21}$ (4)	4.0, 3.5-3.0, 2.5	2261.1689	0.0001
	5.0, 4.5-4.0, 3.5	2261.1723	-0.0012
	6.0, 5.5-6.0, 5.5	2261.1763	0.0007
$^{Q}P_{22}+^{Q}Q_{22}$ (7)	10.0, 9.5-9.0, 8.5	2260.2388	0.0037
	9.0, 8.5-9.0, 8.5	2260.2408	-0.0007
	8.0, 7.5-8.0, 7.5	2260.2454	-0.0014
	6.0, 5.5-6.0, 5.5	2260.2491	-0.0022
	7.0, 6.5-7.0, 6.5	2260.2536	0.0019
$^{Q}P_{21}+^{Q}Q_{21}$ (7)	7.0, 6.5-6.0, 5.5	2260.3799	-0.0001
	8.0, 7.5-8.0, 7.5	2260.3861	-0.0007
	9.0, 8.5-9.0, 8.5	2260.3911	0.0005

${}^{Q}P_{22}+{}^{Q}Q_{22}$ (6)	8.0, 7.5-7.0, 6.5	2260.5060	-0.0023
	8.0, 7.5-8.0, 7.5	2260.5110	-0.0020
	7.0, 6.5-7.0, 6.5	2260.5160	-0.0017
	6.0, 5.5-6.0, 5.5	2260.5210	-0.0009
	5.0, 4.5-5.0, 4.5	2260.5257	0.0000
${}^{Q}P_{21}+{}^{Q}Q_{21}$ (6)	6.0, 5.5-5.0, 4.5	2260.6525	0.0013
	7.0, 6.5-7.0, 6.5	2260.6590	0.0017
	8.0, 7.5-8.0, 7.5	2260.6630	0.0024
	Sdt. Dev.= 0.00153 cm^{-1}		

Table 4.5. The spectroscopic parameters in wavenumbers (cm^{-1}) for the $A^2\Pi$-$X^2\Sigma^+$ (0,0) band system of ^{135}BaF and ^{137}BaF

Parameter	^{137}BaF	^{135}BaF
$X^2\Sigma^+(\upsilon=0)$		
B	0.21613878[a]	0.21675(5)
$10^7\times D$	1.85[b]	1.85[c]
γ	0.002702703[a]	0.00270270[c]
b_F(Ba)	0.077587[a]	0.0702(5)
c(Ba)	0.0250173[a]	0.002237381[d]
eq_0Q(Ba)	-.00390270[a]	-0.003490348[d]
b_F(F)	0.002209873[a]	0.002209873[a]
c(F)	0.000274323[a]	0.000274323[a]
$A^2\Pi$ (υ=0)		
A	632.2802(8)	632.2803(10)
$10^5\times A_D$	3.1[c]	3.1[c]
B	2.11937(12)	0.2125(4)
$10^7\times D$	2.00[b]	2.00[b]
$(p+2q)$	-0.2581(2)	-0.25755[c]
d(Ba)	0.0076(10)	0.00685[d]
T_{00}	11945.3152(6)	11946.3034(10)
Std. Dev.	0.0014	0.0015

[a] Ref. 20.

[b] Ref. 19.

[c] Constrained to value scaled from the fit of the ^{138}BaF transitions.

[d] Constrained to value obtained from scaling the value for ^{137}BaF.

4.3. Franck Condon-factors of ytterbium monofluoride, YbF. The goal is to precisely determine the FCF for the $A^2\Pi$, $X^2\Sigma^+$ band systems

A low-resolution study on ytterbium monofluoride, YbF, [27] shows that there are two band systems in the 500–620 nm region and one in the 450 nm region. The first two systems were assigned as $A^2\Pi$– $X^2\Sigma^+$ and $B^2\Sigma^+$– $X^2\Sigma^+$, respectively. High resolution spectroscopy of these bands of the even isotopologues of YbF, ^{172}YbF, ^{174}YbF, and ^{176}YbF were studied by Dunfield et. al [28]. For that study, vibrational, rotational, and spin–rotation constants have been determined for the $X^2\Sigma^+$ state of the three even isotopologues. The $A^2\Pi$ state is heavily perturbed. The Fourier transform microwave studies of the $X^2\Sigma^+$ state precisely determined the optimized set of field free spectroscopic parameter of ^{174}YbF [29]. The electric dipole moment of $X^2\Sigma^+$ (v = 0) and $A^2\Pi_{1/2}$(v = 0) were determined to be μ_e= 3.91(4)D [30] and μ_e=2.48(3)D [31], respectively. The fine and hyperfine interaction parameters in the $A^2\Pi_{1/2}$(v = 0) and $X^2\Sigma^+$ (v = 0) states of the odd metal nuclear spin isotopologues, ^{171}YbF and ^{173}YbF, have been determined by Steimle et. al. [32]. The Zeeman spectra of $^{O}P_{12}$ branch of the $A^2\Pi_{1/2}$–$X^2\Sigma^+$ (0,0) transition of the ^{171}YbF, ^{172}YbF, and ^{174}YbF isotopologues have been recorded and analyzed by Ma et. al [33]. My work on the dispersed fluorescence resulting from $A^2\Pi_{1/2}$–$X^2\Sigma^+$ (0,0) to ν"=0,1 and 2 excitation puts together a complete picture of YbF to help with the current eEDM measurements [6].

4.3.1. Observation

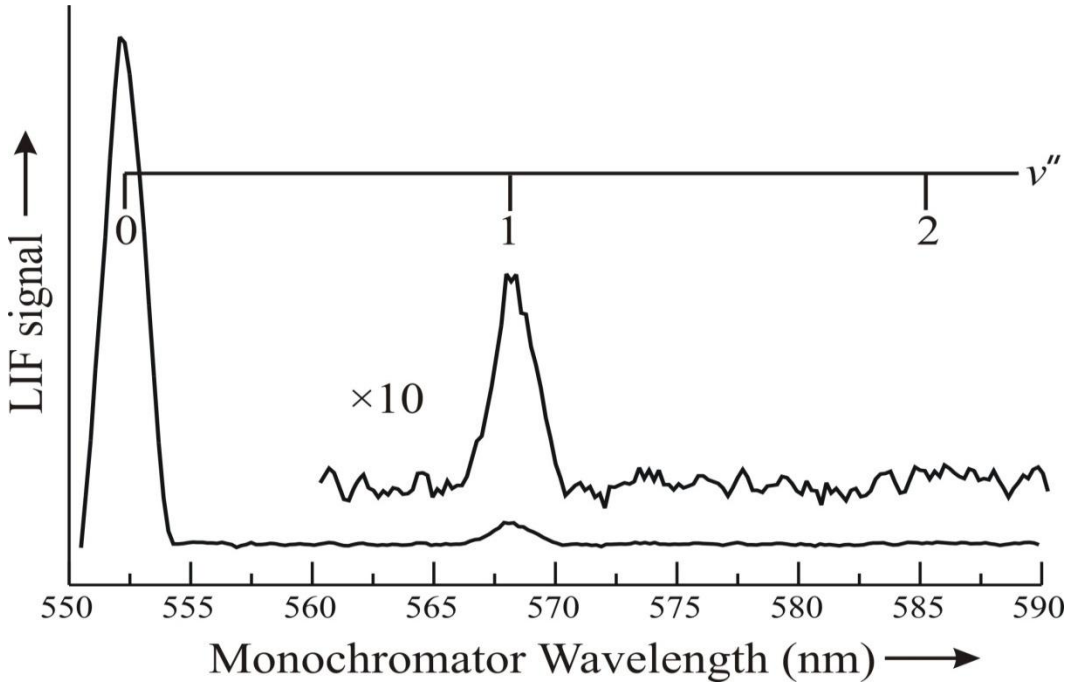

Figure 4.9. The DLIF spectrum resulting from excitation of the $R_1(2)$(ν=18109.454 cm^{-1}) branch feature of the $A^2\Pi_{1/2} \leftarrow X^2\Sigma^+$ (0,0) transition of ^{174}YbF and viewed through a 2/3 m scanning monochromator.

The dispersed laser induced fluorescence (DLIF) of the ^{174}YbF resulting from exciting the $R_1(2)$ branch feature is shown in Figure 4.9. The spectrum was recorded through the 2/3 m scanning monochromator with the step size of 0.1 nm (1Å). The background spectrum was taken separately under the same condition however the ablation laser was blocked to eliminate the chemiluminescence and scatter light. The spectrum shown in Figure 4.9 resulted from subtracting the background spectrum. The intense feature near 552.5nm is the DLIF resulting from excitation of the $R_1(2)$(ν=18109.454 cm^{-1}) is $A^2\Pi_{1/2}(v=0) \rightarrow X^2\Sigma^+(v=0)$. The second feature at 567.8nm is the $A^2\Pi_{1/2}(v=0) \rightarrow X^2\Sigma^+(v=1)$. The spacing due to the vibrational in the $X^2\Sigma^+$ state is

~506.67cm^{-1}. The DLIF spectra of the $R_1(2)$(ν=18109.454 cm^{-1}) line was recorded several times. The integrated areas of the two DLIF features were measured to determine the relative intensity ratio. This ratio was taken as the ratio of the Franck-Condon factors. The measured and predicted Franck-Concon factors (FCF) are also given in Table 4.6.

Table 4.6. Measured and predicted Franck-Condon factors, $f_{v'\text{-}v''}$, from the $R_1(2)$(ν=18109.454 cm^{-1}), $A^2\Pi_{1/2} \leftarrow X\,^2\Sigma^+$ (0,0), transition of YbF

$f_{v'\text{-}v''}$	Measured	Predicted [a]
$f_{0\text{-}0}$	0.927±0.010	0.915
$f_{0\text{-}1}$	0.073±0.010	0.083
$f_{0\text{-}2}$	<0.005	2.7×10^{-3}

[a] $R(2)$ transition predicted using an RKR1 potential with the parameters (cm^{-1}): B_e'' = 0.241294, B_e' =0.247629, D_e'' = 2.388×10^{-7}, D_e' =1.999×10^{-7}, ω_e''= 506.674 ,$\omega_e x_e''$= 2.245,ω_e' =537.0, $\omega_e x_e'$ =3.0.

4.3.2. Discussion

The calculated FCFs were calculated using the program by Prof. LeRoy at Waterloo University [34]. The FCF calculation used the calculated potential energy curve obtained via the first-order Rydberg-Klein-Rees (RKR) method [35]. The RKR1 potential was calculated with the parameters (cm^{-1}): B_e'' = 0.241294, B_e' =0.247629, D_e'' = 2.388×10^{-7}, *De*'=1.999×10^{-7}, ω_e''= 506.674, $\omega_e x_e''$= 2.245, ω_e' =537.0, $\omega_e x_e'$ =3.0. These parameters were taken from Ref. [28, 32]. The calculated for $f_{0\text{-}0}$=0.915 was slightly smaller than the measured values of $f_{0\text{-}0}$ =0.927(10). The calculated FCF factor for $f_{0\text{-}1}$=0.083 was slightly larger than measured values $f_{0\text{-}1}$ =0.073(10). Note that, the measured value for $f_{0\text{-}2}$ is slightly above the noise level. This result shows that it's

possible to quantitatively predict the FCF using existing spectroscopic parameter for the $A^2\Pi_{1/2} \leftarrow X^2\Sigma^+$ (0,0).

4.4. Hafnium monofluoride, HfF

Hafnium monofluoride cation (HfF^+) is one of the candidate species for experiments to measure the electron electric dipole moment (eEDM) [5]. Studies of the neutral are relevant because photoionization schemes can be used to produce the cations. More importantly, computational methodologies used to predict the electronic wavefunction of HfF^+ can be effectively assessed by making a comparison of predicted and experimental properties of the neutral, which are more readily determinable.

Hafnium has six naturally occurring isotopes at relatively high natural abundance: ^{174}Hf (0.16%), ^{176}Hf (5.26%), ^{177}Hf (18.60%), ^{178}Hf (27.28%), ^{179}Hf (13.62%), and ^{180}Hf (35.08%). The odd isotope ^{177}Hf (I=7/2) and ^{179}Hf (I=9/2) have extremely large nuclear quadrupole coupling constant, Q, of 336.5 fm^2 and 379.3 fm^2, respectively. Spectrum of hafnium monohalides was first observed by Moskvitina et al. [36]. Three molecular bands of HfF at 589.3 nm, 590.6 nm, and 593.1 nm were recorded. Unfortunately, the recorded spectra showed extremely complicated structure and were not analyzable. The first high-resolution study was performed by Adam et al. [37]. Nine bands in the range 17000 cm^{-1}-24000cm^{-1} of HfF were rotationally analyzed for both ^{178}HfF and ^{180}HfF. The band at 18489 cm^{-1}, which is the focus of the current study, was assigned as the (1,0)[17.9]2.5-$X^2\Delta_{3/2}$ transition based upon the rotational analysis. The ground state of HfF were assigned as a $^2\Delta$ by analogy with the predicted energy level of HfCl [38]. Recently, motivated by eEDM experiments, eight bands were recorded, rotationally assigned and analyzed in the range from 13400cm^{-1}-14500cm^{-1} by Grau et al. [39]. There

are two resonance-enhanced multi-photon ionization (REMPI) studies [40, 41] that include the transition in the excited states as high as 33000 cm^{-1}. The molecular constant for the $X^1\Sigma^+$, $^3\Delta_1$, $^3\Delta_2$, $^3\Delta_3$ states of HfF^+ have recently been determined using PFI-ZEKE [40]. The focus of my project is the experimental determination of the $\vec{\mu}_{el}$, and hyperfine parameters for the $X\,^2\Delta_{3/2}$(v=0) and [17.9]2.5(v=1) states.

4.4.1. Observation

4.4.1.1. Field free spectra

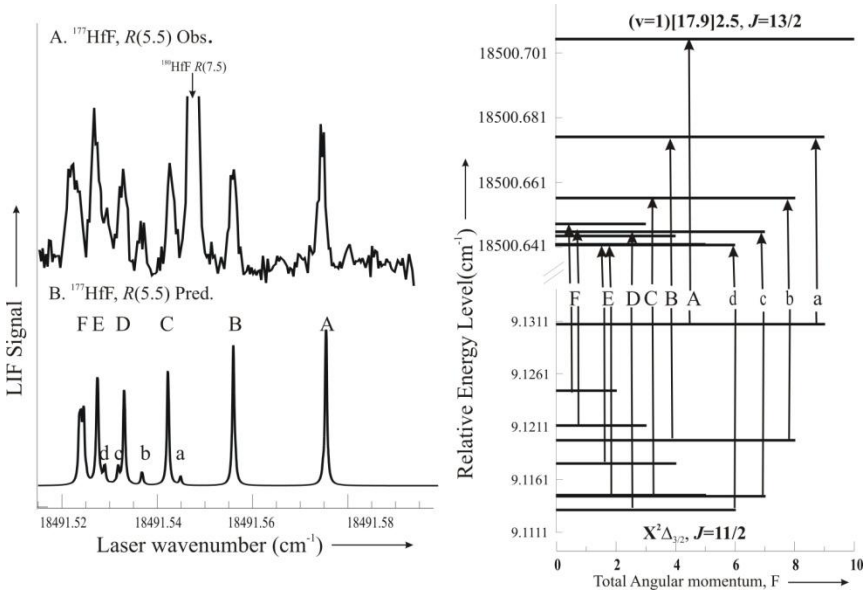

Figure 4.10. The observed and calculated R(11/2) branch feature of ^{177}HfF along with the associated energy levels and assigned transitions. The intense feature is the R(15/2) transition of the ^{180}HfF isotopologue.

The accuracy of the current measurements for the ^{180}HfF isotopologue is approximately 20 times greater than that previously obtained [37]. Furthermore, the ^{19}F hyperfine was not previously resolved but is observed here. Accordingly, the twenty two branch features of the major isotopologue, ^{180}HfF , were precisely measured and are

presented in Table 4.7 along with the assignment and the difference between the predicted (*vide infra*) and observed transition wavenumbers. The ^{19}F hyperfine splitting was observed for the *P*(7/2), *R*(3/2), *R*(5/2), *Q*(5/2) and *Q*(7/2) branch features. A comparison of the various branches revealed that the small ^{19}F hyperfine structure is primarily due to splitting in the [17.9]2.5(v=1) state. The splitting in the J =5/2 and 7/2 levels of the [17.9]2.5(v=1) state were determined to be 55 MHz and 24 MHz, respectively.

The spectral features due to the ^{177}HfF and ^{179}HfF isotopologue are markedly more complex than those of ^{180}HfF because of the large hyperfine interaction in both the $X\,^2\Delta_{3/2}$(v=0) and $[17.9]_{5/2}$ (v=1) states. The observed and calculated *R*(11/2) branch feature of ^{177}HfF are given in Figure 4.10 along with the associated energy levels and assigned transitions, as predicted from the final analysis (*vide infra*). The intense feature in Figure 4.10 is the *R*(15/2) transition of the ^{180}HfF isotopologue. The observed and calculated *R*(15/2) branch feature of ^{179}HfF, along with the associated energy level diagram are given in Figure 4.11. This feature is overlapped with the much more intense *R*(19/2) transition of ^{180}HfF. The most intense line of the *R*(11/2) branch features of ^{177}HfF appears at highest wavenumber (Figure 4.10) whereas the most intense line of the *R*(19/2) branch features of ^{179}HfF appears at lowest wavenumber (Figure 4.11). Thus, the hyperfine structure for these relatively low-J branch features are dominated from the magnetic hyperfine interactions because the nuclear magnetic moment for ^{177}Hf and ^{179}Hf have opposite sign. A total of 172 and 179 features for the ^{177}HfF and ^{179}HfF isotopologues, respectively, were precisely measured. The measured wavenumbers,

assignment and the difference between the observed and calculated values can be found in the Table 4.8 and Table 4.9.

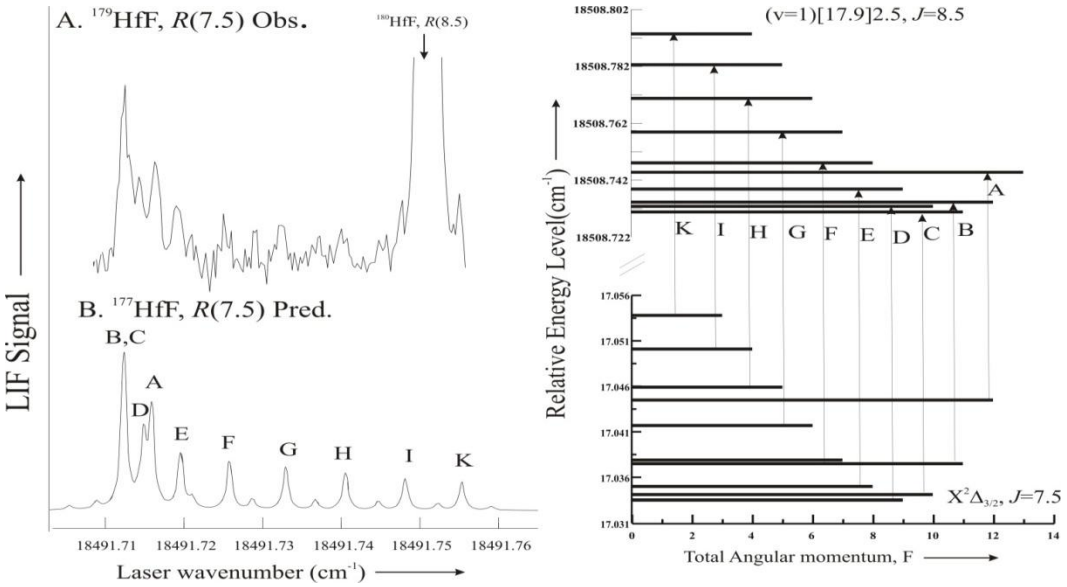

Figure 4.11. The observed and calculated R(15/2) branch feature of ^{179}HfF, along with the associated energy level diagram and assignment. The intense feature is the R(19/2) transition of ^{180}HfF.

4.4.1.2. Stark spectra

The R(3/2), Q(5/2) and P(7/2) lines of the ^{180}HfF isotopologues were selected for optical Stark studies because they are intense, unblended and exhibit large Stark tuning. The R (1.5) line was recorded under field-free and in the presence of a 1732 V/cm static field with parallel ($\Delta M_J = 0$) and perpendicular ($\Delta M_J = \pm 1$) orientations that are presented in Figure 4.13. The spectral features marked with "*" are features of the opposite orientation due to unclean polarization. The R(1.5) line symmetrically splits around the field-free spectral feature due to the degeneracy of the *e*- and *f*-parity components in both the [17.9]2.5(v=1) and $X^2\Delta_{3/2}$ states. The associated energy splitting patterns as a function

of applied electric fields are also presented in Figure 4.13. The *J'*=3/2 rotational level in the $X^2\Delta_{3/2}$ splits to 4(=2×J+1) components. Similarity, The *J'*=5/2 rotational level in the [17.9] 2.5(*v*=1) splits to 6(=2×J+1) components. Four parallel transitions associated with $\Delta M_J = 0$ are labeled as "A-D", eight perpendicular transitions associated with $\Delta M_J = \pm 1$ are labeled as "a-h". The energy splitting was calculated using the optimized μ_e values of 1.66 D and 0.419 D for $X^2\Delta_{3/2}$ and [17.9] 2.5(*v*=1) state, respectively. The assignments, observed Stark shifts, and the differences from the calculated Stark shifts are presented in Table 4.10.

4.4.2. Analysis

4.4.2.1. Analysis field free spectra

The fitting of the ^{180}HfF isotopologue field-free spectrum proceed in a two-step process. In the first step, the small [17.9] 2.5(*v*=1) state ^{19}F hyperfine splitting was fit and in the second step the transition wavenumbers were directly fit with the ^{19}F hyperfine parameters constrained. The [17.9] 2.5(*v*=1) state, *J*=5/2 and *J*=7/2 level splittings of 56 MHz and 22 were fit to the Hund's case ($a_{\beta J}$) limit expectation value expression:

$$\left\langle \mathrm{Case(a}_{\beta J}) \left| \hat{\mathrm{H}}^{\mathrm{mhf}} \right| \mathrm{Case(a}_{\beta J}) \right\rangle = h_{5/2}\Omega \left(\frac{[F(F+1) - J(J+1) - I(I+1)]}{2J(J+1)} \right). \qquad (5)$$

The effective magnetic hyperfine fitting parameter, h_Ω, can be expressed in terms of the Frosch and Froley parameters as [17] $h_\Omega = \{a\Lambda + (b_F + \frac{2}{3}c)\sum\}$. The optimized $h_{5/2}(^{19}\mathrm{F})$ value for the [17.9] 2.5(*v*=1) state is 55 MHz (=0.0018 cm^{-1}).

In the second step, the energies for the $X^2\Delta_{3/2}$(*v*=0) and [17.9]2.5(*v*=1) states were modeled using the effective Hamiltonian operator:

$$\hat{\mathrm{H}}^{\mathrm{eff}} = A\hat{\mathrm{L}}_z\hat{\mathrm{S}}_z + B\hat{\mathrm{R}}^2 - D\hat{\mathrm{R}}^4 + h_\Omega(^{19}\mathrm{F})\hat{\mathrm{I}}\cdot\hat{\mathrm{F}} \quad , \qquad (6)$$

where $\hat{R}$, $\hat{I}$, and $\hat{F}$ are rotational, nuclear spin and total angular momenta operators, respectively. There was no evidence of Ω-doubling in either the previously recorded spectra by Adam et. al [37], which included very high rotational levels, or the spectra recorded in this study. The field-free eigenvalues and eigenvectors for the $X^2\Delta_{3/2}(v=0)$ and [17.9]2.5(v=1) states of ^{180}HfF were obtained by constructing and numerically diagonalizing a representation using Hund's case $a_{\beta J}$ basis. The spin-orbit parameters, A, for both the $X^2\Delta_{3/2}(v=0)$ and [17.9]2.5(v=1) states were constrained to 2850 cm^{-1}, which is the suggested value for the $X^2\Delta$ state implied from the dispersed LIF spectrum [37]. The analysis is insensitive to any values for A greater than approximately 500 cm^{-1}. The centrifugal distortion correction, D, for the $X^2\Delta_{3/2}(v=0)$ and [17.9]2.5(v=1) states were constrained to the values determined Adam et. al. [37]. The 26 precisely measured field-free transition wavenumbers were least squares fit to produce optimized upper and lower state rotational parameters, B, and the band origin, T_{00}. The resulting parameters and associated errors are presented in Table 4.11. The standard deviation is 0.00094 cm^{-1}, which is in agreement with the measurement uncertainty.

The analyses of the ^{177}HfF and ^{179}HfF spectra are more complicated because the irregular pattern due to a very large electric nuclear quadrupole interaction and a smaller, but significant, magnetic hyperfine interaction. The ^{19}F hyperfine splitting was not resolved in the spectra for the odd isotopologues and these molecules were treated as one nuclear spin systems. The energies for the $X^2\Delta_{3/2}(v=0)$ and [17.9]2.5(v=1) states of the ^{177}HfF and ^{179}HfF isotopologues were modeled by replacing the ^{19}F hyperfine term with the corresponding metal magnetic hyperfine terms,

$$\hat{H}^{mhf} = h_{\Omega}(^{177,179}Hf)\hat{I}\times\hat{F} \quad , \tag{7}$$

and adding electric quadrupole terms,

$$\hat{H}^{quad} = eQq_0(^{177,179}Hf)\frac{3\hat{I}_z^2 - \hat{I}^2}{4I(2I-1)} \quad , \tag{8}$$

to Eq. 5. In the Hund's case ($a_{\beta J}$) limit, which is a good approximation for the low-rotational levels of the $X^2\Delta_{3/2}$(v=0) and [17.9]2.5(v=1) states, the quadrupole hyperfine energy is [42]:

$$\left\langle case(a_{\beta J})\left|\hat{H}^{quad}\right|case(a_{\beta J})\right\rangle = eQq_0 \times \frac{[0.75C(C+1) - I(I+1)J(J+1)]}{2I(2I\text{-}1)(2J\text{-}1)(2J+3)} \times \left\{\frac{3\Omega^2}{J(J+1)} - 1\right\}, \tag{9}$$

where $C = F(F+1) - J(J+1) - I(I+1)$. A plot of $\left\langle case(a_{\beta J})\left|\hat{H}^{quad}\right|case(a_{\beta J})\right\rangle$ as a function of J for the $X^2\Delta_{3/2}$(v=0) state of ^{177}HfF using the optimized eQq_0 (*vide infra*) is presented in Figure 4.12. At high J, the energy pattern evolves into four groups which are characterized by $F=J\pm7/2$, $F=J\pm5/2$, $F=J\pm1/2$ and $F=J\pm3/2$, whereas for the low-J levels the pattern is less obvious. As evident from Eq. 1, the magnetic hyperfine contribution rapidly decreases with increasing J. Therefore, the high-J spectral features were readily assigned and are primarily sensitive to the electric quadrupole parameter, eQq_0 whereas h_{Ω} is determined from low-J values spectral features.

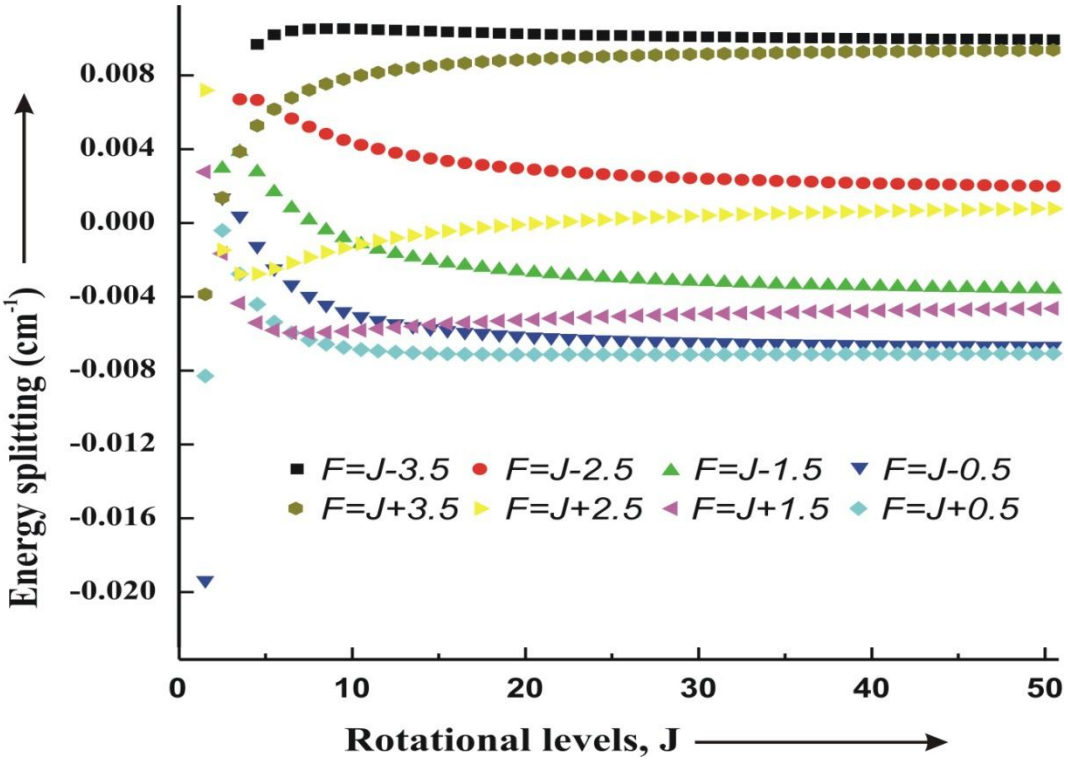

Figure 4.12. A plot of predicted electric quadrupole splitting as a function of J for the $X\,^2\Delta_{3/2}(v=0)$ state of ^{177}HfF using the optimized hyperfine parameters. The prediction was made using the Hund's case ($a_{\beta J}$) limit expression (Eq. 9).

4.4.2.2. Analysis of the Stark spectra

Each rotational level consist of a degenerate pair of levels of opposite parity because there was no evidence of Ω-doubling in either $X\,^2\Delta_{3/2}(v=0)$ or [17.9]2.5(v=1) states. Accordingly, the Stark shifts were modeled using the expression given by degenerate perturbation theory,

$$\Delta E(\mathrm{MHz}) = \frac{\mu(\mathrm{D})\vec{E}(\mathrm{V/cm})M_J\Omega}{J(J+1)}.50348 \qquad (10)$$

The 0.5348 factor is the conversion factor for MHz and V/cm units. The appropriate combinations of ΔE were compared with the observed spectral shifts in a

linear least squares fitting routine to produce $|\vec{\mu}_{el}|$ values of 1.66 ± 0.01 D and 0.4193± 0.0069 D for $X^2\Delta_{3/2}(v=0)$ and [17.9]2.5(v=1) states, respectively. The error limits represent a 90% statistical confidence level, which is slightly smaller than the estimated maximum systematic error of 2%. The correlation coefficient of the fit is 0.78 and the standard deviation was 8 MHz, which is commensurate with the estimated measurement error. The quantum number assignments, observed Stark induced shifts, difference between the observed and calculated shifts, and field strengths are listed in Table 4.10.

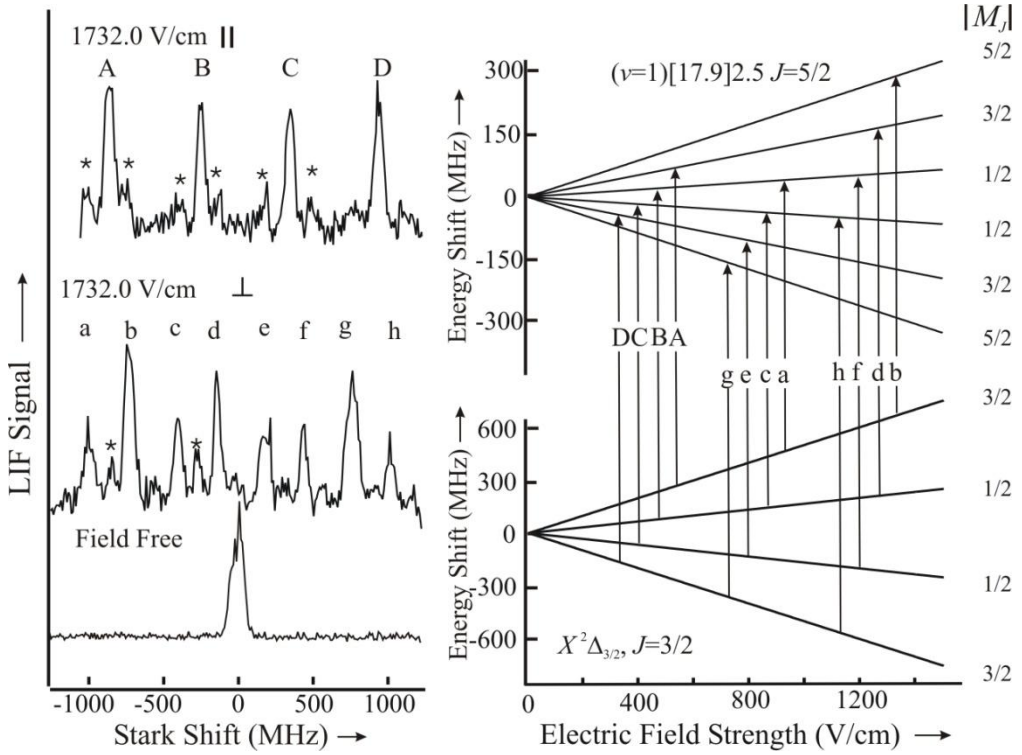

Figure 4.13.The observed $R(3/2)$ line of ^{180}HfF recorded field-free and in the presence of a 1732 V/cm static field with parallel ($\Delta M_J = 0$) and perpendicular ($\Delta M_J = \pm 1$) orientations and associated energy levels. The spectral features marked with "*" are features of the opposite field orientations.

4.4.3. Discussion

4.4.3.1. Field free spectra

The newly determined ^{180}HfF rotational parameters, *B*, for the $X\,^2\Delta_{3/2}(v=0)$ and [17.9]2.5(v=1) states of 0.283714(37) cm^{-1} and 0.264427(35) cm^{-1} differ slightly from the previously determined [37] values of 0.284001(7) cm^{-1} and 0.264401(8) cm^{-1}. This is most likely due to the inclusion of only low-*J* transitions in the present study. The lack of observable ^{19}F hyperfine interaction in the $X\,^2\Delta_{3/2}(v=0)$ state and the very small splitting in the [17.9]2.5(v=1) state ($h_{5/2}(^{19}\mathrm{F})$=0.0018 cm^{-1}) demonstrates that the unpaired electrons are primarily centered on the Hf. The lack of ^{19}F hyperfine interaction in the $X\,^2\Delta_{3/2}(v=0)$ places an upper limit for $h_{3/2}(^{19}\mathrm{F})$ of approximately 50 MHz, which is consistent with the calculated value of 35 MHz.

The ratio of magnetic hyperfine parameter for the $X\,^2\Delta_{3/2}(v=0)$ state, $h_{3/2}(^{177}\mathrm{Hf})/h_{3/2}(^{179}\mathrm{Hf})$, is -1.68 ± 0.16 and for the [17.9]2.5(v=1) state the ratio $h_{5/2}(^{177}\mathrm{HfF})/h_{5/2}(^{179}\mathrm{HfF})$ is -1.55 ± 0.03, which are in agreement with nuclear g_I-factors: $\dfrac{\mu(^{177}\mathrm{Hf})/\mathrm{I}(^{177}\mathrm{Hf})}{\mu(^{179}\mathrm{Hf})/\mathrm{I}(^{179}\mathrm{Hf})} = -1.59$. Similarly, the ratios $eQq_0(^{177}\mathrm{Hf})/eQq_0(^{179}\mathrm{Hf})$ for the $X\,^2\Delta_{3/2}(v=0)$ and [17.9]2.5(v=1) states are 0.96 ± 0.08 and 0.95 ± 0.06, which are in reasonably good agreement with the ratio of the quadrupole moments, $^{177}Q/^{179}Q$ of 0.89. These agreements suggest that the magnetic hyperfine and nuclear electric quadrupole terms in the effective Hamiltonian used to model the spectra are not contaminated too severely by higher order terms.

Insight into the proposed bonding mechanism and nature of the electronic state can be garnered by using the known atomic hyperfine information to predict the $X^2\Delta_{3/2}(v=0)$ hyperfine parameters. The simplest interpretation of $h_{3/2}$(Hf) for the $X^2\Delta_{3/2}(v=0)$ state assumes that the sole unpaired electron occupies the Hf-centered $5d_{\pm 2}$ orbital. Atomic information for Hf^+ is limited, thus estimates for the required expectation values will be derived using neutral Hf data. The $5d^2 6s^2$ configuration of Hf is most relevant to the description of the $X^2\Delta_{3/2}(v=0)$ state of HfF. The effective Hamiltonian that describes atomic magnetic hyperfine interaction within a single $nl^n n's^2$ configuration (e.g. $5d^2 6s^2$) is [43, 44]:

$$\hat{H}^{mhf} = \sum_{i=1}^{N}\left[\hat{l}_i a_{nl}^{01} - (10)^{1/2}(\hat{s},\hat{C}^2)_i^1 a_{nl}^{12} + \hat{s}_i a_{nl}^{10}\right]\bullet\hat{I} \quad , \qquad (11)$$

where $\hat{l}_i$, $(\hat{s},\hat{C}^2)_i^1$, and $\hat{s}_i$ are the orbital, spin dipolar and spin operators for the electrons with the orbital angular momenta. The three effective atomic hyperfine parameters, a_{nl}^{01}, a_{nl}^{12}, and a_{nl}^{10} are defined as [32,33]:

$$a_{nl}^{ij} = 95.4128(\text{MHz}/\text{a.u.}^{-3})g_I\left\langle r^{-3}\right\rangle_{nl}^{ij} \quad , \qquad (12)$$

where the conversion factor assumes that the units of $\left\langle r^{-3}\right\rangle_{nl}^{ij}$ and $\left\langle r^{-3}\right\rangle_{n's}^{10}$ are a_0^{-3}. Büttgenbach et al [45] modeled the atomic hyperfine parameters associated with the $^3F_2$, $^3F_3$ and $^3F_4$ levels arising from the $5d^2 6s^2$ configuration to determine $\left\langle r^{-3}\right\rangle_{5d}^{01}$, $\left\langle r^{-3}\right\rangle_{5d}^{12}$, and $\left\langle r^{-3}\right\rangle_{5d}^{10}$ of $4.021\,a_0^{-3}$, $1.094\,a_0^{-3}$, and $0.738\,a_0^{-3}$, respectively. In the simple model for the nature of the $X^2\Delta_{3/2}(v=0)$ state (i.e. a $\ldots\sigma^2\delta(5d_{\pm 2})^1$configuration), the $h_{3/2}$(Hf)

parameter is given by:

$$h_{3/2}(\mathrm{Hf}) = 95.412(\mathrm{MHz/a.u.}^{-3}) \cdot g_I \cdot \left[2\left\langle r^{-3} \right\rangle_{5d}^{01} - \frac{1}{2}\left(\left\langle r^{-3} \right\rangle_{5d}^{10} + \left(-\frac{4}{7} \right) \left\langle r^{-3} \right\rangle_{5d}^{12} \right) \right]. \qquad (13)$$

The -4/7 factor in Eq. 9 is the expectation value $\left\langle d_{\pm 2} \left| \left(3\cos^2 \chi - 1 \right) \right| d_{\pm 2} \right\rangle$. The effective atomic expectation values of Ref. 34 when substituted into Eq. 13 gives 170 MHz for the ^{177}HfF isotopologue, which compares surprisingly well with the experimentally determined value of 176 ±11 MHz and the *ab initio* value predicted here of 216(27) MHz.

It is interesting to compare the experimentally determined eQq_0 value for the $X^1\Sigma^+$ states of ^{177}HfO (-5952.649 ± 0.035 MHz) [35] with that for the $X\,^2\Delta_{3/2}(v=0)$ state of ^{177}HfF (= -2320± 900 MHz). Although the precision of the ^{177}HfF value extracted from the analysis of electronic spectra performed here is much less than that for HfO, which was obtained from the analysis of pure rotational spectra, it is evident that eQq_0 (HfF) is much smaller than eQq_0 (HfO). The dominant configuration of the of HfO differs from that for HfF by having a vacant $\delta(5d_{\pm 2})$ orbital. The effect on eQq_0 for this difference can be readily estimated. The electric quadrupole coupling parameter, eQq_0, expressed in spherical polar coordinates is:

$$eQq_0(\mathrm{MHz}) = Q\left[\frac{\mathrm{e} \times 10^{-6}}{4\pi\varepsilon_0 h} \right] \left\langle \Lambda \left| \sum_{\mathrm{i}} \frac{\left(3\cos\theta_{\mathrm{i}} - 1 \right)}{\mathrm{r}^{-3}} \right| \Lambda \right\rangle$$

$$= -234.96 \times Q \left\langle \Lambda \left| \sum_{\mathrm{i}} \frac{\left(3\cos\theta_{\mathrm{i}} - 1 \right)}{\mathrm{r}^{-3}} \right| \Lambda \right\rangle, \qquad (14)$$

where the summation runs over all electrons and the conversion factor assumes that Q is in Barnes and $\left\langle \mathrm{r}^{-3} \right\rangle$ is in a_0^{-3}. Using the experimental $\left\langle r^{-3} \right\rangle_{5d}^{01}$ value [45] it is expected

that the $\delta(5d_{\pm 2})$ electron contributes +2429 MHz to eQq_0 for HfF. Thus, making the crude assumption that all orbitals other than the $\delta(5d_{\pm 2})$ orbital remain the same in HfF and HfO, then eQq_0 (Hf) for the $X\,^2\Delta_{3/2}(v=0)$ state of ^{177}HfF is predicted to be -3523 MHz (= -5952 MHz + 2429 MHz). The agreement with the experimentally determined value of -2320± 900 MHz and the *ab initio* value predicted here of -2788 MHz is good. Similarly, the eQq_0 for the $X^1\Sigma^+$ state HfF^+, which has a configuration with an unoccupied $\delta(5d_{\pm 2})$ orbital, is estimated to be approximately that for the $X^1\Sigma^+$ state of HfO (=-5952 MHz), which is consistent with the *ab initio* value predicted here of -4903 MHz, given the assumptions made.

4.4.3.2. Stark spectra

The spectra are only sensitive to the magnitude of $\vec{\mu}_{el}$, but it is reasonable to assume that the charge distribution is $Hf^{+\delta}F^{-\delta}$. The molecular electric dipole moment $|\vec{\mu}_{el}|$ values of 1.66 ± 0.01 D and 0.4193± 0.0069 D for $X\,^2\Delta_{3/2}(v=0)$ and [17.9]2.5(v=1) states, respectively, are unexpectedly small given the high electron affinity of F and the low ionization potential of Hf. Based on the calculations, which predicts a dominant…$\sigma^2\delta(5d_{\pm 2})^1$ configuration, the following qualitative explanation can be given. Free hafnium and fluoride atoms have $6s^25d^2$ and $2s^22p^5$ electron configuration, respectively. As the two atoms approach, the F atom accepts an electron from d_σ-orbital of Hf, resulting in formation of a σ^2-orbital which is mainly consisting of $2p_z$(F) (i.e. ionic Hf^+–F^- bonding). At closer internuclear distances, Coulomb repulsion with F^- fragment induces back-polarization of the 6*s* electrons on hafnium. The resulting 6*s*/6*p*

orbital is doubly occupied. Given the large average radius of the 6*s* and 6*p* orbitals of hafnium, this polarization gives a significant contribution to $|\vec{\mu}_{el}|$.

Table 4.7. Observed and calculated line positions in wavenumber (cm^{-1}) of (1,0)[17.9]2.5-$X^2\Delta_{3/2}$ band of ^{180}HfF

	F'	F''	Observed	Obsed-calced
P (3.5)	2	3	18486.1265	0.0011
	3	4	18486.1285	0.0018
P (4.5)	4	5	18485.4257	0.0013
P (5.5)	5	6	18484.6835	-0.0001
P (6.5)	6	7	18483.9045	0.0003
Q (2.5)	2	2	18488.1120	0.0009
	3	3	18488.1138	0.0014
Q (3.5)	3	3	18487.9762	-0.0002
	4	4	18487.9768	-0.0006
Q (4.5)	5	5	18487.8037	-0.0002
Q (5.5)	6	6	18487.5912	-0.0006
Q (8.5)	9	9	18486.7235	-0.001
Q (9.5)	10	10	18486.3572	-0.0011
Q (10.5)	11	11	18485.9535	-0.0001
Q (11.5)	12	12	18485.5108	0.0006
Q (12.5)	13	13	18485.0276	-0.0007
Q (13.5)	14	14	18484.5060	-0.0018
Q (14.5)	15	15	18483.9481	-0.0005
R (1.5)	2	1	18489.5303	0.0008
	3	2	18489.5315	0.0008
R (2.5)	3	2	18489.9609	-0.0012
	4	3	18489.9621	-0.001
R (3.5)	5	4	18490.3562	-0.0007
R (4.5)	6	5	18490.7121	-0.0001
R(7.5)	9	8	18491.5463	-0.0003
R(24.5)	26	25	18489.7061	0.0011
Rms=0.00094cm^{-1} σ =0.00100 cm^{-1}				

Table 4.8. Observed and calculated line positions in wavenumber (cm^{-1}) of (1,0)[17.9]2.5-$X^2\Delta_{3/2}$ band of ^{177}HfF

Lines	F'	F''	Observed	Observed-calced	Lines	F'	F''	Observed	Observed-calced
P(6.5)	5	6	18484.3886	-0.0006	*Q*(3.5)	3	3	18488.4500	-0.0009
	6	7	18484.3959	-0.0007		3	4	18488.4516	-0.0003
	7	8	18484.4055	-0.0014		4	3	18488.4699	0.0004
	7	7	18484.4073	-0.0010		4	5	18488.4708	0.0015
	8	9	18484.4196	-0.0013		4	4	18488.4723	0.0019
	9	10	18484.4384	-0.0012		5	6	18488.4849	-0.0007
Q(11.5)	11	11	18486.0020	0.0000		5	5	18488.4911	0.0005
	10	10	18486.0028	-0.0002		6	7	18488.4982	-0.0002
	12	12	18486.0038	-0.0005		6	6	18488.5094	0.0005
	9	9	18486.0058	-0.0008		6	5	18488.5147	0.0009
	13	13	18486.0106	-0.0002		7	7	18488.5216	-0.0001
	8	8	18486.0131	0.0012		7	6	18488.5331	0.0009
	14	14	18486.0218	-0.0009	*Q*(2.5)	2	3	18488.5387	-0.0015
	14	13	18486.0282	-0.0001		3	4	18488.5813	-0.0009
	15	15	18486.0386	-0.0022		3	2	18488.5838	-0.0022
Q(10.5)	10	9	18486.4426	-0.0001		4	5	18488.6230	-0.0001
	10	10	18486.4461	0.0003		4	4	18488.6278	-0.0005
	9	9	18486.4471	0.0006		4	3	18488.6303	-0.0006
	11	11	18486.4489	0.0004		5	6	18488.6500	0.0008
	8	8	18486.4502	0.0008		5	5	18488.6577	-0.0004
	7	7	18486.4533	-0.0007		6	6	18488.6577	0.0006
	12	12	18486.4550	-0.0003		5	4	18488.6636	0.0003
	13	13	18486.4663	-0.0010		6	5	18488.6663	0.0003
	14	14	18486.4838	-0.0019	*R*(1.5)	2	3	18489.9579	-0.0024
	14	13	18486.4962	0.0003		2	2	18489.9772	-0.0012
Q(9.5)	8	7	18486.8462	-0.0003		3	4	18489.9892	-0.0018
	9	9	18486.8507	-0.0003		3	3	18490.0036	-0.0013
	8	8	18486.8523	0.0012		3	2	18490.0227	-0.0003
	10	10	18486.8534	-0.0006		4	4	18490.0368	-0.0003
	7	7	18486.8544	0.0011		4	3	18490.0511	0.0001
	11	11	18486.8609	-0.0002		5	4	18490.0722	0.0001
	11	10	18486.8627	-0.0002		6	5	18490.0807	0.0014
	12	12	18486.8727	-0.0007	*R*(2.5)	2	2	18490.4260	-0.0012
	12	11	18486.8790	0.0000		3	2	18490.4426	0.0003
	13	13	18486.8908	-0.0013		4	4	18490.4569	-0.0001
	13	12	18486.9016	-0.0008		4	3	18490.4606	0.0009

Q(7.5)	7	6	18487.5408	-0.0009		5	5	18490.4734	0.0003
	6	6	18487.5433	0.0002		5	4	18490.4782	-0.0001
	5	5	18487.5433	0.0000		6	6	18490.4876	0.0001
	7	7	18487.5454	0.0006		6	5	18490.4966	0.0002
	4	4	18487.5454	0.0010		7	6	18490.5105	-0.0003
	8	7	18487.5475	-0.0004	*R*(3.5)	2	1	18490.8333	0.0016
	8	8	18487.5492	0.0000		2	2	18490.8354	0.0020
	9	9	18487.5573	0.0000		2	3	18490.8371	0.0019
	10	10	18487.5695	-0.0007		3	2	18490.8396	0.0018
	10	9	18487.5752	-0.0005		4	3	18490.8465	0.0002
	11	11	18487.5877	-0.0016		4	4	18490.8476	0.0003
	11	10	18487.5992	-0.0007		5	6	18490.8518	0.0007
Q(6.5)	4	3	18487.8260	0.0015		5	4	18490.8573	0.0001
	5	5	18487.8287	-0.0013		6	6	18490.8651	-0.0004
	5	4	18487.8287	0.0026		6	5	18490.8712	0.0008
	4	4	18487.8308	0.0023		7	7	18490.8755	0.0001
	6	6	18487.8319	-0.0013		7	6	18490.8864	0.0005
	7	6	18487.8366	-0.0008		8	7	18490.9037	0.0003
	7	7	18487.8374	-0.0013	*R*(4.5)	3	2	18491.1980	-0.0002
	8	9	18487.8414	-0.0009		2	1	18491.1980	0.0014
	8	8	18487.8470	-0.0007		4	3	18491.2016	0.0002
	9	9	18487.8596	-0.0015		4	3	18491.2037	0.0023
	9	8	18487.8651	-0.0014		4	4	18491.2051	0.0011
	10	10	18487.8777	-0.0025		5	4	18491.2076	0.0011
	10	9	18487.8896	-0.0013		5	5	18491.2095	0.0016
Q(5.5)	2	2	18488.0709	0.0009		6	5	18491.2148	0.0008
	4	4	18488.0752	-0.0012		7	7	18491.2209	0.0014
	5	4	18488.0770	-0.0019		7	6	18491.2257	0.0011
	4	5	18488.0791	-0.0003		8	8	18491.2284	0.0004
	5	5	18488.0806	-0.0013		8	7	18491.2401	0.0012
	5	6	18488.0831	-0.0002		9	8	18491.2582	0.0007
	6	6	18488.0879	-0.0015	*R*(5.5)	4	3	18491.5215	-0.0003
	7	8	18488.0929	-0.0017		3	2	18491.5224	0.0004
	7	7	18488.0990	-0.0009		5	4	18491.5255	0.0026
	7	6	18488.1019	0.0008		6	5	18491.5260	0.0001
	8	7	18488.1189	-0.0003		7	6	18491.5320	0.0005
	9	9	18488.1307	-0.0019		8	8	18491.5355	0.0001
	9	8	18488.1430	-0.0005		8	7	18491.5416	0.0010
Q(4.5)	2	1	18488.2687	-0.0019		9	8	18491.5546	0.0004
	2	2	18488.2716	-0.0013		10	9	18491.5731	0.0000
	2	3	18488.2750	-0.0007	*R*(6.5)	6	5	18491.8066	0.0025
	3	2	18488.2760	-0.0013		5	4	18491.8066	0.0021

3	3	18488.2795	-0.0006	7	6	18491.8078	0.0021
3	4	18488.2822	-0.0005	8	8	18491.8088	0.0001
4	3	18488.2854	-0.0014	8	7	18491.8132	0.0031
4	5	18488.2907	-0.0002	9	9	18491.8160	0.0031
5	6	18488.2986	-0.0011	9	8	18491.8200	0.0016
7	6	18488.3339	-0.0006	10	10	18491.8217	0.0011
8	8	18488.3456	-0.0009	10	9	18491.8341	0.0027
8	7	18488.3576	0.0002	11	10	18491.8524	0.0021

Rms=0.00115 cm^{-1} σ= 0.00117 cm^{-1}

Table 4.9. Observed and calculated line positions in wavenumber (cm^{-1}) of (1,0)[17.9]2.5-$X^2\Delta_{3/2}$ of ^{179}HfF

	F'	F''	Observed	Observed-Calced		F'	F''	Observed	Observed-Calced
P(6.5)	10	11	18484.0499	-0.0015	*Q*(3.5)	6	5	18488.1537	0.0004
	9	10	18484.0597	0.0010		6	6	18488.1559	-0.0001
	8	9	18484.0658	-0.0009		5	4	18488.1629	-0.0011
	7	8	18484.0743	-0.0008		5	5	18488.1679	-0.0002
	6	7	18484.0830	-0.0004		5	6	18488.1706	-0.0002
Q(11.5)	14	14	18485.6692	0.0001		4	3	18488.1727	0.0020
	13	13	18485.6692	-0.0004		3	2	18488.1756	0.0010
	12	12	18485.6726	-0.0002		2	1	18488.1779	0.0009
	15	15	18485.6727	0.0009		4	5	18488.1806	0.0015
	12	13	18485.6748	0.0016		6	5	18488.2795	-0.0011
	11	11	18485.6790	0.0009		6	6	18488.2822	-0.0014
	16	16	18485.6800	0.0015		6	7	18488.2854	0.0000
	9	9	18485.6942	0.0016	*R*(1.5)	7	6	18489.6431	-0.0005
	8	8	18485.7000	-0.0009		6	5	18489.6925	-0.0007
	7	7	18485.7084	-0.0009		6	6	18489.7150	0.0025
Q(10.5)	13	13	18486.1128	0.0001		5	4	18489.7251	0.0008
	12	12	18486.1142	0.0003		5	5	18489.7268	-0.0012
	14	14	18486.1152	0.0006		2	3	18489.7296	-0.0007
	11	11	18486.1179	0.0003		3	4	18489.7343	0.0009
	15	15	18486.1218	0.0013		4	4	18489.7378	0.0021
	9	9	18486.1297	-0.0005		4	3	18489.7425	0.0016
	8	8	18486.1372	-0.0007	*R*(2.5)	8	7	18490.0945	-0.0008
	7	7	18486.1456	-0.0004		7	6	18490.1227	0.0010
	6	6	18486.1531	-0.0009		6	5	18490.1390	0.0003
Q(9.5)	12	12	18486.5179	0.0002		6	6	18490.1422	0.0005
	13	13	18486.5190	0.0002		5	4	18490.1492	-0.0004

	11	11	18486.5190	-0.0007		5	5	18490.1532	-0.0003
	10	10	18486.5226	-0.0015		4	3	18490.1558	-0.0008
	14	14	18486.5240	0.0004		4	4	18490.1596	-0.0010
	9	9	18486.5295	-0.0006		3	3	18490.1633	-0.0012
	9	10	18486.5322	-0.0003		2	2	18490.1672	0.0008
	8	7	18486.5336	0.0006		3	4	18490.1683	-0.0003
	8	8	18486.5364	-0.0008	*R*(3.5)	9	8	18490.5013	0.0001
	8	9	18486.5412	0.0004		8	7	18490.5149	0.0003
	7	6	18486.5412	0.0008		7	6	18490.5252	0.0001
	7	7	18486.5442	-0.0007		6	5	18490.5340	0.0001
	7	8	18486.5485	-0.0007		6	6	18490.5371	0.0005
	6	6	18486.5509	-0.0019		5	4	18490.5410	-0.0005
	5	5	18486.5584	-0.0018		5	5	18490.5452	-0.0003
Q(8.5)	12	12	18486.8839	-0.0002		4	3	18490.5479	-0.0002
	11	11	18486.8849	0.0006		4	4	18490.5516	-0.0009
	13	13	18486.8872	-0.0003		3	2	18490.5560	0.0023
	10	10	18486.8872	-0.0001		3	3	18490.5573	-0.0004
	9	9	18486.8938	0.0015		2	2	18490.5608	-0.0006
	8	8	18486.8976	-0.0012		2	3	18490.5640	-0.0014
	8	9	18486.9004	-0.0011	*R*(4.5)	10	9	18490.8655	0.0009
	7	6	18486.9016	-0.0003		9	8	18490.8712	0.0007
	7	7	18486.9048	-0.0013		8	7	18490.8773	0.0005
	7	8	18486.9090	-0.0008		7	6	18490.8842	0.0006
	6	6	18486.9129	-0.0008		6	5	18490.8904	-0.0003
Q(6.5)	11	11	18487.4971	0.0002		6	6	18490.8941	0.0002
	10	10	18487.4992	0.0004		5	4	18490.8969	-0.0009
	9	9	18487.5032	0.0003		4	4	18490.9086	-0.0001
	8	7	18487.5060	-0.0007		3	2	18490.9135	0.0028
	8	8	18487.5083	-0.0003		3	3	18490.9146	0.0002
	7	6	18487.5111	-0.0011		2	1	18490.9178	0.0018
	7	7	18487.5150	-0.0004		2	2	18490.9195	0.0007
	7	8	18487.5172	-0.0002	*R*(5.5)	11	10	18491.1882	0.0012
	6	5	18487.5179	-0.0009		10	9	18491.1894	0.0010
	6	6	18487.5219	-0.0009		9	8	18491.1929	0.0011
	5	5	18487.5292	-0.0009		8	7	18491.1980	0.0011
	4	4	18487.5355	-0.0014		7	6	18491.2037	0.0005
Q(5.5)	10	10	18487.7391	-0.0024		6	5	18491.2098	-0.0003
	9	9	18487.7466	-0.0017		5	4	18491.2172	-0.0001
	9	8	18487.7501	-0.0006		5	5	18491.2209	-0.0005
	8	8	18487.7536	-0.0021		4	3	18491.2257	0.0014
	7	7	18487.7640	0.0006	*R*(6.5)	11	10	18491.4697	0.0019
	6	6	18487.7724	0.0012		10	9	18491.4697	0.0005

	6	7	18487.7732	-0.0005		12	11	18491.4704	0.0011
	5	4	18487.7741	-0.0005		9	8	18491.4730	0.0001
	5	5	18487.7771	-0.0016		9	9	18491.4730	0.0002
	4	3	18487.7800	-0.0015		8	7	18491.4782	-0.0001
	5	6	18487.7826	0.0002		8	8	18491.4800	-0.0003
	4	4	18487.7871	0.0016		7	6	18491.4843	-0.0006
	3	2	18487.7888	0.0008		6	5	18491.4910	-0.0012
	3	3	18487.7927	0.0013		5	4	18491.4987	-0.0008
Q(4.5)	9	9	18487.9430	-0.0018		4	3	18491.5055	-0.0011
	8	8	18487.9599	-0.0003	*R*(7.5)	11	10	18491.7097	0.0013
	8	7	18487.9616	0.0001		12	11	18491.7104	0.0019
	7	8	18487.9698	-0.0012		10	9	18491.7115	0.0005
	6	5	18487.9801	0.0009		13	12	18491.7134	0.0014
	6	6	18487.9821	-0.0003		9	8	18491.7161	0.0004
	6	7	18487.9839	0.0000		9	9	18491.7177	0.0005
	5	5	18487.9890	-0.0018		8	7	18491.7218	-0.0001
	5	5	18487.9923	0.0015		8	8	18491.7253	0.0005
	5	6	18487.9944	0.0004		7	6	18491.7285	-0.0005
	4	3	18487.9951	0.0016		6	5	18491.7356	-0.0010
	3	2	18487.9996	0.0002					
Rms=0.00099 cm^{-1} σ= 0.00101cm^{-1}									

Table 4.10. Observed and calculated Stark shift for (1,0)[17.9]2.5-$X^2\Delta_{3/2}$ band of ^{180}HfF

Lines, Polarizations	Field (V/cm)	M_J"	M_J'	Obs (MHz)	Dif (MHz)
R(1.5), ∥	577.37	1.5	1.5	-242	-5.22
		0.5	0.5	-70	8.93
		-0.5	-0.5	92	13.07
		-1.5	-1.5	252	15.22
R(1.5),∥	866	1.5	1.5	-353	2.14
		0.5	0.5	-112	6.38
		-0.5	-0.5	130	11.62
		-1.5	-1.5	366	10.86
R(1.5), ∥	1732	1.5	1.5	-692	18.29
		0.5	0.5	-242	-5.24
		-0.5	-0.5	237	0.24
		-1.5	-1.5	704	-6.29
R(1.5), ⊥	1732	1.5	0.5	-816	-1.25
		1.5	2.5	-590	15.82
		0.5	-0.5	-331	10.22

		0.5 1.5	-126	6.30
		-0.5-1.5	141	8.70
		-0.5 0.5	340	-1.22
		-1.5-2.5	619	13.18
		-1.5-0.5	818	3.25
Q(2.5), ∥	1154.7	2.5 2.5	-233	5.75
		1.5 1.5	-148	-4.75
		0.5 0.5	-47	0.75
		-0.5-0.5	48	0.25
		-1.5-1.5	135	-8.25
		-2.5-2.5	232	-6.75
Q(2.5), ∥	1443.42	2.5 2.5	-285	13.45
		1.5 1.5	-172	7.07
		0.5 0.5	-48	11.69
		-0.5-0.5	68	8.31
		-1.5-1.5	185	5.93
		-2.5-2.5	305	6.55
P(3.5), ∥	2309.46	2.5 2.5	-107	3.52
		1.5 1.5	-60	6.31
		0.5 0.5	-25	-2.90
		-0.5-0.5	28	5.90
		-1.5-1.5	76	9.69
		-2.5-2.5	120	9.48
P(3.5), ∥	2886.84	2.5 2.5	-152	-13.85
		1.5 1.5	-77	5.89
		0.5 0.5	-30	-2.37
		-0.5-0.5	29	1.37
		-1.5-1.5	77	-5.89
		-2.5-2.5	131	-7.15
R(1.5), ⊥	1443.42	1.5 0.5	-695	-16.00
		1.5 2.5	-504	0.88
		0.5 -0.5	-277	7.36
		0.5 1.5	-113	-2.74
		-0.5-1.5	119	8.74
		-0.5 0.5	290	5.63
		-1.5-2.5	503	-1.88
		-1.5-0.5	684	5.00

rms=8.32 MHz

Table 4.11. Spectroscopic parameters in wavenumber (cm^{-1}) of (1,0)[17.9]2.5-$X^2\Delta_{3/2}$ band for ^{180}HfF, ^{179}HfF, ^{177}HfF

States	Parameters	^{180}HfF	^{179}HfF	^{177}HfF
$X^2\Delta_{3/2}$	B''	0.283714(37)	0.283819[a]	0.284128[a]
	$h''_{3/2}$(Hf)		-0.00348(34)	0.00586(38)
	eQq_0''(Hf)		-0.0805(35)	-0.0774(30)
	μ_e''	1.66(1) [b]		
[17.9]2.5 (v=1)	T_0(18400)	89.30435(41)	89.47775(20)	89.81514(21)
	B'	0.264427(35)	0.264511(3)	0.264806(4)
	$h'_{5/2}(^{19}F)$	0.00149		
	$h'_{5/2}$(Hf)		-0.01660(26)	0.02572(27)
	eQq_0'(Hf)		-0.2101 (43)	-0.1998(36)
	μ_e'	0.419(7)[b]		

a. Constrained to value isotopically scaled from the fit of the ^{180}HfF transitions.

b. Permanent electric dipole moments (debye, D)

References

1. T. D. Lee and C. N. Yang, Phys. Rev. 104, 254 (1956)

2. C. S. Wu, E. Ambler, R. W. Hayward, D. D. Hoppes, and R. P. Hudson, *Phys. Rev.* ***105****, 1413–1415 (1957).*

3. M. A. Bouchiat, C. Bouchiat J. Phys. France, **35**, 899-927 (1974)

4. P. G. H. Sandars, Atomic Physics, **4**, 71-92 (1975).

5. A.E. Leanhard, J.L. Bohn, H. Loy, P. Maletinsky, E.R. Meyer, L.C. Sinclair, R.P. Stutz and E.A. Cornell, J. Mol. Spectrosc. **270**, 1-25 (2011).

6. D. DeMille; S. B. Cahn, D. Murphree, D Rahmlow; M G Kozlov Phys. Rev. Lett. **100** 023003-01 023003-04 (2008).

7. M G Kozlov and L N Labzowsky 1995 *J. Phys. B: At. Mol. Opt. Phys.* **28** 1933

8. F. Faglioni, A. Ligabue, S. Pelloni, A. Soncini, P. Lazzeretti, Chemical Physics, **304** 289–299, (2004).

9. M. G. Kozlov and L. N. Labzowsky, Journal of Physics B: Atomic, Molecular and Optical Physics, **28**, 1933 (1995).

10. M. G. Kozlov, A. V. Titov, N. S. Mosyagin, and P. V. Souchko, Physical Review A: Atomic, Molecular, and Optical Physics **56(5)**, R3326 (1997).

11. J.A.J. Fitzpatrick, F. R. Manby and C. M. Western, J. Chem . Phys. **122** 084312/1-12 (2005).

12. W.E. Ernst and J.O. Schröder, Chem. Phys. **78,** 363 (1983)

13. C. Nitsch, J.O. Schröder and W.E. Ernst, Chem. Phys. Lett, **148**, 130, (1988).

14. J. Kändler, T. Martell, and W. E. Ernst, Chem. Phys. Lett. **155**, 470 (1989).

15. T.C. Steimle, D. A. Fletcher, and C.T. Scurlock, J. Mol. Spectrosc. **158**, 487 (1993).

16. Y. Azuma, W.J. Childs, G.L. Goodman , and T.C. Steimle, J. Chem. Phys., **93**, 5533 (1990).

17. J. M. Brown and A. Carrington, *Rotational Spectroscopy of Diatomic Molecules* (Cambridge University Press, Cambridge, 2003).

18. C. Effantin, A Bernard,. J. D'Incan, G. Wannous, J. Verges, and R. F.Barrow, Mol. Physics , **70**, 735 (1990).

19 Ch. Ryzlewicz and T. Törring, Chem. Phys. **51**, 329 (1980).

20. Ch. Ryzlewicz, H.-U. Schütze-Pahlmann J. Hoeft and T. Törring, Chem. Phys. **71**, 389 (1982).

21. B. Guo, K. Q. Zhang, and P.F. Bernath, J. Mol. Spectrosc. **170**, 59, (1995).

22. T. Törring, W.E. Ernst, and J. Kändler, J. Chem. Phys. **90**, 4927 (1989).

23. W.E. Ernst, J. Kändler and T. Törring, J. Chem. Phys. **84**, 4769 (1986).

24. L.-E. Berg, T. Olsson, J. C. Chanteloup, A. Hishikawa, and P. Royen, Mol. Phys. **79**, 721 (1993).

25. L.-E. Berg, N. Gador, D. Husain, H. Ludwigs, and P. Royen, Chem. Phys. Lett. **287**, 89 (1998).

26. A. Bernard, C. Effantin, J. D'Incan, J. Verges, and R. F.Barrow. Mol. Physics , **70**, 747- 735 (1990).

27. H. U. Lee and R. N. Zare, *J. Mol. Spectrosc.* **64,** 233–243 (1977).

28. K. L. Dunfield, C. Linton, T. E. Clarke, J. McBride, A. G. Adam, and J. R. D. Peers, J. Mol. Spec. **174**, 433 (1995).

29. C.S. Dickinson, J.A. Coxon, N.R. Walker and M.C.L. Gerry, J. Chem. Phys. **115,** 6979(2001).

30. B.E. Sauer, J. Wang and E.A. Hinds, J. Chem. Phys. **105**, 7412 (1996).

31. P.C. Condylis, J.J. Hudson, M.R. Tarbutt, B.E. Sauer and E.A. Hinds, J. Chem. Phys. **123**, 131101(2005).

32. T. C. Steimle, T. Ma and C. Linton, *J. Chem. Phys.*, 2007, **127**, 234316; T. C. Steimle, T. Ma and C. Linton, *J. Chem. Phys.*, 2008, **128**, 209903, T. C. Steimle, T. Ma and C. Linton, *J. Chem. Phys.*, 2012 **137**, 109901.

33. T. Ma, C. Butler, J. M. Brown, C. Linton, and T.C. Steimle, J. Phys. Chem. A. 113, 8038 (2009).

34. R. J. Le Roy, Level 8.0: A Computer Program for Solving the Radial Schrodinger Equation for Bound and Quasibound Levels, University of Waterloo Chemical Physics Research Report CP-663 (2007); see http://leroy.uwaterloo.ca/programs/.

35. R. J. Le Roy, RKR1 2.0: A Computer Program Implementing the First-Order RKR Method for Determining Diatomic Molecule Potential Energy Curves, University of Waterloo Chemical Physics Research Report CP-657R (2004). The source code and manual for this program may be obtained from the "Computer Programs" link at http://leroy.uwaterloo.ca .

36. E. N. Moskvitina, Y.Y. Kuzyakov, *Spectroscopy Letter*, 1999, **32**(5), 719-728.

37. A. G. Adam, W. S. Hopkins, and D.W. Tokaryk, *J. Mol. Spectrosc*. 2004, **225**, 1-7.

38. R. S. Ram, A. G. Adam, W. Sha, A. Tsouli, J. Liévin, and P. F. Bernath, J. Chem. Phys. **114**, 3977 (2001).

39. M. Grau, A. E. Leanhardt, H. Loh, L. C. Sinclair, R. P. Stutz, T. S. Yahn, and E. A. Cornell, *J. Mol. Specstrosc*., 2012, **272**, 32-35.

40. B. J. Barker, I. O. Antonov, V. E. Bondybey, and M.C. Heaven, *J. Chem. Phys*., 2011, **134**, 201102.

41. H. Loh, R. P. Stutz, T. S. Yahn, H. Looser, R.W. Field, E. A. Cornell, *J. Mol. Specstrocs*. 2012, **276-277**, 49-56.

42. C. H. Townes and A. L. Schawlow, *Microwave Spectroscopy* (McGraw-Hill, New York, 1955.

43. W.J. Childs, *Phys. Rev*., 1967, **156**, 71.

44. S. Büttgenbach, *Hyperfine Structure in 4d and 5d-Shell Atoms* , Springer Tracts in Modern Physics (Springer-Verlag, Berlin, 1982).

45. S. Büttgenbach, R. Dicke and H. Gebauer, *Phys. Letts.* , **62A**, 307. (1977).

Chapter 5

FRANCK-CONDON FACTOR CALCULATION AND NORMAL MODE ANALYSIS FOR TRIATOMIC C_{2V} MOLECULES: TIO_2, ZRO_2

Dioxygen binding and activation at metal centers are of major importance in a wide range of catalytic and biological processes. The triatomic transition-metal oxides that consist of a single transition metal and two oxygen atoms represent a significant increase in complexity over the simplest case of the diatomic molecule and can shed light on binging and metal activation. A recent review by Gong et al [1] shows that the spectroscopy of the transition metal dioxides is far less well known than those for gas-phase studies of the transition metal diatomics. The dioxides can have one of three isomeric forms; a) the inserted form, with a large apex angle, b) a "T-Shaped" form with a small apex angle and an O-O distance close to that of O_2, and c) a M-O-O superoxide form. The bent inserted structures has been observed for both TiO_2 [2, 3], an ZrO_2 [4, 5]. The inserted dioxides are water-like molecules have the C_{2v} symmetry.

5.1. Titanium Dioxide, TiO_2

Titanium dioxide, TiO_2, is a well-known photo-activated catalysis under ultraviolet (UV) light. TiO_2 is also a photocatalyst under visible and UV light when doped with nitrogen or other metal oxides [6]. Numerous studies have focused on trying to find the best metal doping to shift the photo-activation threshold to the visible spectrum. Understanding the properties of gas-phase TiO_2 from the UV to visible spectrum will help in this process.

The molecular beam electric deflection experiment on TiO_2 back in 1967 determined that TiO_2 has a bent structure with dipole moment [4]. Later on, the first

emission spectrum of TiO_2 were observed [7] and the origin was assigned at 18880 cm^{-1}, a strong band shifted by 934.8cm^{-1} was assigned to the asymmetric stretch, ν_3, and a weaker band shifted by 962.0 cm^{-1} was assigned to symmetric stretch, ν_1. The infrared absorption spectrum of an argon matrix isolated sample was recorded and analyzed by Chertihin and Andrews [8]. The vibrational frequency for the symmetric stretch and asymmetric stretch were determined to be 946.9 cm^{-1} and 917.1 cm^{-1}, respectively. Photoelectron spectroscopy of TiO_n^-(n=1-3) and $(TiO_2)_n^-$ (n=1-4) anions were also studied to obtain the vertical detachment energy [9]. For TiO_2^-, the measured electron affirmity is 1.59(3) eV, ω_1=960(40) cm^{-1}, the binding energy of $\tilde{A}^3B_2$ was measured to be 3.55(10) eV, and the binding energy of $\tilde{a}^1B_2$ was estimate to be 4.0(2) eV. There are numerous calculation studies for TiO_2 and TiO_2 cluster [10, 11,12].

Two complete studies of gas-phase TiO_2 [2, 3] have been published by the Steimle group. The ν_1 and ν_2 vibrational frequencies for the $\tilde{X}^1A_1$ state were experimentally determined to be: ω_1=968(7) cm^{-1}, ω_2=323(1) cm^{-1}. There was no experimentally evidence of the asymmetric stretch, ν_3, in the ground state. The vibrational frequencies for the $\tilde{A}^1B_2$ state were experimentally determined to be: ω_1=876(3) cm^{-1}, ω_2=184(1) cm^{-1}, ω_3=316(2) cm^{-1}. The rotational constants and electric dipole moments of four bands of the $\tilde{A}^1B_2(\nu_1,\nu_2,\nu_3) \leftarrow \tilde{X}^1A_1(0,0,0)$ electronic transition are also determined.

5.1.1 Observation and analysis

The excitation spectrum of TiO_2 were recorded and analyzed by Dr. Zhang (a former postdoc in Prof. Steimle's lab). My contribution to this project was to simulate the spectrum. The description of the observed laser induced fluorescence (LIF) spectrum recored by Dr. Zhang in this thesis is only for comparison with the simulation spectra obtained using multidimensional Franck-Condon Factors (FCFs) calculation. The LIF excitation of TiO_2 in the region from 17500 cm^{-1}-18900 cm^{-1} is complicated and is present in Figure 5.1. The spectrum was assigned to a progression of $\tilde{A}^1B_2(\nu_1,\nu_2,\nu_3) \leftarrow \tilde{X}^1A_1(0,0,0)$. There are no features to the red of the 17591cm^{-1} band, so it was assigned to the transition $\tilde{A}^1B_2(0,0,0) \leftarrow \tilde{X}^1A_1(0,0,0)$ (the origin was reassigned in comparison with the previous study [7]). The features at 17960 cm^{-1} and at 18655 cm^{-1} are more intense because they are overlapped with the $B^3\Pi_0(\nu=2)\leftarrow X^3\Delta_1(\nu=0)$ and $B^3\Pi_0(\nu=3)\leftarrow X^3\Delta_1(\nu=0)$ transition of TiO, respectively. The first four features on Figure 5.1 were assigned to the progression of bending mode, ν_2, $\tilde{A}^1B_2(0, \nu_2,0) \leftarrow \tilde{X}^1A_1(0,0,0)$. The feature at 18231 cm^{-1} was assign to the two quanta of the asymmetric stretch, ν_3, $\tilde{A}^1B_2(0, 0,2) \leftarrow \tilde{X}^1A_1(0,0,0)$. The feature at 18472.9 cm^{-1} was assigned to the first quantum of the symmetric mode, ν_1. The assignment, transition wavenumber and the predicted Franck-Condon factors are given in Table 5.1.

The fluorescence decay curves of ten intense bands in the LIF spectrum were recorded using a digital storage oscilloscope. An example of fluorescence decays resulting from excitation of the $\tilde{A}^1B_2(1,0,0)$- $\tilde{X}^1A_1(0,0,0)$ transition at 18471.10 cm^{-1} is

shown in Figure 5.2. The curves of the ten bands mreasured all exhibit single exponential decays and were fit to the equation:

$$Y = Y_0 + Ae^{\frac{-(t+t_0)}{\tau}}, \qquad (1)$$

where t_o is set to the time after detection had recovered from initial laser scatter (usually about 20 ns). The data after 3 μs were removed because the molecules drift out the LIF collecting region. The fitted lifetimes, τ, and the associated errors are also listed in Table 5.1.

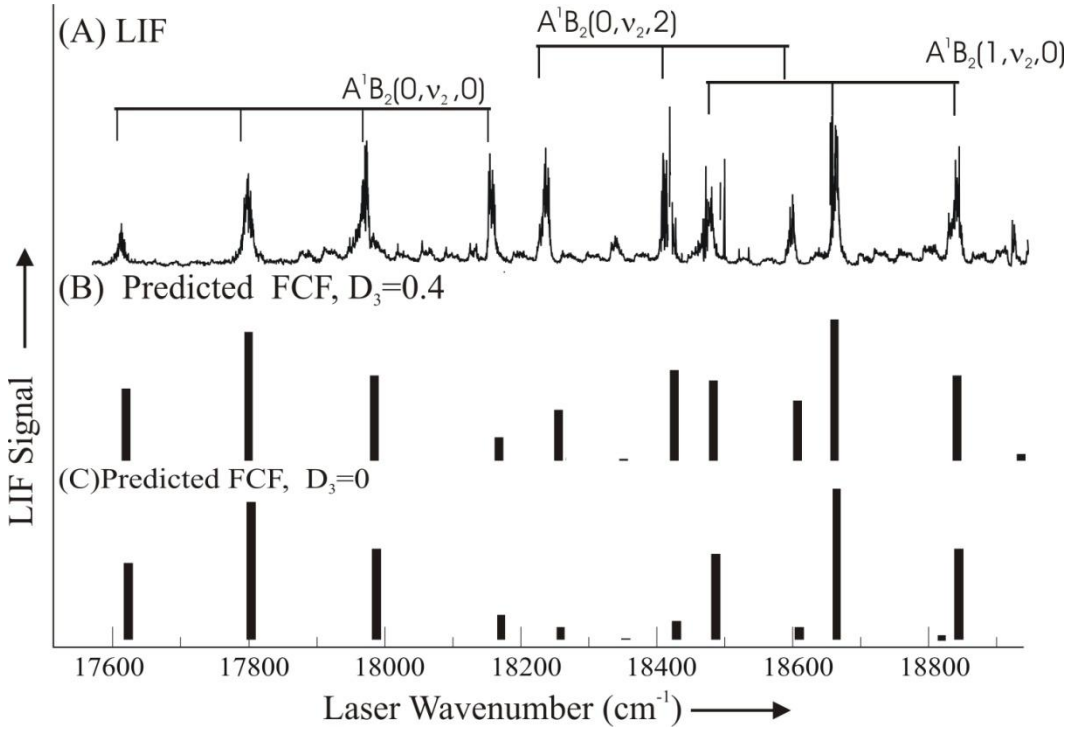

Figure 5.1. The observed laser induced fluorescence (LIF) spectrum (A) with the vibrational assignments, the predicted (B) stick diagram of LIF spectrum with displacement D_3=0.4 Å (see text), and the predicted (C) stick diagram of LIF spectrum with displacement D_3=0Å (see text).

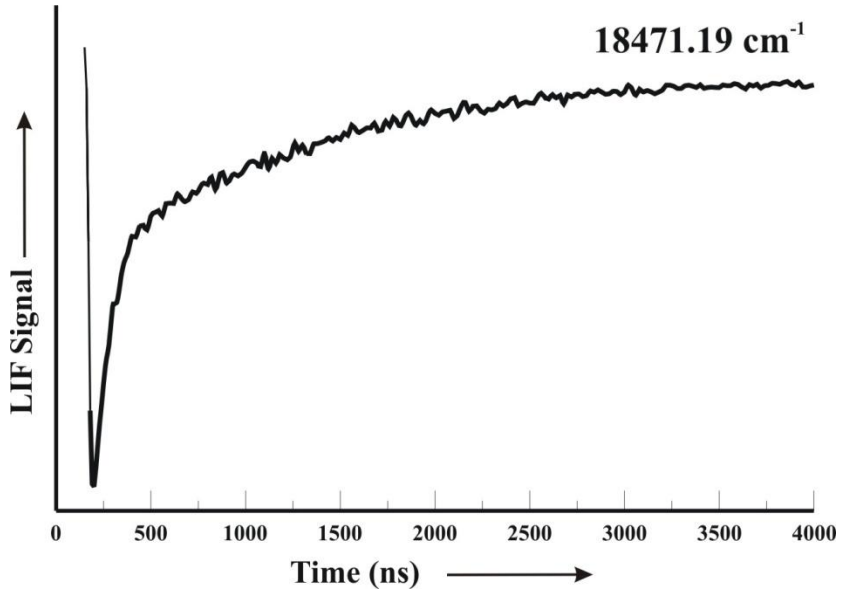

Figure 5.2. Fluorescence decay curve resulting from excitation $\tilde{A}^1B_2(1,0,0)$ at band 18471.10 cm^{-1}.

5.1.2 Discussions

Franck-Condon Factors (FCFs) predictions:

The square of the overlap integral between two electronic states is called Franck-Condon Factor. The method for calculating the FCFs for one dimensional harmonic oscillator has been well established [13,14]. However, for polyatomic molecules, the multidimensional oscillators with the inclusion of Duschinsky effects [15] makes the FCFs calculations much more difficult in comparison with those for the one dimensional problem.

For C_{2v} molecules, the FCFs problem separates into two problems: a two dimension a_1-symmetry modes and a 1-dimensional problem for the b_2-symmetry mode:

$$\mathrm{FCF} = \left|\left\langle \upsilon_1' \upsilon_1' \middle| 00 \right\rangle\right|^2 \left|\left\langle \upsilon_3' \middle| 0 \right\rangle\right|^2 . \qquad (2)$$

The vibrational overlap integral between vibronic levels $|00\rangle$ and $|\upsilon_1'\upsilon_1'\rangle$ given by:

$$\langle \upsilon_1'\upsilon_1'|00\rangle = \mathrm{N}'\int_{-\infty}^{\infty}\int_{-\infty}^{\infty} \mathrm{H}_{\upsilon_1(\tilde{A}^1B_2)}\sqrt{\alpha_1(\tilde{A}^1B_2)}Q_1(\tilde{A}^1B_2)\mathrm{H}_{\upsilon_2(\tilde{A}^1B_2)}\sqrt{\alpha_2(\tilde{A}^1B_2)}Q_2(\tilde{A}^1B_2)$$
$$\exp(-\frac{1}{2}\alpha_1(\tilde{A}^1B_2)Q_1(\tilde{A}^1B_2)-\frac{1}{2}\alpha_2(\tilde{A}^1B_2)Q_2(\tilde{A}^1B_2) \quad , (3)$$
$$-\frac{1}{2}\alpha_1(\tilde{X}^1A)Q_1(\tilde{X}^1A)^2-\frac{1}{2}\alpha_2(\tilde{X}^1A)Q_2(\tilde{X}^1A)^2)dQ_1(\tilde{A}^1B_2)dQ_2(\tilde{A}^1B_2)$$

where $N' = \frac{1}{\pi}\frac{\sqrt{\alpha_1(\tilde{A}^1B_2)\alpha_2(\tilde{A}^1B_2)\alpha_1'(\tilde{X}^1A)\alpha_2'(\tilde{X}^1A)}}{2^{\upsilon_1(\tilde{A}^1B_2)+\upsilon_2(\tilde{A}^1B_2)}\upsilon_1(\tilde{A}^1B_2)!\upsilon_2(\tilde{A}^1B_2)!}$, (4)

and $\alpha_i = \frac{\omega_i}{\hbar}$. (5)

In equation 3, H_{υ_i} is the Hermite polynomial, **Q_1** and **Q_2** are the normal coordinates. Equation 3 shows that the vibrational overlap integral are related to the normal coordinates of the excited state **Q**($\tilde{A}^1B_2$) and the normal coordinates of ground state **Q**($\tilde{X}^1A_1$). The Duschinsky effect [16], relates the normal coordinates of the excited state **Q**($\tilde{A}^1B_2$) and the normal coordinates of ground state **Q**($\tilde{X}^1A_1$) by equation [17]:

Q ($\tilde{A}^1B_2$)=**J. Q** ($\tilde{X}^1A_1$)+**D**, (6)

where matrix **J** is block diagonal of a 2×2 (a_1)and 1×1(b_2) matrix of the normal vibrational modes, due to the C_{2v} symmetry. The displacement vector, **D,** vector has a dimension of 1×3. Displacement vector, **D**, composed of two elements associated with the a_1-symmetry modes, and one element associated with the asymmetric stretch vibrational mode, b_2-symmetry mode. The calculation for those normal coordinates, **Q**, of

both $\tilde{A}^1B_2$ and $\tilde{X}^1A_1$ states are described in details in the section on the normal mode analysis of ZrO_2. For TiO_2, due to lack of experimental data (i.e: the asymmetric stretch vibrational frequency, ω_3, for the ground $\tilde{X}^1A_1$ state), the Duschinsky matrix, **J,** matrix and displacement vector, **D,** vector were calculated by Professor Steimle. The geometrical displacement for asymmetric stretch mode, D_3, should be zero, by symmetry. The FCF calculation for the 1-dimensional, b_2-symmetry, mode used the analytical expression from Chang [18]. The FCF calculation for the 2-dimensional, a_1-symmetry, modes used the equation from Chang [19]. Both calculations assume the harmonic oscillator motion. The *Mathematica* notebook is given in the APPENDIX A**.** Using Equation 1, the predicted spectra are show in Figure 5.1(C)**.** The relative intensity of the predicted spectrum is not in good agreement with the observation. For example, the predicted spectrum using analytical expression from Chang [18, 19] underestimated the transition intensities for bands involving two quanta of asymmetric modes $\tilde{A}^1B_2$ $(0,\nu_2,2)\leftarrow \tilde{X}^1A_1(0,0,0)$. In order to reproduce the observation spectral intensity, the displacement, D_3, was set to a finite number of 0.4Å. The predicted spectra with displacement element D_3=0.4Å also presents in Figure 5.1(B) and the associated FCFs given in Table 5.1**.** The use of $D_3 \neq 0$, which is non-physical, is to compensate for the harmonic motion assumption. The *ab initio* shows that the $\tilde{A}^1B_2$ states of TiO_2 have a very shallow potential energy surface in the bending coordinate [10] as the function of bond O-Ti-O angle, therefore the harmonic oscillator assumption from Ref. 18 and Ref 19 is not appropriated.

Another way of explaining the nonzero displacement vector component D_3 is by vibronic coupling. Evidence for vibronic coupling is seen in the trend of the measured lifetimes. The trends in the measured fluorescence radiative lifetime, τ, given Table 5.1, are plotted in Figure 5.3. The fluorescence lifetimes decrease with the increasing quanta of ν_2. For example: τ=1.62(11) μs for $\tilde{A}^1B_2$ (0,0,0) band where as it reduces to τ=1.32(05) μs for the $\tilde{A}^1B_2$ (0,3,0) band. If two quanta of the asymmetric stretch were added, the same trend was observed: the fluorescence lifetimes decrease as the increasing in the quanta of ν_2. However, the opposite trend is observed if one quantum of the symmetric stretch is also present. For example: $\tilde{A}^1B_2$ (1,0,0)(τ=1.23(05)μs) increases to the $\tilde{A}^1B_2$ (1,2,0) (τ=1.78(15)μs). If TiO_2 is a rigid molecule like water or SO_2, the vibrational motion of a_1-symmetry and b_2-symmetry are completely separated, and D_3 strictly equals to zero. Since, TiO_2 is not a rigid C_{2v} molecule, there is a possibility that vibrational motion of b_2-symmetry under "intensity borrowing" mechanism from either a_1-symmetry vibrational motion or from a nearby $\tilde{B}^1A_1$ state [20].

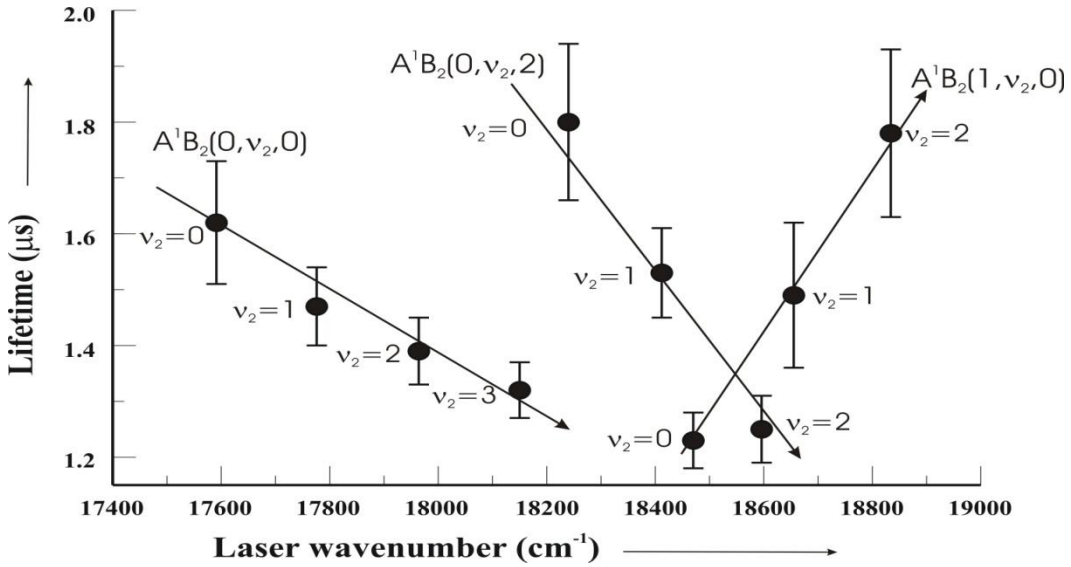

Figure 5.3. Trend in fluorescence radiative lifetime for $\tilde{A}^1B_2(\nu_1,\nu_2,\nu_3) \leftarrow \tilde{X}^1A_1(0,0,0)$ trantion of TiO_2.

Table 5.1. Assignment of the $\tilde{A}^1B_2(\nu_1, \nu_2, \nu_3) \leftarrow \tilde{X}^1A_1(0,0,0)$ transition, observed transition wavenumber (cm^{-1}), calculated Franck-Condon Factors, and fluorescence lifetime measurement (μs) for the $\tilde{A}^1B_2(\nu_1, \nu_2, \nu_3)$ state of TiO_2

Assignment $(0,0,0) \rightarrow (\nu_1, \nu_2, \nu_3)$	Transition wavenumber[a] (cm^{-1})	FCF[b]	τ (μsec)[c]
0, 0, 0	17593	0.0236	1.62(11)
0 ,1, 0	17776.1	0.0421	1.47(07)
0 ,2 ,0	17963	0.0279	1.39(06)
0 ,3, 0	18152.7	0.0076	1.32(05)
0 ,0 ,2	18231	0.0166	1.80(14)
0, 4 ,0	18333.6	0.0005	
0 ,1 ,2	18413.5	0.0297	1.53(08)
1 ,0, 0	18472.9	0.0263	1.23(05)
0 ,2 ,2	18594.4	0.0196	1.25(06)
1, 1, 0	18655.9	0.0462	1.49(13)
1 ,2 ,0	18836.4	0.0279	1.78(15)

[a] Measured maximum intensity peak in the low-resolution LIF spectrum of $\tilde{A}^1B_2$ (ν_1, ν_2, ν_3)$\leftarrow$ $\tilde{X}^1A_1$ (0,0,0) transitions of TiO_2.

[b] Predicted Franck-Condon factors with D_3=0.4Å.

[c] Systematic errors estimated to be ± 0.01 μsec.

5.2. Zirconium Dioxide, ZrO_2

Although considered less important than TiO_2 for catalytic activities, zirconium dioxide, ZrO_2, is however one of the most studies ceramic materials. The gas-phase properties of ZrO_2 have been studied much less than those of TiO_2. The first study on ZrO_2 was done part of a study with TiO_2 [4], where electric field deflection, determined that ZrO_2 is bent and has a dipole moment. In conjunction with an infrared absorption study with TiO_2 [8], the symmetric stretch vibrational frequency, ν_1, and the asymmetric stretch vibrational frequency, ν_3, of ZrO_2 were determined to be 884.3 cm^{-1} and 818.0 cm^{-1}, respectively. Later on, a Fourier transform microwave spectroscopy study of ZrO_2 [5] determined the bond length, $R_{Zr\text{-}O}$, of 1.7710±0.0007 Å, a O-Zr-O bond angle, θ, of 108.11 ± 0.08º, and the electric dipole moment, μ= 7.80 ± 0.02D. Numerous calculation have been carried [21]. A comparison of the ability of the calculation to predict the relative intensity of the photodetactment spectrum of ZrO_2 was made. The highest level prediction using the CCSD(T)/ACVTZ-PP method gives: the bond length of $R_{Zr\text{-}O}$ 1.7776 Å bond angle θ, of 108.26 and the vibrational frequency of the ground state $\tilde{X}^1A_1$ are 909cm^{-1}, 278 cm^{-1}, and 841 cm^{-1} for ω_1, ω_2, ω_3, respectively. My work represents the first report on the electronic transition for ZrO_2 using laser induced fluorescence (LIF) detection.

5.2.1. Observation

The Laser Induced Fluorescence (LIF) spectrum in the region of 17000 cm^{-1}-18800 cm^{-1} is presented in Figure 5.4. Since there is no feature to the red, the first band at 17034 cm^{-1} was assigned as the origin: $\tilde{A}^1B_2(0,0,0) \leftarrow \tilde{X}^1A_1(0,0,0)$. The transition wavenumbers and assignments of $\tilde{A}^1B_2(\nu_1,\nu_2,\nu_3) \leftarrow \tilde{X}^1A_1(0,0,0)$ are given in Table 5.2. The excitation spectra shows strong bands involving the progression on ν_1, ν_2. In additional to the combination band $\tilde{A}^1B_2(0,n\nu_2,n\nu_3) \leftarrow \tilde{X}^1A_1(0,0,0)$ with n=0,1,2… , there are also, surprisingly, progressions on both odd and even quanta of ν_3. The first transition associated with asymmetry stretch mode, ν_3, is tentatively assigned at 17551 cm^{-1} which gives ω_3= 518 cm^{-1}. The symmetric stretch has a spacing of ω_1=819 cm^{-1} similar to TiO_2. The first transition associated with symmetric stretch mode, ν_1, was tentatively assigned to the band at 17873.2 cm^{-1}. There is a progression in the bending mode, ν_2, with the spacing of ω_2 = 149 cm^{-1} built on top of both symmetric stretch, ν_1 and asymmetric stretch, ν_3. Strong spectral feature at 18025.73 is an overlap of the $\tilde{A}^1B_2$ $(0,0,2) \leftarrow \tilde{X}^1A_1(0,0,0)$, $\tilde{A}^1B_2(0,3,1) \leftarrow \tilde{X}^1A_1(0,0,0)$, and $\tilde{A}^1B_2(1,1,0) \leftarrow \tilde{X}^1A_1(0,0,0)$ bands. The spectral feature marked with "*" is the $C^1\Sigma^+$-$X^1\Sigma^+(1,0)$ transition of ZrO, which has been suppressed by adjusting the production condition (i.e.: lowering the laser power of the ablation) and way to collecting the LIF signal (i.e.: use of long gatewidth because $\tau(ZrO) \ll \tau(ZrO_2)$).

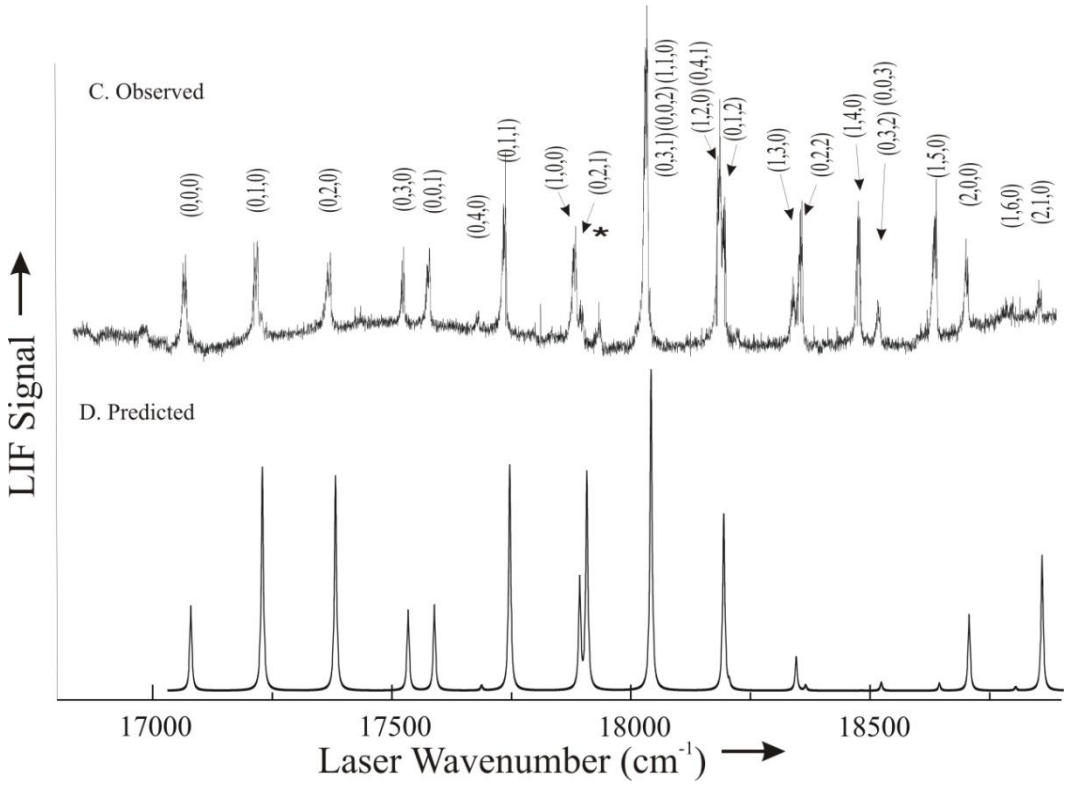

Figure 5.4. The observed laser induced fluorescence (LIF) spectrum of ZrO_2 with the $\tilde{A}^1B_2(\nu_1, \nu_2, \nu_3) \leftarrow \tilde{X}^1A_1(0,0,0)$ assignments (A), and the predicted spectrum of ZrO_2 with vibronic coupling constants c=1.1(B).

The dispersed laser induced fluorescence (DLIF) spectra of thirteen LIF bands were recorded. The DLIF spectra resulting from exciting the $\tilde{A}^1B_2(0,0,0) \leftarrow \tilde{X}^1A_1(0,0,0)$ at 17041 cm^{-1}, $\tilde{A}^1B_2(0,0,1) \leftarrow \tilde{X}^1A_1(0,0,0)$ at 17562 cm^{-1}, and $\tilde{A}^1B_2(1,0,0) \leftarrow \tilde{X}^1A_1(0,0,0)$ at 17870 cm^{-1} bands are presented in Figure 5.5 as A, B, C, respectively. The DLIF spectra are very complicated and have long progression to the red. The DLIF spectrum from $\tilde{A}^1B_2(0,0,0) \leftarrow \tilde{X}^1A_1(0,0,0)$ at 17041cm^{-1} are similar from those observed DLIF spectra of TiO_2 [3], with long progression on bending mode, ν_2. The other DLIF resulting from: $\tilde{A}^1B_2(0,0,1) \leftarrow \tilde{X}^1A_1(0,0,0)$ at 17562 cm^{-1}, and $\tilde{A}^1B_2(1,0,0) \leftarrow \tilde{X}^1A_1$

(0,0,0) at 17870cm^{-1} shows much more complicated spectra. Beside long progression in the bending mode, ν_2, and long progression in the symmetric stretch, ν_1, a long progression in the asymmetric stretch, ν_3, is also observed. All together, 268 dispersed fluorescence shifts were used to map out the energy levels of the $\tilde{X}^1A_1(\nu_1, \nu_2, \nu_3)$ state (Figure 5.5(D)). The bold and/or bold-dash line shows the symmetry forbidden DLIF transition on asymmetric stretch, ν_3.

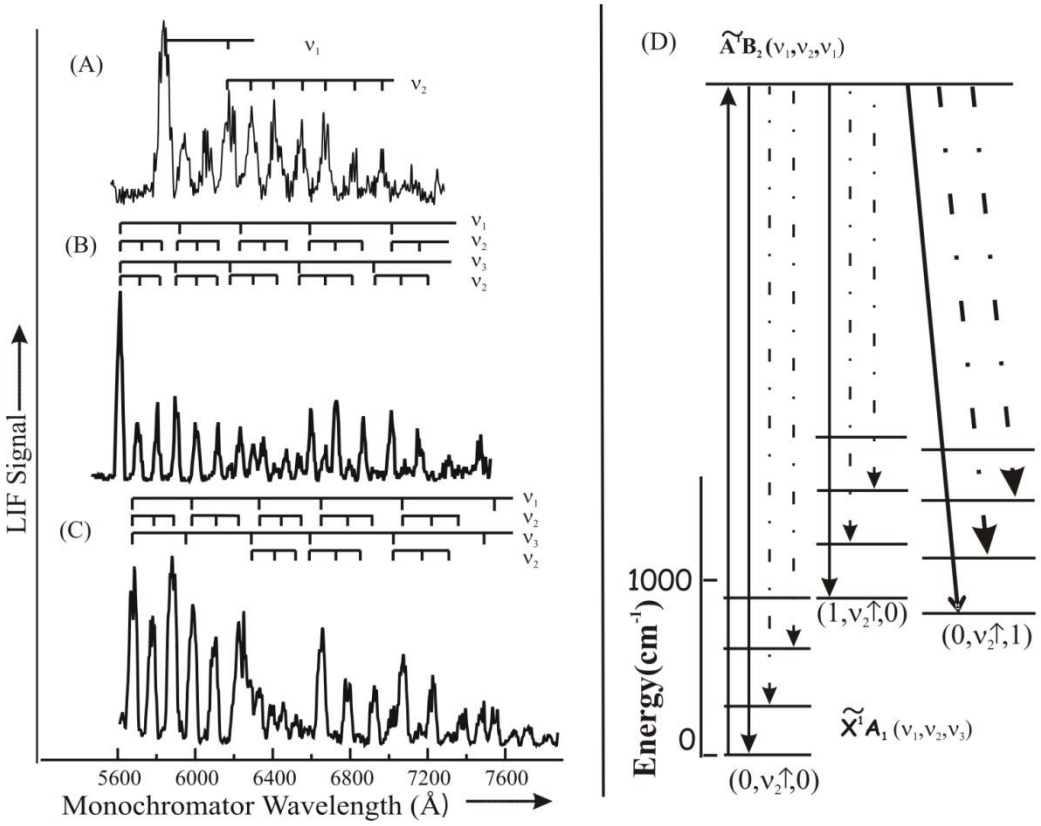

Figure 5.5. Dispersed laser induced fluorescence (DLIF) spectra resulting from excitation of: (A) $\tilde{A}^1B_2(0,0,0) \leftarrow \tilde{X}^1A_1(0,0,0)$ band at 17041cm^{-1}, (B) $\tilde{A}^1B_2(0,0,1) \leftarrow \tilde{X}^1A_1(0,0,0)$

band at 17562 cm^{-1}, and (C) $\tilde{A}^1B_2\,(1,0,0)\leftarrow \tilde{X}^1A_1\,(0,0,0)$ band at 17870cm^{-1}; and (D) the associated energy level of the ground states $\tilde{X}^1A_1$.

Fluorescence decays curves from thirteen LIF bands were recorded. The fluorescence decay curves for the $\tilde{A}^1B_2\,(0,0,0)\leftarrow \tilde{X}^1A_1\,(0,0,0)$ band at 17041 cm^{-1} and for the $\tilde{A}^1B_2\,(0,0,1)\leftarrow \tilde{X}^1A_1\,(0,0,0)$ band at 17561 cm^{-1} are presented in Figure 5.6. It is obvious that the fluorescence lifetime from the $\tilde{A}^1B_2\,(0,0,0)\leftarrow \tilde{X}^1A_1\,(0,0,0)$ band is a much shorter than that for the $\tilde{A}^1B_2\,(0,0,1)\leftarrow \tilde{X}^1A_1\,(0,0,0)$ band.

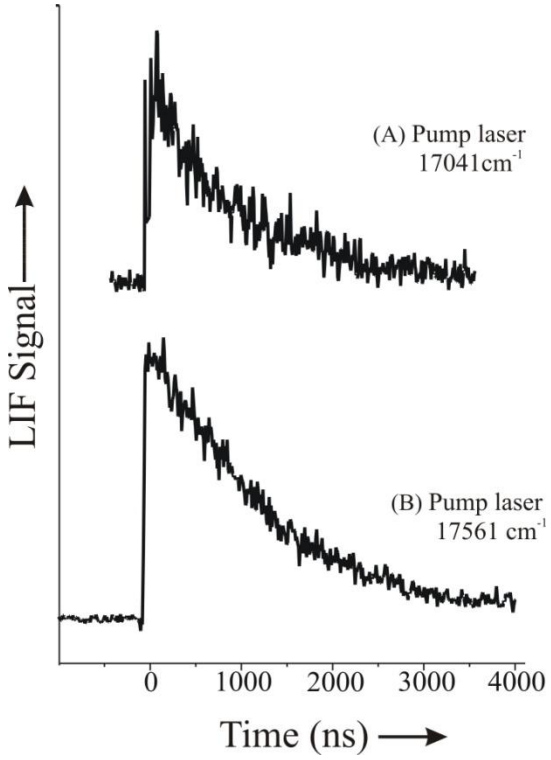

Figure 5.6. Fluoresence decay curves resulting from the excitation of (A) $\tilde{A}^1B_2\,(0,0,0)\leftarrow \tilde{X}^1A_1\,(0,0,0)$ at 17041cm^{-1}, (B) $\tilde{A}^1B_2\,(0,0,1)\leftarrow \tilde{X}^1A_1\,(0,0,0)$ at 17561 cm^{-1}

5.2.2. Analysis

The 268 DLIF spectral features from the thirteen bands of were precisely measured and fit to the phenomenal expression [22]:

$$G(v_1, v_2, v_3) = T_0 + \sum_{i=1\to 3} \varpi_i (v_i + \frac{1}{2}) + \sum_{i=1\to 3} \sum_{k=1\to 3} \chi_{ik} (v_i + \frac{1}{2})(v_k + \frac{1}{2}) \qquad (7)$$

Vibrational frequencies, ω_1, ω_2, and ω_3, of the $\tilde{X}^1A_1$ states were experimentally determined. Various fits were performed and the best fit includes the anhamornicity constants χ_{22} and χ_{33}. The anharmonicity constant on ν_3 mode, χ_{33}=9.86(52) cm^{-1} is unusually large. The standard deviation of the fit (σ=9.45 cm^{-1}) is consistent with the measurement uncertainty. The experimentally determined values of vibrational frequencies of three mode ω_1, ω_2, and ω_3, the anhamornicity constants χ_{22} and χ_{33} and theirs associated errors of the $\tilde{X}^1A_1$ states are listed in Table 5.3.

Fourty features of the LIF excitation spectrum and mass-selected-Resonance-Enhanced Multiphoton Ionization (MS-REMPI) spectrum were measured and assigned. All bands originate from the $\tilde{X}^1A_1(0,0,0)$ state giving 45 excited state levels. The MS-REMPI spectrum came from Prof. Maier's group at University of Basel. Various fits were performed using Equation 7. Those spectral features from LIF spectra were weighted three times more than the REMPI features because LIF spectral features were measured more precisely than those spectral features from REMPI spectrum. Vibrational frequencies, ω_1, ω_2, and ω_3, of the excited $\tilde{A}^1B_2$ states were experimentally determined. The best fit was achieved when the harmonic parameters, ω_1, ω_2, and ω_3, and the anhamornicity parameters χ_{12}, χ_{23}, and χ_{33} were varied. The standard deviation of the fit

(σ=9.64cm^{-1}) is slightly larger than with the measurement uncertainty. Similar to the $\tilde{X}^1A_1$ states, the anharmonicity constant on ν_3 mode, χ_{33}=–8.50(78) cm^{-1}, is large. It also has the opposite sign. The experimentally determined values of vibrational frequencies of three mode ω_1, ω_2, ω_3, the anhamornicity constants χ_{12}, χ_{23}, and χ_{33}, the origin T_e and the associated errors for the $\tilde{A}^1B_2$ states are listed in Table 5.3.

The fluorescence decay curves from thirteen bands were fitted using a single exponential decay function of Equation 1. The data collected after 4 μs were ignored because the molecules drift out of the LIF collecting region. The result of the fitted lifetime measurements and the associated errors are present in Table 5.4.

5.2.3. Normal modes analysis of the $\tilde{X}^1A_1$ *and* $\tilde{A}^1B_2$ *states*

The normal coordinate analyses were performed using the Wilson **GF** matrix approach, which is well documented in the classic text by Wilson, Decius and Cross et. al [23]. However, the mathematical process is not trivial. The Zr-O bond displacements, Δr_1 and Δr_2, and distortion of the O-Zr-O angle, $\Delta\theta$, were used as the internal coordinates. The experimental bond length, $R_{Zr\text{-}O}$ of 1.7710±0.0007 Å and O-Zr-O bond angle, θ, of 108.11 ± 0.08º for the $\tilde{X}^1A_1$ were taken from Ref. 5. The $R_{Zr\text{-}O}$ and θ for the $\tilde{A}^1B_2$ state were taken to be 1.828Å and 99º (estimated values based on visual compare FCFs prediction with the observation). The bond stretches Δr_1, and Δr_2, are motion along the Zr-O bond which described in $\vec{e}_{12}$ and $\vec{e}_{13}$ vectors such that:

$$\vec{e}_{12} = \vec{e}_{13} = \frac{\left[\left(x_O - x_{Zr}\right)\vec{i} + \left(y_O - y_{Zr}\right)\vec{j} + \left(z_O - z_{Zr}\right)\vec{k}\right]}{R_{Zr-O}} \qquad (8)$$

where (x_O, y_O, z_O) and (x_{Zr}, y_{Zr}, z_{Zr}) are Cartesian coordinates of atom O and Zr, respectively and $R_{Zr\text{-}O}$ is the equilibrium bond length. The $\vec{e}_{12}$ and $\vec{e}_{13}$ vectors are normalized unit vectors along the bonds between Zr and O. The valence angle bend, $\Delta\theta$, can be described using $\vec{e}_{12}$ and $\vec{e}_{13}$ such that:

$$\vec{s}_i = \frac{\left(Cos\theta \times \vec{e}_{12} - \vec{e}_{13}\right)}{R_{Zr-O} \times Sin\theta} \tag{9}$$

$$\vec{s}_k = \frac{\left(Cos\theta \times \vec{e}_{13} - \vec{e}_{12}\right)}{R_{Zr-O} \times Sin\theta} \tag{10}$$

and

$$\vec{s}_j = -\left(\vec{s}_i + \vec{s}_k\right). \tag{11}$$

The $\vec{s}_i$, vector at the end of one of the O, is perpendicular with the bond Zr-O, and point outward, this is the direction in which the displacement of O will be the most effective in increasing the bond angle. Similarly, vector $\vec{s}_k$ is the vector at the end of the other oxygen. As the result, vector $\vec{s}_j$ is the vector at Zr atom, has the amplitude as the sum of vectors $\vec{s}_i$ and $\vec{s}_k$ but has the opposite direction. The $\vec{e}_{ij}$ and $\vec{s}$, internal coordinates are selected to optimize the separation of vibrations from rotation. This is done by fulfilling the Eckhart conditions [24].

The **B** matrix elements are the first derivative of each internal coordinate with respect to each of the 3N Cartesian coordinates. For each internal coordinate, there are three component of the **B** matrix correspond to the x,y,z components of Cartesian coordinates of vector $\vec{s}_i$. Therefore, the **B** matrix element can be calculated as using the table:

$$\mathbf{B}= \begin{array}{c|ccccccccc} & x_1 & y_1 & z_1 & x_2 & y_2 & z_2 & x_3 & y_3 & z_3 \\ \Delta r_1 & -\vec{e}_{12} & -\vec{e}_{12} & -\vec{e}_{12} & \vec{e}_{12} & \vec{e}_{12} & \vec{e}_{12} & 0 & 0 & 0 \\ \Delta r_1 & \vec{e}_{13} & \vec{e}_{13} & \vec{e}_{13} & \vec{e}_{13} & \vec{e}_{13} & \vec{e}_{13} & 0 & 0 & 0 \\ \Delta\theta & \vec{s}_j & \vec{s}_j & \vec{s}_j & \vec{s}_i & \vec{s}_i & \vec{s}_i & \vec{s}_k & \vec{s}_k & \vec{s}_k \end{array} \quad (12)$$

The **G** matrix is related to the **B** matrix by $\mathbf{B}.\mathbf{M}^{-1}.\mathbf{B}^{\mathbf{T}}$, where **M** is the diagonal mass matrix. The **G** matrices for $\tilde{X}^1A_1$ and $\tilde{A}^1B_2$ become:

$\mathbf{G}(\tilde{X}^1A_1)=$

$$\begin{vmatrix} 0.07364\ \text{amu}^{-1} & -0.00174\text{amu}^{-1} & -0.006010\ \text{amu}^{-1}\text{Å}^{-1} \\ -0.00174\text{amu}^{-1} & 0.07364\ \text{amu}^{-1} & -0.006010\ \text{amu}^{-1}\text{Å}^{-1} \\ -0.006010\ \text{amu}^{-1}\text{Å}^{-1} & -0.006010\ \text{amu}^{-1}\text{Å}^{-1} & 0.04512\ \text{amu}^{-1}\text{Å}^{-2} \end{vmatrix} \quad (13)$$

and $\mathbf{G}\ (\tilde{A}^1B_2)=$

$$\begin{vmatrix} 0.07364\ \text{amu}^{-1} & -0.003457\ \text{amu}^{-1} & -0.005969\ \text{amu}^{-1}\text{Å}^{-1} \\ -0.003457\ \text{amu}^{-1} & 0.07364\ \text{amu}^{-1} & -0.005969\ \text{amu}^{-1}\text{Å}^{-1} \\ -0.005969\ \text{amu}^{-1}\text{Å}^{-1} & -0.005969\ \text{amu}^{-1}\text{Å}^{-1} & 0.04917\ \text{amu}^{-1}\text{Å}^{-2} \end{vmatrix} \quad (14)$$

The **G** matrices for the $\tilde{X}^1A_1$ and $\tilde{A}^1B_2$ states in a symmetrized coordinate system (i.e. one that transforms according to the irreducible representative of C_{2v} pointgroup) are related to those in the Δr_1, Δr_2 and $\Delta\theta$ displacement coordinated system by:

$$\mathbf{G_{sym}} = \mathbf{U}\cdot\mathbf{G}\cdot\mathbf{U}^{\mathbf{T}} \quad (15)$$

where **U** is:

$$\mathbf{U}= \begin{vmatrix} 1/\sqrt{2} & 1/\sqrt{2} & 0 \\ 0 & 0 & 1 \\ 1/\sqrt{2} & -1/\sqrt{2} & 0 \end{vmatrix} \quad (16)$$

The unsymmetrized force matrices, **F,** for the $\tilde{X}^1A_1$ and $\tilde{A}^1B_2$ states, are constructed using the stretch force constant, f_r, stretch-stretch coupling force constant, f_{rr}, bending force constant, f_θ, and bend-stretch coupling force constant, $f_{\theta r}$. The

unsymmetrized and symmetrized **F** matrices for the $\tilde{X}^1A_1$ and $\tilde{A}^1B_2$ states related to one another by using the transformation,

$$\mathbf{F_{sym}=U.F.U^T} \tag{17}$$

where

$$\mathbf{F}= \begin{vmatrix} f_r + f_{rr} & \frac{2}{\sqrt{2}} f_{\theta r} & 0 \\ \frac{2}{\sqrt{2}} f_{\theta r} & f_\theta & 0 \\ 0 & 0 & f_r - f_{rr} \end{vmatrix} \tag{18}$$

$$\mathbf{F_{sym}}= \begin{vmatrix} f_r & f_{rr} & f_{\theta r} \\ f_{rr} & f_r & f_{\theta r} \\ f_{\theta r} & f_{\theta r} & f_\theta \end{vmatrix} \tag{19}$$

The secular equation can be described as **GF**, for nonsymmetrized form and $\mathbf{GF_{sym}}$, for symmetrized form. The geometry matrix, **G**, is defined as the matrix that gives the kinetic energy directly in term of momenta [23], and the force matrix, **F**, is related to potential energy, $\mathbf{F}=\delta(2\mathbf{V})/\delta\boldsymbol{Q}$, where 2V is potential energy. The eigenvalues of the secular equation of the product matrix of **G** and **F**, **GF** or $\mathbf{GF_{sym}}$ related to vibrational frequencies:

$$\left|\mathrm{GF} - \lambda_n E\right| = 0, \tag{20}$$

where $\lambda_n = 4\pi^2 \upsilon_n^{\,2}$, ν_n is the harmonic vibrational frequencies. $\mathbf{GF_{sym}}$ matrices for the $\tilde{X}^1A_1$ and $\tilde{A}^1B_2$ states are not a symmetric matrices, however it is separated into a 2×2 and a 1×1 matrix. Therefore, the asymmetric stretch mode, b_1, can be separated. From the

observed harmonic frequencies of asymmetric stretch mode, ν_3 the symmetrized force component $f_r - f_{rr}$ can be directly determined for both the $\tilde{X}^1A_1$ and $\tilde{A}^1B_2$ states.

There are four force constants and only three vibrational frequencies, ω_i. therefore, some assumptions need to be made. In the $\tilde{X}^1A_1$ state, because $\omega_1(898cm^{-1}) \cong \omega_3(808cm^{-1})$, it is realistic to assume that the stretch-stretch coupling force constant, f_{rr}, is zero. Therefore, f_r=4.9863mdyn Å^{-1} is derived from the measured ω_3. The $\mathbf{F_{sym}}$ for the $\tilde{X}^1A_1$ state became:

$$\mathbf{Fsym}(\tilde{X}^1A_1) = \begin{vmatrix} 4.9863\text{mdyn Å}^{-1} & \frac{2}{\sqrt{2}} f_{\theta r} & 0 \\ \frac{2}{\sqrt{2}} f_{\theta r} & f_\theta & 0 \\ 0 & 0 & 4.9863\text{mdyn Å}^{-1} \end{vmatrix} \quad (21)$$

The f_θ, and $f_{\theta r}$ can be determined by setting the eigenvalues of 2×2 matrix separated from $\mathbf{F_{sym}}(\tilde{X}^1A_1)$ to be equal to the vibrational frequencies of the symmetric stretch mode, ω_1, and the bending mode, ω_2.

$$\mathbf{F_{sym}}(\tilde{X}^1A_1) = \begin{vmatrix} 4.9863\text{mdyn Å}^{-1} & -2.5169\text{ mdyn Å}^{-1}\text{rad}^{-1} & 0 \\ -2.5169\text{ mdyn Å}^{-2}\text{rad}^{-1} & 2.7351\text{mdyn Å}^{-2}\text{rad}^{-1} & 0 \\ 0 & 0 & 4.9863\text{mdyn Å}^{-1} \end{vmatrix} \quad (22)$$

Using the relationship between **F** and $\mathbf{F_{sym}}$ from Eqn(17), the $\mathbf{F}(\tilde{X}^1A_1)$ became:

$$\mathbf{F}(\tilde{X}^1A_1)= \begin{vmatrix} 4.9863 \text{ mdyn Å}^{-1} & 0 & 1.7797 \text{ mdyn Å}^{-1} \text{ radian}^{-1} \\ 0 & 4.9863 \text{ mdyn Å}^{-1} & 1.7797 \text{ mdyn Å}^{-1} \text{ radian}^{-1} \\ 1.7797 \text{ mdyn Å}^{-1} \text{ radian}^{-1} & 1.7797 \text{ mdyn Å}^{-1} \text{ radian}^{-1} & 2.7351 \text{ mdyn Å}^{-1} \text{ radian}^{-2} \end{vmatrix} \quad (23)$$

In the $\tilde{A}^1B_2$ state, because $\omega_1(819\text{cm}^{-1})$ is much greater than $\omega_3(518\text{cm}^{-1})$, the realistic assumption is that bend-stretch coupling force constant, $f_{\theta r}$, is zero. The $\mathbf{F_{sym}}$ for the $\tilde{A}^1B_2$ state became:

$$\mathbf{F_{sym}}(\tilde{A}^1B_2)= \begin{vmatrix} f_r + f_{rr} & 0 & 0 \\ 0 & f_\theta & 0 \\ 0 & 0 & 2.0967 \text{ mdyn Å}^{-1} \end{vmatrix} \quad (24)$$

The f_θ, and $f_r + f_{rr}$ can be determined by setting the eigenvalues of 2×2 matrix separated from $\mathbf{F_{sym}}(\tilde{A}^1B_2)$ to be equal to observed the vibrational frequencies of the symmetric stretch mode, ω_1, and the bending mode, ω_2. Therefore, the $\mathbf{F_{sym}}(\tilde{A}^1B_2)$ is determined to be:

$$\mathbf{F_{sym}}(\tilde{A}^1B_2)= \begin{vmatrix} 5.4908 \text{ mdyn Å}^{-1} & 0 & 0 \\ 0 & 0.2967 \text{ mdyn Å}^{-1} \text{ radian}^{-2} & 0 \\ 0 & 0 & 2.0967 \text{ mdyn Å}^{-1} \end{vmatrix} \quad (25)$$

The unsymmetrized force matrix for the $\tilde{A}^1B_2$, and $\mathbf{F}(\tilde{A}^1B_2)$, is:

$$\mathbf{F}(\tilde{A}^1B_2)= \begin{vmatrix} 3.7938 \text{ mdyn Å}^{-1} & 1.6971\text{mdyn Å}^{-1} & 0 \\ 1.6971\text{mdyn Å}^{-1} & 3.7938\text{mdyn Å}^{-1} & 2.1099 \text{ mdyn Å}^{-1} \text{ radian}^{-1} \\ 0 & 0 & 0.29667\text{mdyn Å}^{-1} \text{ radian}^{-2} \end{vmatrix} \quad (26)$$

Each eigenvalue, λ_n, there is a corresponding eigenvector. A set of column eigenvectors defines matrices **V** as:

V($\tilde{X}^1A_1$)=

	Q_1	Q_2	Q_3
Δr_1	-0.6275	0.3751	0.7071
Δr_2	-0.6275	0.3751	-0.7071
$\Delta\theta$	0.461	0.8477	0

(27)

V($\tilde{A}^1B_2$)=

	Q_1	Q_2	Q_3
Δr_1	-0.7019	0.00467	0.7071
Δr_2	-0.7019	0.00467	-0.7071
$\Delta\theta$	0.1213	0.9999	0

(28)

The internal symmetry coordinates, S, are related to the normal coordinates, Q, by

$$\mathbf{S=L.Q} \tag{29}$$

where **L** and **V** differ only by a normalization constant [25] chosen to assure that $\mathbf{L.L^T}$ = **G.** The normalized eigenvectors, **L**, is defined as:

$$\mathbf{L=V\times N} \tag{30}$$

with

$$\mathbf{N}=\left[\mathbf{V^{-1}}\cdot\mathbf{G}\cdot\left(\mathbf{V^T}\right)^{-1}\right]^{1/2} \tag{31}$$

The results are:

L($\tilde{X}^1A_1$)=

	Q_1	Q_2	Q_3
Δr_1	-0.1688	0.08133	0.1963
Δr_2	-0.1688	0.08133	-0.1963
$\Delta\theta$	0.124	0.1838	0

(32)

L($\tilde{A}^1 B_2$)=

	Q_1	Q_2	Q_3
Δr_1	0.1896	0.00098	0.1941
Δr_2	0.1896	0.00098	-0.1941
$\Delta\theta$	-0.03278	0.2099	0

(33)

The atomic displacement matrix, **AA,** is calculated by:

$$AA = M^{-1} \cdot B^T . (L^{-1})^T \ , \tag{34}$$

AA($\tilde{X}^1 A_1$)=

	Q_3	Q_2	Q_1
y_{Zr}	0	0	-0.0459
x_{Zr}	-0.0221	-0.0493	0
z_{Zr}	0	0	0
y_{O2}	0.1614	-0.0722	0.1289
x_{O2}	0.062	0.1386	-0.0935
z_{O2}	0	0	0
y_{O1}	-0.1614	0.07218	0.1289
x_{O1}	0.062	0.1386	0.09346
z_{O1}	0	0	0

(35)

and **AA**($\tilde{A}^1 B_2$)=

	Q_3	Q_2	Q_1
y_{Zr}	0	0	-0.0436
x_{Zr}	-0.0381	0.03829	0
z_{Zr}	0	0	0
y_{O2}	0.1253	0.1247	0.1224
x_{O2}	0.1071	-0.1076	-0.1045
z_{O2}	0	0	0
y_{O1}	-0.1253	-0.1247	0.1224
x_{O1}	0.1071	-0.1076	0.1046
z_{O1}	0	0	0

(36)

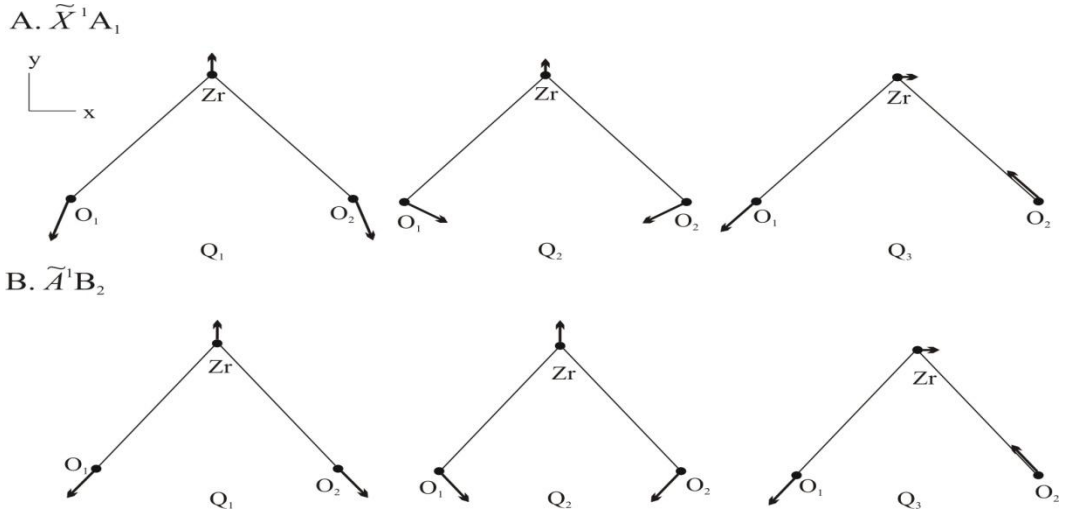

Figure 5.7. Displacement vector of the three vibrational modes of $\tilde{X}^1A_1$ (A) and $\tilde{A}^1B_2$ (B) states using experimentally derived vibrational frequency

The displacement vectors for the three vibrational modes of the $\tilde{X}^1A_1$ and $\tilde{A}^1B_2$ states are presented in Figure 5.7(A) and Figure 5.7(B), respectively. The *Mathematica* notebook for the normal mode analysis is presented in APPENDIX B. Figure 5.7 **(**A) and Figure 5.7(B) with arrows attached to individual atoms, indicating the unit displacement along that mode. The arrows are multiply by two to emphasize the normal modes. These normal coordinate **Q** will now be used to calculate FCFs.

5.2.4. Discussion

Treating the Duschinsky effect involves expansion of the potential energy of the excited state in terms of the ground state normal coordinate displacements, **Q**:

$$\mathbf{Q}(\tilde{A}^1B_2) = \mathbf{J}.\,\mathbf{Q}(\tilde{X}^1A_1) + \mathbf{D} \qquad (37)$$

where **J** is the Duschinsky rotational matrix and column vector **D** defined the linear transformation.

A linear transformation of an arbitrary distortion between $\tilde{X}^1A_1$ and $\tilde{A}^1B_2$ states in cartesian coordinate, **X** can be describe using:

$$\mathbf{X}(\tilde{A}^1B_2)=\mathbf{Z}.\ \mathrm{X}(\tilde{X}^1A_1)+\mathbf{R} \qquad (38)$$

where **R** is the change in equilibrium geometry between $\tilde{X}^1A_1$ and $\tilde{A}^1B_2$ states. In many cases **Z**=1 in order to satisfy the Eckhart conditions[26].

The cartesian coordinates, **X** then can be transformed to internal symmetry coordinates, **S**, and to the normal coordinates, **Q** by matrix **L** and matrix **B** described in subchapter 5.2.3 (normal mode analysis). The atomic displacement matrix, **AA,** is calculated by Equation (33) related between Cartesian coordinate, **X**, to normal coordinates, **Q**. Therefore, the 3×3 Duschinsky rotation matrix, **J** , is given by [26]:

$$\mathbf{J} = \left(\mathbf{L}(\tilde{A}^1B_2)\cdot\mathbf{B}(\tilde{A}^1B_2)\right)\cdot M^{-1}\cdot\left(\left(\mathbf{L}(\tilde{X}^1A_1)\right)^{-1}\cdot\mathbf{B}(\tilde{X}^1A_1)\right)^T. \qquad (39)$$

J is block diagonal of a 2×2 and 1×1 matrix, due to the C_{2v} symmetry:

$$\mathbf{J} = \begin{vmatrix} 0.935 & 0.3546 & 0 \\ -0.3546 & 0.935 & 0 \\ 0 & 0 & 0.9971 \end{vmatrix} \qquad (40)$$

Interestingly, J_{33} is not unity implying that the ν_3 vibrational mode couples with rotation about the *c*-principal axis, both having b_2 symmetry [19]. Even though the Eckhart conditions were met, the separation between rotation and vibration was not perfect.

The Duschinsky displacement vector, **D**, is given by [26]:

$$\mathbf{D} = \left(\mathbf{L}(\tilde{A}^1B_2)\cdot\mathbf{B}(\tilde{A}^1B_2)\right)^{-1}\left(\mathbf{R_{eq}}(\tilde{A}^1B_2)-\mathbf{R_{eq}}(\tilde{X}^1A_1)\right), \qquad (41)$$

where $\mathbf{R_{eq}}$ is the 9×1 vector of equilibrium Cartesian center of mass coordinates.

The FCF problem separates into a 2-dimensional problem for the two a_1-symmetry modes and a 1-dimensional problem for the b_2-symmetry mode as in Equation 2. FCF calculation is similar to those calculated for TiO_2. However, using the expressions from Chang et al [18, 19], the relative intensity for those odd-ν_3 transitions are predicted to be zero. The observation of even-ν_3 transitions from $\tilde{X}^1A_1$ (0,0,0) ground states can be easily described using symmetry (e.g $b_2 \times b_2 \in a_1$). The observation of odd-ν_3 transitions on $\tilde{A}^1B_2$ states can be explained by introducing the vibronic coupling term between the $\tilde{A}^1B_2$ and yet to be observed $\tilde{B}^1A_1$ states. This mechanism that allowed the strongly observed odd-ν_3 transitions to have intensities comparable with the even-ν_3 transitions was first proposed in the interpretation of the electronic spectra of SO_2 [20]. In the case of ZrO_2, the excited electronic states is assigned as $\tilde{A}^1B_2$ (i.e. mainly has B_2 character). However, there is maybe strong mixing with $\tilde{B}^1A_1$ state, therefore the eigenstates of $\tilde{A}^1B_2$ become: $\tilde{\mathrm{A}}^1\mathrm{B}_2 = |\text{mixed } A_1 / B_2\rangle$. The transition matrix element from $\tilde{X}^1A_1$ (0,0,0) state to the mixed excited stated has the form: $\langle \text{mixed } A_1/\mathrm{B}_2 |\boldsymbol{\mu}| A_1 \rangle$. The transition dipole moment $\boldsymbol{\mu}$ can be written as the product of $\boldsymbol{\mu_{10}}$, electronic transition moment of $\tilde{A}^1B_2 \leftarrow \tilde{X}^1A_1$, and $\boldsymbol{\mu_{20}}$, electronic transition moment of $\tilde{B}^1A_1 \leftarrow \tilde{X}^1A_1$ with some adjustable parameters. The excitation spectra can be explained: $\langle \text{mixed } A_1/\mathbf{B_2} |\boldsymbol{\mu_{10}}| A_1 \rangle$ for the even-ν_3 transitions and with the "intensity borrowing" from the $\tilde{B}^1A_1$ state, $\langle \text{mixed } \boldsymbol{A_1}/\mathrm{B}_2 |\boldsymbol{\mu_{20}}| A_1 \rangle$ for the odd-ν_3 transitions become nonzero.

The excitation spectrum of $\tilde{A}^1B_2 \leftarrow \tilde{X}^1A_1$ transitions can be described using perturbation theory. To a first approximation, the transition moment is proportional to the square of FCF:

$$I \cong \left|\left\langle \Theta_v(\tilde{A}^1B_2)\middle|\left\langle \Phi_1(\tilde{A}^1B_2)\middle|\mu\middle|\Phi_1(\tilde{X}^1A_1)\right\rangle\middle|\Theta_v(\tilde{X}^1A_1)\right\rangle\right|^2, \quad (42)$$

where and Φ and Θ are electronic and vibrational wave function, respectively. Since the electronic $\tilde{A}^1B_2$ state is couple with electronic $\tilde{B}^1A_1$ state, Φ becomes:

$$\Phi_1(\tilde{A}^1B_2) = \Phi_1^0(\tilde{A}^1B_2) + \frac{\lambda_{21}Q_3}{E(\tilde{A}^1B_2) - E(\tilde{B}^1A_1)}\Phi_2^0(\tilde{B}^1A_1), \quad (43)$$

where

$$\lambda_{21} \equiv \left\langle \Phi_2^0(\tilde{B}^1A_1)\middle|(\partial V/\partial Q_3)_0\middle|\Phi_1^0(\tilde{A}^1B_2)\right\rangle. \quad (44)$$

The coefficient, λ_{21}, is the vibronic coupling parameter between $\tilde{A}^1B_2$ and $\tilde{X}^1A_1$ states with the vibronic coupling term, $\partial V/\partial Q_3$. The magnitude of the coefficient, λ_{21}, was adjusted from visual comparisons of predicted and observed spectra. Note the mixing term (second term of equation 43) depends on the difference between the energy of $\tilde{A}^1B_2$ and $\tilde{B}^1A_1$ states. An estimate of ΔE (≈6970cm^{-1}) between $\tilde{A}^1B_2$ and $\tilde{B}^1A_1$ states was made using the result of a TD-DFT/LannaL2DZ calculation (in collaboration with National Chiao Tung University) [27]. The transition dipole moment between $\tilde{A}^1B_2$ and $\tilde{X}^1A_1$ states then become:

$$\left\langle \Phi_1(\tilde{A}^1B_2)\middle|\mu\middle|\Phi_1(\tilde{X}^1A_1)\right\rangle = \left\langle \left(\Phi_1^0(\tilde{A}^1B_2) + \frac{\lambda_{21}Q_3}{E(\tilde{A}^1B_2) - E(\tilde{B}^1A_1)} \Phi_2^0(\tilde{B}^1A) \right) \middle| \boldsymbol{\mu} \middle| \Phi_1(\tilde{X}^1A_1) \right\rangle$$

$$= \left\langle \left(\Phi_1^0(\tilde{A}^1B_2)\right) \middle| \boldsymbol{\mu} \middle| \Phi_1(\tilde{X}^1A_1) \right\rangle + \frac{\lambda_{21}Q_3}{E(\tilde{A}^1B_2) - E(\tilde{B}^1A_1)} \left\langle \left(\Phi_2^0(\tilde{B}^1A)\right) \middle| \boldsymbol{\mu} \middle| \Phi_1(\tilde{X}^1A_1) \right\rangle \qquad (45)$$

$$= \boldsymbol{\mu}_{\mathbf{10}}^{\mathbf{0}} + \frac{\lambda_{21}Q_3}{E(\tilde{A}^1B_2) - E(\tilde{B}^1A_1)} \boldsymbol{\mu}_{\mathbf{20}}^{\mathbf{0}},$$

where $\mathbf{Q_3}$ is normal coordinate associated with asymmetric stretching of b_2 symmetry. The square of the transition moment then became:

$$\begin{aligned}
&\left| \left\langle \Theta_v(\tilde{A}^1B_2) \middle| \left\langle \Phi_1(\tilde{A}^1B_2) \middle| \mu \middle| \Phi_1(\tilde{X}^1A_1) \right\rangle \middle| \Theta_v(\tilde{X}^1A_1) \right\rangle \right| \\
&= \left| \left\langle \upsilon_1'\upsilon_2'\upsilon_3' \middle| \boldsymbol{\mu}_{\mathbf{10}}^{\mathbf{0}} + \frac{\lambda_{21}Q_3}{E(\tilde{A}^1B_2) - E(\tilde{B}^1A_1)} \boldsymbol{\mu}_{\mathbf{20}}^{\mathbf{0}} \middle| 000 \right\rangle \right| \\
&= \left| \boldsymbol{\mu}_{\mathbf{10}}^{\mathbf{0}} \left\langle \upsilon_1'\upsilon_2'\upsilon_3' \middle| 000 \right\rangle + \frac{\lambda_{21}}{E(\tilde{A}^1B_2) - E(\tilde{B}^1A_1)} \boldsymbol{\mu}_{\mathbf{20}}^{\mathbf{0}} \left\langle \upsilon_1'\upsilon_2'\upsilon_3' \middle| Q_3 \middle| 000 \right\rangle \right| \\
&= \left| \boldsymbol{\mu}_{\mathbf{10}}^{\mathbf{0}} \left\langle \upsilon_1'\upsilon_2'\upsilon_3' \middle| 000 \right\rangle + \frac{1}{\sqrt{2}} \frac{\lambda_{21}}{E(\tilde{A}^1B_2) - E(\tilde{B}^1A_1)} \boldsymbol{\mu}_{\mathbf{20}}^{\mathbf{0}} \left\langle \upsilon_1'\upsilon_2'\upsilon_3' \middle| 001 \right\rangle \right|
\end{aligned} \qquad (46)$$

$$\begin{aligned}
&\left| \left\langle \Theta_v(\tilde{A}^1B_2) \middle| \left\langle \Phi_1(\tilde{A}^1B_2) \middle| \mu \middle| \Phi_1(\tilde{X}^1A_1) \right\rangle \middle| \Theta_v(\tilde{X}^1A_1) \right\rangle \right|^2 \\
&\approx |\boldsymbol{\mu}_{\mathbf{10}}|^2 \left| \langle v_1'v_2' \,|\, 00 \rangle \right|^2 \left| \langle v_3' \,|\, 0 \rangle \right|^2 + \frac{1}{2} \left(\frac{\lambda_{21}}{E(\tilde{A}^1B_2) - E(\tilde{B}^1A_1)} \right)^2 |\boldsymbol{\mu}_{\mathbf{20}}|^2 \left| \langle v_1'v_2' \,|\, 00 \rangle \right|^2 \left| \langle v_3' \,|\, 1 \rangle \right|^2
\end{aligned} \qquad (47)$$

According to Equation 45, both even-ν_3 odd-ν_3 transitions can be predicted by symmetry. The *Mathematica* notebook for this prediction is given in APPENDIX C.

The FCFs were predicted using $c = \frac{1}{2}\left(\frac{\lambda_{21}}{E(\tilde{A}^1B_2) - E(\tilde{B}^1A_1)} \right)^2$ =1.1, and the structure of the $\tilde{A}^1B_2$ states as those are in normal mode analysis in section *5.3.2* in this chapter. The optimized value for c and $R_{Zr\text{-}O}$ and θ are 1.1, 1.828Å and 99˚ obtained from visual comparison between predicted and observed spectra. The predicted and observed

laser induced fluorescence (LIF) spectra from 17000 cm^{-1}-18800 cm^{-1} are present in Figure 5.4(B). Overall, the predicted LIF spectrum is in good agreement with the observations except for those spectral features in higher wavenumber. The REMPI spectra and the predicted spectra are show in Figure 5.8. The relative intensities of the higher wavenumber portion of the REMPI spectrum are not perfectly predicted. One of explanations is that the vibronic coupling between $\tilde{A}^1B_2$ and $\tilde{B}^1A_1$ states is expected to be stronger at the higher wavenumber because ΔE is smaller. At higher wavenumber, there is more of the $\tilde{B}^1A_1$ state character mixed into the normal $\tilde{A}^1B_2$ state. Another explanation is anharmonicity of the potential energy, since FCFs calculation here uses simple analytical expression under the assumption of both $\tilde{A}^1B_2$ and $\tilde{X}^1A_1$ potentials can be modeled as displaced and distorted harmonic oscillators. The experimentally determined anharmonicity constants in both $\tilde{A}^1B_2$ and $\tilde{X}^1A_1$ states, as seen in from Table 5.3, are evidences supporting the later explanation.

Finally, the trend in the measured fluorescence radiative lifetime, τ, of thirteen LIF bands were plotted out in Figure 5.9. The trend in the fluorescence lifetimes is completely different from those observed TiO_2. Overall, the fluorescence lifetimes increase with laser energy. For those bands having no quanta of the symmetric stretch and asymmetric stretch, the fluorescence lifetime increase with the increasing excitation of the bending mode. For example: $\tilde{A}^1B_2$ (0,0,0)(τ=0.900(32)μs) increases to the $\tilde{A}^1B_2$ (0,3,0)(τ=1.264(25) μs). However, the trend in the fluorescence lifetime dramatically changes for the combination band. If one quantum of the symmetric stretch and asymmetric stretch were added, the trend is decreasing with the increasing in the bending

mode ν_2. For example: $\tilde{A}^1B_2$ (0,0,1)(τ=1.391(28)μs) decreases to the $\tilde{A}^1B_2$ (0,3,1)(τ=1.301(18) μs) and $\tilde{A}^1B_2$ (1,2,0)(τ=1.387(19)μs) decreases to the $\tilde{A}^1B_2$ (1,5,0)(τ=1.227(30) μs). This strange behavior in the trend of the lifetime measurement shows the strong evidence of the ν_3 induced vibronic coupling in the excited state.

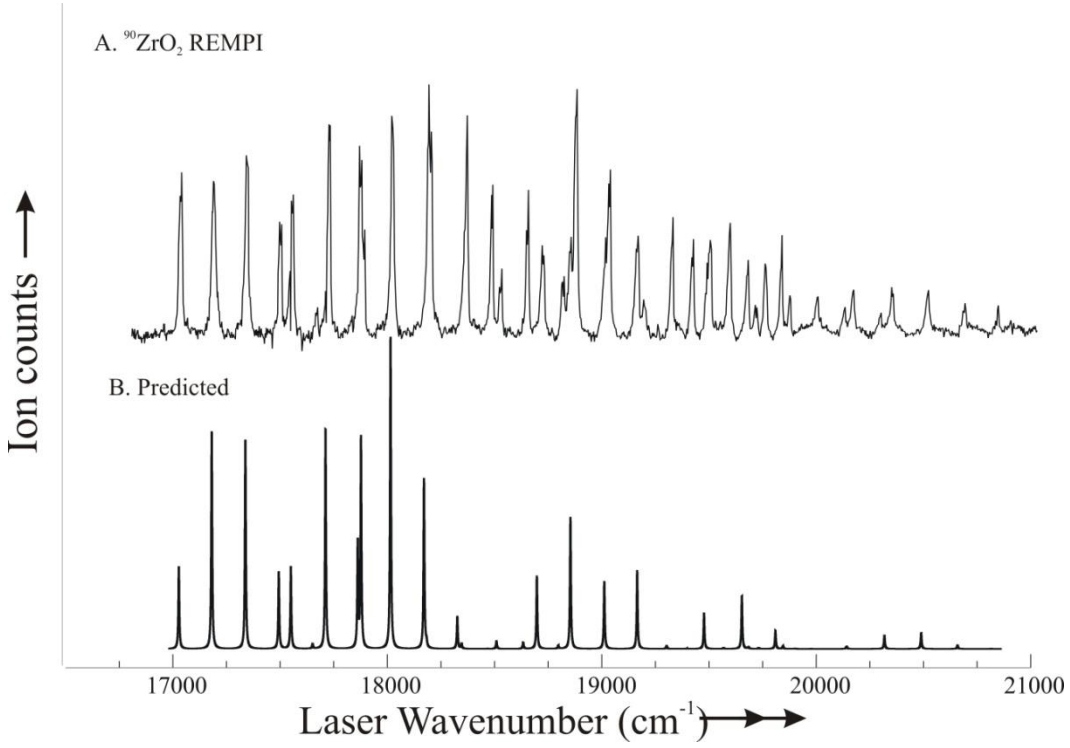

Figure 5.8. The observed mass selected resonance enhanced multiphoton ionization (REMPI) spectrum of ZrO_2 (University of Basel**)** (A), and the predicted spectrum of ZrO_2 with vibronic coupling constants c=1.1(B).

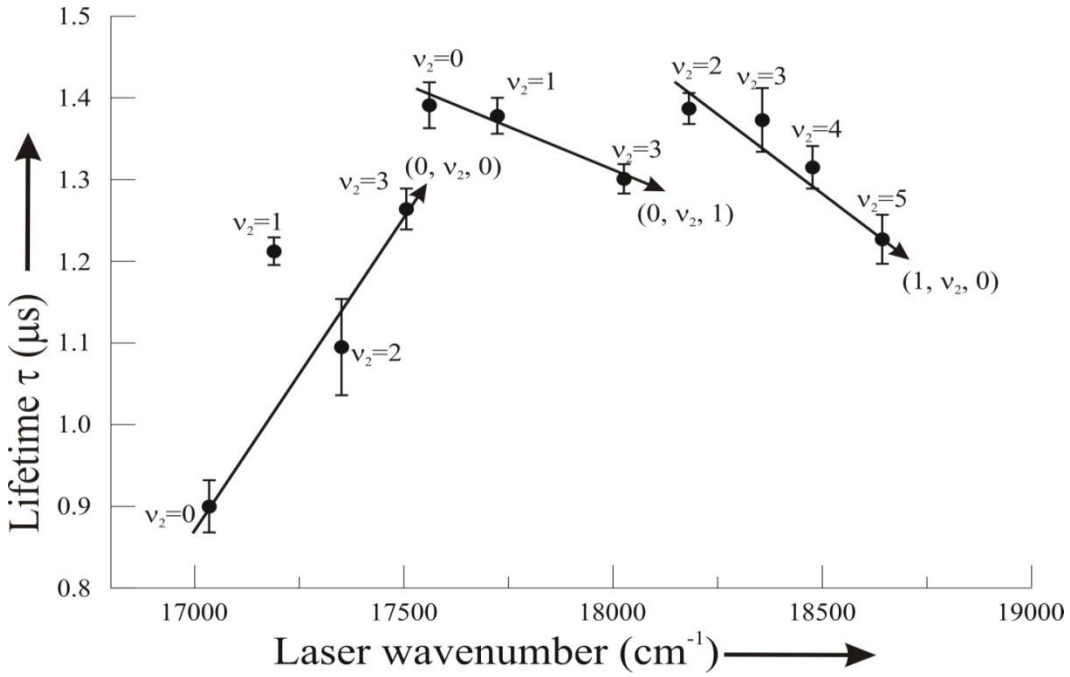

Figure 5.9. Trend in fluorescence lifetime for $\tilde{A}^1B_2$ (ν_1, ν_2, ν_3)← $\tilde{X}^1A_1$ (0,0,0) transitions of ZrO_2.

Table 5.2. The, assignments, observed and calculated transition wavenumbers (cm^{-1}) and Franck-Condon Factors calculations for for the $\tilde{A}^1B_2$ state of ZrO_2.

Assignment (ν_1, ν_2, ν_3)	Observed (cm^{-1})	Obs-calc (cm^{-1})	FCF
(0, 0, 0)	17041.11	-9.3183	0.0522577
(0, 1, 0)	17194.11	-8.6191	0.112915
(0, 2, 0)	17350.6	-4.43	0.0798167
(0, 3, 0)	17506.01	-1.3208	0.0159935
(0, 0, 1)	17562.13	7.5121	0.0527457
(0, 4, 0)	17663.25	3.6184	6.541E-05
(0, 1, 1)	17723.38	12.0307	0.113969
(1, 0, 0)	17873.16	4.0002	0.0410036
(0, 2, 1)	17888.37	20.2894	0.0805619
(0, 0, 2)	18025.73	-15.744	0.0161429
(0, 3, 1)	18025.73	0.918	0.112915
(1, 1, 0)	18025.73	1.4024	0.0012488
(1, 2, 0)	18181.36	1.8645	6.602E-05
(0, 4, 1)	18181.36	-0.1834	0.113161

(0, 1, 2)	18193.19	-9.4459	0.0026984
(1, 3, 0)	18336.4	1.7367	0.0402896
(0, 2, 2)	18356.55	-7.2479	0.0019074
(1, 4, 0)	18476.25	-13.5811	0.0014964
(0, 0, 3)	18518.42	7.4234	0.0038221
(0, 3, 2)	18518.42	-6.5398	0.0037515
(1, 5, 0)	18642.77	-2.229	0.0024368
(2, 0, 0)	18706.34	18.4488	0.0798167
(1, 6, 0)	18806	5.8332	0.0007937
(2, 1, 0)	18862.56	16.6339	0.0641282
(2, 2, 0)	19020	16.039	0.0810465
(2, 3, 0)	19173	11.0042	0.0424394
(2, 0, 1)	19173	-19.0808	0.0189339
(2, 4, 0)	19310	-10.0307	0.005674
(0, 0, 5)	19404	5.9586	0.0002259
(3, 0, 0)	19484	-22.6226	0.0064651
(0, 1, 5)	19575	2.505	0.0004882
(3, 1, 0)	19660	-7.5245	0.0259831
(2, 0, 2)	19691	12.0631	0.0004483
(0, 2, 5)	19738	-8.9486	0.0003451
(3, 2, 0)	19816	-12.4265	0.0401142
(2, 1, 2)	19851	5.1671	0.0015325
(0, 3, 5)	19907	-14.4022	6.914E-05
(3, 3, 0)	19982	-7.3284	0.0279659
(0, 4, 5)	20107	11.1442	3E-08
(3, 4, 0)	20147	-3.2303	0.0069925
(0, 5, 5)	20274	3.6907	0.0000117
(4, 0, 0)	20323	-2.3541	0.0018529
(4, 1, 0)	20494	4.877	0.008542
(4, 2, 0)	20663	10.1081	0.0155793
(4, 3, 0)	20819	2.3391	0.0136159
Rms =9.64 cm^{-1}		σ= 10.02 cm^{-1}	

Table 5.3. Vibrational constants for the $\tilde{X}^1A_1$ and excited $\tilde{A}^1B_2$ of ZrO_2

$\tilde{X}^1A_1$		$\tilde{A}^1B_2$	
Parameter	Value (cm^{-1})	Parameter	Value (cm^{-1})
ω_1	898(1)	T_{000}	15311(8)
ω_2	287(2)	ω_1	819(3)

ω_3	808(3)	ω_2	149(3)
χ_{33}	9.86(52)	ω_3	518(4)
χ_{22}	3.52(48)	χ_{12}	2(1)
		χ_{23}	4.43(75)
		χ_{33}	-8.50(78)

Table 5.4. Lifetime measurements $\tilde{A}^1B_2$ (ν1, ν2, ν3) states of ZrO2

Band (cm^{-1})	(ν_1, ν_2, ν_3)	Lifetime τ (μs)
17034.8	(000)	0.900(32)
17189.7	(010)	1.212(17)
17350.8	(020)	1.095(59)
17506	(030)	1.264(25)
17561	(001)	1.391(28)
17723.4	(011)	1.378(22)
17873.2	(100)	1.128(18)
18025.7	(002)(031)(110)	1.301(18)
18181.4	(120)(041)	1.387(19)
18356.6	(022)	1.373(39)
18476.3	(140)	1.315(26)
18642.8	(150)	1.227(30)
18710.1	(200)	0.925(12)

Table 5.5. The observed and calculated levels for $\tilde{X}^1A_1$ of ZrO_2.

Band (cm^{-1})	Assignment (ν_1, ν_2, ν_3)	Observed (cm^{-1})	Obs-cacl (cm^{-1})
18021.1	(0, 0, 0)	0	-13.4216
	(0, 1, 0)	303.2262	-4.4442
	(0, 2, 0)	596.4152	-12.5456
	(0, 0, 1)	835.8874	-5.1166
	(1, 0, 0)	894.7303	-16.6428
	(1, 1, 0)	1197.1601	-8.4618
	(1, 2, 0)	1489.0923	-17.8201
	(0, 0, 2)	1691.4874	3.1789
	(2, 0, 0)	1797.4178	-11.9069
	(0, 1, 2)	1979.5256	-3.0317

	(2, 1, 0)	2094.4511	-9.1224
	(0, 2, 2)	2269.9865	-13.8613
	(2, 2, 0)	2393.018	-11.8459
	(0, 0, 3)	2562.0674	6.7323
	(3, 0, 0)	2704.0823	-3.1939
	(0, 1, 3)	2855.0157	5.4318
	(3, 1, 0)	3003.003	1.478
	(0, 2, 3)	3159.177	8.3026
	(3, 2, 0)	3290.4775	-12.338
	(4, 0, 0)	3608.7961	3.5684
	(4, 1, 0)	3893.7242	-5.7523
18183	(0, 1, 0)	292.7305	-14.9399
	(0, 2, 0)	607.1257	-1.8351
	(0, 0, 1)	835.7644	-5.2396
	(1, 0, 0)	895.7335	-15.6396
	(1, 1, 0)	1203.8894	-1.7325
	(0, 0, 2)	1680.168	-8.1405
	(2, 0, 0)	1815.206	5.8813
	(0, 1, 2)	1974.3627	-8.1946
	(2, 1, 0)	2091.7135	-11.86
	(0, 2, 2)	2270.9192	-12.9286
	(2, 2, 0)	2396.4985	-8.3654
	(0, 0, 3)	2556.8181	1.483
	(3, 0, 0)	2713.914	6.6378
	(0, 1, 3)	2856.1476	6.5637
	(3, 1, 0)	3007.3113	5.7863
	(0, 2, 3)	3144.2241	-6.6503
	(3, 2, 0)	3311.9297	9.1142
18356	(0, 1, 0)	314.9314	7.261
	(0, 2, 0)	619.244	10.2831
	(0, 0, 1)	836.9891	-4.0149
	(1, 0, 0)	913.4659	2.0928
	(1, 1, 0)	1212.8142	7.1923
	(1, 2, 0)	1516.2732	9.3608
	(0, 0, 2)	1698.8062	10.4977
	(2, 0, 0)	1822.8757	13.551
	(2, 1, 0)	2105.3103	1.7368
	(0, 2, 2)	2275.3683	-8.4795
	(0, 0, 3)	2555.1962	-0.1389
	(3, 0, 0)	2716.0206	8.7444
	(0, 1, 3)	2861.5969	12.013
	(3, 1, 0)	3016.2787	14.7537
	(0, 2, 3)	3144.7727	-6.1017
	(3, 2, 0)	3316.5639	13.7484
	(0, 0, 4)	3451.2298	9.146

	(4, 0, 0)	3605.3253	0.0976
	(0, 1, 4)	3745.5898	9.2572
	(4, 1, 0)	3904.1569	4.6804
	(0, 2, 4)	4049.0806	11.4576
	(4, 2, 0)	4211.1912	10.4242
	(0, 0, 5)	4350.0559	1.5014
18478.29	(0, 1, 0)	302.4702	-5.2002
	(0, 2, 0)	611.1874	2.2265
	(1, 0, 0)	909.5959	-1.7772
	(1, 1, 0)	1213.1311	7.5092
	(1, 2, 0)	1506.3596	-0.5528
	(0, 0, 2)	1677.5656	-10.7429
	(2, 0, 0)	1817.6216	8.2969
	(2, 1, 0)	2117.6762	14.1027
	(2, 2, 0)	2407.1179	2.254
	(0, 0, 3)	2548.0333	-7.3018
	(3, 0, 0)	2698.9687	-8.3075
	(0, 1, 3)	2859.2883	9.7044
	(3, 1, 0)	3004.4121	2.8871
	(0, 2, 3)	3158.6178	7.7434
	(3, 2, 0)	3321.286	18.4705
	(0, 0, 4)	3457.9923	15.9085
	(4, 0, 0)	3614.3998	9.1721
	(0, 1, 4)	3745.8948	9.5622
	(4, 1, 0)	3917.6459	18.1694
	(0, 2, 4)	4043.8551	6.2321
	(4, 2, 0)	4208.7708	8.0038
	(0, 0, 5)	4340.0167	-8.5378
	(5, 0, 0)	4508.0479	4.8686
18708	(0, 1, 0)	309.8099	2.1395
	(0, 2, 0)	609.5264	0.5655
	(0, 0, 1)	835.9729	-5.0311
	(1, 0, 0)	915.4796	4.1065
	(1, 1, 0)	1211.2611	5.6392
	(1, 2, 0)	1512.1693	5.2569
	(0, 0, 2)	1687.7973	-0.5112
	(2, 0, 0)	1817.182	7.8573
	(0, 1, 2)	1986.6658	4.1085
	(2, 1, 0)	2111.5635	7.99
	(0, 2, 2)	2275.2201	-8.6277
	(2, 2, 0)	2395.8601	-9.0038
	(0, 0, 3)	2553.985	-1.3501
	(3, 0, 0)	2709.0739	1.7977
	(0, 1, 3)	2848.6456	-0.9383
	(3, 1, 0)	2998.1548	-3.3702

	(0, 2, 3)	3144.8715	-6.0029
	(3, 2, 0)	3300.7534	-2.0621
	(0, 0, 4)	3441.8983	-0.1855
	(4, 0, 0)	3603.3337	-1.894
	(0, 1, 4)	3739.014	2.6814
	(4, 1, 0)	3905.2249	5.7484
	(0, 2, 4)	4035.5595	-2.0635
	(4, 2, 0)	4195.2858	-5.4812
	(0, 0, 5)	4351.5721	3.0176
	(5, 0, 0)	4494.4328	-8.7465
17870	(0, 1, 0)	313.8385	6.1681
	(0, 2, 0)	616.8456	7.8847
	(0, 0, 1)	851.8244	10.8204
	(1, 0, 0)	923.9484	12.5753
	(1, 1, 0)	1206.4343	0.8124
	(1, 2, 0)	1506.4888	-0.4236
	(0, 0, 2)	1691.8712	3.5627
	(2, 0, 0)	1808.8439	-0.4808
	(0, 1, 2)	1987.4774	4.9201
	(2, 1, 0)	2112.6596	9.0861
	(0, 2, 2)	2272.4769	-11.3709
	(2, 2, 0)	2405.1968	0.3329
	(0, 0, 3)	2559.1653	3.8302
	(3, 0, 0)	2698.5941	-8.6821
	(0, 1, 3)	2858.0859	8.502
	(3, 1, 0)	3003.2125	1.6875
	(0, 2, 3)	3145.5604	-5.314
	(3, 2, 0)	3306.4585	3.643
	(0, 0, 4)	3453.4903	11.4065
	(4, 0, 0)	3607.7657	2.538
	(0, 1, 4)	3738.8253	2.4927
	(4, 1, 0)	3896.8605	-2.616
	(4, 2, 0)	4193.2104	-7.5566
	(5, 0, 0)	4495.1745	-8.0048
18645	(0, 1, 0)	307.5233	-0.1471
	(1, 0, 0)	908.8325	-2.5406
	(1, 1, 0)	1202.5373	-3.0846
	(1, 2, 0)	1501.3684	-5.544
	(2, 0, 0)	1804.3121	-5.0126
	(0, 1, 2)	1972.6623	-9.895
	(2, 1, 0)	2110.4033	6.8298
	(0, 2, 2)	2272.7168	-11.131
	(2, 2, 0)	2405.5627	0.6988
	(0, 0, 3)	2562.1585	6.8234
	(3, 0, 0)	2703.074	-4.2022

	(3, 1, 0)	3002.1124	0.5874
	(0, 2, 3)	3159.4528	8.5784
	(3, 2, 0)	3313.6584	10.8429
	(0, 0, 4)	3441.7605	-0.3233
	(4, 0, 0)	3601.7349	-3.4928
	(4, 1, 0)	3900.9354	1.4589
	(0, 2, 4)	4051.4369	13.8139
	(4, 2, 0)	4209.3145	8.5475
	(0, 0, 5)	4343.4033	-5.1512
17034.8	(0, 1, 0)	312.8388	5.1684
	(0, 2, 0)	627.834	18.8731
	(1, 0, 0)	905.2411	-6.132
	(1, 1, 0)	1210.9999	5.378
	(1, 2, 0)	1505.3727	-1.5397
	(1, 3, 0)	1835.2477	20.0032
	(1, 4, 0)	2140.3242	9.706
	(1, 5, 0)	2465.2358	12.2023
	(1, 6, 0)	2796.5255	14.035
17194.11	(0, 1, 0)	305.0127	-2.6577
	(0, 2, 0)	613.1566	4.1958
	(1, 0, 0)	910.2596	-1.1135
	(1, 1, 0)	1209.6943	4.0724
	(1, 2, 0)	1510.63	3.7176
	(0, 0, 2)	1668.9542	-19.3543
	(1, 3, 0)	1824.1143	8.8698
	(1, 4, 0)	2113.9482	-16.67
	(1, 5, 0)	2425.8558	-27.1777
	(0, 0, 3)	2566.3266	10.9915
	(3, 0, 0)	2704.1509	-3.1253
	(3, 1, 0)	3002.4403	0.9153
	(3, 2, 0)	3298.3639	-4.4516
	(0, 0, 4)	3460.6408	18.557
	(4, 0, 0)	3600.7114	-4.5163
	(0, 1, 4)	3756.0443	19.7117
	(4, 1, 0)	3907.868	8.3915
	(4, 2, 0)	4193.0033	-7.7637
17506.2	(0, 1, 0)	316.2303	8.5599
	(0, 2, 0)	592.6611	-16.2998
	(1, 0, 0)	915.6245	4.2513
	(1, 1, 0)	1213.2163	7.5944
	(1, 2, 0)	1513.1348	6.2224
	(0, 0, 2)	1690.35	2.0415
	(2, 0, 0)	1814.5477	5.223
	(0, 1, 2)	1985.1845	2.6272
	(2, 1, 0)	2116.676	13.1025

	(2, 2, 0)	2407.3946	2.5307
	(3, 0, 0)	2709.2858	2.0096
	(0, 1, 3)	2861.1201	11.5362
	(3, 1, 0)	3009.8716	8.3466
	(3, 2, 0)	3298.4937	-4.3218
	(0, 0, 4)	3458.321	16.2372
	(4, 0, 0)	3604.929	-0.2987
	(0, 1, 4)	3748.5099	12.1773
	(4, 1, 0)	3889.1566	-10.3199
	(4, 2, 0)	4197.5556	-3.2114
	(5, 0, 0)	4492.3015	-10.8778
	(5, 1, 0)	4790.4885	-6.9396
17723.382	(0, 2, 0)	619.6957	10.7349
	(1, 0, 0)	920.5915	9.2184
	(1, 1, 0)	1211.0688	5.4469
	(1, 2, 0)	1517.8852	10.9728
	(0, 0, 2)	1686.3047	-2.0038
	(2, 0, 0)	1800.8638	-8.4609
	(2, 1, 0)	2086.3125	-17.261
	(2, 2, 0)	2396.8962	-7.9677
	(0, 0, 3)	2559.0696	3.7345
	(3, 0, 0)	2684.1	-23.1762
	(0, 1, 3)	2851.305	1.7211
	(3, 1, 0)	2993.2326	-8.2924
	(0, 2, 3)	3143.0742	-7.8002
	(3, 2, 0)	3310.6258	7.8103
	(0, 0, 4)	3433.7798	-8.304
	(0, 1, 4)	3722.8746	-13.458
	(0, 2, 4)	4019.2244	-18.3986
	(4, 2, 0)	4203.8383	3.0713
	(0, 0, 5)	4330.131	-18.4235
	(0, 1, 5)	4627.2196	-15.5837
	(0, 2, 5)	4927.7229	-16.3709
17350.6	(0, 1, 0)	295.7554	-11.915
	(0, 2, 0)	595.635	-13.3258
	(1, 0, 0)	912.2	0.8269
	(1, 1, 0)	1230.0183	24.3964
	(1, 2, 0)	1510.741	3.8286
	(0, 0, 2)	1672.0725	-16.236
	(2, 0, 0)	1818.1034	8.7787
	(2, 1, 0)	2113.7613	10.1878
	(0, 2, 2)	2274.4637	-9.3841
	(2, 2, 0)	2398.3706	-6.4933
	(0, 0, 3)	2564.0877	8.7526
	(3, 0, 0)	2694.0391	-13.2371

	(3, 1, 0)	2988.5519	-12.9731
	(0, 2, 3)	3141.5083	-9.3661
	(3, 2, 0)	3291.2399	-11.5756
	(0, 0, 4)	3457.1648	15.081
	(4, 0, 0)	3590.8955	-14.3322
	(4, 1, 0)	3914.2203	14.7438
17562.13	(0, 1, 0)	302.4803	-5.1901
	(0, 2, 0)	594.7071	-14.2537
	(1, 0, 0)	891.0703	-20.3028
	(1, 1, 0)	1217.329	11.7071
	(1, 2, 0)	1518.2186	11.3062
	(0, 0, 2)	1683.4314	-4.8771
	(2, 0, 0)	1820.5892	11.2645
	(0, 1, 2)	1967.5356	-15.0217
	(2, 1, 0)	2099.8442	-3.7293
	(0, 2, 2)	2265.0208	-18.827
	(2, 2, 0)	2403.8142	-1.0497
	(0, 0, 3)	2562.5862	7.2511
	(3, 0, 0)	2707.0643	-0.2119
	(0, 1, 3)	2859.5718	9.9879
	(3, 1, 0)	2987.8188	-13.7062
	(0, 2, 3)	3145.0115	-5.8629
	(3, 2, 0)	3308.9842	6.1687
	(0, 0, 4)	3449.4269	7.3431
	(4, 0, 0)	3606.5774	1.3497
	(0, 1, 4)	3741.2371	4.9045
	(4, 1, 0)	3891.9825	-7.494
	(0, 2, 4)	4021.2092	-16.4138
	(4, 2, 0)	4210.5263	9.7593
	(0, 0, 5)	4333.82	-14.7345
	(5, 0, 0)	4497.5452	-5.6341
	(0, 1, 5)	4632.3038	-10.4995
	(5, 1, 0)	4788.7576	-8.6705
Rms =9.45 cm^{-1}		σ= 9.56 cm^{-1}	

References

1. Y.Gong, M.Zhou, L. Andrews, Spectroscopic and Theoretical Studies of Transition Metal Oxides and Dioxygen Complexes. Chem. Rev. **109**, 6765 (2009).

2. H. Wang, T.C. Steimle, C. Apetrei and J. P. Maier Phys. Chem.Chem. Phys. **11**, 2649 (2009).

3. X. Zhuang, A. Le, T.C. Steimle, R. Nagarajan, V.Gupta, J.P. Maier Phys. Chem.Chem. Phys. **12,** 15018-15028, (2010).

4. M. Kaufman, J. Meunter, and W. Klemperer, J. Chem. Phys. **47**, 3365 (1967).

5. D.J. Burgh, R. D.Seunram, and W. J. Stevens, J. Phys. Chem. **111**, 3526 (1999).

6. A Zaleska, Recent Patents on Engineering, **2**,157-164 (2008).

7. N. S. McIntyre, K. R. Thompson, and W. Welter, J. Phys. Chem. **75**, 3243(1971)

8. G.V.Chertihin, L. Andrews, J. Phys. Chem. **97**, 6356 **(**1995).

9. H. Wu, L-S, Wang, J. Chem. Phys. **107,** 20**,** 8221(1997).

10. F. Grein, J. Chem. phys. **126**, 034313 (2007).

11. G. L. Gutsev, B. K. Rao, and P. Jena, *J. Phys. Chem. A*, **104** (51), pp 11961–11971, (2000).

12. Z-W. Qu, and G-J. Kroes ,J. Phys. Chem. B, **110,** 8998-9007, (2006).

13. R. J. Le Roy, RKR1 2.0: A Computer Program Implementing the First-Order RKR Method forDetermining Diatomic Molecule Potential Energy Curves, University of Waterloo Chemical Physics Research Report CP-657R (2004). The source code and manual for this program may be obtained from the "Computer Programs" link at http://leroy.uwaterloo.ca .

14. R. J. Le Roy, Level 8.0: A Computer Program for Solving the Radial Schrodinger Equation for Bound and Quasibound Levels, University of Waterloo Chemical Physics Research Report CP-663 (2007); see http://leroy.uwaterloo.ca/programs/.

15. P.T. Ruhoff, Chemical Physics, **186** 355-374, (1994).

16. F. Duschinsky, Acta Physicochim. URSS **7**, 551 (1937)

17. T. E. Sharp and H. M. Rosenstock J. Chem. Phys. **41**, 3453 (1964)

18. J. L. Chang, J. Mol. Spectrosc. **232,** 102 (2005).

19. J. L. Chang, J. Chem. Phys. **128**, 174121 (2008)

20 P.C. Ray, M. F. Arendt, and L. J. Butler, J. Chem. Phys. **109,** 13 (1998)

21. D. K. W. Mok, F. Chau, J. M. Dyke, and E. P. F. Lee, Chem. Phys. Letts. **458,** 11 (2008).

22. G. Herzberg; *Molecular Spectra and Molecular Structure; Vol III-Electronic Spectra and Electronic Structure of Polyatomic Molecules* (Kreiger, Malabar, 1991).

23. E.B. Wilson, Jr. J.C. Decius, and P.C. Cross, *Molecular Vibrations* (McGraw-Hill, New York, 1955).

24. P. R. Bunker and Per Jensen, *Molecular Symmetry and Spectroscopy,* (Canadian Science Publishing (NRC Research Press); 2nd Revised edition (December 23, 2009).

25. G.L. Goodman and J. Berkowitz In: J. Berkowitz and K.O. Groenveld, Editors, *Molecular Ions*, Plenum Press, New York pp.69 (1983).

26. P. Chen, in *Unimolecular and Bimolecular Reaction Dynamics*, edited by C. Y. Ng, T. Baer, and I. Powis (John Wiley & Sons, NYC, 1994), **3**, 372.

27. A. Le, T.C. Steimle, V. Gupta, C. A. Rice, J. P. Maier, S. H. Lin, and C.-K. Lin, J. Chem. Phys. **135**, 104303 (2011).

Chapter 6

OTHER CONTRIBUTION, AND CONCLUSION

6.1. Iridium silicide, IrSi

Transition metal silicides possess many desirable physical properties, including high melting points, low densities, and low chemical reactivity. Specific species, such as nickel and platinum silicides, are known as electrical conductors have been found to have many applications as protective coatings against high temperature oxidation [1] and in microelectronics as Schottky barrier detectors for IR-imaging arrays[2]. Iridium is one of the rarest transition metal elements in the earth's crust but with great technological importance. Ir-based silicide is previously identified the optimum phase and temperature window to obtain the lowest Schottky barrier height [3].

Iridium has two naturally occurring isotopes: ^{191}Ir (37.3%) and ^{193}Ir (62.7%). The two isotope ^{191}Ir (I=3/2) and ^{193}Ir (I=3/2) have similar quadrupole moments, *Q*, of 81.6 fm^2 and 75.1 fm^2, respectively, and similar magnetic moments of $0.1507\mu_N$ and $0.1637\mu_N$, respectively. Spectroscopic investigation of gas-phase iridium containing molecules are limited to only four molecules: IrC [4, 5],IrN [5], IrO [6], and IrF [7, 8, 9]. Marr et al. [5] determined the ground state dipole moments of 1.66(1) and 1.60(7) D for IrN ($X^1\Sigma^+$) and IrC ($X^2\Delta_{5/2}$), respectively, using a laser ablation supersonic expansion source and high resolution LIF optical Stark spectroscopy. Previously, there were only two theoretical studies [10, 11] of IrSi. First calculation study by Han[10] used UB3LYP/LanL2DZ level methods to predict Ir-Si bond lengths with spin S=1/2, 3/2 and 5/2 are 2.1447Å, 2.3736Å, and 2.3691Å, respectively. The S=1/2 is the most stable geometry and suggested that corresponding ground state is $^2\Sigma$. More recently, Wu et al

[11] using density functional method B3LYP with LanL2DZ basis set calculated several properties. For the spin multiplicities, S=2, bond distances, r_e=2.105 Å, vibrational frequency, ω_e=527cm^{-1}, dipole moments, μ_e=0.44 D. The ground state of IrSi was predicted to be $^2\Delta$ state with electron configuration is $8\sigma^2 3\pi^4\delta^3$. There was only one experimental study on IrSi in the gas-phase using REMPI spectroscopy reporting the observation of thirty-one bands included 14 electronic band systems. *Ab initio* calculations using CASSCF and MS-CASPT2 method were also carried out in that same study in support the experimental results [12]. The two bands at 18350 cm^{-1} and 18520 cm^{-1}, which are the focus of this study, were identified as (6,0)[16.0]1.5- $X^2\Delta_{5/2}$, (7.0)[16.0]3.5- $X^2\Delta_{5/2}$ band systems. In this study, the hyperfine parameters for the [16.0]1.5(v=6), [16.0]3.5(v=7) and $X^2\Delta_{5/2}$ states are determined for both ^{191}IrSi and ^{193}IrSi isotopologue. The electric dipole moment, μ_{el} of the $X^2\Delta_{5/2}$(v=0) and [16.0]1.5(v=6) state are also reported. The spectroscopy of IrSi is expected to be similar with isovalent IrC, however, irregular spectral features were observed.

6.1.1. Observation

6.1.1.1. Field free spectra

A 10cm^{-1} portion of the (6,0)[16.0]1.5-$X^2\Delta_{5/2}$, (7.0)[16.0]3.5- $X^2\Delta_{5/2}$ bands of IrSi at 18350 cm^{-1}, and 18520 cm^{-1} were recorded. Figure 6.1 shows the portion of the LIF spectrum of 18350 cm^{-1} band and 18520 cm^{-1}, in the range of 5 cm^{-1}. Figure 6.1(A) illustrates the characteristic for Ω'=3.5←Ω''=2.5 transition: a particularly intense *R* branch at *R*(5/2), the *R* branch quickly forms a head at *R*(9/2, 11/2), a strong *Q* branch beginning at *Q*(7/2), and a much weaker *P* branch beginning at *P*(9/2). The (6,0)[16.0]1.5- $X^2\Delta_{5/2}$ band system in Figure 6.1(B) exhibits characteristics for Ω'=1.5 ←

Ω″=2.5 transition with strong *P* and *Q* branches, and a significantly weaker *R* branch, in contrast to the (7.0)[16.0]3.5- $X^2\Delta_{5/2}$ band system. The isotopic shifts between ^{191}IrSi and ^{193}IrSi for both band systems are approximately 1.5 cm^{-1}.

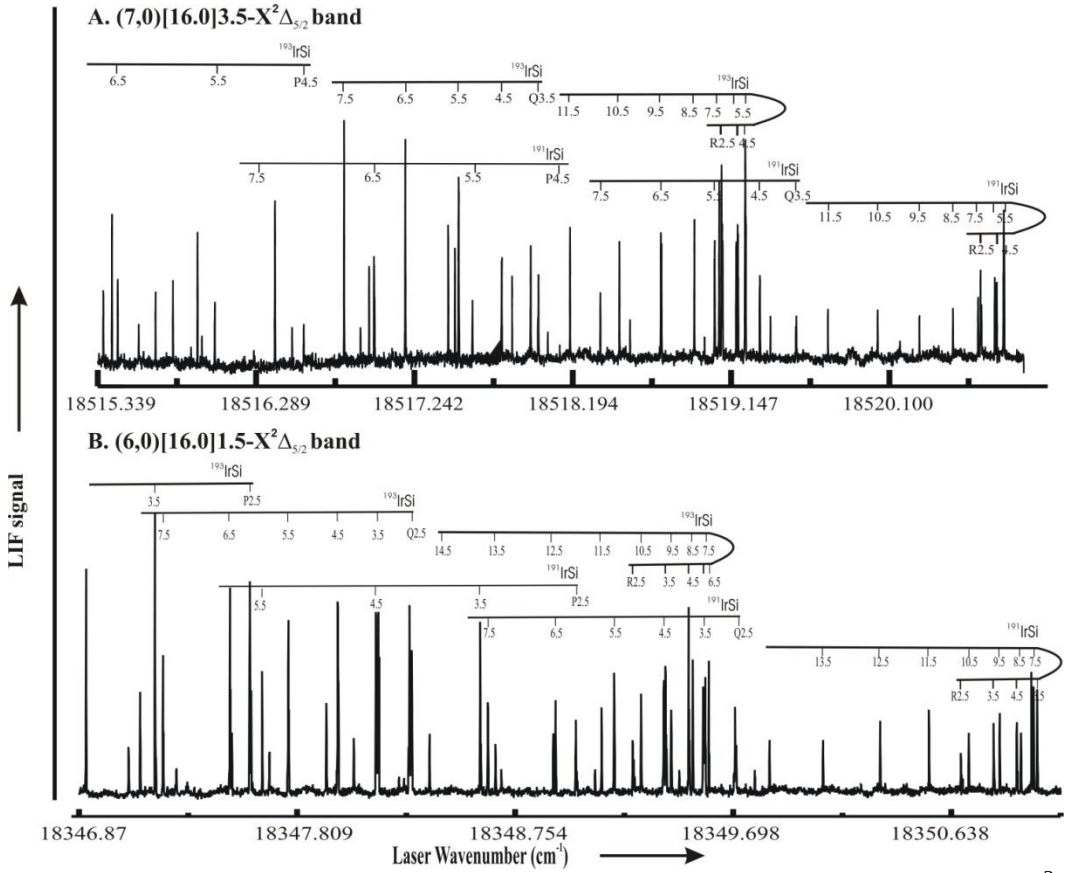

Figure 6.1. A portion of the high resolution LIF spectra of the (6,0)[16.0]1.5 - $X^2\Delta_{5/2}$ and the (7,0)[16.0]3.5- $X^2\Delta_{5/2}$ band systems in a range of 5cm^{-1}. The line widths of unblended spectral features are approximately 35 MHz**.**

The observed and calculated slow scans of the *P*(5/2), *Q*(7/2), and *R*(5/2) branch features of ^{193}IrSi of the (6,0)[16.0]1.5- $X^2\Delta_{5/2}$ are given in Figure 6.2. The calculated spectra were predicted using the parameters from the final analysis (*vide infra*) in Table 6.1. The *P*(5/2) and *R*(5/2) spectral features in Fig. 2 are transitions from the same energy

level in the $X^2\Delta_{5/2}$ state. The $Q(7/2)$ and $R(5/2)$ spectral features in Figure 6.2 are transitions with the same energy level in the [16.0]1.5(v=6) state. A comparison between various spectral features indicates that the hyperfine structure are due to both the $X^2\Delta_{5/2}$ and [16.0]1.5(v=6) states.

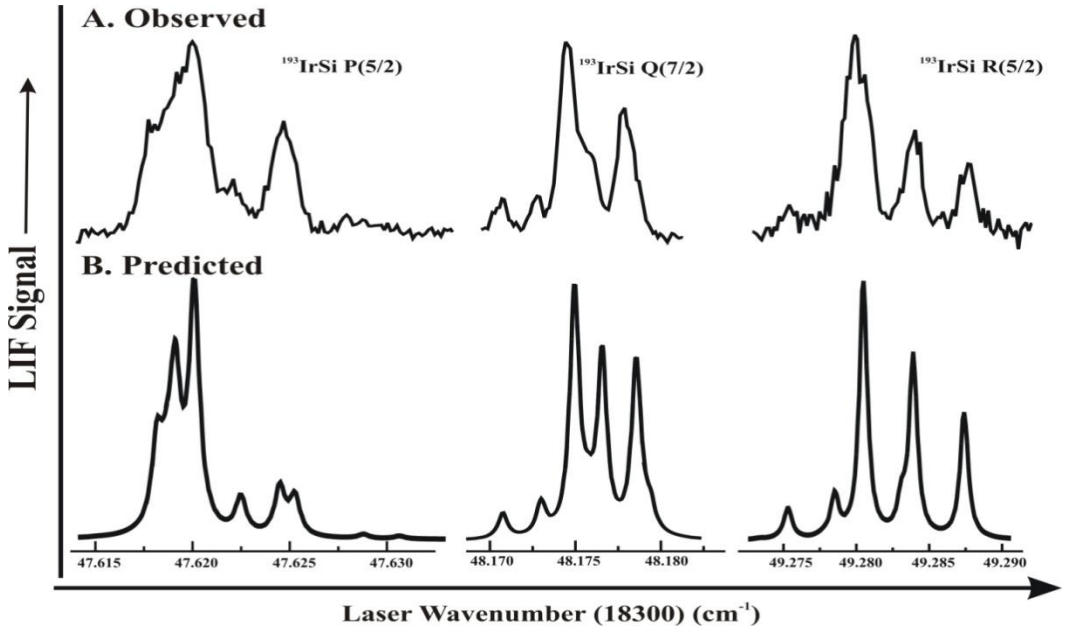

Figure 6.2. The observed slow scan and predicted spectra of $P(5/2)$, $Q(7/2)$ and $R(5/2)$ transition of ^{193}IrSi isotopologue in the (6,0)[16.0]1.5 - $X^2\Delta_{5/2}$ band system. The calculated spectra were obtained using the optimized set of parameters in Table 1.

The observed and calculated slow scans of the $P(9/2)$, $Q(7/2)$ and $R(5/2)$ spectral features of ^{193}IrSi isotope of the (7.0)[16.0]3.5- $X^2\Delta_{5/2}$ band system are shown in Figure 6.3. Figure 6.3 indicates that the hyperfine structure are due to both the $X^2\Delta_{5/2}$ and [16.0]3.5(v=7) states. The irregular pattern on both band system suggest that the electric nuclear quadrupole interactions in the $X^2\Delta_{5/2}$, [16.0]3.5(v=7) and [16.0]1.5(v=6) states are needed in the analysis.

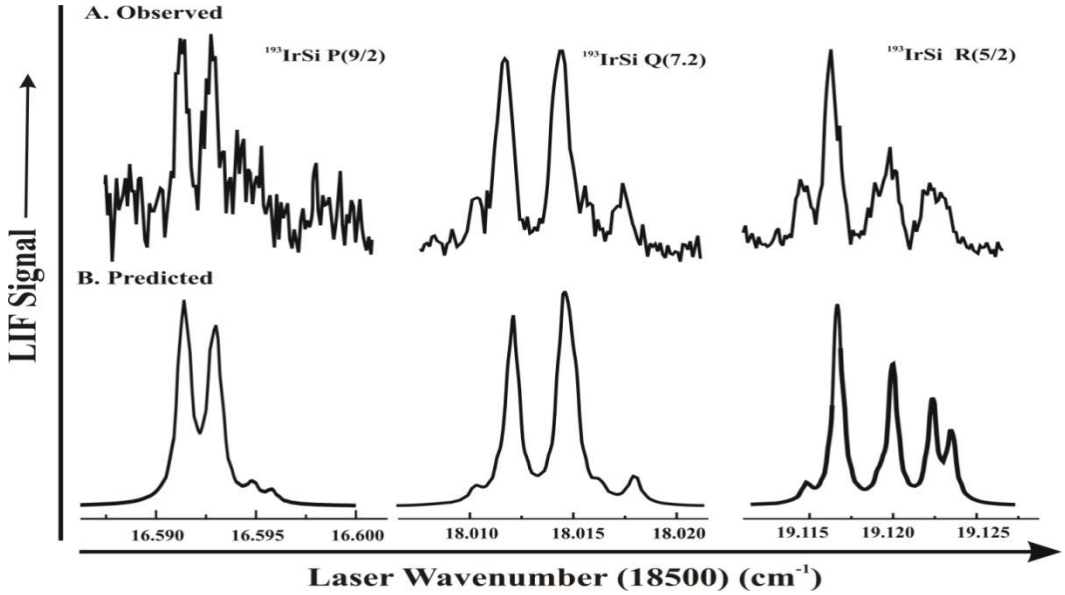

Figure 6.3. The observed slow scan and predicted spectra of *P*(9/2), *Q*(7/2) and *R*(5/2) transition of ^{193}IrSi isotopologue in the (7,0)[16.0]3.5- $X^2\Delta_{5/2}$ band system. The calculated spectra were obtained using the optimized set of parameters in Table 1.

6.1.1.1. Stark spectra

The *P*(5/2) line of the ^{193}IrSi and the *Q*(5/2) of the ^{191}IrSi isotopologue were selected for optical Stark studies because they are unblended and have the fewest components upon the application of electric field. The observed *P*(5/2) line the ^{193}IrSi isotopologue recorded field-free and in the presence of a 1754.4 V/cm static field with parallel (ΔM_J = 0) polarization is presented in Figure 6.4. The Stark spectrum is complicated and appears and to be un-analyzable at first glance. The field free spectrum is highly overlapped with high-*J* line of both ^{193}IrSi and ^{191}IrSi isotopologues, leading to the fact that the applied electric field cannot be tuned really high voltage. The associated tuning of the energy levels as a function of the applied electric fields and the predicted spectrum are also presented in Figure 6.4. The *J''*=5/2 level rotational level in the

$X^2\Delta_{5/2}(v=0)$ state rapidly splits into 24(=(2×J+1)(2×I+1)) components. Similarly, the J'=1/2 rotational level in the [16.0]1.5(v=6) state splits into 16(=(2×J+1)(2×I+1)) components. The energy pattern was calculated using the optimized $\vec{\mu}_{el}$ values of -0.4139(64)D and 0.7821(63) D for $X^2\Delta_{3/2}(v=0)$ and [16.0]1.5 (v=6) states, respectively. The assignments, observed Stark shifts, and the differences from the calculated Stark shifts are presented in Table 6.6.

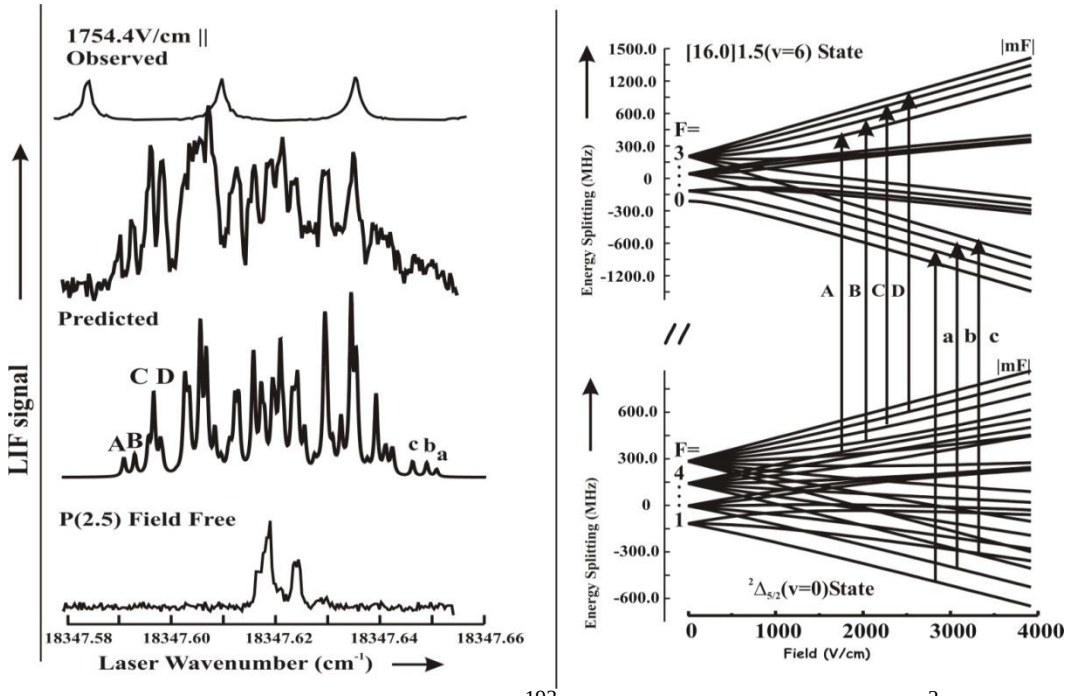

Figure 6.4. The observed $P(5/2)$ line of ^{193}IrSi of the (6,0)[16.0]1.5 - $X^2\Delta_{5/2}$ band system recorded field-free and in the presence of a 1754.4 V/cm static field with parallel (ΔM_J = 0) associated energy levels.

6.1.2. Analysis

6.1.2.1. Field free spectra

The energies for the $X^2\Delta_{5/2}(v=0)$, [16.0]1.5(v=6) and [16.0]3.5(v=7) states were modeled using the effective Hamiltonian operator:

$$\hat{H}^{eff} = A\hat{L}_z\hat{S}_z + B\hat{R}^2 - D\hat{R}^4 + h_\Omega(^{191\&193}\text{Ir})\hat{I}\cdot\hat{F} + eQq_0(^{191\&193}\text{Ir})\frac{3\hat{I}_z^2 - \hat{I}^2}{4I(2I-1)}, \qquad (1)$$

where $\hat{R}$, $\hat{I}$, and $\hat{F}$ are rotational, nuclear spin and total angular momenta operators, respectively. There was no evidence of Ω-doubling in the. The centrifugal distortion correction, *D*, for the $X^2\Delta_{5/2}$(*v*=0), [16.0]1.5(v=6) and [16.0]3.5(v=7) states were constrained to zero.

The measured 91 transitions of the (6,0)[16.0]1.5- $X^2\Delta_{5/2}$ and 74 transitions for (7.0)[16.0]3.5- $X^2\Delta_{5/2}$ band system of ^{191}IrSi were identified and are given in Table 6.3 and Table 6.2, respectively. Similarly, the measured 111 transitions of the (6,0)[16.0]1.5- $X^2\Delta_{5/2}$ and 74 transitions for (7.0)[16.0]3.5- $X^2\Delta_{5/2}$ band system of ^{193}IrSi were identified and are given in Table 6.5 and Table 6.4, respectively. The assigned marked "*" in the Tables 6.6-6.9 were entered two times in the fit give a total of 316 transition wavenumbers of ^{193}IrSi and 281 transition wavenumbers of ^{191}IrSi. Each isotope was fit directly. The eigenvalues and eigenvectors were obtained by construct and numerically diagonalizing of the matrix representation with dimension of 16 (=2×(2*S*+1)×[2*I*(^{191,193}Ir)+1]) a Hund's case ($a_{\beta J}$) basis set (ψ=|ηΛ>|SΣ>|*J*Ω(*JI*$_1$)*F*>). Similar to IrC analysis, the spin-orbit parameters, *A*, for the $X^2\Delta_{5/2}$ (*v*=0), [16.0]1.5 (*v*=6) and [16.0]3.5(v=7) states were constrained to 1500 cm^{-1}[5]. The analysis is insensitive to any values of the spin-orbit parameters greater than approximately 500 cm^{-1} of the $X^2\Delta_{5/2}$(*v*=0), [16.0]1.5(v=6) and [16.0]3.5(v=7) states. Fits using various combinations of ground and excited state parameters were performed. In the end, satisfactory modeling of the spectra could be achieved by fitting both band systems simultaneously. A total of 11 parameters including the h_Ω(^{191,193}Ir), eQq_0(^{191,193}Ir) and the origins for the

$X^2\Delta_{5/2}(v=0)$, [16.0]1.5(v=6), and [16.0]3.5(v=7) states were used. The optimized parameters and associated errors are given in Table 6.1. The standard deviation of the ^{191}IrSi and ^{193}IrSi fits are 0.00053 cm^{-1} and 0.00052 cm^{-1}, respectively, which are in agreement with the measurement uncertainty.

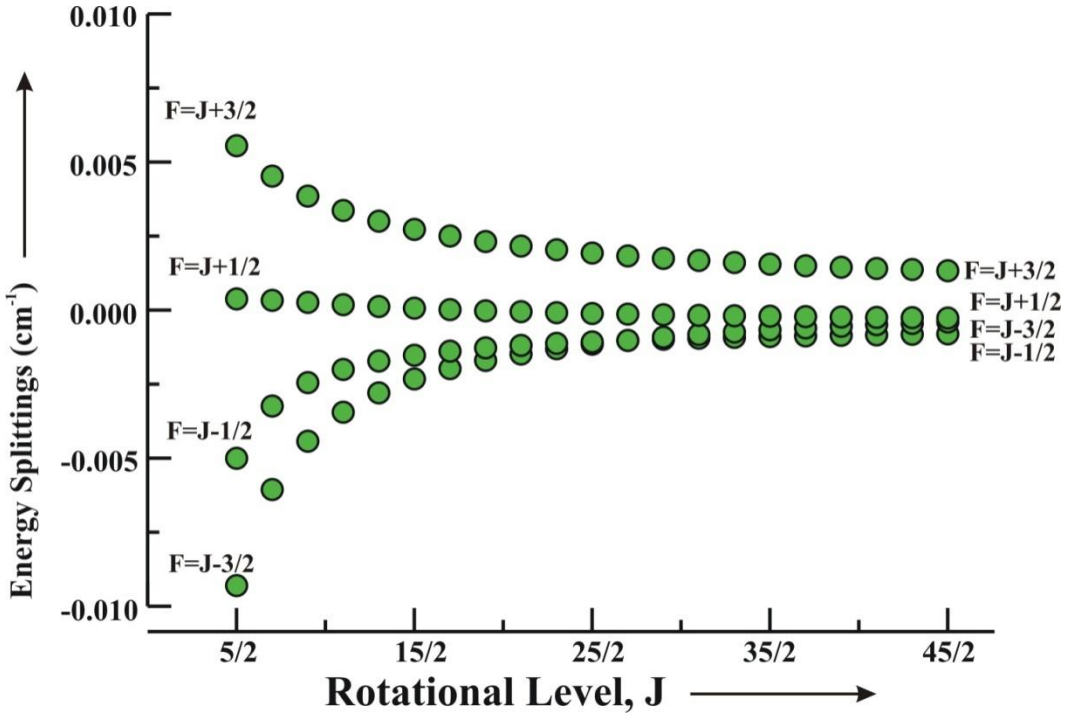

Figure 6.5. The calculated ^{193}IrSi hyperfine and quadrupole energy pattern as the function of rotational quantum number, *J*, in the $X^2\Delta_{5/2}$ state.

The calculated energy patterns of the ^{193}IrSi for the $X^2\Delta_{5/2}(v=0)$ state using the parameter in Table 6.1 from the final analysis are shown in Figure 6.5. Figure 6.5 illustrates the contribution of the magnetic hyperfine and quadrupole splitting by subtracted rotational energy [$\approx B\times J(J+1)$]. Figure 6.5 shows that at very low-*J*, the asymmetry splitting of the energy patterns due to the quadrupole parameter in the $X^2\Delta_{5/2}(v=0)$ state. At *J*=27/2 and beyond, the energy level of *F*=*J*-3/2 switches around with the energy level of *F*=*J*-1/2.

6.1.2.2. Stark spectra

The interaction between the static electric field, E, and the molecular electric dipole moment, μ, is represented by the Stark Hamiltonian,

$$\hat{H}^{Stark} = -\mu.E \qquad (2)$$

the matrix representation of $\hat{H}^{Stark}$ is block diagonal in M_F. The predicted Stark shifts in the $X^2\Delta_{5/2}(v=0)$ and [16.0]1.5(v=6) states were obtained by numerical diagonalizing of a 96×96 matrix representation constructed using the Hund's case $a_{\beta J}$ basis set for F''=1-6 and F'=0-5. The observed Stark shifts for $P(5/2)$ line of the ^{193}IrSi and the $Q(5/2)$ of the ^{191}IrSi isotopologues were entered in the non-linear least square fitting program all together in which μ_e for the $X^2\Delta_{5/2}(v=0)$ and [16.0]1.5(v=6) states were simultaneously optimized. The resulting μ_e values are of -0.4139(64)D and 0.7821(63) D for $X^2\Delta_{5/2}(v=0)$ and [16.0]1.5(v=6) states, respectively. The error limits represent a 90% statistical confidence level which is slightly smaller than the estimated maximum systematic error of 2%. The correlation coefficient was 0.66 and the standard deviation of the fit was 21 MHz, which is commensurate with the measurement uncertainty.

6.1.2. Discussion

The ratio of magnetic hyperfine parameter for the $X^2\Delta_{5/2}(v=0)$ state, $h_{5/2}(^{191}\text{IrSi})/h_{5/2}(^{193}\text{IrSi})$, is 0.91 ± 0.03, for the [16.0]1.5(v=6) state the ratio $h_{1/2}(^{191}\text{IrSi})/h_{1/2}(^{193}\text{IrSi})$ is 0.85 ± 0.05, and for the [16.0]3.5(v=7) state the ratio $h_{3/2}(^{191}\text{IrSi})/h_{3/2}(^{193}\text{IrSi})$ is 0.92 ± 0.07, which are in agreement with nuclear g_I-factors: $\frac{\mu(^{191}\text{Ir}) / I(^{191}\text{Ir})}{\mu(^{193}\text{Ir}) / I(^{193}\text{Ir})} = 0.92$. These agreements suggest that the magnetic hyperfine is not

contaminated too severely by higher order terms. Similarly, the ratios $eQq_0(^{191}\text{Ir})/eQq_0(^{193}\text{Ir})$ for the $X\,^2\Delta_{5/2}(v=0)$, [16.0]1.5(v=6), and [16.0]3.5(v=7) states are 0.83±0.20, 0.77±0.14 and 1.14±0.26, this ratio is in reasonable agreement when in comparison with $^{191}\text{Ir}(Q)/^{193}\text{Ir}(Q)$ of 1.086.

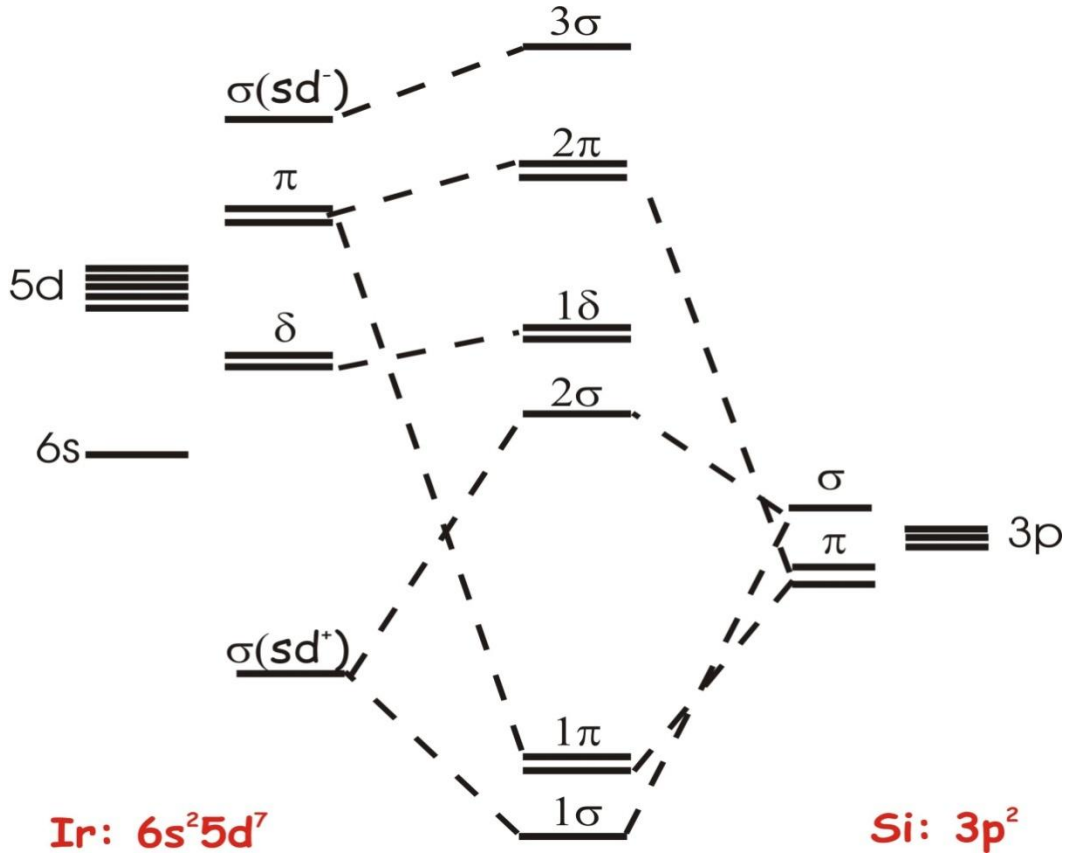

Figure 6.6. A molecular orbital correlation diagram IrSi. The relevant configurations for the $X^2\Delta_{5/2}$ of IrSi is $1\sigma^2 1\pi^4 2\sigma^2 1\delta^3$.

A molecular orbital configuration diagram similar to that for IrC [5], was constructed and is shown in Figure 6.6. Similar to IrC, the 6s orbital is significantly stabilized relative to the 5d orbital. Similar to IrC, The 3*s* atomic orbital of Si is not expected to participate significantly in bonding. Based upon this simple molecular orbital

correlation diagram of Figure 6.6, the dominant configuration in the $X^2\Delta$ state is predicted to be [11, 12]:$1\sigma^2 1\pi^4 2\sigma^2 1\delta^3$.

The effective magnetic hyperfine fitting parameter, h_Ω, can be expressed in terms of the Frosch and Froley parameters as [13] $h_\Omega = \{a\Lambda + (b_F + \frac{2}{3}c)\Sigma\}$. The simplest interpretation of $h_{5/2}$(Ir) for the $X^2\Delta_{5/2}$(v=0) state assumes that the sole unpaired electron occupies the Ir-centered $5d_{\pm 2}$ orbital. The simple molecular orbital diagram suggests that b_F=0 because there is no open shell s-orbital character, therefore, $h_{5/2}$=2a+c/3 for the $X^2\Delta_{5/2}$ where a and c parameters are followed:

$$a(X^2\Delta_{5/2})(\mathrm{Hz}) = (\frac{\mu_0}{4\pi h})2g_I\mu_B\mu_N\langle 1\delta|r^{-3}|1\delta\rangle \quad (3)$$

$$c(X^2\Delta_{5/2})(\mathrm{Hz}) = (\frac{\mu_0}{4\pi h})\frac{3}{2}g_e g_I \mu_B \mu_N \langle 1\delta|\frac{(3\cos^2\theta_i - 1)}{r^3}|1\delta\rangle \quad (4)$$

There is no previous prediction for the expectation of $\langle 1\delta|r^{-3}|1\delta\rangle$. Similar to IrC [5], atomic information can be used to evaluate a and c parameters using the expectation of $\langle 5d|r^{-3}|5d\rangle$ for Ir have previously determined [14 15], and the value $\langle 5d|r^{-3}|5d\rangle$ =6.07×10^{-25} cm^{-1} were taken out of Ref. 16. The $a(X^2\Delta_{5/2})$ parameter is calculated to be 0.002876 and 0.003124 cm^{-1}, $c(X^2\Delta_{5/2})$ parameter is calculated to be -0.002465 and -0.002677 cm^{-1} for ^{191}IrSi and ^{193}IrSi, respectively. Combining c and a, the simple molecular orbital model predict that $h_{5/2}(X^2\Delta_{5/2})$=0.00493 cm^{-1} for ^{191}IrS and 0.00536 cm^{-1} for ^{193}IrSi. These values give a surprisingly good agreement in comparison with the

experimental values from Table 1, $h_{5/2}(X^2\Delta_{5/2})$=0.00501(13) and 0.00553(13) cm^{-1} for ^{191}IrSi and ^{193}IrSi, respectively.

Similar calculation was performed for the electric quadrupole hyperfine interactions by assuming that the field gradient at the Ir nucleus is the sum of the gradients associated with the bonding valence electrons and the gradients associated with the polarization of the core electrons. Using the radial expectation values $\left\langle r^{-3}\right\rangle \approx \left\langle 5d\left|r^{-3}\right|5d\right\rangle = 6.07\times10^{-25}\,cm^{-3}$, the quadrupole coupling parameters for IrSi are calculated to be:

$$eQq_0(X^2\Delta_{5/2}) = -\frac{e^2Q}{4\pi\varepsilon_0 hc}\left\langle\Lambda\left|\sum_i \frac{(3\cos\theta_i - 1)}{r^{-3}}\right|\Lambda\right\rangle \qquad (5)$$

The predicted value of the quadrupole coupling parameters in the $X^2\Delta_{5/2}(v=0)$ state for ^{191}IrSi (0.0373 cm^{-1}) and ^{193}IrSi (0.0343 cm^{-1}) are large and not in correct sign in comparison with the observation of -0.00334(63) and -0.00403(64) cm^{-1} for ^{191}IrSi and ^{193}IrSi. The calculation was done under the assumption that the molecule is in the form of $Ir^{+\delta}Si^{-\delta}$. However, the determined dipole moment $\mu(X^2\Delta_{5/2})$= -0.4139(64)D suggest that the molecule is in the form of $Ir^{-\delta}Si^{+\delta}$ in the ground state. Upon excitation, charge transfer occurs resulting in the dipole moment of [16.0]1.5 (v=6) state is 0.7821(63) D. These results suggest that the assumption was made earlier that the field gradient at the Ir nucleus in the ground state was not correct.

Table 6.1. Spectroscopic parameters in wavenumber (cm^{-1}) of the (6,0) [16.0]1.5-$X\,^2\Delta_{5/2}$ and (7,0) [16.0]3.5-$X\,^2\Delta_{5/2}$ bands for ^{193}IrSi, ^{191}IrSi.

States	Parameters	^{193}IrSi	^{191}IrSi
$^2\Delta_{5/2}$ (v=0)	B	0.157939(5)	0.158158(6)
	$h_{5/2}$(Ir)	0.00553(13)	0.00501(13)
	eQq_0(Ir)	-0.00403(64)	-0.00334(63)
	μ_{el}	-0.4139(64)D	
	T_0	(-18300)47.816747(75)	49.229956
[16.0]1.5 (v=6)	B	0.138469(5)	0.138656(5)
	$h_{1/2}$(Ir)	0.00622(21)	0.00533(22)
	eQq_0(Ir)	-0.00672(67)	-0.00518(79)
	μ_{el}	0.7821(63) D	
	T_0	(-18500)19.059713(90)	20.614422(92)
[16.0]3.5 (v=7)	B	0.133375(5)	0.133556(5)
	$h_{3/2}$(Ir)	0.00282(14)	0.00261(14)
	eQq_0(Ir)	-0.00389(67)	-0.00444(69)

Table 6.2 The observed and calculated line positions in wavenumber (cm^{-1}) of the (7.0)[16.0]3.5- $X^2\Delta_{5/2}$ band system of ^{191}IrSi. The line marked with (*) are the measurement from very slow scan and were enter twice in the total fit.

Lines	F'	F''	Observed	Obsed-Calced	Lines	F'	F''	Observed	Obsed-Calced
R(6.5)	9	8	18520.7589	0.0011	R(3.5)*	6	5	18520.7668	-0.0005
R(7.5)	10	9	18520.6568	0.0007		5	4	18520.7689	-0.0005
R(8.5)	11	10	18520.5067	0.0016		4	3	18520.7706	0.0000
R(9.5)	12	11	18520.3047	-0.0002		3	2	18520.7712	0.0000
R(10.5)	13	12	18520.0555	-0.0001		5	5	18520.7651	-0.0005
R(11.5)	14	13	18519.7570	0.0000		4	4	18520.7668	-0.0006
R(12.5)	15	14	18519.4093	0.0001		3	3	18520.7681	-0.0005
R(13.5)	16	15	18519.0123	0.0001	R(5.5)*	8	7	18520.8100	-0.0002
Q(5.5)	7	7	18519.0741	-0.0001		7	6	18520.8114	0.0001
Q(6.5)	8	8	18518.7553	0.0007		6	5	18520.8124	0.0003
Q(7.5)	9	9	18518.3863	0.0005		5	4	18520.8124	-0.0002
Q(8.5)	10	10	18517.9679	0.0002		7	7	18520.8081	-0.0004
Q(9.5)	11	11	18517.5009	0.0005	Q(3.5)*	5	5	18519.5651	-0.0005
Q(10.5)	12	12	18516.9850	0.0011		4	4	18519.5678	-0.0001
Q(11.5)	13	13	18516.4178	-0.0004		2	2	18519.5683	0.0007
Q(12.5)	14	14	18515.8030	-0.0003		3	3	18519.5683	0.0000

Q(13.5)	15	15	18515.1389	-0.0003		4	5	18519.5642	0.0001
Q(14.5)	16	16	18514.4263	0.0004		4	3	18519.5713	0.0001
Q(15.5)	17	17	18513.6632	-0.0002		3	2	18519.5709	0.0001
Q(16.5)	18	18	18512.8517	0.0000		3	4	18519.5651	0.0001
Q(17.5)	19	19	18511.9898	-0.0010	*Q*(4.5)*	6	6	18519.3441	-0.0005
P(5.5)	6	7	18517.6065	0.0011		5	5	18519.3465	0.0004
P(6.5)	7	8	18517.0184	-0.0002		4	4	18519.3465	-0.0001
P(7.5)	8	9	18516.3833	0.0007		3	3	18519.3465	0.0001
P(8.5)	9	10	18515.6975	0.0000		4	3	18519.3484	0.0000
P(9.5)	10	11	18514.9629	-0.0001		5	4	18519.3484	-0.0002
P(10.5)	11	12	18514.1796	0.0002		6	5	18519.3481	0.0003
R(2.5)*	5	4	18520.6717	0.0000		5	6	18519.3420	-0.0009
	4	3	18520.6746	-0.0004		4	5	18519.3441	0.0000
	3	2	18520.6766	-0.0003	*P*(4.5)*	5	6	18518.1427	-0.0001
	2	1	18520.6773	-0.0002		4	5	18518.1447	0.0001
	4	4	18520.6701	-0.0001		3	4	18518.1447	0.0005
	3	3	18520.6725	0.0004		2	3	18518.1427	-0.0001
	2	2	18520.6736	-0.0001		5	5	18518.1463	0.0002
R(4.5)*	7	6	18520.8132	-0.0002		4	4	18518.1474	0.0003
	6	5	18520.8148	-0.0001		3	3	18518.1463	0.0003
	5	4	18520.8161	0.0003					
	4	3	18520.8161	-0.0002					

Table 6.3. The observed and calculated line positions in wavenumber (cm^{-1}) of the (6,0)[16.0]1.5- $X^2\Delta_{5/2}$ band system of ^{191}IrSi. The line marked with (*) are the measurement from very slow scan and were enter twice in the total fit.

Lines	*F'F"*	Observed	Obsed-Calced	Lines	*F'F"*	Observed	Obsed-Calced
R(9.5)	12 11	18350.8622	0.0002	*Q*(5.5)*	7 7	18349.1981	-0.0005
*R(*10.5)	13 12	18350.7294	-0.0003		6 6	18349.1981	-0.0007
R(11.5)	14 13	18350.5583	-0.0001		5 5	18349.2003	0.0006
R(12.5)	15 14	18350.3483	0.0002		4 4	18349.2003	-0.0007
R(13.5)	16 15	18350.0991	0.0004	*R*(7.5)*	10 9	18351.0104	0.0010
R(14.5)	17 16	18349.8099	-0.0005		7 6	18351.0121	0.0005
R(15.5)	18 17	18349.4821	-0.0009	*P*(3.5)*	4 5	18348.6182	-0.0002
Q(7.5)	9 9	18348.6527	0.0001		3 4	18348.6182	0.0000
Q(9.5)	11 11	18347.9510	0.0005		2 3	18348.6182	-0.0007
Q(10.5)	12 12	18347.5411	0.0001		1 2	18348.6209	0.0010

Q(11.5)	13	13	18347.0939	0.0015		4	4	18348.6222	0.0000
Q(12.5)	14	14	18346.6049	0.0001		3	3	18348.6215	0.0000
Q(13.5)	15	15	18346.0778	-0.0003	*R*(4.5)*	7	6	18350.9382	0.0004
Q(14.5)	16	16	18345.5122	-0.0003		6	5	18350.9382	-0.0002
P(6.5)	7	8	18347.1421	-0.0008		5	4	18350.9397	-0.0001
P(7.5)	8	9	18346.5734	0.0003		4	3	18350.9422	0.0007
P(8.5)	9	10	18345.9627	-0.0016		5	5	18350.9371	-0.0002
P(9.5)	10	11	18345.3172	0.0008	*P*(2.5)*	3	4	18349.0322	-0.0001
P(10.5)	11	12	18344.6295	0.0000		2	3	18349.0317	0.0000
P(11.5)	12	13	18343.9034	-0.0002		1	2	18349.0310	-0.0002
P(12.5)	13	14	18343.1395	0.0008		0	1	18349.0322	0.0004
P(5.5)*	6	7	18347.6733	-0.0005		3	3	18349.0375	0.0005
	3	4	18347.6748	-0.0006		2	2	18349.0375	0.0010
Q(3.5)*	5	5	18349.5881	-0.0002		1	1	18349.0352	0.0002
	4	4	18349.5881	-0.0007	*R*(3.5)*	6	5	18350.8352	-0.0005
	3	3	18349.5910	0.0007		5	4	18350.8352	-0.0014
	2	2	18349.5921	0.0000		4	3	18350.8373	-0.0012
Q(4.5)*	6	6	18349.4119	-0.0011		3	2	18350.8399	-0.0008
	5	5	18349.4123	-0.0010		5	5	18350.8339	0.0011
	4	4	18349.4147	0.0002		4	4	18350.8352	-0.0001
	3	3	18349.4147	-0.0012	*Q*(2.5)*	4	4	18349.7256	0.0011
	5	6	18349.4106	0.0005		3	3	18349.7256	0.0003
P(4.5)*	5	6	18348.1651	-0.0005		2	2	18349.7275	-0.0001
	4	5	18348.1651	-0.0004		1	1	18349.7301	0.0003
	3	4	18348.1660	-0.0003		2	3	18349.7234	0.0007
	2	3	18348.1669	-0.0004		3	4	18349.7214	0.0009
	5	5	18348.1684	-0.0004		2	1	18349.7316	0.0002
	4	4	18348.1684	0.0004		1	2	18349.7256	-0.0004
	3	3	18348.1684	0.0003		4	3	18349.7301	0.0009
R(5.5)*	8	7	18351.0013	0.0006		3	2	18349.7301	0.0000
	7	6	18351.0016	0.0005	*R*(2.5)*	5	4	18350.6943	-0.0001
	6	5	18351.0019	-0.0003		4	3	18350.6952	-0.0007
	5	4	18351.0041	0.0004		3	2	18350.6984	-0.0006
	7	7	18350.9994	0.0011		2	1	18350.7022	0.0002
	6	6	18351.0002	0.0000		3	3	18350.6944	0.0002
						2	2	18350.6984	0.0002

Table 6.4 The observed and calculated line positions in wavenumber (cm^{-1}) of the (7,0)[16.0]3.5- $X^2\Delta_{5/2}$ band system of ^{193}IrSi. The line marked with (*) are the measurement from very slow scan and were enter twice in the total fit.

Lines	*F'*	*F''*	Observed	Obsed-Calced	Lines	*F'*	*F''*	Observed	Obsed-Calced
R(7.5)	10	9	18519.1014	0.0000	R(3.5)*	6	5	18519.2122	0.0000
R(8.5)	11	10	18518.9514	0.0007		5	4	18519.2147	0.0002
R(9.5)	12	11	18518.7514	0.0005		4	3	18519.2165	0.0006
R(10.5)	13	12	18518.5024	0.0004		3	2	18519.2165	-0.0002
R(11.5)	14	13	18518.2032	-0.0007		5	5	18519.2105	0.0002
Q(5.5)	7	7	18517.523	0.0014		3	3	18519.2147	0.0008
Q(6.5)	8	8	18517.2033	0.0008	*R*(4.5)*	7	6	18519.2584	0.0000
Q(7.5)	9	9	18516.8347	0.0005		6	5	18519.2603	0.0003
Q(8.5)	10	10	18516.4178	0.0010		5	4	18519.2619	0.0008
Q(9.5)	11	11	18515.9499	-0.0003		4	3	18519.2619	0.0002
Q(10.5)	12	12	18515.4345	0.0000	*Q*(3.5)*	5	5	18518.0115	-0.0007
Q(11.5)	13	13	18514.8697	0.0000		4	4	18518.0143	-0.0003
Q(12.5)	14	14	18514.2558	0.0000		2	2	18518.0143	-0.0004
Q(13.5)	15	15	18513.5926	-0.0001		3	3	18518.0143	-0.0008
Q(14.5)	16	16	18512.88	-0.0005		4	5	18518.0097	-0.0007
Q(15.5)	17	17	18512.1181	-0.0011		4	3	18518.0181	0.0000
Q(16.5)	18	18	18511.3083	-0.0004		3	2	18518.0181	0.0002
Q(17.5)	19	19	18510.4496	0.0005		5	4	18518.0158	-0.0006
P(5.5)	6	7	18516.0556	0.0008	*Q*(4.5)*	6	6	18517.7918	0.0003
P(6.5)	7	8	18515.4691	0.0003		5	5	18517.7935	0.0003
P(7.5)	8	9	18514.8337	-0.0001		4	4	18517.7935	-0.0003
P(8.5)	9	10	18514.149	-0.0006		3	3	18517.7935	-0.0002
P(9.5)	10	11	18513.4162	-0.0001		4	3	18517.7957	0.0000
P(10.5)	11	12	18512.634	0.0002		5	4	18517.7957	-0.0002
P(11.5)	12	13	18511.8024	0.0002		6	5	18517.7957	0.0006
P(12.5)	13	14	18510.9221	0.0006		5	6	18517.7899	0.0003
R(2.5)*	5	4	18519.1163	-0.0004	*R*(6.5)*	9	8	18519.2029	0.0000
	4	3	18519.1201	0.0001		8	7	18519.2039	-0.0001
	3	2	18519.1227	0.0003		7	6	18519.2046	-0.0001
	2	1	18519.1238	0.0003		6	5	18519.2048	-0.0003
	4	4	18519.1148	-0.0001	*P*(4.5)*	5	6	18516.5913	-0.0002
	2	2	18519.119	-0.0002		4	5	18516.5928	-0.0004
R(5.5)*	8	7	18519.2553	0.0001		3	4	18516.5928	-0.0001

7	6	18519.2568	0.0003	2	3	18516.5913	-0.0004
6	5	18519.2571	-0.0003	5	5	18516.5945	-0.0006
5	4	18519.2584	0.0005	4	4	18516.5953	-0.0007
7	7	18519.2533	-0.0001	3	3	18516.5945	-0.0004

Table 6.5. The observed and calculated line positions in wavenumber (cm^{-1}) of the (6,0)[16.0]1.5- $X^2\Delta_{5/2}$ band system of ^{193}IrSi. The line marked with (*) are the measurement from very slow scan and were enter twice in the total fit.

Lines	*F'*	*F''*	Obseved	Obsed-Calced	Lines	*F'*	*F''*	Obseved	Obsed-Calced
R(9.5)	12	11	18349.4467	-0.0003	*R*(5.5)*	8	7	18349.5851	-0.0002
R(10.5)	13	12	18349.3146	-0.0004		7	6	18349.5858	0.0003
R(11.5)	14	13	18349.1444	0.0003		7	7	18349.5833	0.0010
R(12.5)	15	14	18348.9337	-0.0004	*Q*(3.5)*	5	5	18348.1744	-0.0003
R(13.5)	16	15	18348.6852	-0.0001		4	4	18348.1754	0.0004
R(14.5)	17	16	18348.3972	-0.0002		3	3	18348.1762	-0.0004
R(15.5)	18	17	18348.0702	-0.0004		2	2	18348.1787	0.0001
R(16.5)	19	18	18347.704	-0.0009		3	2	18348.1786	-0.0008
R(17.5)	20	19	18347.2996	-0.0006		5	4	18348.1786	-0.0003
Q(7.5)	9	9	18347.2415	0.0010		4	3	18348.1786	0.0000
Q(8.5)	10	10	18346.9102	0.0007		4	5	18348.1704	-0.0004
Q(9.5)	11	11	18346.5392	-0.0004		3	4	18348.1727	-0.0003
Q(10.5)	12	12	18346.1308	0.0002	*Q*(4.5)*	6	6	18347.9998	0.0001
Q(11.5)	13	13	18345.6831	0.0004		5	5	18348.0002	0.0004
Q(12.5)	14	14	18345.1966	0.0007		4	4	18348.0004	-0.0006
Q(13.5)	15	15	18344.6699	-0.0002		3	3	18348.003	0.0003
Q(14.5)	16	16	18344.1058	0.0005		5	6	18347.9959	-0.0003
Q(15.5)	17	17	18343.5022	0.0006		3	4	18347.9998	-0.0009
Q(16.5)	18	18	18342.8589	-0.0001		6	5	18348.003	-0.0003
P(6.5)	7	8	18345.7336	0.0007		5	4	18348.003	0.0005
P(7.5)	8	9	18345.1641	0.0002		4	3	18348.003	0.0000
P(8.5)	9	10	18344.5554	-0.0005	*R*(4.5)*	7	6	18349.5227	0.0003
P(9.5)	10	11	18343.9092	0.0002		6	5	18349.5227	-0.0001
P(10.5)	11	12	18343.2237	0.0005		5	4	18349.5243	0.0000
P(11.5)	12	13	18342.4983	0.0000		4	3	18349.5265	0.0002
P(12.5)	13	14	18341.7341	-0.0005		5	5	18349.5215	-0.0001
P(13.5)	14	15	18340.9314	-0.0005		4	4	18349.5252	0.0008
R(7.5)*	10	9	18349.5949	0.0008	*P*(2.5)*	3	4	18347.6199	0.0003

	7	6	18349.5972	0.0009		2	3	18347.6192	0.0006
R(8.5)*	11	10	18349.5399	-0.0002		1	2	18347.6174	-0.0003
	8	7	18349.5419	-0.0001		0	1	18347.6192	0.0010
P(5.5)*	6	7	18346.2629	0.0000		3	3	18347.6243	-0.0004
	3	4	18346.2641	-0.0004		2	2	18347.6243	0.0003
R(2.5)*	5	4	18349.2787	-0.0005		1	1	18347.6217	-0.0003
	4	3	18349.2797	-0.0008	*P*(3.5)*	4	5	18347.206	-0.0002
	3	2	18349.2829	-0.0010		3	4	18347.206	0.0003
	2	1	18349.2869	-0.0005		2	3	18347.2072	0.0008
	4	4	18349.2736	-0.0017		1	2	18347.208	0.0006
	3	3	18349.2787	0.0002		3	3	18347.209	-0.0003
	2	2	18349.2817	-0.0014		4	4	18347.2099	-0.0005
Q(2.5)*	4	4	18348.3105	-0.0002	Q(5.5)*	7	7	18347.7865	0.0009
	3	3	18348.3105	-0.0007		6	6	18347.7865	0.0009
	2	2	18348.3147	0.0010		5	5	18347.7875	0.0009
	1	1	18348.3161	-0.0001		4	4	18347.7885	0.0004
	4	3	18348.3161	0.0002		6	7	18347.7828	0.0004
	3	2	18348.3161	-0.0005		5	6	18347.7847	0.0003
R(3.5)*	6	5	18349.4202	-0.0002		7	6	18347.7904	0.0016
	5	4	18349.4202	-0.0009		5	4	18347.7885	0.0005
	4	3	18349.4225	-0.0007		6	5	18347.7885	0.0007
	3	2	18349.4254	-0.0003		4	5	18347.7865	-0.0002
P(4.5)*	5	6	18346.7536	-0.0004	*R*(6.5)*	9	8	18349.6095	0.0003
	4	5	18346.7536	-0.0001		8	7	18349.6095	0.0002
	3	4	18346.7541	-0.0003		7	6	18349.6108	0.0005
	2	3	18346.7551	-0.0005		6	5	18349.612	0.0002
	5	5	18346.7581	0.0005		8	8	18349.6063	-0.0001
						7	7	18349.6075	-0.0009

Table 6.6. Observed and calculated Stark shifts for the (6,0) [16.0]1.5-$X\,^2\Delta_{5/2}$ band of Q(5/2) of ^{191}IrSi and P(5/2) of ^{191}IrSi

Lines[a] and polarization	*mF*'	*mF*''	Field[b] (V)	Observed shift (MHz)	Obs-Calced (MHz)	Lines[a] and polarization	*mF*'	*mF*''	Field[b] (V)	Observed shift (MHz)	Obs-Calced (MHz)
P(5/2) ∥	2	2	4000	687.9	44.0	P(5/2) ⊥	1	2	3000	-369.9	-25.6
	3	3	4000	656.7	-18.3		2	3	3000	-257.1	3.7
	0	0	4000	-486.6	19.5		0	1	3000	-429.2	-18.9
	0	0	4000	-486.6	19.5		3	4	3000	-295.4	7.0
	1	1	4000	-454.1	9.8		1	2	3000	-182.9	3.2

2	2	4000	-385	22.1		0	1	3000	-285	-13.3
3	3	4000	-329.5	28.6		2	3	3000	-114.1	-17.7
0	0	4000	-473.8	8.2		1	2	3000	-178	-3.6
0	0	4000	-473.8	8.2		1	2	3000	-261.8	14.0
3	3	4000	634.1	3.2		2	3	3000	-206.6	25.7
2	2	4000	524.3	12.4		0	1	3000	-323.9	10.8
0	0	4000	398.8	10.0		1	0	3000	-203.8	-11.2
0	0	4000	398.8	10.0		1	2	3000	-187.8	-22.2
1	1	4000	416.7	7.1		1	2	3000	-135.7	-29.8
2	2	4000	-245	-6.7		0	1	3000	414.6	25.0
3	3	4000	-202.4	-25.8		1	2	3000	367.3	9.6
1	1	4000	-275	39.7		2	3	3000	429.3	8.8
0	0	4000	-430.33	18.3		3	4	3000	537.9	21.5
0	0	4000	-430.33	18.3		0	1	3000	355.2	13.7
2	2	4000	-222.4	-20.5		0	1	3000	170.3	25.0
1	1	4000	-260.3	18.4		1	2	3000	240.2	-14.9
1	1	4000	-321.2	-10.5		1	0	3000	104.1	40.8
2	2	4000	-321.2	-22.0		1	2	3000	277	31.4
1	1	4000	-158.9	29.2		1	2	2000	149.8	-18.8
1	1	4000	-131.2	21.8		2	3	2000	359.5	-15.4
2	2	4000	-100.3	30.2		3	4	2000	326.6	33.5
1	1	4000	-143.3	6.7		3	4	2000	-249.6	16.1
1	1	4000	200	-11.9		0	1	2000	-226.9	33.1
1	1	4000	-121	-23.3		2	3	2000	0	17.6
0	0	4000	131.2	-2.6		1	2	2000	0	9.8
0	0	4000	131.2	-2.6	Q(5/2)II	3	3	4000	-533.4	5.7
1	1	4000	232.3	28.9		2	2	4000	-533.4	12.7
1	1	4000	283.5	44.0		1	1	4000	-533.4	-4.1
2	2	4000	103	8.1		4	4	4000	-477	25.9
1	1	4000	322.4	14.5		2	2	4000	-356	31.4
2	2	4000	483.9	31.8		1	1	4000	-356	30.1
0	0	4000	256.6	15.0		3	3	4000	-356	9.4
0	0	4000	256.6	15.0		3	3	4000	-300.25	16.9
1	1	4000	292.7	22.9		2	2	4000	-300.25	22.1
0	0	4000	295.7	14.7		1	1	4000	-300.25	-2.4
0	0	4000	295.7	14.7		0	0	4000	-242.6	7.4
3	3	3500	584.9	-8.1		0	0	4000	-242.6	7.4
2	2	3500	558.9	20.1		1	1	4000	-369.7	20.2
1	1	3500	592.9	2.4		2	2	4000	-356.1	-4.9
0	0	3500	-400.8	24.4		3	3	4000	-152.8	-9.4

0	0	3500	-400.8	24.4
1	1	3500	-337.2	35.9
2	2	3500	-253.9	52.4
3	3	3500	-198.7	52.8
0	0	3500	-352.91	54.1
0	0	3500	-352.91	54.1
2	2	3500	-107.2	36.3
3	3	3500	-162.7	28.0
1	1	3500	-196.9	33.5
0	0	3500	-335.1	48.7
0	0	3500	-335.1	48.7
1	1	3500	-209.1	53.4
2	2	3500	-209.4	29.5
1	1	3500	-130.1	37.0
1	1	3500	-175.7	38.0
0	0	3500	-296.7	-8.4
0	0	3500	-296.7	-8.4
1	1	3500	-137.7	-32.3
1	1	3500	-102.4	35.9
1	1	3500	-131.8	-15.6
0	0	3500	123.9	25.0
0	0	3500	123.9	25.0
0	0	3500	133.3	16.2
0	0	3500	133.3	16.2
0	0	3500	108.5	30.2
0	0	3500	108.5	30.2
0	0	3500	203.6	29.3
0	0	3500	203.6	29.3
0	0	3500	217.3	24.8
0	0	3500	217.3	24.8
1	1	3500	217.3	8.6
1	1	3500	196.1	18.1
0	0	3500	242.2	6.5
0	0	3500	242.2	6.5
0	0	3500	192.9	-22.8
0	0	3500	192.9	-22.8
2	2	3500	397.7	20.4
1	1	3500	296.5	59.0
2	2	3500	156.1	-7.1
3	3	3500	539.5	4.8
2	2	4000	-248.8	-0.3
0	0	4000	-235.2	-9.8
0	0	4000	-235.2	-9.8
0	0	4000	-73.5	7.2
0	0	4000	-73.5	7.2
1	1	4000	-118.8	39.6
2	2	4000	-118.8	8.6
1	1	4000	514.8	-7.8
2	2	4000	463.9	-3.5
1	1	4000	427.3	0.0
3	3	4000	380.8	-18.1
4	4	4000	432.6	-18.3
2	2	4000	325.1	-6.3
1	1	4000	267	13.3
3	3	4000	232	2.7
0	0	4000	232	9.9
0	0	4000	232	9.9
2	2	4000	337.1	2.8
3	3	4000	448.6	14.1
0	0	4000	248.3	42.9
0	0	4000	248.3	42.9
1	1	4000	142	-7.2
2	2	4000	264.7	-6.8
3	3	4000	264.7	-0.3
1	1	4000	125.3	4.0
0	0	4000	107.8	4.0
0	0	4000	107.8	4.0
2	2	4000	136	0.4
3	3	3000	-379.8	-15.6
2	2	3000	-379.8	2.3
1	1	3000	-379.8	-0.4
4	4	3000	-308.7	7.8
1	1	3000	-383.7	-4.0
2	2	3000	-238.2	-3.1
3	3	3000	-196.8	12.3
2	2	3000	-196.8	2.2
1	1	3000	-196.8	-5.1
3	3	3000	-217.5	4.0
1	1	3000	-247.8	6.7
2	2	3000	-213	9.3

1	1	3500	442.7	0.7
2	2	3500	445.7	24.0
0	0	3500	314.6	3.4
0	0	3500	314.6	3.4
1	1	3500	314.6	-11.9
0	0	3000	-378.5	-31.8
0	0	3000	-378.5	-31.8
1	1	3000	-304	-18.6
2	2	3000	-230.9	-23.1
0	0	3000	-346.2	-12.7
0	0	3000	-346.2	-12.7
3	3	3000	-250.5	4.2
1	1	3000	-286.9	-2.9
0	0	3000	-310.3	8.6
0	0	3000	-310.3	8.6
1	1	3000	-149.6	-4.1
1	1	3000	-232.5	-15.6
2	2	3000	-202	-22.7
1	1	3000	-163.4	-15.2
0	0	3000	-270.3	-28.6
0	0	3000	-270.3	-28.6
1	1	3000	-195.6	20.0
1	1	3000	-110.5	17.5
1	1	3000	-118.3	-11.7
1	1	3000	189.4	-1.8
3	3	3000	494.7	10.7
2	2	3000	421	-13.8
1	1	3000	496.4	6.4
1	1	3000	256	10.3
0	0	3000	256	17.7
0	0	3000	256	17.7
2	2	3000	346.4	14.2
1	1	3000	360.1	-17.9
3	3	3000	465.4	27.3
1	1	3000	187.9	19.2
1	1	3000	167.4	-1.3
0	0	3000	167.4	6.3
0	0	3000	201.7	11.5
0	0	3000	201.7	11.5
2	2	3000	301.7	3.3
1	1	3000	-196.3	-4.2
2	2	3000	-143.1	11.3
1	1	3000	-87.1	-13.2
3	3	3000	-87.1	-20.7
0	0	3000	-158.3	-5.1
0	0	3000	-158.3	-5.1
0	0	3000	-58.4	-19.1
0	0	3000	-58.4	-19.1
2	2	3000	-30	9.1
0	0	3000	-116.7	17.9
0	0	3000	-116.7	17.9
1	1	3000	382.8	20.5
2	2	3000	319.8	17.4
1	1	3000	275	-5.1
3	3	3000	341.7	2.5
2	2	3000	160.6	-26.0
4	4	3000	444.2	32.8
0	0	3000	148.3	11.7
0	0	3000	148.3	11.7
1	1	3000	148.3	16.3
2	2	3000	204.4	4.9
3	3	3000	204.4	8.9
2	2	3000	191.9	30.1
3	3	3000	298.2	11.4
0	0	3000	165	25.8
0	0	3000	165	25.8
0	0	3000	83.9	28.9
0	0	3000	83.9	28.9
1	1	3000	83.9	30.1
1	1	3000	77	26.1
2	2	3000	168	8.3
3	3	3000	102	-41.2
2	2	3000	44	0.2
0	0	3000	44	7.6
0	0	3000	44	7.6

1	1	3000	156.5	22.9	
1	1	3000	304.7	1.5	
0	0	3000	158.5	12.0	
0	0	3000	158.5	12.0	
0	0	3000	106.4	-6.6	
0	0	3000	106.4	-6.6	
1	1	3000	-102.8	-23.1	
0	1	3000	-440.5	-28.9	Rms=21.01 MHz σ^2=21.01 MHz

[a] P(5/2) lines is ^{193}IrSi, Q(5/2) lines is ^{191}IrSi isotopologue

[b] Spacing of the Stark plates is 1.71±0.02 cm.

6.2. Conclusion

In this thesis the electronic transitions of ^{87}SrF, $^{135\&137}$BaF, HfF, and IrSi have been recorded at high resolution, ~ 30MHz, using laser induced fluorescence detection/laser ablation for sample preparation technique. The fine and hyperfine structures of these molecules have been accurately measured and analyzed. Stark shifts of ^{180}HfF, and IrSi had been measured and analyzed to determine the permanent electric dipole moments of both ground and excited electronic states. The low-resolution electronic spectrum of ZrO_2, and lifetime measurements of TiO_2 and ZrO_2 have been recorded. Vibrational analysis and multi-dimensional Franck-Condon factor (FCFs) calculations were performed for TiO_2 and ZrO_2.

The predicted Zeeman tuning for ^{87}SrF, and $^{135\&137}$BaF in the region of interest where the opposite parity energy levels are nearly degenerate, have been predicted. Since this is the relevant region for parity non-conservation (PNC) measurement, sensitive LIF detection schemes have been developed. DeMille [17] at Yale University, is currently attempting to measure the anapole moment using our ^{137}BaF results. Recently, Prof. Steven Hoekstra at Kernfysisch Versneller Instituut (University of Groningen, The

Netherlands) proposed to carry out the anapole moment measurement of the nucleus using ultra-cold, magnetically trapped ^{87}SrF. The latter work build upon our spectroscopy results.

The calculated and measured FCF for YbF are important contributions to current eEDM experiments being performed by Prof. Ed Hinds's group at Imperial College (UK). The magnetic hyperfine, quadrupole parameters and molecular electric dipole moment (μ_{el}) for ^{177}HfF, ^{179}HfF, ^{180}HfF were experimentally determined. HfF^+ is a more recent target for eEDM in comparison with YbF. Prof. Cornell at U. Colorado is currently using HfF^+ for eEDM experiments. Knowing the spectroscopy of the neutral HfF is relevant because photo-ionization schemes can be used to produce the cations. Our experimentally determined values for μ_{el} and hyperfine parameters are benchmark data for the computational community to improve their method for precisely calculating Ψ_{el}, which is critical for the PNC experiments. Currently our collaborator Prof. A. Titov is using a two-step method for calculating the core properties, in combination with a two-component relativistic Fock-space CCSD method. This two-step method includes: (i) treatment of the electron correlation for valence and outer core electrons, inner-core electrons are excluded from calculation using the GRECP method, and (ii) recovery of the inner-core structure of wavefunction using a non-variational one-center restoration procedure. The results of these high level two-step calculations for hyperfine constants differ by less than 10% from the corresponding experimental data. However, an uncertainty of 10% in calculation should have no impact on the eEDM experiment result [18].

Studies of the properties of transition metal silicides have been motivated in part by their potential use in electronic technology. Transition metal silicides have many technological desirable physical properties including: low resistivity, high melting points, low density, and resistance to oxidation. Understanding the chemical bonding between the metal atom and silicon atom will shed light onto the process of obtaining the low Schottky barrier height. One surprising result was the determination of the negative dipole moment in the $X^2\Delta_{5/2}$ state. This is the first determination of a negative dipole moment for those metal-containing diatomic molecules. The negative dipole moment in the ground state indicates that silicon is acting like a metal (donating electron) in IrSi. However, upon excitation, charge transfer occurs resulting in the positive dipole moment. The positive dipole moment indicates that silicon is acting like a non-metal (accepting electron) in the excited state. The transfer back and forth upon excitation confirms the metalloid properties of silicon.

Studies on the bonding of triatomic metal-dioxides, TiO_2 and ZrO_2, are important to physical sciences because, in part, they are the basic building blocks of large metal clusters. These simple metal dioxides TiO_2 and ZrO_2 are biradicals in the excited state and exhibit complicated electronic spectra. Solid TiO_2 is well known for its technological applications in photo-catalysis [19], and semiconductor technology [20]. The literature is full of electronic structure predictions for TiO_2 and ZrO_2. However, these are the first report on experimental results which can be used to evaluate those predictions. Numerous studies have focused on trying to find the best metal doping to shift the photo-activation threshold to the visible spectrum. Understanding the properties of gas-phase TiO_2 from the UV to visible spectrum will help in this process. Unlike TiO_2, the isovalent ZrO_2 does

not have many technological applications in photo-catalysis and semi-conductor. The vibrational spectra in the ground and excited state of ZrO_2 appear much more complicated than those of TiO_2. Unlike the observed spectrum of TiO_2, the forbidden odd-ν_3 (b_1-symmetry) transition intensities are nearly equal to those of the symmetry allowed transitions, this is maybe a result of spin-orbit coupling effects. High-resolution field free and Stark spectra of ZrO_2 have been recorded and are shown in Figure 6.7 and Figure 6.8, respectively. However, zirconium has several isotopes, hence the spectral features of all ZrO_2 isotopologues are overlapped in the 10 cm^{-1} recorded region. An analysis of the high-resolution of ZrO_2 is needed and this requires technique that can separately detect different isotopologue (i.e. REMPI is prefered). The low-resolution LIF spectrum of the product of ablated Hf with O_2 has been recorded (Figure 6.9) but not assigned. Accordingly, further work needs to be performed.

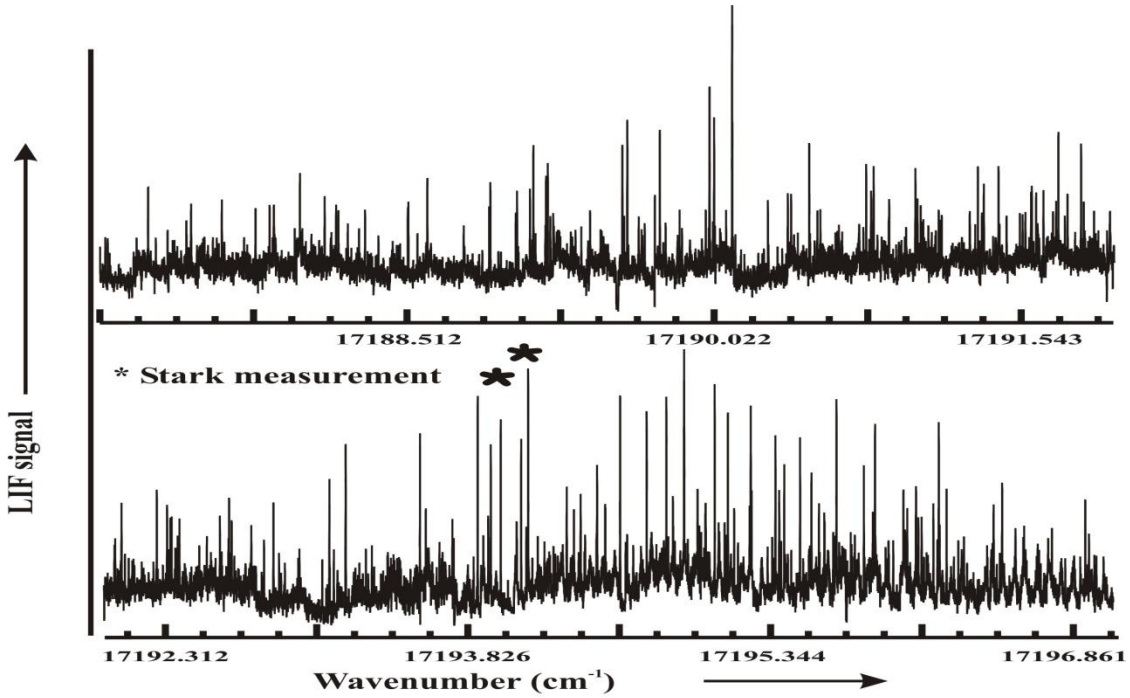

Figure 6.7. The observed high-resolution LIF $A^1B_1(0,1,0) \leftarrow X^1A_1(0,0,0)$ band of ZrO_2. The spectral features marked "*"were selected to do the Stark shift.

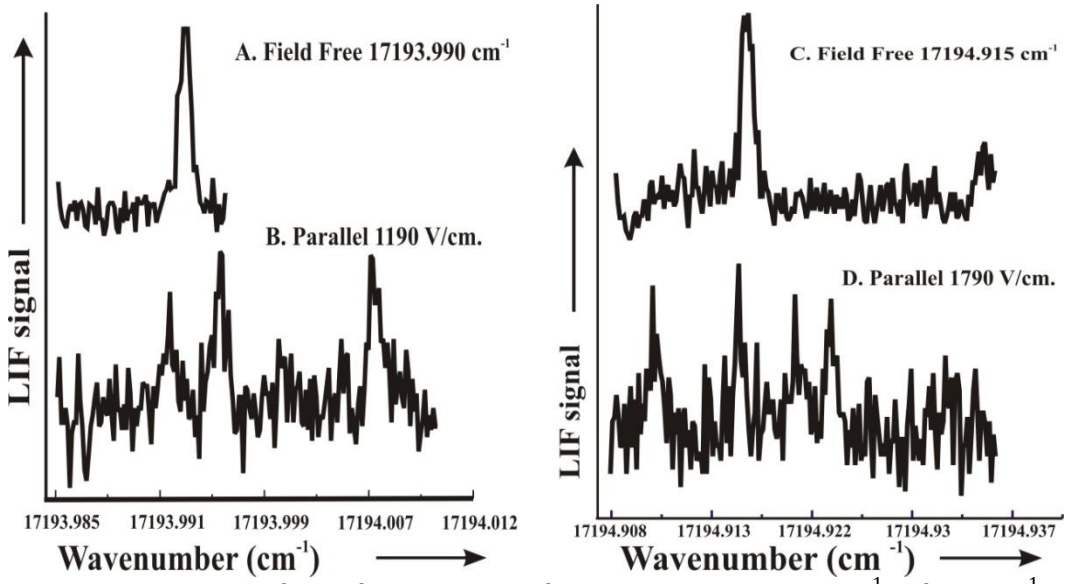

Figure 6.8. (A)the field free spectral feature at 17193.990cm^{-1} of the $A^1B_1(0,1,0) \leftarrow X^1A_1(0,0,0)$ transition. (B) The spectral feature at 17193.990 $cm^{-1}$with the presence of 1190V/cm parallel polarization. (C) The field free spectral feature at 17194.915 $cm^{-1}$of

the $A^1B_1(0,1,0) \leftarrow X^1A_1(0,0,0)$ transition, (D) The spectral feature at 17194.915 cm^{-1} with the presence of 1790V/cm parallel polarization.

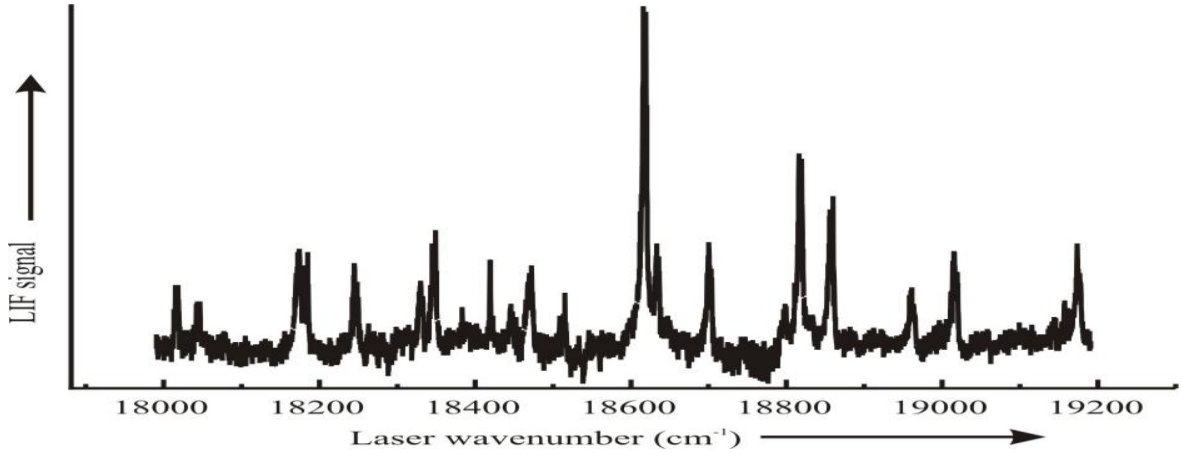

Figure 6.9. The observed laser induced fluorescence (LIF) spectrum of ablated $Hf+O_2$.

References

1. X. B. Liu, L. G. Yu, and H. M. Wang, J. Mater. Sci. Lett. **20**, 1489, (2001).

2. J. Kurianski, J. Van Damme, J. Vermeiren, K. Maex, and C. Claeys, Proc.SPIE1308,27,(1990).

3. G. Larrieu, E. Dubois, X. Wallart, and J. Katcki, J. Appl. Phys. **102**, 094504 (2007).

4. T. Ma, J. W.-H. Leung, and A. S.-C. Cheung, Chem. Phys. Lett. **385**, 259, (2004).

5. A. J. Marr, M. E. Flores, and T. C. Steimle, J. Chem. Phys. **104**, 8183 (1996)

6. K. Jansson and R. Scullman, J. Mol. Spectrosc. **43**, 208 (1972)

7. A. G. Adam, A. G. Granger, L. E. Downie, D. W. Tokaryk, and C. Linton, Can. J. Phys. **87**, 557 (2009)

8. X. Zhuang,T. C. Steimle,and C. Linton, J. Chem. Phys. **133**, 164310 (2010);

9. C. Linton, X. Zhuang, T. C. Steimle, and Allan G. Adam, J. Chem. Phys. **135**, 034305 (2011).

10. J.-G., Han, Chemical Physics, 286, 181-192 (2003)

11. Z.J., Wu, Z.M., Su, Journal of chemical physics, **124,** 184306 (2006).

12. M. A. Garcia, C. Vietz, F. Ruiprez, M. D. Morse, and I. Infante, K. Fakultatea, E. Herriko. *J. Chem. Phys.*, (submitted)

13. J.M. Brown and A. Carrington in *Rotational Spectroscopy of Diatomic Molecules*, Cambridge University Press, Cambridge, (2003)

14. S. Büttgenbach, R. Dicke, H. Gebauer, R. Kuhnen, and F. Träber, Z. Phys. A **286**, 333 (1978)

15. G. Sawatzky and R. Winlker, Z. Phys. D, **14**, 9 (1989).

16. L. Gianfrani and G. M. Tino, Z. Phys. D **25**, 113 -116 (1993).

17. D. DeMille; S. B. Cahn, D. Murphree, D Rahmlow; M G Kozlov, Phys. Rev. Lett. **100,** 023003,1-4 (2008).

18. J. J. Hudson, D. M. Kara, I. J. Smallman, B. E. Sauer, M. R. Tarbutt, and E. A. Hinds, Nature, **473**, 493–496, (2011)

19. K. Hashimoto, H. Irie, and A. Fujishima, Japanese Journal of Applied Physics, **44**(12), 8269–8285, (2005).

20 W-J, Yin, H Tang, S-H. Wei, M. M. A-J., J. Turner, and Y. Yan, Phys. Rev. B, **82**, 045106, (2010).

APPENDIX A

MATHEMATICA NOTEBOOK TO CALCULATE FRANCK-CONDON FACTOR FOR TITANIUM DIOXIDE

h=6.626`20.*10^{-34};

c=2.9979`20.*10^{10};

hbar=h/(2π);(*J.s/rad*);

atm=1.660538*10^{-27};

ω1Up=2*π*c*876.00`20;

ω2Up=2*π*c*184.0`20;

ω1Lo=2*π*c*968.000`20;

ω2Lo=2*π*c*323.0`20 ;

J={{1.026, -.0164}, {.017, .9743}}; (*J=1.026-.0164 0.017.9743 Duschinsky matrix*)

D0={{-.076},{0.775}}; (* -.287 0.622 ;D0=.229 1.478 differences*)

Alpha1Up=(ω1Up*atm)/hbar *10^{-20};(*ω angular frequency of the oscillators, in 1/m^2*)

Alpha2Up=(ω2Up*atm)/hbar*10^{-20}; (*ω angular frequency of the oscillators, in 1/m^2*)

Alpha1Lo=(ω1Lo*atm)/hbar *10^{-20} ;(*ω angular frequency of the oscillators, in 1/m^2*)

Alpha2Lo=(ω2Lo*atm)/hbar*10^{-20}; (*ω angular frequency of the oscillators, in 1/m^2*)

A1=(1/2)*(Alpha1Up+Alpha1Lo*J[[1,1]]^2+Alpha2Lo*J[[2,1]]^2);

B1=(1/(2A1))*(Alpha1Lo*J[[1,1]]*J[[1,2]]+Alpha2Lo*J[[2,1]]*J[[2,2]]);

C1=(1/(2A1))*(Alpha1Lo*J[[1,1]]*D0[[1,1]]+Alpha2Lo*J[[2,1]]*D0[[2,1]]);

A2=(1/2)*(Alpha2Up+Alpha1Lo*J[[1,2]]^2+Alpha2Lo*J[[2,2]]^2)-A1*B1^2;

C2=(1/(2A2))*(Alpha1Lo*J[[1,2]]*D0[[1,1]]+Alpha2Lo*J[[2,2]]*D0[[2,1]]-
2*A1*B1*C1);

E0=Exp[-(1/2)Alpha1Lo*D0[[1,1]]^2-1/2Alpha2Lo*D0[[2,1]]^2+A1*C1^2+A2*C2^2]

$a1=\sqrt{\text{Alpha1Up}}$; $a2=-\sqrt{\text{Alpha1Up}}$*B1; $b1=-\sqrt{\text{Alpha1Up}}$ (C1-B1*C2);

$a3 = \sqrt{Alpha2Up}$; b2=-$\sqrt{Alpha2Up}$*C2 ;

F1=(2/A1)$^{1/2}$*a1; F2=(2/A2)$^{1/2}$*a2; F3=(2/A2)$^{1/2}$*a3;

$Nu[v1\_, v2\_] := (\sqrt{Alpha1Up * Alpha2Up * Alpha1Lo * Alpha2Lo} / (2^{(v1+v2)} v1!v2!A1*A2))^{1/2}$

$$H[v1\_,v2\_] := \sum_{k1=0}^{v1} \sum_{k2=0}^{v1-k1} \sum_{k3=0}^{v2} \left(\frac{v1!}{k1!(v1-k1)!} * \frac{(v1-k1)!}{k2!(v1-k1-k2)!} * \frac{v2!}{k3!(v2-k3)!} *\right.$$

HermiteH[v1-k1-k2,b1]*HermiteH[v2-k3,b2]*F^{k1}*F^{k2}*F^{k3}*

If[EvenQ[k1]&&EvenQ[k2+k3],(k1-1)!!*(k2+k3-1)!!,0])

Overlab[v1_,v2_]:=Nu[v1,v2]*E0*H[v1,v2]

FCF[v1_,v2_]:= Overlab[v1,v2]^2

TableForm[Table[{v2,FCF[0,v2],FCF[1,v2],FCF[2,v2],FCF[3,v2],FCF[4,v2],FCF[5,v2],

FCF[6,v2]},{v2,0,20,1}]]

ω3Up=2*π*c*316`20. ;Be

ω3Lo=2*π*c*946`20 ;

Alpha3Up=(ω3Up*atm)/hbar *10^{-20};(*ω angular frequency of the oscillators, in 1/m^2*)

Alpha3Lo=(ω3Lo*atm)/hbar *10^{-20} ;(*ω angular frequency of the oscillators, in 1/m^2*)

d=.0; (*xUp-xLo;*)

bLo=(Alpha3Up* $\sqrt{Alpha3Lo}$ *d)/(Alpha3Up+Alpha3Lo);

bUp=(Alpha3Lo* $\sqrt{Alpha3Up}$ *d)/(Alpha3Up+Alpha3Lo);

(*y=xLo +(Alpha3Up*d)/(Alpha3Up+Alpha3Lo);*)

A=2*($\sqrt{Alpha3Lo}$ * $\sqrt{Alpha3Up}$)/(Alpha3Lo+Alpha3Up);

S=(Alpha3Lo*Alpha3Up*d^2)/(Alpha3Up+Alpha3Lo);

$$FCF[v3\_]:=((A*e^{(-S)})/(2^{v3}*v3!))\left(\sum_{kUp=0}^{v3}\left(\frac{v3!}{kUp!(v3-kUp)!}\right)\right)*HermiteH[0,bLo]*$$

$$HermiteH[v3-kUp,bUp]*(2*\sqrt{Alpha3up})^{kUp}$$

$$If[EvenQ[kUp],\frac{(2*\frac{kUp}{2}-1)!!}{(Alpha3Lo+Alpha3Up)^{\frac{kUp}{2}}},0])^2$$

FCFtotal[v1_,v2_,v3_]:=FCF[v1,v2]*FCF3[v3]

A=TableForm[Table[{{v2,v3},FCFtotal[0,v2,v3],FCFtotal[1,v2,v3],FCFtotal[2,v2,v3],FCFtotal[3,v2,v3],FCFtotal[4,v2,v3],FCFtotal[5,v2,v3],FCFtotal[6,v2,v3]},{v2,0,10,1},{v3,0,10,2}]]

APPENDIX B

MATHEMATICA NOTEBOOK TO CALCULATE NORMAL MODE ANALYSIS FOR C_{2V} TRIATOMIC MOLECULE WITH AN EXAMPLE OF ZIRCONIUM DIOXIDE

(*Grond state*)

h=6.626`20.*10^(-34) ;

c=2.9979`20.*10^10;

hbar=h/(2π);(*J.s/rad*);

atm=1.660538*10^(-27);

mO=15.994;

mZr=89.904703;

μ1=1/mO;

μ2=1/mZr;

ϕgrnd=108.11;(*Degree*)

tgrnd=Cos[ϕgrnd/2 Degree];

sgrnd=Sin[ϕgrnd /2 Degree];

ωLo1=897.9515;

ωLo2=297;

ωLo3=807.8604;

ωup1=819;

ωup2=149;

ωup3=518;

μ=(mO*mZr)/(2*mZr+mO)*1.660538782*10^(-27);

sp=2.998*10^10;

rgrnd=1.771; (*Angstrons microwave paper*)

Zgrnd={{0,0,(rgrnd*tgrnd)/(2*mO+mZr)*2*mO},{0,rgrnd*sgrnd,(-

rgrnd*tgrnd)/(2*mO+mZr)*mZr},{0,-rgrnd*sgrnd,(-
rgrnd*tgrnd)/(2*mO+mZr)*mZr}}(*center of mass*)

egrnd12=Normalize[Zgrnd[[2]]-Zgrnd[[1]]]; (*using McIntosh and Michaelian 1979 formula*)

egrnd13=Normalize[Zgrnd[[3]]-Zgrnd[[1]]]; (*using McIntosh and Michaelian 1979 formula*)

Si=(Cos[ϕgrnd Degree]*egrnd12-egrnd13)/(rgrnd*Sin[ϕgrnd Degree]); (*using McIntosh and Michaelian 1979 formular*)

Sk=(Cos[ϕgrnd Degree]*egrnd13-egrnd12)/(rgrnd*Sin[ϕgrnd Degree]); (*using McIntosh and Michaelian 1979 formula*)

Sj=-(Si+Sk); (*using McIntosh and Michaelian 1979 formula*)

Bgrnd={{-egrnd12[[1]], -egrnd12[[2]], -egrnd12[[3]], egrnd12[[1]], egrnd12[[2]], egrnd12[[3]], 0, 0, 0},{-egrnd13[[1]],-egrnd13[[2]],-egrnd13[[3]], 0, 0, 0, egrnd13[[1]], egrnd13[[2]], egrnd13[[3]]},{Sj[[1]], Sj[[2]], Sj[[3]], Si[[1]], Si[[2]], Si[[3]], Sk[[1]], Sk[[2]], Sk[[3]]}};

M={{mZr, 0, 0, 0, 0, 0, 0, 0, 0},{0, mZr, 0, 0, 0, 0, 0, 0, 0}, {0, 0, mZr, 0, 0, 0, 0, 0, 0}, {0, 0, 0, mO, 0, 0, 0, 0, 0}, {0, 0, 0, 0, mO, 0, 0, 0, 0}, {0, 0, 0, 0, 0, mO, 0, 0, 0}, {0, 0, 0, 0, 0, 0, mO, 0, 0}, {0, 0, 0, 0, 0, 0, 0, mO, 0}, {0, 0, 0, 0, 0, 0, 0, 0, mO}};(*using McIntosh and Michaelian 1979 formula*)

Gngrnd={{μ1+μ2,μ2*Cos[ϕgrnd Degree],-((μ2*Sin[ϕgrnd Degree])/rgrnd)}, {μ2*Cos[ϕgrnd Degree], μ1+μ2,-((μ2*Sin[ϕgrnd Degree])/rgrnd)},{-((μ2*Sin[ϕgrnd Degree])/rgrnd), -((μ2*Sin[ϕgrnd Degree])/rgrnd), (2*μ1)/rgrnd^2+μ2*((2-2*Cos[ϕgrnd Degree])/rgrnd^2)}};(*using Wilson,

Decius, Cross formula*)

U={{$1/\sqrt{2}$, $1/\sqrt{2}$, 0},{0, 0, 1},{$1/\sqrt{2}$, -($1/\sqrt{2}$), 0}};

Gsgrnd=U.Gngrnd.Transpose[U];

k3grnd=(ωLo3/1302.9)^2/Gsgrnd[[3,3]];

Fsgrnd={{k3grnd, a, 0},{a, b, 0},{0, 0, k3grnd}};

λ=Eigenvalues[Gsgrnd.Fsgrnd]

Simplify[Solve[{$\sqrt{\lambda[[2]]}^2$ ==(ωLo2/1302.9)^2, $\sqrt{\lambda[[3]]}^2$ ==(ωLo1/1302.9)^2}, {a,b}]]

a=a/.%35[[1,1]] (*%35 output number from last input*)

b=b/.%35[[1,2]] (*%35 output number from last input*)

Fngrnd=Inverse[U].Fsgrnd.Inverse[Transpose[U]];

MatrixForm[Inverse[U].Fsgrnd.Inverse[Transpose[U]]]

V=Transpose[Eigenvectors[Gngrnd.Fngrnd]];

No=(Abs[Inverse[V].Gngrnd.Inverse[Transpose[V]]])^(1/2);

L=V.No

AtomDisGrnd=Inverse[M].Transpose[Bgrnd].Transpose[Inverse[L]]//MatrixForm

(*Atom Displacement matrix on the ground state*)

(*Excited state*)

ϕup=99;(*from preliminary results calculation**87*)

tup=Cos[ϕup/2 Degree];

sup=Sin[ϕup/2 Degree];

rup=1.828;(*1.84*);

Zup={{0,0,(rup*tup)/(2*mO+mZr)*2*mO},{0, rup*sup, (-rup*tup)/(2*mO+mZr)*mZr},

```
        {0, -rup*sup, (-rup*tup)/(2*mO+mZr)*mZr}}
eup12=Normalize[Zup[[2]]-Zup[[1]]];
eup13=Normalize[Zup[[3]]-Zup[[1]]];
Supi=(Cos[ϕup Degree]*eup12-eup13)/(rup*Sin[ϕup Degree]);
Supk=(Cos[ϕup Degree]*eup13-eup12)/(rup*Sin[ϕup Degree]);
Supj=-(Supi+Supk);
Bup={{-eup12[[1]], -eup12[[2]], -eup12[[3]], eup12[[1]], eup12[[2]], eup12[[3]],0,0,0},
        {-eup13[[1]],eup13[[2]],-eup13[[3]],0,0,0,eup13[[1]],eup13[[2]],eup13[[3]]},
        {Supj[[1]],Supj[[2]],Supj[[3]],Supi[[1]],Supi[[2]],Supi[[3]],Supk[[1]],Supk[[2]],S
        upk[[3]]}}
Gnup1={{μ1+μ2,μ2*Cos[ϕup Degree],-((μ2*Sin[ϕup Degree])/rup)}, {μ2*Cos[ϕup
        Degree], μ1+μ2,-((μ2*Sin[ϕup Degree])/rup)},{-((μ2*Sin[ϕup Degree])/rup),-
        ((μ2*Sin[ϕup Degree])/rup), (2*μ1)/rup^2+μ2*((2-2*Cos[ϕup Degree])/rup^2)}}
Gsup=U.Gnup1.Transpose[U];
k3up=(ωup3/1302.9)^2/Gsup[[3,3]];
Fsup=({{aup, 0, 0},{0, bup, 0},{0, 0, k3up}});
λup=Eigenvalues[Gsup.Fsup]
Simplify[Solve[{√λup[[2]]^2 ==(ωup2/1302.9)^2, √λ[[3]]^2 ==(ωup1/1302.9)^2},
        {aup,bup}]]
aup=aup/.%59[[2,1]] (*%59 output number from last input*)
bup=bup/.%59[[2,2]] (*%59 output number from last input*)
Fnup=Inverse[U].Fsup.Inverse[Transpose[U]];
```

```
Gnup1. Fnup;

V1 =Transpose[ Eigenvectors[Gnup1. Fnup]]

No1 = (Abs[Inverse[V1] . Gnup1. Inverse[Transpose[V1]]])^(1/2);

Lup = V1. No1

AtomDisUp=Inverse[M].Transpose[Bup].Transpose[Inverse[Lup]]//MatrixForm

        (*Atomdisplacement matrix*)
```

APPENDIX C

MATHEMATICA NOTEBOOK TO CALCULATE FRANCK-CONDON FACTOR FOR ZIRCONIUM DIOXIDE

```
J=Transpose[(Inverse[L].Bgrnd).Inverse[M].Transpose[Inverse[Lup].Bup]];
MatrixForm[Transpose[(Inverse[L].Bgrnd).Inverse[M].Transpose[Inverse[Lup].Bup]]]
Rgrnd={{0},{0},{(rgrnd*tgrnd)/(2*mO+mZr)*2*mO},{0}, {rgrnd*sgrnd},{(-
        rgrnd*tgrnd)/(2*mO+mZr)*mZr}, {0},{-rgrnd*sgrnd},{-((rgrnd*tgrnd)/
        (2*mO+mZr))*mZr}}
Rup={{0},{0},{(rup*tup)/(2*mO+mZr)*2*mO},{0},{rup*sup},{(-
        rup*tup)/(2*mO+mZr)*mZr},{0},-rup*sup},{(-rup*tup)/(2*mO+mZr)*mZr}}
Dus=Abs[(Inverse[L].Bgrnd).(Rup-Rgrnd)];
MatrixForm[Dus]
(*FCF CALCULATION*)
ω1Up=2*π*c*ωup1;(*879.00`20.s^-1*)
ω2Up=2*π*c*ωup2  ;(*185.0`20s^-1*)
ω1Lo=2*π*c*ωLo1;(*968.00`20s^-1*)
ω2Lo=2*π*c*ωLo2 ;(*323.0`20s^-1*)
J={{Abs[J[[1,1]]], J[[3,1]]},{-J[[1,3]], J[[3,3]]}};
D0={{Abs[Dus[[3,1]]]},{Dus[[1,1]]}};
Alpha1Up=((ω1Up*atm)/hbar)*10^(-20);(*ω angluar frequency of the ocilator, in
        1/m^2*)
Alpha2Up=((ω2Up*atm)/hbar)*10^(-20); (*ω angular frequency of the oscillator, in
        1/m^2*)
Alpha1Lo=((ω1Lo*atm)/hbar )*10^(-20) ;(*ω angular frequency of the oscillator, in
        1/m^2*)
```

Alpha2Lo=((ω2Lo*atm)/hbar)*10^(-20); (*ω angular frequency of the oscillator, in 1/m^2*)

A1=(1/2)* (Alpha1Up+Alpha1Lo*J[[1,1]]^2+Alpha2Lo*J[[2,1]]^2);

B1=(1/(2A1))*(Alpha1Lo*J[[1,1]]*J[[1,2]]+Alpha2Lo*J[[2,1]]*J[[2,2]]);

C1=(1/(2A1))*(Alpha1Lo*J[[1,1]]*D0[[1,1]]+Alpha2Lo*J[[2,1]]*D0[[2,1]]);

A2=(1/2)*(Alpha2Up+Alpha1Lo*J[[1,2]]^2+Alpha2Lo*J[[2,2]]2)-A1*B1^2;

C2=(1/(2A2))*(Alpha1Lo*J[[1,2]]*D0[[1,1]]+Alpha2Lo*J[[2,2]]*D0[[2,1]]-2*A1*B1*C1);

E0=Exp[-(1/2)Alpha1Lo*D0[[1,1]]^2-(1/2)*Alpha2Lo*D0[[2,1]]^2+A1*C1^2+A2*C2^2]

a1= $\sqrt{\text{Alpha1Up}}$; a2=- $\sqrt{\text{Alpha1Up}}$ *B1;

b1=- $\sqrt{\text{Alpha1Up}}$ (C1-B1*C2);

a3= $\sqrt{\text{Alpha2Up}}$; b2=- $\sqrt{\text{Alpha2Up}}$ *C2;

F1=((2/A1)^1/2)*a1; F2=((2/A2)^1/2)*a2; F3=((2/A2)^1/2)*a3;

Nu[v1_,v2_]:=($\sqrt{\text{Alpha1Up}*\text{Alpha2Up}*\text{Alpha1Lo}*\text{Alpha2Lo}}$ /(2^(v1+v2) v1!v2!A1*A2))$^{1/2}$

$$H[v1\_,v2\_]:=\sum_{k1=0}^{v1}\sum_{k2=0}^{v1-k1}\sum_{k3=0}^{v2}\left(\frac{v1!}{k1!(v1-k1)!}*\frac{(v1-k1)!}{k2!(v1-k1-k2)!}*\frac{v2!}{k3!(v2-k3)!}*\right.$$

HermiteH[v1-k1-k2,b1]*HermiteH[v2-k3,b2]*F^{k1}*F^{k2}*F^{k3}*

If[EvenQ[k1]&&EvenQ[k2+k3],(k1-1)!!*(k2+k3-1)!!,0])

Overlab[v1_,v2_]:=Nu[v1,v2]*E0*H[v1,v2]

FCF[v1_,v2_]:= Overlab[v1,v2]^2

(*Even quata for nu3*)

ω3Up=2*π*c*ωup3;(*316`20.s^-1*)

ω3Lo=2*π*c*ωLo3 ;(*879.00`20.s^-1*)

Alpha3Up=(ω3Up*atm)/hbar *10^(-20);(*ω angular frequency of the oscillator, in 1/m^2*)

Alpha3Lo=(ω3Lo*atm)/hbar *10^(-20);(*ω angluar frequency of the ocilator, in 1/m^2*)

d=0.0;

bLo=(Alpha3Up* $\sqrt{\text{Alpha3Lo}}$ *d)/(Alpha3Up+Alpha3Lo);

bUp=(Alpha3Lo* $\sqrt{\text{Alpha3Up}}$ *d)/(Alpha3Up+Alpha3Lo);

A=2*($\sqrt{\text{Alpha3Lo}}$ * $\sqrt{\text{Alpha3Up}}$)/(Alpha3Lo+Alpha3Up);

S=(Alpha3Lo*Alpha3Up*d2)/(Alpha3Up+Alpha3Lo);

$$\text{FCF3even}[v3\_]:=((A*e^{(-S)})/(2^{v3}*v3!))\left(\sum_{kUp=0}^{v3}\left(\frac{v3!}{kUp!\,(v3-kUp)!}\right)\right)*\text{HermiteH}[0,bLo]*\text{HermiteH}[v3-kUp,bUp]*(2*\sqrt{\text{Alpha3up}})^{kUp}\,\text{If}\left[\text{EvenQ}[kUp],\frac{(2*\frac{kUp}{2}-1)!!}{(\text{Alpha3Lo}+\text{Alpha3Up})^{\frac{kUp}{2}}},0\right]^2$$

FCFeven[v1_,v2_,v3_]:=FCF[v1,v2]*FCF3even[v3]

(*Odd quanta for νu3*)

$$\text{Odd}[vLo\_,v3\_]:=\left(\frac{(A*e^{(-S)})}{(2^{v3+vLo}*v3!vLo!)}\left(\sum_{kLo=0}^{vLo}\sum_{kUp=0}^{v3}\left(\frac{v3!}{kUp!(v3-kUp)!}\right)*\right.\right.$$

$$\text{HermiteH}[vLo-kLo,bLo]*\text{HermiteH}[v3-kUp,bUp]*$$

$$(2*\sqrt{\text{Alpha3Lo}})^{kLo}*(2*\sqrt{\text{Alpha3Up}})^{kUp}$$

$$\left.\left.\text{If}[\text{EvenQ}[kLo+kUp],\frac{(2*\frac{kLo+kUp}{2}-1)!!}{(\text{Alpha3Lo}+\text{Alpha3Up})^{\frac{kLo+kUp}{2}}},0]\right)^2\right)$$

FCF3odd[v3_]:=Odd[1,v3]

FCFodd[v1_,v2_,v3_]:=FCF[v1,v2]*FCF3odd[v3]

FCFtotal[v1_,v2_,v3_]:=FCFeven[v1,v2,v3]+1.06FCFodd[v1,v2,v3]

A=TableForm[Table[{{v2,v3},FCFtotal[0,v2,v3],FCFtotal[1,v2,v3],FCFtotal[2,v2,v3],

FCFtotal[3,v2,v3],FCFtotal[4,v2,v3],FCFtotal[5,v2,v3]},{v2,0,6,1},{v3,0,5,1}]]